Monitoring the Interface of Carbon Fibre and Epoxy Microcomposites Using Raman Spectroscopy with Single Walled Carbon Nanotubes as Strain Sensors

A thesis submitted to The University of Manchester for the degree of Doctor of Philosophy in the Faculty of Engineering and Physical Sciences

2013

Siyu Jin

CONTENTS

Word count: 59,587

LIST OF FIGURES

LIST OF TABLES

LIST OF SYMBOLS

Å	Unit of length equal to 10^{-10} meters
P_z	Orbital with angular momentum quantum number of 1
sp^2	Mixing of one s and two p atomic orbitals
L_a	Lateral size of crystallite
L_c	Stacking height of crystallite
(m, n)	Indices defining the nanotube structure
$I_{//}$	Intensity of Raman line with the incident light polarised parallel to the direction of analyser
$I_{\pm}$	Intensity of Raman line with the incident light polarised perpendicular to the direction of analyser
ρ	Depolarisation ratio
ε_f	Fibre strain
τ	Interfacial shear stress
x	Distance along the fibre
r	Radius
l	Fibre length
E	Young's modulus
G	Shear modulus
n	Adjustable parameter relating to fitting stress or strain distribution
β	Shear lag parameter
R	Effective concentration cylinder in matrix

G_m	Matrix shear modulus
ν	Poisson ratio
V_m	Volume fraction of matrix
V_f	Volume fraction of fibre
E_f	Young's modulus of fibre
F	Force
Ω	Omega
$I(x)$	Intensity of the Raman peak at any given wavenumber x.
Γ	FWHM
n	The order of the reflection
λ	Wavelength
d	Spacing between planes of given Miller indices
K	Spring constant
l_0	Initial length of fibre
σ	Stress
A_0	Original cross-sectional area
l_i	Instantaneous length
l_c	Critical length
Δl	Length change
D	Average crystallite size
k	Scherrer algorithm
θ	Angle

I_D	Intensity of D band
I_G	Intensity of G band
I_{VV}	Raman band intensity of polarised configuration of VV
I_{VH}	Raman band intensity of polarised configuration of VH
S_{VV}	Raman band shift rates based on polarised configuration of VV
S_{VH}	Raman band shift rates based on polarised configuration of VH
σ_f	Fibre stress
σ_{app}	Applied stress
σ_{fra}	Fibre fracture stress
h	Height of microdroplet
L	Embed length
R	Radius of the resin block
l_d	Interfacial debonding length
ε_{app}	Applied strain
ε_f	Fibre strain
ε_m	Matrix strain

LIST OF ABBREVIATIONS

AFM	Atomic force microscopy
SWNTs	Single walled carbon nanotubes
HiPCO SWNTs	High pressure CO conversion single walled carbon nanotubes
COOH SWNTs	Carboxylic acid modified functionalized single walled carbon nanotubes
SEM	Scanning electron microscopy
XRD	X-ray diffraction
μm	Micrometer
wt%	Weight%
PAN	Polyacrylonitrile
GPa	GigaPascals
MPa	MegaPascals
kJ	Kilojoule
vol%	Volume%
IFSS	Interfacial shear strength
ISS	Interfacial shear stress
h	Hour
^{o}C	Celsius degree
nm	Nanometre
min	Minute

s	Second
FWHM	Full width at half maximum
g	Gram
HCP	Hexagonal close packed
GPCF	General purpose carbon fibre
HPCF	High performance carbon fibre
ACF	Activated carbon fibre
CNTs	Carbon nanotubes
MWNTs	Multi walled carbon nanotubes
CVD	Chemical vapour deposition
PECVD	Plasma-enhanced chemical vapour deposition
TPa	TeraPascal
RTM	Resin transfer modelling
mPa	Milli Pascal
MMCs	Metal matrix composites
CMCs	Ceramic matrix composites
VN	Normal configuration of Raman spectroscopy
VH	Polarisation configuration in which incident and scattering lights are perpendicular to each other
VV	Polarisation configuration in which incident and scattering lights are parallel to each other
Pa	Pascal
KeV	kiloelectron volt

eV	Electron volt
BSE	Back scattered electrons
KV	Kilowatts
SC	Simple cubic
BCC	Body centred cubic
FCC	Face centred cubic
mW	Milli Watts
cm^3	Cubicmetre
cm^{-1}	Wavenumber
cm	Centimetre
RBM	Radial breathing modes
mm	millimetre

ABSTRACT

Monitoring the Interface of Carbon Fibre and Epoxy Microcomposite Using Raman Spectroscopy with Single Walled Carbon Nanotubes as Strain Sensors

The University of Manchester

Siyu Jin

Doctor of Philosophy

05 August, 2013

The interfacial micromechanics of both high modulus and low modulus carbon fibres have been investigated using Raman spectroscopy. The innovative step was to make low modulus carbon fibres more Raman active by coating them with SWNTs to act as as a strain sensor. Two types of SWNTs have been employed; namely HiPCO SWNTs and COOH SWNTs.

Single fibre deformation tests were carried out and the Raman band shift rates with respect to fibre strain have been determined. Meanwhile, different SWNTs coating methods have been investigated. The method of adding COOH SWNTs into the silane layer and within a hot cured epoxy layer was found to generate the highest band shift rates. Furthermore, an investigation of the effect of SWNTs on the strength of the interface was also carried out. A coating of COOH SWNTs was found to significantly improve the interfacial shear strength.

Micromechanical tests have been carried out and the stress transfer between the carbon fibres and an epoxy resin was monitored using three different model composite geometries; namely microdroplet-fibre, a film-fibre and a standard fragmentation approach. The result of interfacial shear stress determined from microdroplet-fibre method varied and was found to be highly dependent on the droplet size and shape; this gave the lowest values of interfacial shear stress (ISS). The method of film-fibre obtained an intermediate ISS value which is between that from the microdroplet model test and the fragmentation test. The standard fragmentation test using Raman technique gives the highest ISS and HiPCO SWNTs were found to be a better strain sensor without affecting the original interfacial properties.

DECLARATION

No portion of the work referred to in the thesis has been submitted in support of an application for another degree or qualification of this or any other university or other institute of learning.

COPY RIGHT STATEMENT

To my parents, wife Lili and newborn son Tiantian

ACKNOWLEDGEMENTS

First and foremost, I would like to sincerely thank my supervisors Prof. Stephen Eichhorn and Prof. Robert Young for the guidance and encouragement during the last four years of this PhD study. Nothing can be done without your supervisions. I will be always grateful and it is of great fortune to be supervised by both of you.

I would like to thank all staff of Raman group for their kind help and especially Mr. Andrew Zadoroshnyj for his support of Raman spectroscopy and mechanical testing. I would like to express my appreciations to Dr. Christopher Wilkins for his assistance of SEM, Mr. Gary Harrison for his technical support of XRD, Mr Andrew Forrest for his help on AFM and Mr. Kenneth Gyves for his suggestions on Optical microscopy. My thanks also go to Dr. Libo Deng for his advice and helpful discussions.

I would like to thank my parents for your endless love and financial support, without you to study abroad in the UK would just a unrealistic dream for me. Finally I would like to thank my wife Ms. Lili Yang for her constant encouragement and support beside me.

CHAPTER 1 Introduction

1.1General Introduction

Carbon fibre reinforced composites are widely used in industrial applications such as transportation manufacturing, aerospace and construction due to their high strength to weight ratio. For all composite materials, the interface acts as a key role in the mechanical performance of composites since it links the fibre and matrix together and produces a combination of mechanical properties that cannot be achieved with either component acting alone. In recent years, there has been intensive research into the interfacial properties of composites. Raman spectroscopy has been proven to be a powerful, sophisticated and non-destructive tool to monitor the deformation of high performance fibres in composites. However, there are no reports on using this technique to analyse low modulus carbon fibres since they are typically less Raman active. It has been previously impossible to monitor local fibre deformation using the shifts in the Raman band position typically used for higher modulus fibres. Lower modulus carbon fibres are widely used in industrial applications such as sports equipment and more recently in the automotive sector. Therefore, it is necessary to analyse the interfacial properties of low modulus carbon fibres. This thesis demonstrates an approach to doing this by coating Single Walled Carbon Nanotubes (SWNTs) onto the fibre surface. These SWNTs are then used as strain sensors to map local stress in the fibres which are embedded in a composite. Furthermore, the effect of the nanotubes on modification of the interface has also been investigated.

This project is mainly focused on the stress transfer occurring at the interface between carbon fibres and an epoxy resin matrix. Higher modulus carbon fibres are also used in this work to compare with results with from lower modulus carbon fibres. Furthermore, an investigation of the effect of SWNTs on the strength of the interface was also carried out. Two types of SWNTs have also been investigated; namely HiPCO SWNTs and COOH SWNTs have been applied to sense strain. Their relative effects as strain sensors on the stress transfer across carbon fibre/ epoxy interface was compared. First of all, all key materials used in this project will be characterized. Both types of carbon fibres have been examined using optical microscopy, Scanning Electron Microscopy, X-ray Diffraction and Atomic Force Microscopy, in order to observe their surface and cross

section morphology, fibre diameter and crystal structure. Tensile testing of both types of carbon fibres has also been carried out to determine their modulus, breaking strain and strength. Raman spectra from both types of carbon fibre and two types of SWNTs have been recorded and all band positions characterised. Single fibre deformation tests were then carried out and the Raman band shift rates with respect to fibre strain were determined. Meanwhile, different SWNTs coating methods including SWNTs in epoxy layer or silane layer, epoxy hot cured or cold cured were investigated as the bonding between carbon fibres and SWNTs was affected by many factors. Then the best SWNTs coating method was determined according to the magnitudes of the Raman band shift rates with respect to fibre strain. Finally, micromechanical tests have been carried out and the stress transfer between the carbon fibres and an epoxy resin was monitored using three different model composite geometries; namely microdroplet-fibre, a film-fibre and a standard fragmentation approach.

1.2 Objectives

This project is carried out with the following objectives:

1. To determine the stress transfer between low modulus carbon fibres and an epoxy resin matrix. Compare model composite geometries where stress transfers from the fibre to the matrix and where transfer from the matrix to fibre takes place.
2. To find the best SWNTs coating method which will give the best sensitivity by showing the highest Raman band shift rate with respect to fibre strain.
3. To compare the HiPCO SWNTs and COOH SWNTs and find out which is better strain sensor as can successfully sense the stress transfer between carbon fibre and epoxy.
4. To quantitatively analyse the change of interfacial properties by means of interfacial shear stress with distribution SWNTs at the interfacial area.
5. To analyse three model composite geometries for monitoring the interfacial stress transfer efficiency and find the most suitable for carbon fibre/ epoxy resin composites.

6. To compare the Interfacial Shear Stress (ISS) values obtained from fragmentation using a Raman technique and from a conventional test.

1.3 Structure of Thesis

The whole thesis consists of nine chapters with the general descriptions of each chapter as follows:

- Chapter One: A general introduction to the whole project with the background of studying composite interfaces, the objectives for this project, the thesis structure and experimental flow chart.
- Chapter Two: Literature review of the study of carbon fibres, SWNTs and carbon fibre-based composites interfaces in recent years.
- Chapter Three: Background to each material characterization technique including Raman spectroscopy, tensile testing, optical microscopy, SEM, X-ray diffraction and AFM. Also this chapter provides data about the specification of all materials used in this study. Furthermore, all sample preparation methods are described.
- Chapter Four: The characterization of the key materials used in this study.
- Chapter Five: Single fibre deformation whereby Raman band shift rates with respect to fibre strain for a range of samples were determined. The best method for coating SWNTs on the carbon fibre surface as strain sensor was also determined.
- Chapter Six: Micromechanical tests using a micro-droplet method including the specific experimental methodology and sample preparation for this test, Raman point to point stress mapping along the interface and determined results of interfacial shear stress across the interface.
- Chapter Seven: Micromechanical test in epoxy film including the specific experimental methodology and sample preparation for this test. The results of stress mapping across the interface and determined interfacial shear stress for low modulus carbon fibre/epoxy and high modulus carbon fibre/epoxy sample system.

- Chapter Eight: Fragmentation test both using both conventional and Raman spectroscopy method. The results by means of interfacial shear stress for a sample system of a high modulus carbon fibre/epoxy resin, low modulus carbon fibre/SWNTs/epoxy resin and high modulus carbon fibre/SWNTs/epoxy resin.
- Chapter Nine : Final conclusions for this project including a comparison and analysis of all the results from the three different micromechanical tests, and an analysis of the two types of SWNTs used as strain sensors.

1.4 Experimental Flow Chart

The overview of the experimental approach used for this project is shown in Figure 1.1.

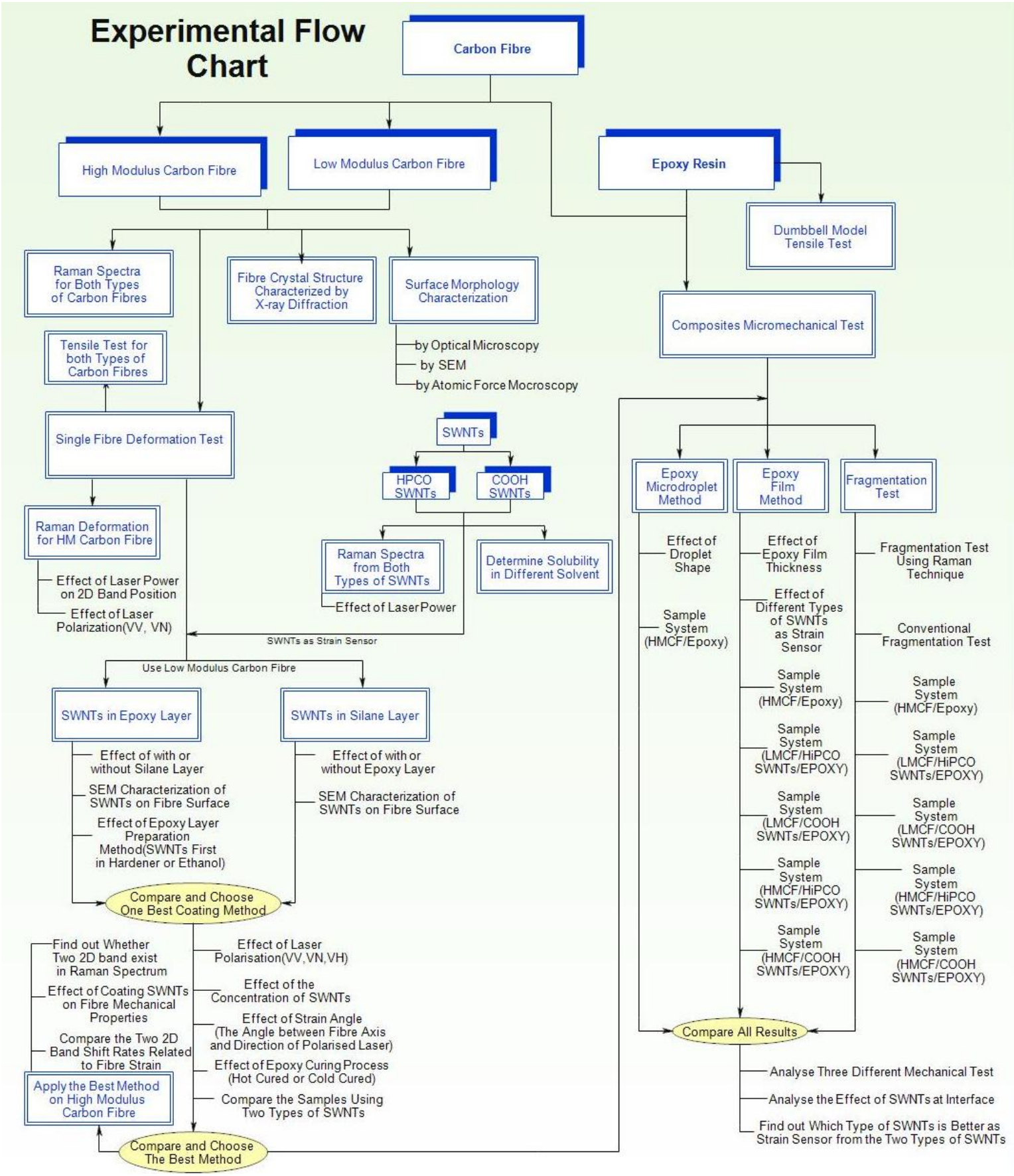

Figure 2.1 *Experimental Flow Chart for this Project*

CHAPTER 2 Literature Review

2.1 Carbon Fibre

2.1.1 General Introduction and Background

Carbon fibres are a form of carbon material that are produced in a fibrous form. The fibres have diameters about 5-10 μm and contain at least 92 wt.% carbon in composition. The carbon atoms are bonded together in crystals that are relatively well aligned parallel to the fibre axis which is the basis of the high strength to volume ratio (Fitzer, 1990).

The first carbon fibre in history can be traced back to the year of 1879, with the invention of the incandescent light bulb, where a carbonised filament of cotton thread or bamboo sliver was used. When the mostly cellulose cotton and bamboo filament was heated and carbonized, a so-called carbon fibre was created but with weak mechanical properties. A high performance carbon fibre was first produced by Roger Bacon in 1958, where whiskers of graphite in a high pressure carbon arc were found with amazing mechanical properties; tensile strength of 20 GPa and Young's modulus of 700 GPa. These fibres were just a laboratory phenomenon, and not a practical development. Later in the US, Curry Ford and Charles Mitchell created a process for making carbon fibres by heat treating rayon fibres to temperatures up to 3000°C; a Young's modulus of 172 GPa was obtained. This development proved to be the best commercially available carbon fibres at the time and also led to the entry of carbon fibres into the advanced composites industry in 1963. After that in the early 1960s, a type of carbon fibre with about 55% carbon in composition and a modulus of more than 140 GPa was made by Dr. Akio Shindo from polyacrylonitrile (PAN) precursor. In the same year William Watt of the Royal Aircraft Establishment in the UK created an even higher modulus fibre from PAN. This showed quite clearly that potential existed for increasing the properties of carbon fibres from PAN precursors and British carbon fibres were soon put into commercial production. It has to be noted that in the year around 1970 the Japanese finally took the lead in making PAN based carbon fibres for which they created a superior process. PAN was turned out to be a better precursor than rayon and they eventually dominated the word market. Later in 1970s another important process of producing carbon fibres from a petroleum pitch was found that was able to make fibres contained about 85% carbon. From that time on PAN and pitch have become the two

main precursors for producing high performance and commercial carbon fibres (Johnson *et al*., 1968).

2.1.2 The Microstructure and Mechanical Properties of Carbon Fibre

There are three types of structures that a carbon fibre can take; namely crystalline, amorphous and partly crystalline (Fitzer, 1990). A typical microstructure for a carbon fibre is shown in Figure 2.1; graphite is one structural type which forms crystalline domains. This graphite structure is made of sp^2 hybridized carbon atoms which are organized in a two-dimensional honeycomb structure in the *x*-*y* plane. Carbon atoms in one layer are bonded by covalent bonding and together with metallic bonding. The distance between the hexagonally bound carbon atoms which are part of the layers is 1.42Å. Nevertheless the distance between the layers is 3.35Å and this gives rise to the anisotropy of properties (Bacon and Tang, 1964). The covalent bonds are formed through overlap of the sp^2 hybridized orbitals, and metallic bonds are created by the delocalization of the P_z orbitals. This is the reason why graphite is a good electric conductor and a good thermal conductor in the *x*-*y* plane. The layers are connected by van der Waals' bonds; therefore the carbon layers can easily slide past each other. In the direction perpendicular to the layers, graphite is an electrical insulator and a thermal insulator. As a result, graphite is highly anisotropic which is attributed to the difference between the in-plane and out of plane bonding. Moreover, a higher modulus is obtained in the direction parallel to the plane; on the contrary a lower modulus is obtained perpendicular to the plane. The bond strength within the layer plane is about 600 kJ/gm atom, whereas the interlayer binding energy is estimated to be only 5.4 kJ/gm atom. Young's modulus parallel to the layers can be 30 times of that perpendicular to them (Peters, 1970). Similarly, for the structure of a high modulus carbon fibre, the graphene layers should be parallel to the fibre axis in order to obtain a higher modulus. This crystallographic favoured orientation is called fibre texture. In other words, for the same reason, in the direction of loading along the fibre axis it has a higher elastic modulus, higher electrical and thermal conductivities, and lower coefficient of thermal expansion also exist. When the degree of alignment of carbon layers parallel to the fibre axis is high, the fibre texture turns out to be stronger, and furthermore, the fibre density, the carbon content, the *c*-axis crystallite, fibre modulus, fibre internal strength, electrical conductivity and thermal expansion are all increased.

As shown in Figure 2.1, the carbon atom layers in a graphite structure are stacked in an AB sequence, as half of the carbon atoms straight above or below them in the nearly layers. It should be noted that this AB sequence is different to that of a hexagonal close packed (HCP) crystal structure. As a carbon fibre may have a graphite region and crystalline regions, the graphite regions of size L_a parallel to the layers while the size L_c perpendicular to the layers, in the crystalline regions, the carbon layers are not stacked in any specific sequence and are called turbostratic carbon. There is another type of carbon that is present in carbon fibres; namely amorphous carbon, which although the carbon layers are well formed, they are not parallel with each other.

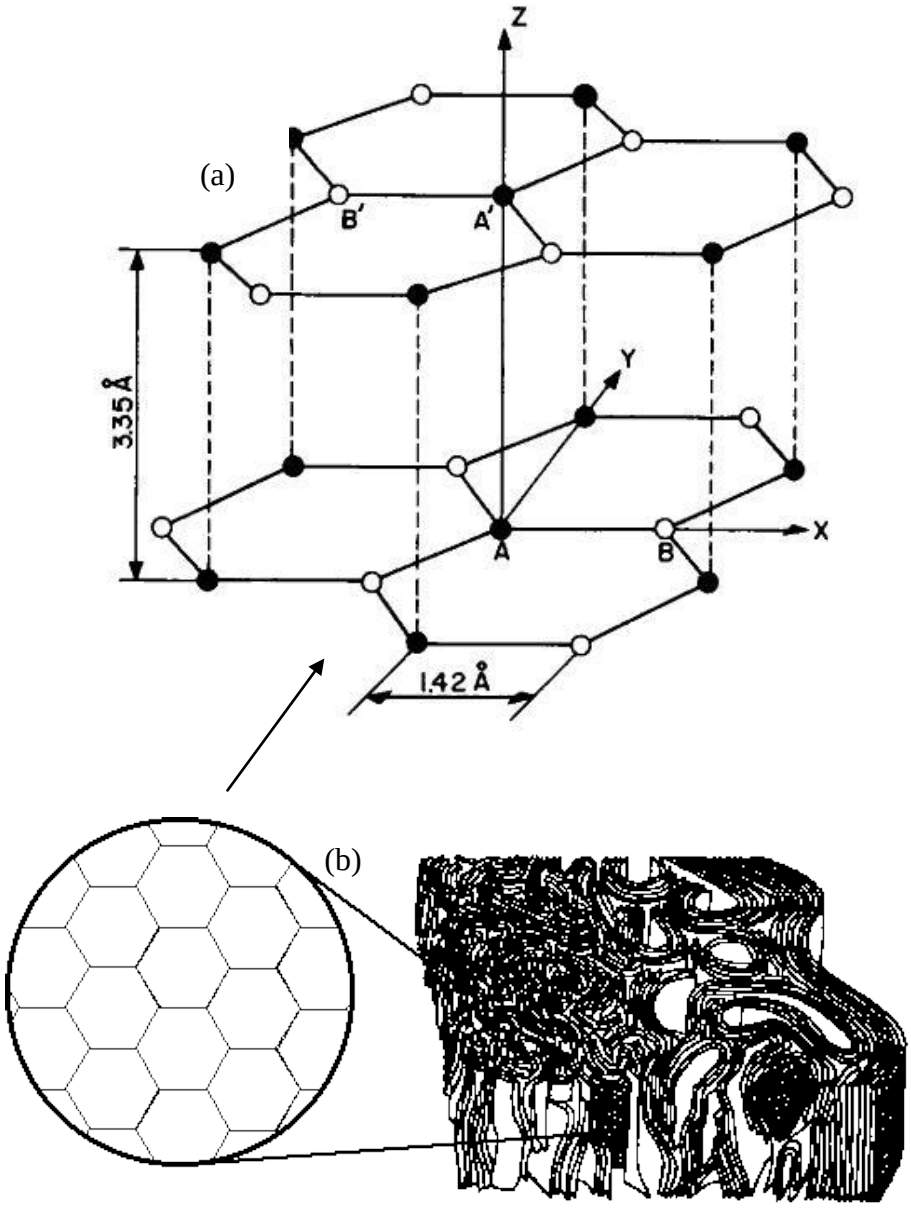

Figure 2.1 *Typical crystal structure of graphite (a) with carbon atom layers lying one on top of the other in a highly ordered; microstructure of a carbon fibre(Chuang,1994) (b) with carbon atom layers parallel to the fibre axis but less ordered for a carbon fibre(Johnson, 1982).*

The proportion of graphite in a carbon fibre varies. The fibre can be considered graphitic if the proportion is high enough, and then it is called a graphite fibre. The structure of a graphite fibre is typically polycrystalline. This is different with graphite whiskers which are single crystals with carbon layers rolled up like a scroll. Graphite whiskers have very high strengths due to their lack of flaws. However, since the cost of production of graphite whiskers is extremely high, they are rarely produced industrially. In Table 2.1, different types of fibres are compared according to their density, melting temperature and mechanical properties (Askland, 1989). There are many ways to categorize carbon fibres. Generally, they can be divided into 'high strength' and 'high modulus' as shown in Table.2.1. It can be seen the density of carbon fibres are very low. As a result it makes the specific modulus, which is defined as the ratio of modulus to density remarkably high. When compared to carbon fibres, all other fibres have their drawbacks. For example, although polymer fibres (polyethylene, Kevlar) have lower densities than carbon fibres, they also have low melting temperatures. Ceramic fibres (glass, SiO_2, SiC and Al_2O_3) not only have high densities, but most of them (except glass fibre) suffer from high production costs and are hard to make in a continuous form. It should be noted that ductility, which is defined as the strain at break for each fibre for the reason that their stress and strain curved are straight lines until fibre fracture. The ductility has proven to be the main drawback for the mechanical properties of carbon fibres. The ductility of carbon fibres is lower than Kevlar fibres, glass fibres and SiO_2 fibres. Moreover, for high modulus carbon fibres, the ductility is even lower still.

Table 2.1 *Comparison of the mechanical properties between carbon fibre and some other types of fibres which can be used to reinforce resins (Askeland , 1989).*

Material	Density (g/ cm3)	Tensile Strength (GPa)	Modulus (GPa)	Ductility (%)	Melting Temp (^oC)	Specific Modulus (10^6m)	Specific Strength (10^4m)

E-glass	2.55	3.4	72.4	4.7	<1725	2.90	14
S-glass	2.50	4.5	86.9	5.2	<1725	3.56	18
SiO_2	2.19	5.9	72.4	8.1	1728	3.38	27.4
$Al_2 O_3$	3.95	2.1	380	0.55	2015	9.86	5.3
Carbon (high-strength)	1.50	5.7	280	2.0	3700	18.8	19
Carbon (high-modulus)	1.50	1.9	530	0.36	3700	36.3	13
Kevlar	1.44	4.5	120	3.8	500	8.81	25.7
Polyethylene	0.97	2.59	120	2.2	147	12.4	27.4
ZrO_2	4.84	2.1	340	0.62	2677	7.26	4.3
BN	1.90	1.4	90	1.6	2730	4.78	7.4
Boron	2.36	3.4	380	0.89	2030	16.4	12
B_4C	2.36	2.3	480	0.48	2450	20.9	9.9
SiC	4.09	2.1	480	0.44	2700	12.0	5.1
TiB_2	4.48	0.10	510	0.02	2980	11.6	0.3
Be	1.83	1.28	300	0.4	1277	19.7	7.1
W	19.4	4.0	410	0.98	3410	2.2	2
$Al_2 O_3$ whiskers	3.96	21	430	4.9	1982	11.0	53.3
BeO	2.85	13	340	3.8	2550	12.3	47.0

whiskers							
B_4C whiskers	2.52	14	480	2.9	2450	19.5	56.1
SiC whiskers	3.18	21	480	4.4	2700	15.4	66.5
Si_3N_4 whiskers	3.18	14	380	3.7	--	12.1	44.5
Graphite whiskers	1.66	21	703	3.0	3700	43	128
Cr whiskers	7.2	8.90	240	3.7	1890	3.40	12

2.1.3 Commercial Carbon Fibres

The carbon fibres that are available on the market can be generally divided into three categories; namely general purpose carbon fibre (GPCF), high performance carbon fibre (HPCF) and activated carbon fibre (ACF). The structure of GPCF is amorphous and isotropic. It has a low tensile modulus, low tensile strength and low manufacturing cost. While the high performance type obviously have comparatively high modulus, strength and cost. Activated carbon fibres have many open micropores in its structure that can be used as adsorption sites. The form of carbon fibre is similar to active carbons, but the fibrous form leads the absorbate to get to the adsorption site faster, thus increasing the speed of the adsorption and desorption processes (Fridman and Grebennikov, 1990). It is reported that the adsorption capacity is highly dependent on the severity of activation, the increase of severity of activation can be reached by treating commercial ACF with sulphuric acid then heating up to 500 ℃ (Mochida and Kawano, 1991). Fibres from a pitch precursor can achieve higher elastic modulus than that from PAN precursor due to pitch being more graphitizable than PAN. A high modulus carbon fibre produced by du Pont can achieve a modulus as high as 894 GPa, which is more than 80% of the theoretical value for a graphite single crystal of 1000 GPa (Chuang, 1994).

2.1.4 The Production of Carbon Fibres

The carbon fibres in market are usually made from pitch or polyacrylonitrile (PAN) precursors. The processes for both precursors are shown in Figure 2.2 (Chuang, 1994). PAN fibres are fabricated by using a wet spinning technique while pitch fibres are produced using melting spinning techniques. The precursor fibres have to be transformed into a form that is flameproof and stable at temperatures as greater than 700℃ during carbonization.

As a result, they are infusibilized for the type of the pitch precursor or stabilized for the type of the PAN precursor prior to carbonization (pyrolysis). An oxidizing atmosphere is needed for both stabilization and the infusibilizing process. Infusiblization is a process for rendering the pitch infusible. Afterwards, an inert atmosphere is needed for the carbonization process to produce general-purpose and high performance fibres. Then subsequently a graphitization process is carried out in an inert atmosphere with temperatures above 2500 ℃ if a high modulus is required, while a reactive atmosphere is needed in order to obtain activated carbon fibres e.g. steam at elevated temperatures. In order to obtain high performance carbon fibres, a final process of graphitization is performed with the fibres in tension to improve the orientation. The orientation is highly related to the graphitization temperature, as the higher the graphitization temperature, the greater the preferred orientation. When producing general purpose carbon fibres using pitch as precursor, isotropic pitch is usually used which gives an isotropic carbon fibre. Anisotropic pitch, of which a good example is mesophase pitch, can be used to produce high performance carbon fibres due to it having the carbon layers preferentially parallel to the fibre axis (Chuang, 1994).

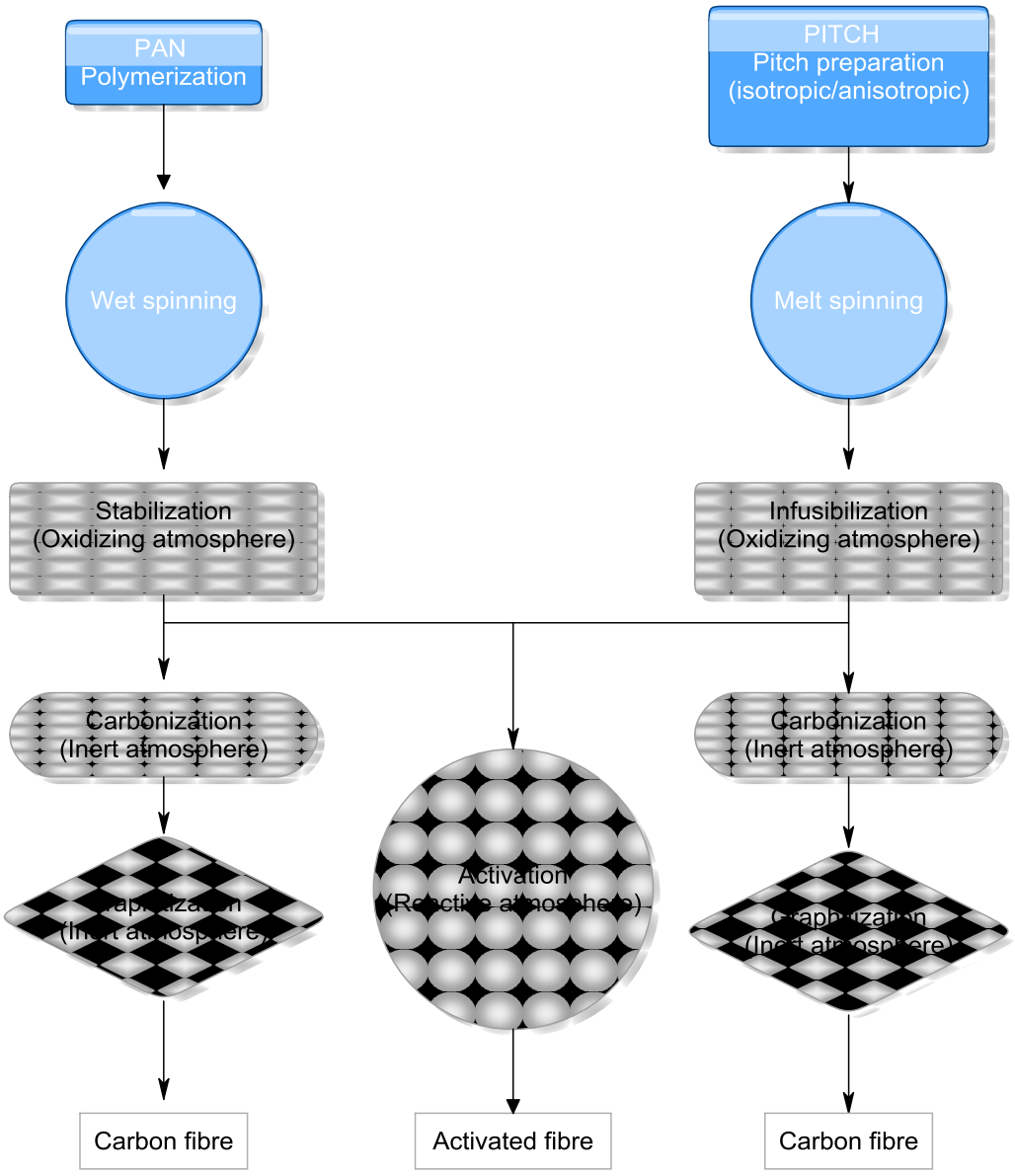

Figure 2.2 *The production process for carbon fibres from PAN and pitch precursors.*

2.2 Carbon Nanotubes

2.2.1 Structure of Carbon Nanotubes (CNT)

In the year of 1991, similar to diamond, graphite and fullerenes (C_{60}), another model of carbon named carbon nanotubes, where the graphene sheet adopts a cylindrical nanostructure was re-discovered by Iijima (1991). CNTs comprise sp^2 carbons, which connect to three nearby carbon atoms. Except the fact that it is stronger than the sp^3 carbon bonds discovered in diamond, the carbon bonds in a CNT are the same as these in graphite. CNTs could present extreme variety and fertility in structure related properties due to their small diameter and the organization of C-C and C=C bonds along the length of the nanotube (Dresselhaus *et al*., 1996). CNTs can be composed of the only one single layer of a graphitic sidewall to form single walled carbon nanotubes (SWNTs). While multi wall carbon nanotubes can be formed if around the SWNT has extra graphitic sidewalls. Generally the diameter of all CNTs is less than 100 nm, however hundreds of microns or even centimetres can be obtained for the lengths of both SWNTs and MWNTs. SWNTs usually have fewer defects than MWNTs, due to their structure being a graphitic hexagonal network (graphene) which just formed with a single piece of sp^2 hybridized carbon atoms. CNTs have great potential for a number of applications. Since only SWNTs are used in this project, the specific details of SWNTs were provided in the following section.

2.2.2 Single-wall Carbon Nanotubes (SWNTs)

As shown in Figure 2.3 one SWNT can be theoretically regarded as a layer of graphene being rolled into a cylinder. The (*m, n*) lattice vector (Dai, 2002) defines chirality which can be explained as the orientation of the graphitic hexagonal rings along the nanotube length and the diameter of SWNTs are decided by the (*m,n*) indices. A ‘zigzag’ can be achieved when $m = 0$, If $n = m$, the nanotubes are called an ‘armchair’ SWNT. The third type of SWNTs is called ‘chiral’ which have other values of *m and n*. Although in such small diameter, SWNTs can be either metallic or semiconducting (Dresselhaus *et al*., 1996). As a result, the physical properties for different CNTs can be different. For semiconducting nanotubes with the same chirality, the band gap is inversely proportional to the diameter.

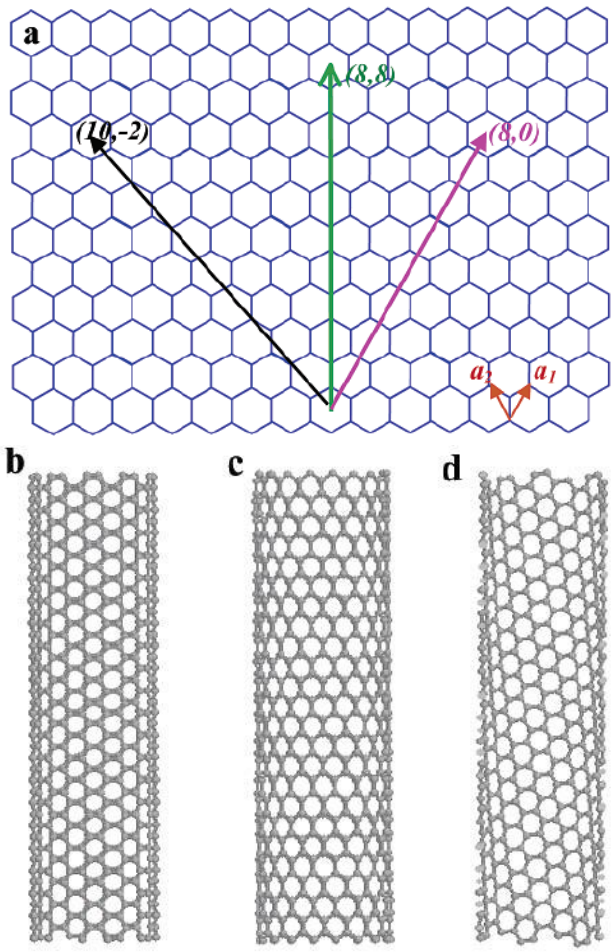

Figure 2.3 *(a) Schematic honeycomb structure of a graphene sheet (adapted from Dai (2002)). Singlewalled carbon nanotubes can be created by rolling a graphene sheet following the direction of lattice vectors.* a_1 *and* a_2 *are two basis vectors. Armchair (b), zigzag (c), and chiral (d) tubes are created by using (m,n) vectors of (8,8),(8,0) and (10,-2), respectively (Dai, 2002).*

Since SWNTs have different electric properties, for example metallic or semiconducting, properties which multi walled carbon nanotubes do not possess, they are the most suitable applicants for miniaturizing electronics (White and Todorov, 1998; Quinn and Lemay, 2006; Yao *et al*., 2000; Pop *et al*., 2006). Therefore, a good production process for mass manufacturing SWNTs at a reasonably low cost is critical for the development of carbon nanotechnology.

2.2.3Production of Carbon Nanotubes

There are three main currently used methods for producing carbon nanotubes; namely arc discharge, laser ablation and chemical vapour deposition (Dai, 2002) It should be noted that there are also many other methods that have been developed to enhance the quality and manufacturing efficiency regarding the cost and customer demand. However, it is worth mentioning that the CNTs made using all techniques always give a mixture of chiralities (Ebbesen, 1992).

2.2.3.1Arc-Discharge Method

First of all, it should be noted that the arc-discharge method is currently the most widely used technique to produce CNTs. Carbon nanotubes were also firstly discovered by using arc discharge method to produce fullerenes in 1991; CNTs were formed at the graphite electrodes (Iijima,1991). Generally, this arc discharge method is dependent on the vaporization of carbon by applying a catalyst (no catalyst is needed for MWNTs synthesis) in an inert atmosphere which can be achieved by injecting argon or helium into a synthesis chamber. The catalyst could be nickle, iron, molybdenum or cobalt. The synthesis of CNTs can be obtained from a plasma composed of carbon vapour and a catalyst vapour which is generated by the arc (Jorio and Dresselhaus, 2004; Thostenson et al., 2001). Meanwhile, arc is produced by using two graphite rods inside of an electric arc chamber. Both SWNTs and MWNTs can be produced by using this method with a yield up to 30% by weight with few structural defects (Collins *et al*., 2000).

However, it should be noted that this method is restricted in the quantity of products and requires further purification to eliminate unwanted bi-products.

2.2.3.2 Laser Ablation or Laser Vaporization Method

Similar to the arc discharge method, the synthesis of CNTs using the laser ablation method also depends on the vaporisation of solid graphite. However, the laser ablation method applies a pulsed laser to vaporize a graphite target in a reactor which is in an inert gas flowing atmosphere with a high temperature. A surface that is cooled by water is used to collect CNTs as the vaporized carbon will condensed on it. It should be noted that a narrow diameter distribution for bundles of CNTs can be achieved by using this method, and the diameter is dependent on temperature increasing speed and the composition of the catalyst (Jorio, 2004). Furthermore, this method is also restricted in

the quantity of products and requires purification to eliminate unwanted products. The SWNTs produced in this method can have a yield of about 70% by weight.

2.2.3.3 Chemical Vapour Sediment Method (CVD)

For the CVD method, a layer of catalyst particles are coated on a substrate. To produce SWNTs, the catalyst is typically iron, nickel or cobalt with a growth temperature of 850-1000 ℃. In order to produce MWNTs, a catalyst of ethylene or acetylene is needed with a growth temperature of 550 – 750 ℃ (Inami *et al*., 2007; Ishigami *et al*., 2008). The substrate is usually a quartz plate or silicon wafer. The diameter of the finally created nanotubes is highly dependent on the catalyst which is measured by the size of the metal particles. During the production process, the gas which contains carbon (ethylene acetylene, methane, or ethanol) is brought into the heated reactor sector by a process gas (nitrogen ammonia, or hydrogen). Afterwards, the gas containing carbon is decomposed at the surface of the catalyst particle to generate the CNTs. The catalyst particles migrate to the tips of the growing nanotube through the growth process or stay at the nanotube base, this is reliant on the adhesion strength between the substrate and the catalyst particle. Both SWNTs and MWNTs can be mass produced in an industrial basis by using a thermal CVD method. Meanwhile, the CNTs produced using this method have high yields but with a lower quality than those produced via arc discharge or laser ablation method. The reason for this is that the productions of CNTs using arc discharge and laser ablation have a higher temperature during the production process which benefits the annealing of defects in the CNTs. On the other hand compared with both laser ablation and arch discharge methods, the thermal CVD does not produce by products (such as soot and amorphous carbon) as well as SWNTs and MWNTs. It should be noted that among the three production methods, laser ablation is one of the most expensive (Collins *et al*., 2000).

2.2.3.4 Other Methods

A plasma-enhanced chemical vapour deposition (PECVD) method was developed to produce SWNTs with aligned arrays and controlled lengths and diameters based on using plasma modifying the growth time and temperature of the CVD method (Thostenson *et al*., 2001). Another method called the plasma torch method which can only produce SWNTs and was firstly developed in 2005 by groups from the University of Sherbrooke and the National Research Council of Canada (Kim *et al*., 2007). Similar

to the arc discharge method, this approach also uses ionized gas which is heated to a high temperature to vaporize carbon including substances and the metal catalysts. The thermal plasma is generated by high frequency oscillating currents in a coil, and is retained in an inert gas flowing atmosphere. SWNTs are finally formed on a cooling feedstock of carbon black and metal catalyst particles. For this method, SWNTs with different diameters can be produced.

Recently a high pressure conversion of carbon monoxide (HiPCO) has been developed to produce SWNTs with purity without an amorphous carbon by-product and at high production rates (Nikolaev *et al*., 1999). It was discovered that the diameter and yield of SWNTs are highly dependent on the high pressure applied during the production process; the higher the pressure applied the smaller the diameter and the higher the yield of the SWNTs obtained. The diameter can be as small as 0.7 nm and the length can be as short as around 1 μm. There is another method with which high quality, high selectivity and an extraordinary narrow diameter distribution of SWNTs can be produced; the CoMoCAT method, which is reliant on the decomposition C and CO_2. One method developed by Hafner *et al*. (1998) suggested that both SWNTs and MWNTs can be produced through the catalytic decomposition of both C_2H_4 and CO. CNTs, typically of arbitrary lengths, can be obtained at rates of milligrams per hour by using this method. Furthermore, it was discovered that SWNT bundles with 80% purity and a narrow distribution with an average diameter of 1.3 nm can be produced using the continuous wavelength of a Nd:YAG laser as a vaporization source (Kingston et al., 2004).

2.2.4 Properties of Carbon Nanotubes

Due to their extraordinary structures of hexagonal networks, there are many outstanding properties of carbon nanotubes, for example, high electrical and thermal conductivities, high mechanical strength, exceptional surface areas and good chemical inertness. The mechanical properties of different types of CNTs are shown in Table 2.2.

CNTs are one of the strongest and stiffest materials yet discovered due to the covalent sp^2 bonds between the individual carbon atoms and the hexagonal network. Lourie *et al*. (2000) tensile tested single MWNTs and reported a strength of 63 GPa. Studies carried out by Peng *et al*. (2008) suggested that an individual CNT shell could have strengths of up to 100 GPa.

CNTs will suffer plastic deformation when excessive tensile deformation is applied. This plastic deformation can start at strains of about 5% and is able to reach the maximum strain before fractured as releasing strain energy. However, for MWNTs the shear strength between neighbouring shells is weak, and so they undergo plastic deformation much sooner (Filleter *et al*. 2011).

CNTs are not nearly as strong under compression as they are in tension. Due to their high aspect ratio and hollow structure, CNTs have poor compressive properties and they are inclined to undergo buckling while under compressive, torsional, or bending stress (Jensen et al. 2007).

Table 2.2 *Mechanical properties of different types of CNTs (Belluci, 2005; Chae and Kumar, 2006; Meo and Rossi, 2006; Sinnott and Andrew, 2001; Yu et al., 2000; Demczyk et al., 2002).*

Type of SWNTs	Young's modulus(TPa)	Tensile strength(GPa)	Elongation at break(%)
SWNT(based on experiments)	1-5	13-53	16
Armchair SWNT (based on theory)	0.94	126.2	23.1
Zigzag SWNT (based on theory)	0.94	94.5	15.6-17.5
Chiral SWNT	0.92	--	--
MWNT(based on experiment)	0.2-0.95	11-63	--

2.2.5 Applications of Carbon Nanotubes

CNTs play an important role in composite materials applications. They can be added to polymers and then made into composite films or nanofibres to enhance their mechanical

performance at high temperatures (Shaffer and Windle, 1999). CNTs can also be used in polymer composites as reinforcement, or can be used as strain sensors (Cao *et al.*, 2005). A study carried out by Halary *et al.* (2004) suggested SWNTs were more sensitive than nanostructured diacetylene copolyurethane coatings when used as strain sensors to measure micromechanical behaviours using Raman spectroscopy. A recent study carried out by Sureeyatanapas and Young (2009) reported that SWNTs can be successfully applied to a glass fibre surface to sense the deformation of a fibre using Raman spectroscopy. Wei *et al*. (2010) have used CNTs as sensor to measure in-plane strains with micrometre spatial solution of both Raman active and Raman inactive materials, the experiments results are reported to be consistent with the actual values of the whole. Alexopoulos *et al*. (2013) embedded pre-stretched polyvinyl alcohol carbon nanotube fibres into glass fibre/polymer composites to enhance performance of monitoring the progressive damage accumulation inside the composite by inspecting the electrical resistance response of CNTs.

CNTs can be used in many areas such as touch sensors in touch screen such as mobile phone and the relevance electronics (Choi *et al*., 2010), corrosion sensors (Lynch *et al*., 2007) and transducers (Hierold *et al*., 2007), electrical conductors (Ramasubramaniam *et al*., 2003), chemical, environmental, biomaterials sensors (Bekyarova *et al*., 2004; Kong *et al*., 2000), pressure sensors (Li and Chou, 2004). One of great advantages for CNTs is that they can strongly affect the conductivities of polymers; the conductivity can be significantly improved by adding CNTs to a polymer matrix (Colchet *et al*., 2001). Due to their lower filler concentration than metal powder materials, CNTs also can be used in aircraft applications in order to obtain high matrix conductivity for anti-static applications (Sandler *et al*., 1999). . They also can be used as heat sinks to avoid the increase of thermal effects which could damage the materials during their operation process (Harris, 2004). Moreover, carbon nanotubes have been confirmed as good nucleating agents since they can change an exothermic reaction to a lower state if they are applied in the reaction process (Puglia *et al*., 2003) Furthermore, research carried out by Jorio and Dresselhaus (2004) suggests that SWNTs produced using an H_2 arc discharge method can be used as a H_2 storage method for fuel applications. Recently, CNTs have been used in a range of commercial products including automotive parts, rechargeable batteries, and sporting goods as boat hulls and water filters (De Volder *et al*., 2013). The progress in large-scale CNTs synthesis, purification, and chemical

modification has enabled the incorporation of CNTs in large area coatings and thin film electronics. So far, CNTs yarns and sheets already have interesting performance characteristics for applications including lightweight electromagnetic shields, super capacitors and actuators (De Volder *et al*., 2013).

2.3 Epoxy Resin

2.3.1 Introduction and Background

Epoxy resins are a category of reactive polymers and pre-polymers which have epoxide groups. Epoxy resins can react with a large variety of co-reactants including acids (and acid anhydrides), phenols, alcohols, polyfunctional amines and thiols. Moreover, epoxy resins can react with themselves during cross-linking catalytic homopolymerisation. These co-reactants are normally known as curatives or hardeners. Strong mechanical properties together with high temperature and chemical resistance can be achieved during reaction of polyepoxides with polyfunctional hardeners forms a thermosetting polymer or with themselves. Epoxy has a wide range of applications, including fibre-reinforced plastic materials, metal coatings, high tension electrical insulators, use in electronics and electrical components, and structural adhesives (Tanaka, 1988).

Epoxy resins, since they were introduced to industry in the late 1940s, have assumed an important place in the spectrum of materials available to the paint chemist (Allen, 1972). This is because the highly versatile nature of these resins allows the formulation of a wide variety of coatings systems. These epoxy coatings range from industrial baking finishes that deliver the maximum performance in solvent and chemical resistance, to maintenance systems for corrosive environments and also include can linings, overprint varnishes, and chemically resistant floor and wall coatings (Allen, 1972).

The first patents on epoxy resins derived from bisphenol and epichlorohydrin were issued to Dr. Pierre Castan, a Swiss chemist, in 1943. These patents covered the curing of a resin by anhydride curing agents, and also alkaline catalysis (Kirk and Othmer, 1957). This was followed by the discovery that epoxy resins could also be cross-linked with polyamines, giving rise to the basic two-package systems now widely used in the industrial and maintenance coatings field. In addition, the versatility of epoxy resins

was further enhanced by the development of the technology of esterifying epoxy resins with drying oil fatty acids. This advance made possible a line of varnish-like compositions of superior chemical resistance and toughness which account for a large percentage of the epoxy resins used in surface coatings (Allen, 1972). Work on these epoxy resin ester varnishes was carried out by S. O. Greenlee and his colleagues, then associated with the Devoe and Raynolds Company. Additional important contributions were made during this period by the Shell Development Co. and Shell Chemical Co. In 1948, Shell Chemical Co. initiated extensive programs to develop markets for all types of epoxy resins (Hamerton, 1996). During this period, Devoe and Raynolds also marketed epoxy resins and epoxy resin esters as well as proprietary paints based on these materials. As the demand for epoxy resins began to grow, other manufacturers entered the market: Ciba Products Co., Dow Chemical Co., Union Carbide Corp., and Reichhold Chemicals, Inc. Each of these companies now also markets a line of epoxy resin curing agents.

2.3.2 Araldite Epoxy Resin

The cold curing epoxy laminating system Araldite LY 5052/Hardener HY 5052 meets the requirements for a large range of applications due to its outstanding features. The mix ratio for the resin and hardener is shown in Table 2.3. The viscosity of the components allows mixing at room temperature and a complete impregnation of all current reinforcement fibres like glass, carbon and aramid. As the viscosity build up over time, as shown in Table 2.4, the low viscosity build-up makes it suitable for processing methods such as wet lay-up and RTM. Depending on the required properties the system can be cold or hot-cured (Huntsman Corporation, 2010).

Table 2.3 *The mix ratio of the resin and hardener (Huntsman Corporation, 2010).*

Mix ratio	Parts by weight	Parts by volume
Araldite LY 5052	100	100
Hardener HY 5052	38	47

Table 2.4 *Viscosity build-up (Huntsman Corporation, 2010).*

Temperature(^{o}C)	Viscosity	Time
25 ^{o}C	To 1500 mPa s	50~60
	To 3000 mPa s	90~110
40^{o}C	To 1500 mPa s	40~45
	To 3000 mPa s	50~60
60^{o}C	To 1500 mPa s	15~18
	To 3000 mPa s	18~22

2.4 Composite Interfaces

2.4.1 Theories of Adhesion and Types of Bonding

The form of bonding not only relies on the molecular structure and chemical organization and atomic assembly of the fibre and matrix, but also on the morphological properties of the fibre and the diffusivity of the interface properties and elements in each component. As a result different fibre-matrix systems have different interfacial bonding characteristics, as shown in Figure 2.4 which including molecular engagement (a), electrostatic attraction (b), inter diffusion of elements (c), chemical reaction between group A on one surface and group B on the other surface(d), chemical reaction following forming new compounds (e) and mechanical interlocking (f) (Kim and Mai, 1991). In general adhesion is highly dependent on the structure and mechanism of the material. However we should not neglect the impact of other bonding, for example the hydrogen and van der Waals. These mechanisms occurred at the interfacial region are highly possibly in the form of combination of types of interfacial bonding rather than just one type of isolation bonding, which just a few exists(Kim and Mai, 1993). However, in this work the chemical bonding of (d) and (e) could have more significant impact on the interfacial bonding as the coating of SWNTs at interface will affect the

chemical reaction between the fibre and epoxy matrix, which will be analysed in this study as well.

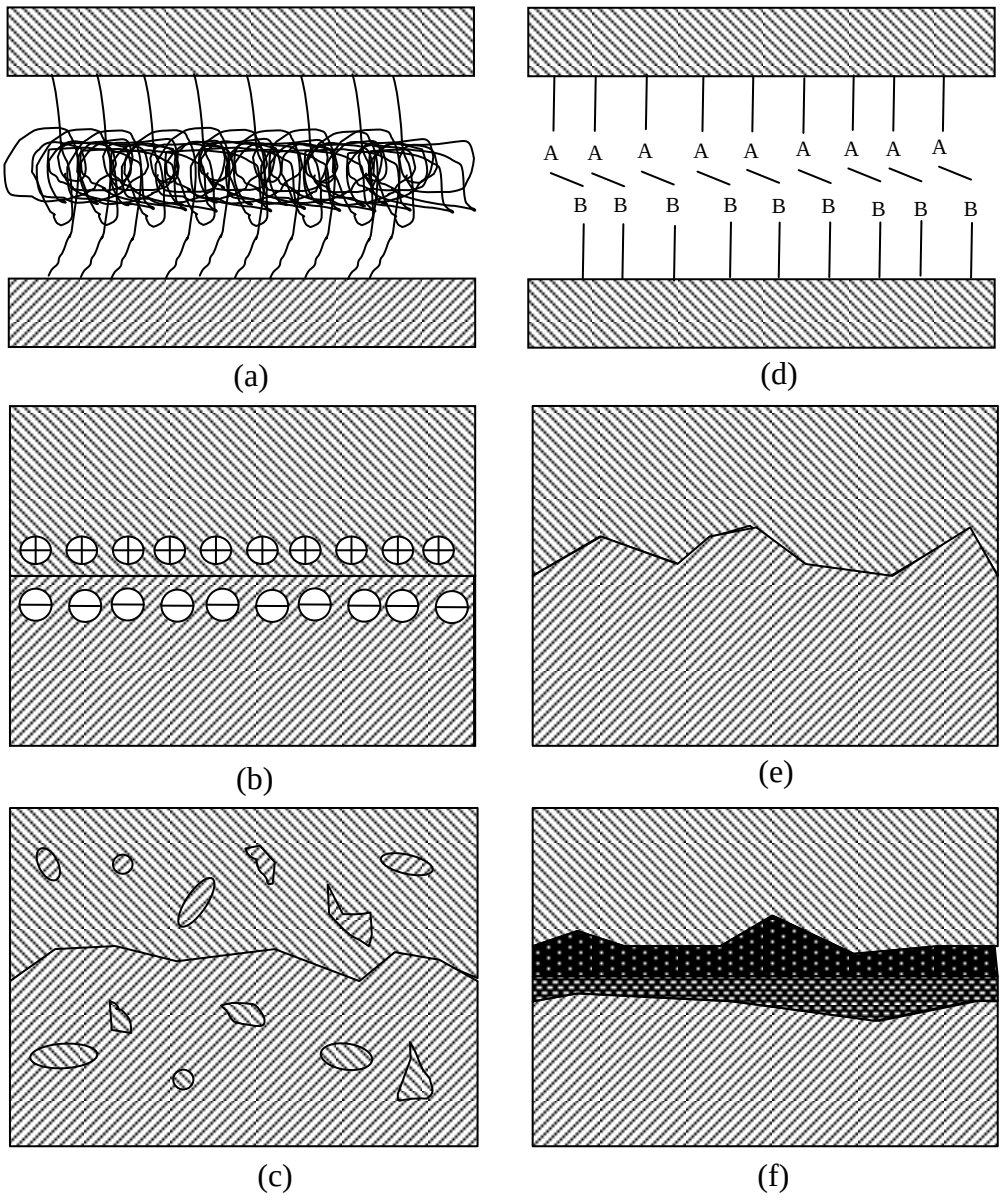

Figure 2.4 *Interface bonds formed (a) by molecular entanglement; (b) by electrostatic attraction; (c) by inter diffusion of elements; (d) by chemical reaction between group A on one surface and group B on the other surface; (e) by chemical reaction following forming new compounds, particularly in MMCs; (f) by mechanical interlocking.*

2.4.2 Electrostatic Attraction

It should not be neglected that at the interfacial area the variation in electrostatic charge between each element is possibly playing a very important role in attractive bonding. The strength of the interface will rely on the charge density. This attraction may not have a critical influence on the ultimate bond strength of the interface; however it could be extremely significant if the fibre surface is coated with a coupling agent (Plueddemann, 1988). According to a study by Plueddemann in 1988, this type of bonding is the reason why silane finishes are particularly efficient for convinced acidic or neutral reinforcements like glass, silica, and alumina, but are not useful for alkaline surfaces such as magnesium, asbestos, and calcium carbonate.

2.4.3 Chemical Bonding

In general, chemical bonding is traditional and well known of all bonding types. Different from the physical adsorption mechanism which is dependent on van der Waal forces or the acid-based interaction, the chemical bonding mechanism is rooted in the initial bond at the interface (Buxton and Baillie, 1995). For polymer matrix composites research the chemical reaction at the interface is of great use as it can help to improve the application of silane coupling agents between glass fibres and thermoset and amorphous thermoplastic matrices. As for carbon fibres, in order to enhance chemical bonding with many different polymer resins surface oxidative treatments have been used for many years (Buxton and Baillie, 1995). Buxton and Baillie (1995) suggested that the adhesion consists of two procedures: the first procedure is the elimination of a weak layer with its structure similar to graphite from the fibre surface especially at low levels of treatment; and the second part is chemical bonding at the acidic regions. Nonetheless much further research is still required to prove this theory.

The main points of this procedure of adhesion are that the interfacial bond is generated by a chemical reaction which happens between the chemical group on the fibre surface and another “friendly” chemical group in the matrix resin (Buxton and Baillie, 1995). One good example of this is the reaction between a silane group in an aqueous solution of a coupling agent and the hydroxyl group at the glass fibre surface; more specifically a group like vinyl will react with the epoxide group in the matrix.

2.4.4 Mechanical Bonding

Mechanical bondings involve exclusively mechanical interlocks at the fibre surface. In most cases mechanical bonding is generated from mechanical anchoring upgraded by surface oxidation treatments, which create various pits and corrugations (Kim, 1998). A good example of this is for carbon fibres a large surface area is known to be the main mechanism of bonding at the interface. However if the re-entrant angles on the fibre surface are not enough, the strength of this type of interface is not very high under transverse tension, conversely the strength in longitudinal shear possibly will be considerable; this is also dependent on the degree of roughness (Kim and Mai, 1998).

Additionally there are many different types of internal stresses existing in composite materials as well that arise from shrinkage of the matrix material and the differential thermal expansion between the fibre and matrix during the manufacturing process. Along with these stresses, the residual clamping stress which performs along the fibre direction gives a synergistic advantage over the mechanical anchoring mentioned previously. These mechanisms have offered the most important bonding at the interface of many CMCs and are extremely significant in modulating their fracture resistance and R-curve behaviour.

2.5Raman Spectroscopy

2.5.1 The Raman Effect

The Raman Effect was first theoretically predicted by Smekal in 1923 (Loader, 1970) but was experimentally observed by Sir C.V. Raman in 1928. Due to this discovery and his succeeding work on the effect, Sir C.V. Raman was honoured with the Noble Prize for Physics in 1930 (Loader, 1970). During his study of molecular light scattering Raman directed a beam of sunlight through a liquid, the sunlight being condensed by a telescope. He detected that the track of the light was totally extinguished when two complementary blue-violet and yellow-green light filters were positioned between the telescope and the container of liquid (Loader, 1970). Conversely, the track became visible when the yellow filter which was behind the container was placed between the

container and the observer's eye. This revealed that the light somehow had been amended by its route through the liquid (Colthup *et al*., 1990).

In a paper submitted to the Royal Society later in 1928, Raman demonstrated the photographically recorded spectra of several liquids including carbon tetrachloride and benzene. The latter spectrum was recorded by employing the 4358Å lines of mercury from a 600 ml vacuum distilled sample, a 3000 c. p. lamp and a 25 hour exposure of the photographic plate (Colthup *et al*., 1990).

During the latter two decades, a great many sources had been tried but all suffered from the instability and difficulty with unnecessary emission lines of equivalent intensity to the preferred exciting line (Colthup *et al*., 1990). The most significant progress in emission lamps emerged in 1952 with the Toronto arc mercury lamp which consists of a four-turn helix of Pyrex tubing. Although the this lamp was able to radiate as much as 50 Watts of energy in the 4358 Å emission lines of mercury, only a small fraction of this excites the Raman spectrum (Colthup *et al*., 1990). Later in 1962 the pulsed ruby masers were used by Porto, Stoicheff and Wood to obtain the Raman spectra of some powerfully scattering liquids (Colthup *et al*., 1990). During the last few years, marvellous improvements have been achieved using lasers and in spectrometer design, with the consequence that Raman spectroscopy has been fully revolutionized, even if these experiments were time-consuming and complicated at that time (Lawrence, 1975). The entire Raman spectrum of a 10 µl fluid sample directly from the container was able to be recorded in less than twenty minutes by using lasers as high power monochromatic sources. Furthermore, excellent quality spectra were obtained from solids, gases and single crystals of all colours and from as little as 0.1 µl of liquid without huge complexity (Colthup *et al*., 1990).

From the time of the invention of the laser, exposure times used by Raman had been reserved for the study of high definition gas phase spectra and later on improvements have been made and it started to be used Pharmaceutical industry, Petrochemistry, industrial chemistry, material science and so on due to its non-destructive analysis and can provide rich information, which including chemical composition and the structure of the investigated materials (Colthup *et al*., 1990).

2.5.2 General Considerations

Once light traverses a transparent medium a small portion of it is scattered by the molecules (Clark, 1982). This scattering consists of two different parts:

a. Rayleigh scattering, for which the light is elastically scattered in all directions by the molecules.
b. Raman scattering, for which the light is inelastically scattered by the molecules. Raman scattering is the weaker of the two effects, however it yields information related to the vibrational and rotational energy levels of the molecules.

If the light scattering from the sample is monochromatic and the scattered light is inspected by a spectrometer, a series of emission lines can be detected (Clark, 1982). The most intense line occurs at the same frequency as the exciting monochromatic light and is caused by Rayleigh scattering. Lines located on both sides of the Rayleigh line are much weaker and are due to the Raman emissions. The Raman emissions on the low frequency side of the Rayleigh line are called Stoke's lines, which have higher intensity than the anti-Stoke's lines. The anti-Stoke's lines are located at the high frequency side of the Rayleigh line (Clark, 1982).

This intensity difference between the two lines is due to the population diversity among the different vibrational energy levels of the molecule. The incoming light is much more likely to interact with a molecule in the ground state and excite it to a higher state rather than collide with a molecule in one of the higher energy states and make it lose energy and fall back to the ground state. This is because at room temperature there will be many more molecules in the ground vibrational state than in the higher vibrational state (Colthup *et al*., 1990).

Once the molecules are excited by the light, they will lose energy and go to a higher vibrational state, then appear with a low frequency. On the other hand, if it goes through a downward transition it will acquire energy and turn up at a higher frequency (Clark, 1982). The dislocation of these lines from the Rayleigh line evaluated in wavenumbers (cm^{-1}) is determined to correspond to the frequencies of the molecular vibrations. What is worth mentioning is that these frequencies can sometimes be measured by absorption spectroscopy using infrared radiation. The Raman and infrared spectra are not

alternatives, and they are both necessary if the maximum amount of information is to be acquired about a molecule (Clark, 1982).

The activity of a specific vibrational mode in the infrared region relies on whether or not there is a change in the dipole moment during the vibration (Clark, 1982). However for a mode to be Raman active there must be a modification in the polarisability of the molecule. This modification can be regarded as being a change in the shape of the electron cloud surrounding it.

2.5.3 Polarisation Measurements

Once the light which illuminating the sample is polarised and monochromatic, and when an analyser is positioned between the light and the spectrometer, the Raman lines will be observed to have diverse intensities for different directions of polarisations of the incident beam.

If $I_{//}$ is the intensity of a Raman line with the incident light polarised parallel to the direction in which the analyser passes the maximum amount of light, and $I_{\pm}$ is the intensity of the line with the incident radiation polarised perpendicular to that direction, then it is possible to define the depolarisation ratio, ρ, as follows (Colthup *et al*., 1990):

$$\rho = \frac{I_{\pm}}{I_{||}} \qquad (2.11)$$

In theory a sample is enlightened by a laser and the maximum value of ρ is 0.75. A line is defined to be depolarized as ρ arises only from non-fully symmetric vibrations. When ρ is less than 0.75, the line is said to be polarised and can only arise from a totally symmetric vibration (Colthup *et al*., 1990). By determine the depolarisation ratios of all the lines in the Raman spectrum of all liquid samples, the allocation of the lines can be made more clearly because of the entirely symmetric modes of vibration.

2.6 Stress Transfer Study by Using Raman Spectroscopy

Raman Spectroscopy has been widely used to study the stress transfer at fibre/matrix interface due to its effective and non-destructive stress mapping along the interface. The study carried out by Young (1996) proved that Raman spectroscopy is an extremely powerful technique for monitoring the high performance fibres (including Kevlar fibres and high modulus carbon fibres) deformations in the model composite used for conventional micromechanical test methods such as fragmentation, pull-out and microbond tests. Mottershead and Eichhorn (2007) have successfully determined the stress transfer between cellulose fibre and polyester resins. Sureeyatanapas and Young (2009) have successfully monitored the stress transfer between glass fibre and epoxy resin matrix by using Raman spectroscopy with applying single walled carbon nanotubes (SWNTs) at the interface as strain sensor.

2.6.1 Stress Transfer in Fragmentation

The mechanics of stress transfer between a high modulus fibre and low modulus matrix are analyzed in this study. A model that stress transferred from matrix to fibre is shown in Figure 2.5, for which a single fibre embedded in matrix model before and after deformation is displayed. It shows that the vertical stress lines operating along the fibre/matrix interface turned into distorted after deformation. The matrix and the fibre undergo different axial displacement locally due to their elastic moduli difference which results in a shear strain at the interface. At the central region of the fibre, the maximum fibre strain in the fibre can reach the applied matrix strain. However, the strain in both fibre ends will be less than that in the matrix (Matthews and Rawkings, 1994).

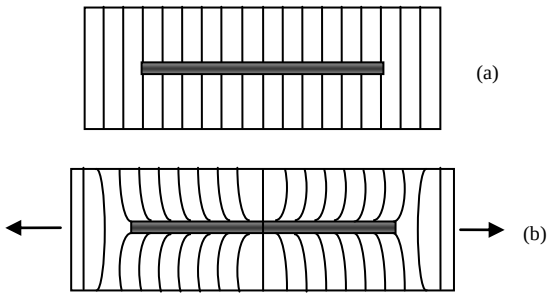

Figure 2.5 *Schematic diagram of a high modulus fibre embedded in a low modulus matrix (a) before deformation and (b) under deformation (Matthews and Rawkings, 1994).*

2.6.1.1Elastic Shear-Lag Model

Elastic shear-lag can be used to analyse axial stress in an embedded fibre. Cox's and Nairn's shear-lag model are the two that mainly used in analysis of axial stress transfer between fibre and matrix (Cox, 1952; Nairn, 1997).

For Cox's shear-lag model, it only can be used when the following conditions meet (Cox, 1952). Firstly, both matrix and fibre should be in elastic state under deformation. Secondly, the fibre should be isotropic and can be regarded as a uniform cylinder. Thirdly, the bonding between the fibre and matrix should be perfect and stress transferred through the shear at interface. Moreover, the stress at both fibre ends should be equal to zero.

Fibre strain (ε_f) and interfacial shear stress (τ) can be obtained by using Equation 2.12 and Equation 2.13 respectively.

$$\varepsilon_f = \varepsilon_m \left[1 - \frac{\cosh\beta\left(\frac{l}{2} - x\right)}{\cosh\beta\frac{l}{2}} \right] \tag{2.12}$$

$$\tau = E_f e_m \left[\frac{G_m}{2E_f \ln\left(\frac{R}{r}\right)} \right]^{\frac{1}{2}} \left[\frac{\sinh\beta\left(\frac{l}{2} - x\right)}{\cosh\beta\frac{l}{2}} \right] \tag{2.13}$$

Where x is the distance along the fibre, r is the fibre radius, ε_m is matrix strain and ε_f is fibre strain, l is the length of the fibre, E is Young's modulus and G is shear modulus, the subscript m and f means matrix and fibre respectively β is the an adjustable parameter and can be obtained by using Equation 2.14.

$$\beta = \left[\frac{2G_m}{E_f r^2 \ln\frac{R}{r}} \right]^{\frac{1}{2}} \tag{2.14}$$

Where R is an effective concentration cylinder in matrix (Feillard *et al*., 1994), G_m can be obtained by using Equation 2.15.

$$G_m = \frac{E_m}{2(1+\nu)} \tag{2.15}$$

ν is Poisson's ratio of matrix.

It can be seen only an effective cylinder around the fibre will affect the stress transfer rather than the whole matrix.

For Nairn's shear-lag model, it is based on the improvement of Cox's shear-lag analysis which is incorrect for low volume fraction composites and moreover, the displacement boundary conditions are inaccuracy as well (Nairn, 1997).

The fibre strain (ε_f) and interfacial shear stress (τ) can be obtained by using Equation 2.16 and Equation 2.17 respectively.

$$\varepsilon_f = \varepsilon_m \left[1 - \frac{\cosh\beta\left(\frac{l}{2} - x\right)}{\cosh\beta\frac{l}{2}} \right] \tag{2.16}$$

$$\tau = E_f e_m \left[\frac{G_m}{2E_f \ln\left(\frac{r_2}{r_1}\right)} \right]^{\frac{1}{2}} \left[\frac{\sinh\beta\left(\frac{l}{2} - x\right)}{\cosh\beta\frac{l}{2}} \right] \tag{2.17}$$

It should be noted that the β here is different than the β of Cox's model (Nairn, 1997). The β here gives reasonable prediction of the stress transfer and strain energy in a finite fibre in an infinite matrix composite. The β here can be obtained by using Equation 2.18.

$$\beta = \left[\frac{2}{r_1^2 E_f E_m} \left[\frac{E_f V_f + E_m V_m}{\frac{V_m}{4G_f} + \frac{1}{2G_m}\left(\left(\frac{1}{V_m}\right)\ln\left(\frac{1}{V_f}\right) - 1 - \frac{V_m}{2}\right)} \right] \right]^{\frac{1}{2}} \tag{2.18}$$

where G_m is the same as that of Cox's model, r_1 and r_2 are fibre radius and matrix radius around fibre respectively. V_m and V_f are the volume fraction of matrix and fibre respectively, they can be calculated by using Equation 2.19 and Equation 2.20.

$$V_m = \frac{r_2^2 - r_1^2}{r_2^2} \tag{2.19}$$

$$V_f = \frac{r_1^2}{r_2^2} \tag{2.20}$$

It is reported that Nairn's shear-lag model was able to predict the average axial stress in the fibre as well (Nairn, 1997).

A typical schematic diagram of fibre strain distribution and interfacial shear stress (ISS) distribution predicted by Nairn's elastic shear-lag model are shown in Figure 2.6(a). It suggested that fibre strain at both fibre ends are zero and it increases and approaches the matrix strain along the interface to the central region. For ISS, it has the highest value at both fibre ends and decreases to zero at the middle region.

2.6.1.2 Plastic Deformation Model

The matrix system experiences plastic deformation when the applied deformations are in some specific high levels. When plastic deformation occurs, the matrix undergoes plastic yielding, which usually started from both fibre ends and then propagated to the central region of the fibre along the interface. The force balance approach between the shear and tensile stress can be expressed as in Equation 2.21 (Kelly and Tyson, 1965).

$$\sigma_f \pi r^2 = \tau 2\pi r \frac{l_c}{2} \tag{2.21}$$

where l_c is critical fibre length and d is the fibre diameter, σ_f is the fibre stress can be calculated by using Equation 2.22.

$$\sigma_f = \frac{2\tau l_c}{d} \tag{2.22}$$

The fibre strain (ε_f) distribution and interfacial shear stress (τ) which is equal to the shear yield stress of the matrix (τ_y) in the plastic yielding region are expressed in Equation 2.23 and Equation 2.24.

$$\varepsilon_f = \frac{2\tau_y}{E_f r}\left(\frac{l}{2} - x\right) \tag{2.23}$$

$$\tau = \tau_y \tag{2.24}$$

A typical schematic diagram of the fibre strain distribution and the interfacial shear stress (ISS) distribution with plastic deformation occurred at both fibre ends are shown in Figure 2.6(b). It can be seen that fibre strain increase linearly to the transition point in the plastic deformation region, then in the elastic region fibre strain distribution undergoes elastic shear-lag model. For the ISS distribution, it is constant with the value of matrix shear yield stress at the plastic deformation region and in the elastic deformation region it has the highest value at both end of this region and decreased to zero at the middle of this region.

2.6.1.3 Interfacial Debonding Model

Interfacial debonding could occur when the deformation of the composite are higher than a specific level. For this region, the partially-elastic model proposed by Piggott (1980) can be used. This model predicted that there is a perfect bonding between fibre and matrix at the central region of the interface, and debonding happened at both fibre ends. Fibre strain (ε_f) and interfacial shear stress (τ) in the debonded region can be calculated by using Equation 2.25 and Equation 2.26.

$$\varepsilon_f = \frac{2\tau_i}{E_f r}\left(\frac{l}{2} - x\right) \tag{2.25}$$

$$\tau = \tau_i \tag{2.26}$$

where τ_i is friction shear stress.

A typical schematic diagram of the fibre strain distribution and the interfacial shear stress (ISS) distribution with interfacial debonding occurred at both fibre ends are shown in Figure 2.6(c). It can be seen that fibre strain increase linearly to the transition point in the debonded region, then in the elastic region fibre strain distribution undergoes elastic shear-lag model. For the ISS distribution, it is constant with the value of equal to friction shear stress at the debonded region and in the elastic deformation region it has the highest value at both end of this region and decreased to zero at the middle of this region.

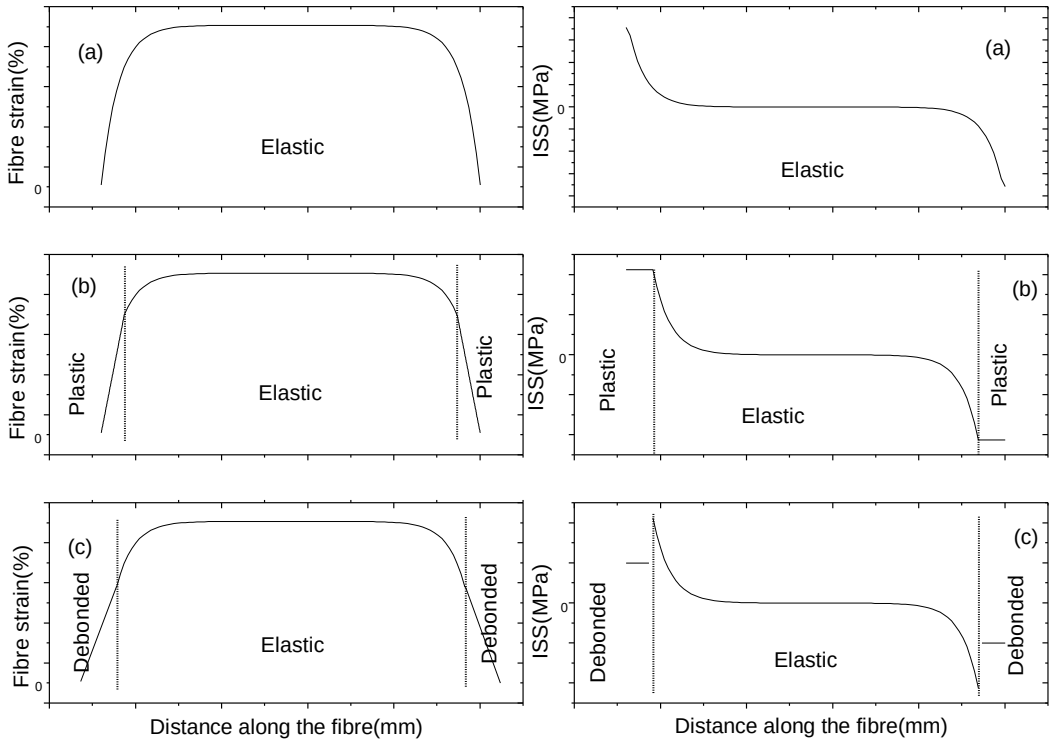

Figure 2.6 *Typical fibre strain and interfacial shear stress (ISS) distributions analysed by (a) elastic shear-lag model, (b) plastic deformation model, and (c) interfacial debonding model respectively.*

2.6.2 Stress Transfer in Pull-out Test

One significant deference of a pull-out test than a fragmentation is that stress is transferred from the high modulus fibre to the low modulus matrix. Bannister *et al.* (1995) have analysed the stress transfer in a single fibre pull-out test for Kevlar/epoxy microcomposite system by using Raman technique and also the conventional method. It is reported that the behaviour undergoes elastic shear-lag analysis at low fibre strains and then plastic deformation occurred at the interface with the increasing of fibre strains. Afterwards, as the applied deformation levels continue increasing, the debonding takes place and it propagates along the interface until the entire fibre is debonded, then the fibre is pulled out from matrix with a frictional shear stress. A model of a typical pull-out process is shown in Figure 2.7 with three different stages including (a) without stress on the fibre (b) stress transfer length reached part of the fibre (c) stress transfer length reached the entire fibre.

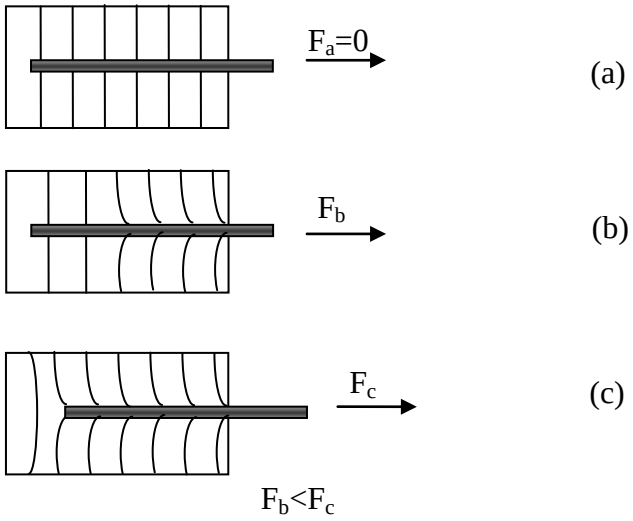

Figure 2.7 *Schematic diagram of a pull out test (a) without stress on the fibre (b) stress transfer length reached part of the fibre (c) stress transfer length reached the entire fibre.*

The elastic shear-lag model, plastic shear-lag model and deboned model described in Section 2.6.1 can also be applied to analyse the pull-out test. Typical fibre strain and interfacial shear stress (ISS) distributions of a pull-out test in shear-lag model, plastic shear-lag model and debonded model are shown in Figure 2.8 respectively.

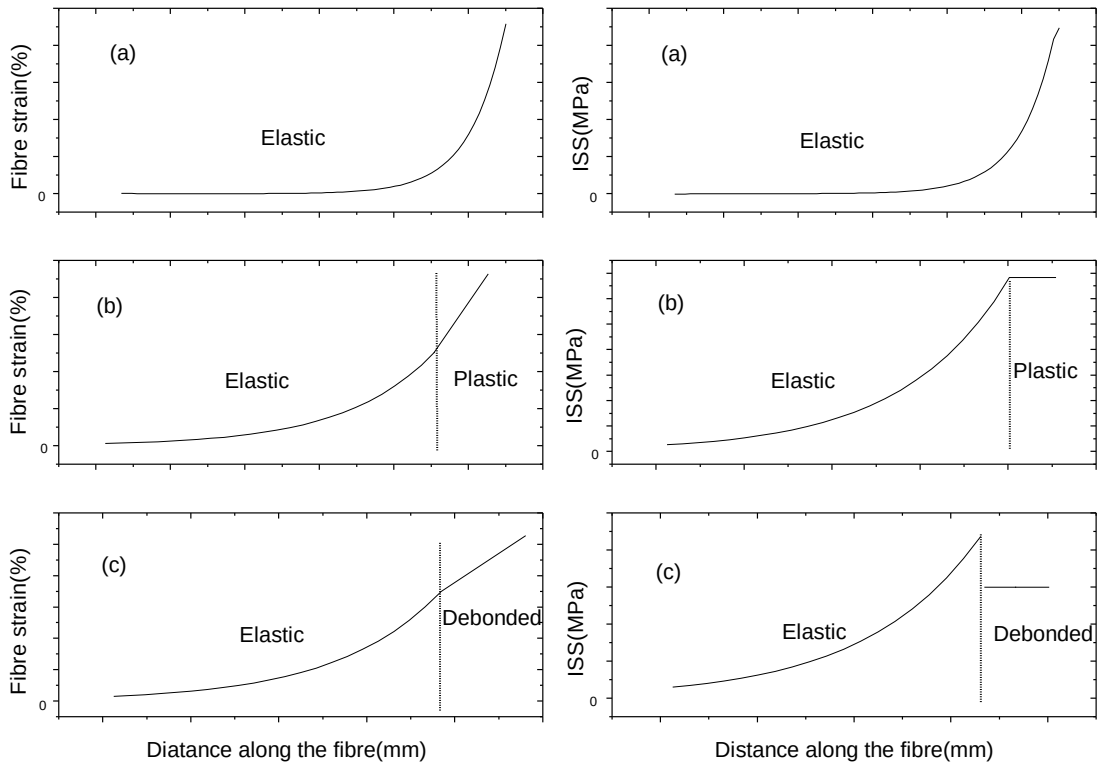

Figure 2.8 *Typical fibre strain and interfacial shear stress (ISS) distributions for pull-out test analysed by (a) elastic shear-lag model, (b) plastic deformation model, and (c) interfacial debonding model respectively.*

References

Alexopoulos, N.D., Jaillet, C., Zakri, C., Poulin, P. and Kourkoulis, S.K. (2013) Improved strain sensing performance of glass fibre polymer composites with embedded pre-stretched polyvinyl alcohol carbon nanotube fibres. Carbon, 59, pp. 65-75.

Askland, D.R. (1989) *The Science and Engineering of Materials*, 2nd edition. PWS-Kent. pp.591.

Amateau, M.F. (1976) Progress in the development of graphite-Al composites using liquid infiltration technology. *J.Composites Mater*. 10, pp. 289-296.

Allen, R.A. (1972) Epoxy resins in coatings, *Federation of societies for paint technology*, pp. 7-19.

Bacon, R. and Tang, M.M. (1964) Carbonization of cellulose fibres.2. physical properties study. *Carbon*, 2(3), PP. 221-&.

Bannister, D.J., Andrews, M.C., Cervenka, A.J. and Young, R.J. (1995) Analysis of the single fibre pull-out test by means of Raman Spectroscopy: Part 2. Micromechanics of deformation for an Aramid/Epoxy system. *Composite Science and Technology*, 53, pp. 411-421.

Belluci, S. (2005) Carbon nanotubes: Physics and applications. *Physica Status Solidi*, 2(1), pp. 34–47.

Bucher, R.A. and Hinkley. J.A. (1992) Fibre/matrix adhesion in graphite/peek composites. *Thermoplastic Composite Mater*, 5, pp. 2-13.

Buxton, A. and Baillie. C.A. (1995) Predicting the behaviour of the carbon-fibre/epoxy interface under different service conditions. *Composite Interface*, 3, pp. 1415- 1423.

Bekyarova, E., Davis, M., Burch, T., Itkis, M.E., Zhao, B., Sunshine, S. and Haddon, R.C. (2004) Chemically functionalized single-walled carbon nanotubes as ammonia sensors. *Journal of Physics and Chemistry B*, 108, pp. 19717-19720.

Chae, H.G. and Kumar, S. (2006) Rigid Rod Polymeric Fibres. *Journal of Applied Polymer Science*, 100 (1), pp. 791–802.

Chuang, D.D.L. (1994*) Carbon fibre composites*. Newton USA: Butterworth-Heinemann.

Collins, P.G., Bradley, K., Ishigami, M. and Zettl, A. (2000) Extreme Oxygen Sensitivity of Electronic Properties of Carbon Nanotubes, *Science*, 287, pp. 1801-1804.

Choi, E.S., Jeong, M.H., Choi, K.W., Lim, C. and Lee, S.B. (2010) Flexible and transparent touch sensor using single wall carbon nanotube thin films. In 2010 3RD International Nanoelectronics Conference. Hong Kong: IEEE, 1, pp. 718-719.

Clark, R.J.H. (1982) *Advances in infrared and Raman spectroscopy*. Chichester: Wiley Heyden, 9, pp. 8-9.

Cochet, M., Maser, W.K., Benito, A.M., Callejas, M.A., Martines, M.T., Benoit, J.M., Schreiber, J. and Chauvet, O. (2001) Synthesis of a new polyaniline/nanotube composite: "In-situ" polymerisation and charge transfer through site-selective interaction. Chemical *Communications*, 16, pp. 1450-1451.

Cao, G., Chen, X., and Kysar, J.W. (2005) Strain sensing of carbon nanotubes: Numerical analysis of the vibrational frequency of deformed single-wall carbon nanotubes. *Physical Review B - Condensed Matter and Materials Physics*, 72(19), pp. 1-6.

Cox, H.L. (1952) The Elasticity and Strength of paper and other fibrous materials. *Brit J Appl Phys*, 3, pp. 9-72.

Cotterell, B. and Mai, Y.W. (1996) *Fracture mechanics of cementitious materials*, Glasgow: Blackie Academic & Professional.

Colthup, N.B. Daly, L.H. and Wiberley, S.E. (1990) *Introduction to Infrared and Raman Spectroscopy*. Third Edition. New York: Academic Press.

Demczyk, B.G., Wang, Y.M., Cumings, J., Hetman, M., Han, W., Zettl, A., Ritchie, R.O. (2002) Direct mechanical measurement of the tensile strength and elastic modulus of multiwalled carbon nanotubes. *Materials Science and Engineering*, 334 (1–2), pp. 173–178.

DeVolder, M.F.L., Tawfick, S.H., Baughman, R.H. and Hart, A.J. (2013) Carbon Nanotubes: Present and Future Commercial Applications. *Science*, 339, pp. 535-539.

Dai, H. (2002) Carbon Nanotubes: Synthesis, Integration, and Properties, *Acc. Chem. Res*, 35, pp. 1035-1044.

Dresselhaus, M.S., Dresselhaus, G. and Eklund, P.C. (1996) *Science of Fullerenes and Carbon Nanotubes*; San Diego:Academic Press. pp. 985.

Edie, D.D. (1990) *Carbon Fibres Filaments and Composites*, edited by Figueredo, J.L., Bernardo, C.A., Baker, R. T. K. and Huttinger, K.J., Dordrecht: Kluwer Academic , pp. 43-72.

Ebbesen, T.W., Ajayan, P.M. (1992) Large-scale synthesis of carbon nanotubes. *Nature*, 358 (6383), pp. 220–222.

Feillard, P., Desarmote, G. and Favre, J.P. (1994) Theoretical aspects of the fragmentation test. *Composites Science and Technology*, 50, pp. 265-279.

Fitzer, E. (1990) *Carbon Fibres Filaments and Composites*, edited by Figueredo, J.L., Bernardo, C.A., Baker, R.T.K. and Huttinger, K.J., Dordrecht: Kluwer Academic, pp. 405-439.

Fitzer, E. and Kunkele, F. (1990) *High Temp-High Pressure*, 22(3), pp. 239-266.

Fridman, L.I. and Grebennikov, S.F. (1990) Khimicheskie Volokna, 6, pp. 10-13.

Filleter, T., Bernal, R., Li, S. and Espinosa, H.D. (2011) Ultrahigh Strength and Stiffness in Cross-Linked Hierarchical Carbon Nanotube Bundles. *Advanced Materials*, 23 (25), pp. 2855-2860.

Hafner, J.H., *et al*. (1998) Catalytic growth of single-wall carbon nanotubes from metal particles. *Chemical Physics Letters*, 296(1-2), pp. 195-202.

Halary, J., *et al*. (2004) Smart nanostructured polymeric coatings for use as remote optical strain sensors. *Advanced Engineering Materials*, 6(9), pp. 729-733.

Hierold, C., *et al*. (2007) *Nano* electromechanical sensors based on carbon nanotubes. *Sensors and Actuators*, 136, pp. 51-61.

HUNTSMAN CORPORATION, (2011) Araldite LY5052/Aradur 5052 Data sheet. [online] Available at:

http://www.chemcenters.com/images/suppliers/169257/Araldite%20LY5052,%20Aradur%205052.pdf [Accessed 13 June 2010]

Hamerton, I. (1996) Recent Developments in Epoxy Resins. *Rapra Review Reports*. Rapra Technology Ltd, 8(7), PP. 5-6.

Harris, P.J.F. (2004) Carbon nanotube composites. *International Materials Reviews*, 49(1), pp. 31-43.

Inami, N. *et al*. (2007) Synthesis-condition Dependence of Carbon Nanotube Growth by Alcohol Catalytic Chemical Vapor Deposition Method, *Sci. Technol. Adv. Mater*, 8, pp. 292-297.

Iijima, S. (1991) Helical Microtubules of Graphitic Carbon, *Nature*, 354, pp. 56-58.

Ishigami, N., Ago, H., Imamoto, K., Tsuji, M., Iakoubovskii, K. and Minami, N. (2008) Crystal Plane Dependent Growth of Aligned Single-Walled Carbon Nanotubes on Sapphire, *J. Am. Chem. Soc*, 130 (30), pp. 9918-0024.

Jorio, A. and Dresselhaus, G. (2004) Fullerenes and Carbon Nanotubes, *in Encyclopedia of Physical Science and Technology*. pp. 315-335.

Johnson, D.J. (1982) Structure and physical properties of carbon fibres. *Chemistry and Industry*, 18, pp.692-698.

Johnson, W., Philips, L.N. and Watt, W. (1968) The production of carbon fibres, *British Patent 1*,110, pp. 791.

Kim, K.K. and Mai, Y.W. (1998) *Engineered interfaces in fibre reinforced composites*. First edition. Oxford: Elsevier Science Ltd, pp. 5-16.

Kim, K.S., Cota-Sanchez, G., Kingston, C., Imris, M., Simard, B. and Soucy, G. (2007). Large-scale production of single-wall carbon nanotubes by induction thermal plasma. *Journal of Physics D: Applied Physics*, 40, pp. 2375-2387.

Kingston, C.T., *et al*. (2004) Efficient laser synthesis of single-walled carbon nanotubes through laser heating of the condensing vaporization plume. *Carbon*, 42(8-9), pp. 1657-1664.

Kim,J.K. and Mai,Y.W.(1991) High strength, high fracture toughness fibre composites with interface control a review. *Compsites Sci.Technol*. 44, pp. 338-378.

Kim, J.K. and Mai, Y.W. (1993) *Interfaces in composites. in:* Structure and Properties of Fibre Composites, Material Science and Technology, Series Vol.13, T. W. Chou ed., Germany: VCH Publishers, Weinheim, pp.239-289.

Kirk, R.E. and Othmer, D.F. (1957) Encyclopaedia of Chemical Technology, first supplement vol. New York: Epoxy Resins Wiley (Inter science), pp. 316.

Kong, J., *et al*. (2000) Nanotube molecular wires as chemical sensors. *Science*, 287(5453), pp. 622-625.

Kelly, A. and Tyson, W. (1965) Tensile properties of fibre-reinforced metals-copper/tungsten and copper/molybdenum. *Journal of the Mechanics and Physics of Solids*, 13, pp. 329-350.

Lynch, J., *et al*. (2007) Multifunctional layer-by-layer carbon nanotubes-polyelectrolyte thin films for strain and corrosion sensing. *Smart Materials and Structures,* 16, pp. 429-438.

Li, C.Y. and Chou, T.W. (2004) Strain and pressure sensing using single-walled carbon nanotubes. *Nanotechnology*, 15(11), pp. 1493-1496.

Loader, J. (1970) Basic Laser Raman Spectroscopy. London: Heyden Sedtier.

Matthews, F. and Rawlings, R. (1994) Composite materials: Engineering and Science. London: Chapman & Hall.

Meo, M., Rossi, M. (2006) Prediction of Young's modulus of single wall carbon nanotubes by molecular-mechanics-based finite element modelling. *Composites Science and Technology* ,66 (11–12), pp. 1597–1605.

Mochida, I. and Kawano, S. (1991) Capture of ammonia by active carbon fibres further active with sulfuric acid. *Industrial Engineering Chemistry Research*, 30(10), pp. 2322-2327.

Mottershead, B. and Eichhorn, S.J. (2007) Deformation micromechanics of model regenerated cellulose fibre-epoxy/polyester composites. *Composites Science and Technology*, 67, pp. 2150-2159.

Nairn, J. (1997) On the use of shear-lag methods for analysis of stress transfer in unidirectional composites. *Mechanics of Materials*, 26, pp. 63-80.

Nikolaev, P., *et al*. (1999) Gas-phase catalytic growth of single-walled carbon nanotubes from carbon monoxide. *Chemical Physics Letters*, 313(1-2), pp. 91-97.

Neumann, A.W., Absolom, D.R., Francis, D.W. and van Oss, C.J. (1980) Conversion tables of contact angles to surface tension: For use in determine the contribution of the Van der Waals attraction or repulsion to various separation processes, *Separ. Purif Mech*.9, pp. 69-163

Owen, D.K. and Wendt, R.C. (1969) Estuation of the surface free energy of polymers. *Journal of Applied Polymer Science*, 13, pp. 1741-1747.

Peters, D.M. (1970) Carbon Fibre, Breakthrough and Early Development, pp. 3-11.

Pop, E., Mann, D., Wang, Q., Goodson, K. and Dai, H.J. (2006) Thermal conductance of an individual single-wall carbon nanotube above room temperature. *Nano Lett*, 6, pp. 96-100.

Puglia, D., Valentini, L. and Kenny, J.M. (2003) Analysis of the cure reaction of carbon nanotubes/epoxy resin composites through thermal analysis and Raman spectroscopy. *Journal of Applied Polymer Science*, 88(2), pp. 452-458.

Plueddemann, E.P. (1988) *Present status and research needs in silane coupling*. In Proc. ICCI-II, Interfaces in Polymer, New York: Ceramic and Metal Matrix Composites. (H.Ishida ed.), Elsevier Sci. Pub, pp. 17-33.

Piggott, M.R. (1980) Load bearing fibre composites. Oxford: Pergamon, pp. 83.

Peng, B., Locascio, M., Zapol, P., Li, S., Mielke, S.L., Schatz, G.C. and Espinosa, H.D. (2008) Measurements of near-ultimate strength for multiwalled carbon nanotubes and irradiation-induced crosslinking improvements. *Nature Nanotechnology*, 3 (10), pp. 626–631.

Quinn, B.M., Lemay, S.G. (2006) Single-Walled Carbon Nanotubes as Templates and Interconnects for Nanoelectrodes, *Adv. Mater*., 18(7), pp. 855-859.

Ramasubramaniam, R., Chen, J. and Liu, H. (2003) Homogeneous carbon nanotube /polymer composites for electrical applications. *Applied Physics Letters*, 83(14), pp. 2928-2930.

Sandler, J., *et al*. (1999) Development of a dispersion process for carbon nanotubes in an epoxy matrix and the resulting electrical properties. *Polymer*, 40(21), pp. 5967-5971.

Shaffer, M.S.P. and Windle, A.H. (1999) Fabrication and characterization of carbon nanotube/poly(vinyl alcohol) composites. *Advanced Materials*, 11(11), pp. 937-941.

Sureeyatanapas, P. and Young, R.J. (2009) SWNT composite coating as strain sensor on glass fibre in model epoxy composites. *Composites Science and Technology*, 69, pp. 1547-1552.

Sinnott, S.B. and Andrews, R. (2001). Carbon Nanotubes: Synthesis, Properties, and Applications. *Critical Reviews in Solid State and Materials Sciences*, 26 (3), pp. 145–249.

Tanaka, Y. (1988) Synthesis and characterization of epoxides. In Epoxy Resins Chemistry and technology. New York: Marcel Dekker, pp. 54-63.

Thostenson, E.T., Ren, Z. and Chou, T.W. (2001) Advances in the science and technology of carbon nanotubes and their composites: a review. *Composites Science and Technology*, 61(13), pp. 1899-1912.

Wei, Q., Yi-Lan, K., Zhen-Kun, L., Qing-Hua, Q., Qiu, L. and Quan, W. (2010) Experimental study of the Raman strain rosette based on the carbon nanotubes strain sensor. *Journal of Raman Spectroscopy*, 41, pp. 1216-1220.

White, C.T. and Todorov, T.N. (1998) Armchair carbon nanotubes as long ballistic conductors. *Nature*, 393, pp. 240-242.

Yu, M.F., Lourie, O., Dyer, M.J., Moloni, K., Kelly, T.F. and Ruoff, R.S. (2000) Strength and Breaking Mechanism of Multiwalled Carbon Nanotubes Under Tensile Load.*Science*, 287 (5453), pp. 637–640.

Yao, Z., Kane, C.L. and Dekker, C. (2000) High-Field Electrical Transport in Single-Wall Carbon Nanotubes, *Phys. Rev. Lett*, 84, pp. 2941-2944.

Young, R.J. (1996) Evaluation of Composite Interface Using Raman Spectroscopy. *Key Engineering Materials*, 116-117, pp. 173-192.

CHAPTER 3 Experimental Methodology and Preparation

3.1 General Introduction

In this chapter firstly the details of the main materials used in this study are given. Furthermore, experimental methods and specific information regarding the techniques employed in this project have been introduced.

3.2 Materials Specification

3.2.1 Carbon Fibres

There are two types of carbon fibres used in this project as they are categorised as high modulus carbon fibre and low modulus carbon fibre. The high modulus carbon fibre was supplied from the Japanese manufacturer 'Toray' with the type of M46J. The low modulus carbon fibre was provided by 'Toho Tenax' with the brand of Tenax-J. The technical data offered from their manufacturer are stated in Table 3.1.

Table 3.1 *Technical data for the two types of carbon fibres.*

Fibre Type	Filament Count	Mas/Unit length (tex)	Tensile Strength (MPa)	Tensile Modulus (GPa)	Elongation (%)	Filament Diameter (μm)	Density (g/cm^3)	Electricity Resistivity (Ω·m)
Toray M46J	6000	223	4200	436	1.0	5.0	1.84	0.9×10^{-3}
Toho Tenax-J	12000	410	5800	290	2.0	5.0	1.80	1.4×10^{-3}

3.2.2 Single Walled Carbon Nanotubes (SWNTs)

Two types of single walled carbon nanotubes are used in this project. The first type is called HiPCO SWNTs, as they are produced using a high pressure and a carbon monoxide process. The HiPCO SWNTs were supplied by the American company

NanoIntegris. The other type of nanotubes was carboxylic acid functionalized SWNTs, which were provided by Sigma-Aldrich Co., Ltd., UK and are synthesised using the electric arc discharge technique. The technical data for both types of SWNTs are shown in Table 3.2(NanoIntegris, 2011; Sigma-Aldrich, 2011).

Table 3.2 *The properties of these two types of SWNTs offered by their supplier.*

	Diameter	Total impurities	Length
HiPCO SWNTs	0.8-1.2 nm	5-8 wt% metals	100-1000 nm
COOH SWNTs	1.3-1.5 nm	< 15 wt% metals	500-1500 nm

3.2.3 Epoxy Resin Matrix Material

The epoxy resin used for a matrix material for the model composites was Araldite resin LY5052, which is categorised as a low viscosity epoxy resin. Together with the Aradur hardener HY5052, which is a combination of polyamines, they are provided by Vantico, Polymer Specialties, UK. The chemical structures of LY5052 and HY5052 are shown in Figure 3.1. The resin LY5052 contains 34–42% butanediol diglycidyl ether and 60–70% epoxy phenol-novolac resin. The hardener HY5052 is composed of 35% isophorone diamine, 50–60% 2,2-dimethyl-4,4-methylenebis (or cyclohexylamine) and 1–5% 2,4,6-tris (or dimethylaminomethyl) phenol(Yusoff *et al*., 2007). The mixing ratio for the epoxy resin and hardener are shown in Table.3.3. The cure circumstances for the system can be adjusted between room temperature and temperatures above 100 ℃ which is subject to the necessary properties.

The low viscosity of the components allows mixing at room temperature, and a complete impregnation of all current reinforcement fibres like glass, carbon and aramid. Table.3.4 shows the viscosity increases at different temperatures. The low viscosity build-up makes it suitable for processing methods such as wet lay-up and RTM. The resultant laminates are renowned for their mechanical and dynamical properties, and the cold curing epoxy laminating system Araldite LY 5052/Hardener HY5052 has achieved the requirements of a large range of applications including industrial and aerospace composites.

The mechanical properties of this resin system after cured vary depending on the curing process but it is reported to have a average Young's modulus of approximately 3 GPa and a shear yield stress of about 43 MPa (Young and Andrews, 1994).

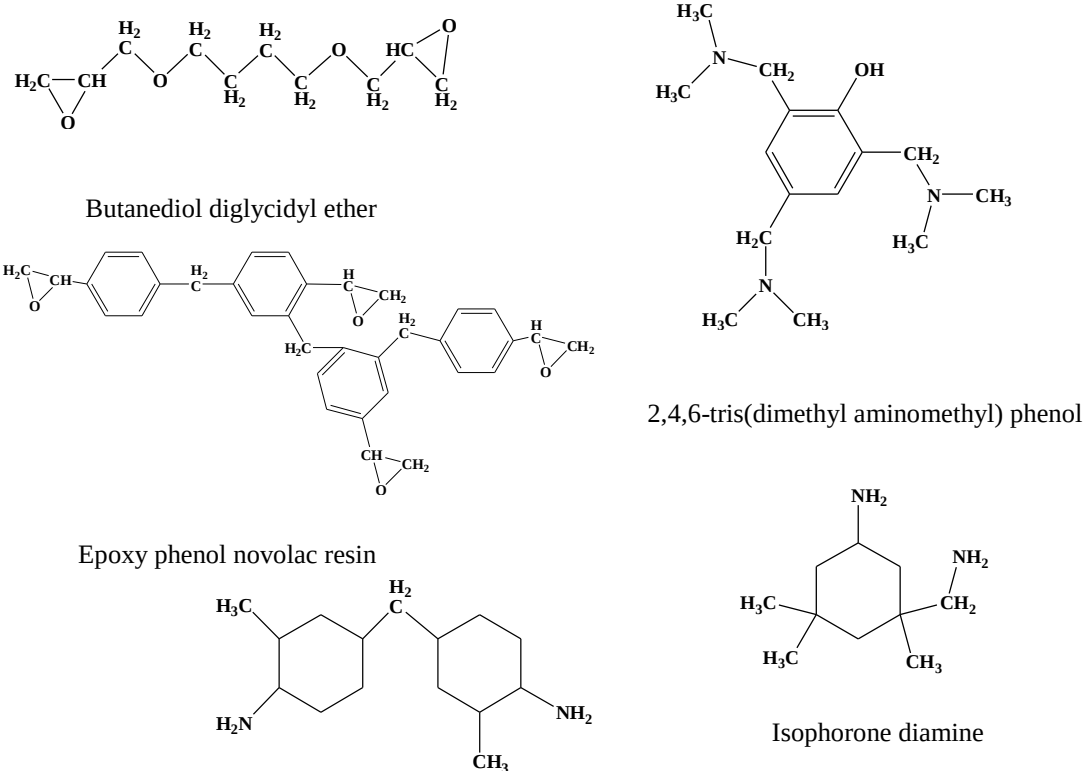

Figure 3.1 *The chemical structures of the components of epoxy resin LY5052 and hardener HY5052.*

Table 3.3 *The mix ratio of resin and hardener.*

Mix ratio	Parts by weight	Parts by volume
Araldite LY 5052	100	100
Hardener HY 5052	38	47

Table 3.4 *Viscosity build-up of Araldite LY 5052/Hardener HY5052.*

Temperature(℃)	Viscosity	Time
25 ℃	To 1500 mPa s	50~60
	To 3000 mPa s	90~110
40 ℃	To 1500 mPa s	40~45
	To 3000 mPa s	50~60
60 ℃	To 1500 mPa s	15~18
	To 3000 mPa s	18~22

3.2.4 Silane Coupling Agents

The silane coupling agent used in this study was 3-aminopropyl-triethoxysilane which is supplied by Avocado Research Chemicals, UK. Their chemical properties are displayed in Table 3.5.

Table 3.5 *Technical data of Silane coupling agents (Alfa Aesar, 2011).*

Formula	$C_9H_{23}NO_3Si$
Chemical structure	$H_2N(CH_2)_3Si(OC_2H_5)_3$
Formula weight(g/mol)	221.37
Boiling point	217 °
Flash point	104 °
Density (g/cm^3)	0.948
Natural pH	10
Purity	98%

3.2.5 Release agents

In this study a release agent named Ambersil Formula 10 was used, which is a dry film, non-silicone mould release agent and was provided by Ambersil House, UK. The chemical structure for this release agent is not provided due to company secrecy. According to the company user guide, fluorinated resins are included in this release agent and act as the active release component. This product has been formulated for injection and compression moulding and is especially effective for application to thermosetting plastics. During the operating process it can generate a dry and non-silicone film for fast and efficient release of thermosetting plastics such as epoxy resins and polyesters, and the dry film does not expand in the mould and assists to enhance surface finish, ease rejects and boost production. In this project the purpose of using the release agent is to get a slip effect and release the epoxy dumbbell shaped samples out from the metal mould (Ambersil, 2011).

3.3 Sample preparation

3.3.1 Single Fibre Card Samples

In order to perform micromechanical deformation on the filament, the single filament has to be gripped in a straight attitude without any stress to be applied before the test start. Therefore, the single filament was designed to be attached onto a fibre card over a cut window as shown in Figure 3.2, and before the test started the middle of this thin fibre card frame will be cut or burned in order for the load to be transferred to the filament (Eichhorn and Young, 2004). Additionally the length of the window is created as the same length as the gauge length of the fibre which is required for the test. During the making of the samples, each fibre was secured along a central line of the window on the fibre card with a small piece of adhesive tape. However in order to secure the fibre more firmly, and prevent detachment from the card when the load is applied, a small amount of cold curing Aradite^{TM} resin droplet was be applied to both ends of the fibre and just to the edge of the frame of the fibre card. This ensured that the gauge length was equal to the length between the two droplets, as shown in Figure 3.2. All samples were conditioned at a room temperature of 23 ℃ and 50% humidity for about 7 days to make sure the droplets were fully cured.

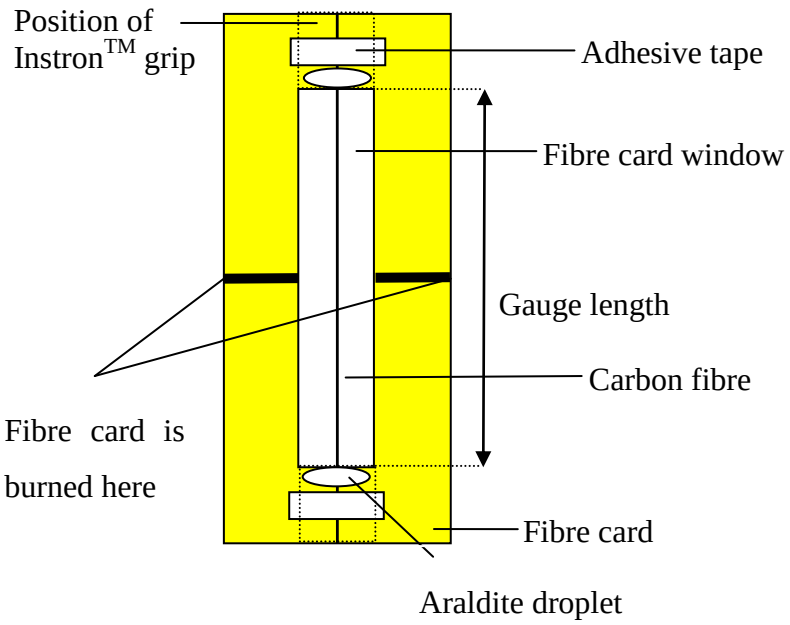

Figure 3.2 *Schematic of a fibre card specimen for tensile testing.*

3.3.2 Specimen Preparation for Optical Microscopy

In order to calculate the number of filaments in a bundle of carbon fibres, optical microscopy was used. The samples were prepared by making a bundle of carbon fibres stand vertically and then embedding them in a resin block. First of all a short bundle of fibre strands was wrapped on a paper card which was then fitted into a plastic sample clip. This clip was placed in the middle of a sample mould. Polyester casting resin was poured into the mould and until the top of the carbon fibres was totally covered. Afterwards the samples were cured at room temperature for 2 hours and released from the mould. These polyester resin blocks were then ground down to expose the cross sectional area of the fibres by using 20 μm and 10μm diamond grinding wheels respectively. Finally the surfaces of the resin blocks were polished by using 6 μm and 3μm diamond polishing wheels to erase surface scratches and ensure the samples had transparent and smooth flat surfaces; thus each filament end can be clearly observed using optical microscopy. A schematic diagram of the specimen and its preparation process was shown in Figure 3.3.

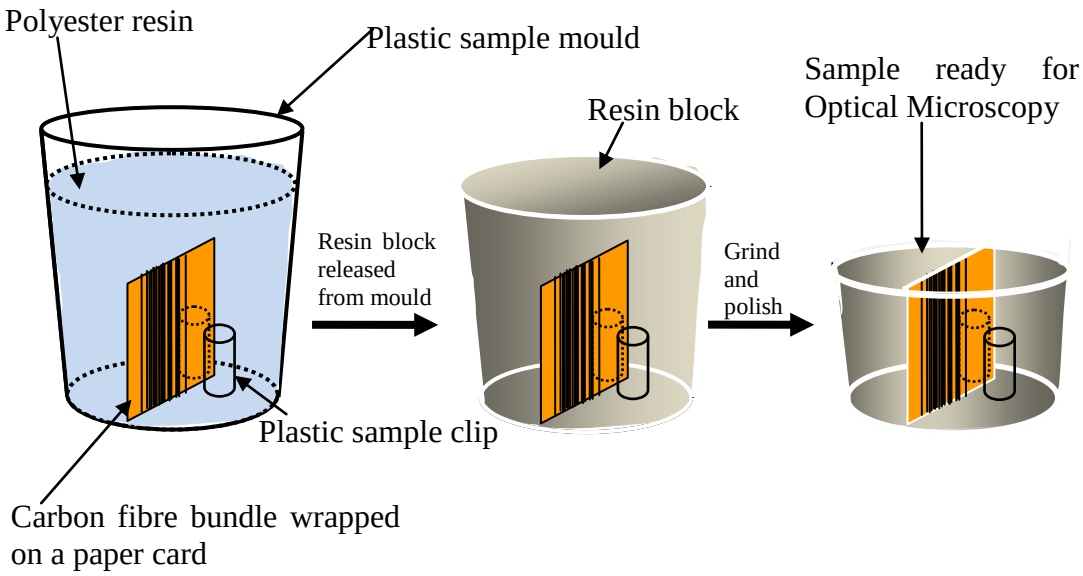

Figure 3.3 *A schematic of the preparation procedure for a vertical carbon fibre-resin block sample for optical microscopy of filament ends.*

3.3.3 Specimen Preparation for SEM

In order to determine the morphology and diameter of carbon fibre surface in longitudinal and transverse directions two types of carbon fibre samples were prepared.

3.3.3.1 Specimen for longitudinal direction

Ten single filaments were randomly selected from a bundle of carbon fibres, so as to take systematic discrepancies into account within the bundle of fibres, and to make sure an accurate and representative mean diameter and surface morphology were obtained. Each fibre filament was placed horizontally onto an adhesive carbon pad which was attached on an SEM stub. The schematic diagram of this sample is shown in Figure 3.4.

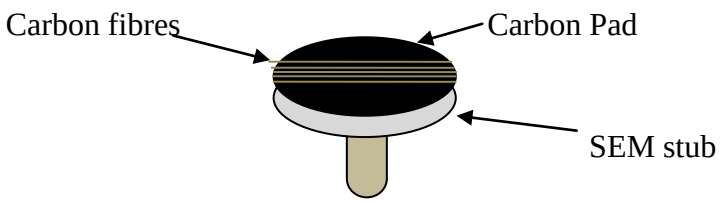

Figure 3.4 *A schematic diagram of the SEM stub sample for longitudinal direction analysis.*

3.3.3.2 Specimen for cross section area analysis

Fibres were attached in a vertical position to copper conduction tape. Then a bundle of fibres was sandwiched by another piece of copper tape on the other side to ensure they stood firmly and perpendicularly on the SEM stub; this benefitted the SEM image resolution. A schematic diagram of this sample is shown in Figure 3.5.

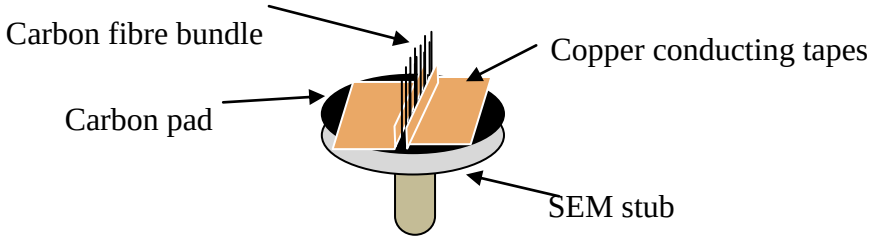

Figure 3.5 *A schematic diagram of the SEM stub sample for fibre cross section area analysis.*

3.4 Characterization Techniques

3.4.1 Raman Spectroscopy

3.4.1.1 Raman Spectroscopy Configuration

All the experiments involving Raman spectroscopy used a Renishaw 1000 spectrometer system (Renishaw Plc, UK) with a He-Ne laser of wavelength (λ) of 633 nm and . The laser beam was focused on the specimen using a 50× objective lens of an Olympus BH-2 long working distance optical microscope, which was also used to collect the scattered radiation. The laser spot size on the sample was about 2 μm in diameter. In order to prevent heating induced by the laser, a minimum laser power of 25% (full power 0.25mW) was used in this study.

The schematic of the Renishaw 1000 spectrometer system is displayed in Figure 3.6 (Renishaw Plc, 2002).

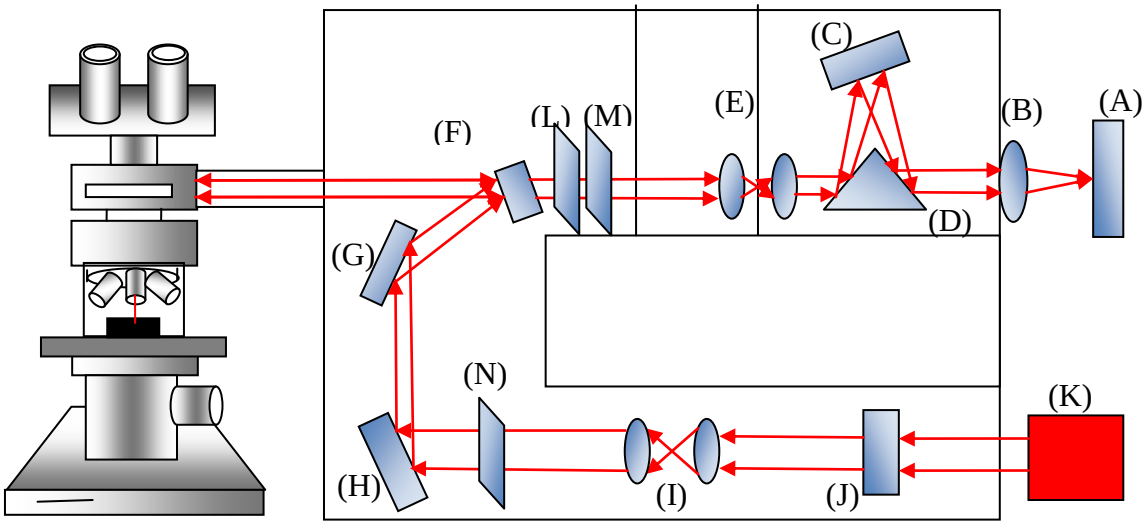

Figure 3.6 *Schematic diagram of a Renishaw Raman spectrometer.*

In Figure 3.6, A is a charge-coupled device (CCD), B is the CCD focussing lens, C is the diffraction grating assembly, D is an isosceles triangle mirror, E is the slit, F is a holographic notch filter, G is a fixed mirror, H is an adjustable mirror, I is a spatial filter, J is a rejection filter, K is the laser, L is a λ/2 plate 2# , M is a polarisation analyser and N is λ/2 plate 1#.

3.4.1.2 Polarized Raman Scattering

In this project polarised Raman spectroscopy was used to characterise the band shift rates of SWNTs on the carbon fibre surface.

Polarized Raman applies polarized laser excitation and a polarization analyser can be employed to obtain spectra; the scattered light can adjusted to either parallel or perpendicular to the polarisation direction of the incident laser. The consequent spectral information can provide an insight into molecular orientation and vibrational symmetry. Basically it can give important knowledge regard to molecular shape such as in synthetic chemistry or polymorph analysis, and is mainly used to determine the orientation of molecules in organized environments for instance polymer samples, crystal lattices and liquid crystals (PerkinElmer, 2012).

Six different polarisation configurations can be achieved by regulating the positions of the $\lambda/2$ plate and polarisation analyser. The direction of the incident and scattered laser refer to the related x axis of the stage and the corresponding positions of the optical components for different polarisation configurations are shown in Table.3.6 (Kao, 2008).

In order to change the angle between the sample axis and the polarisation direction of the laser a rotation stage was employed, and Raman spectra were recorded at different angles.

Table 3.6 *Technical data for different laser polarisation configurations.*

	VN	VV	VH	HN	HH	HV
Direction of incident laser	//	//	//	⊥	⊥	⊥
Direction of scattered laser	Random direction	//	⊥	No orientation	⊥	//
λ/2 Plate 1#	In	In	In	Out	Out	Out

λ/2 Plate 1#	Out	Out	In	Out	In	Out
Polarisation analyser	Out	In	In	Out	In	In

//: Laser parallel to the x axis $\perp$: Laser perpendicular to the x axis

3.4.1.3 Micromechanical deformation of fibres and composites using Raman spectroscopy

The peak wavenumber of the Raman bands of convinced fibres is found to be very sensitive to the levels of the applied stress or strain. This can be explained as that since a material is strained, the interatomic distance changes, giving rise to a change in the interatomic force constant, and therefore a change in the vibrational frequency (Mitra *et al*., 1977; Halary *et al*., 2004). For uniform stress microstructures, the Raman shift rates with respect to strain have been found to be proportional to fibre modulus (Huang and Young, 1995). Therefore, Raman spectroscopy technique has been often applied to the study of the molecular deformation of high performance fibres. It has been confirmed that the Raman spectroscopy is a very strong tool for investigating the deformation behaviour of high molecular polymer fibres *e.g.* polyphenylene benzobisthiazole (PBT) and aramid fibres etc. (Robinson *et al*., 1986; Robinson *et al*., 1987)

In this study of carbon fibres, an analysis of Raman spectra will be given, followed by the deformation micromechanics of the fibres using shifts in the peak position of characteristic Raman bands.

In order to apply load to the carbon fibre, fibre card samples were made. These were then attached to a deformation rig, shown in Figure 3.2 using cyanoacrylate adhesive. Tensile deformation was not started until the adhesive was totally cured; this typically took 30 minutes. After that the fibre card frame was burned through the middle, as before for tensile testing methodology reported in Section 3.4.6 allowing load to be applied to the carbon fibre. Deformation of the fibre was actuated by adjusting the micrometer on the fibre rig (Figure 3.7). All these operations were performed while the deformation rig was housed under the spectrometer microscope. The position of one specific band will be determined at different strain level until fibre fractured. Finally the relationship between the Raman shift and fibre strain and stress were obtained. The

specific Raman band, increments of strain and exposure time used for collecting the data varied for different samples and will be described and discussed in Chapter 5.

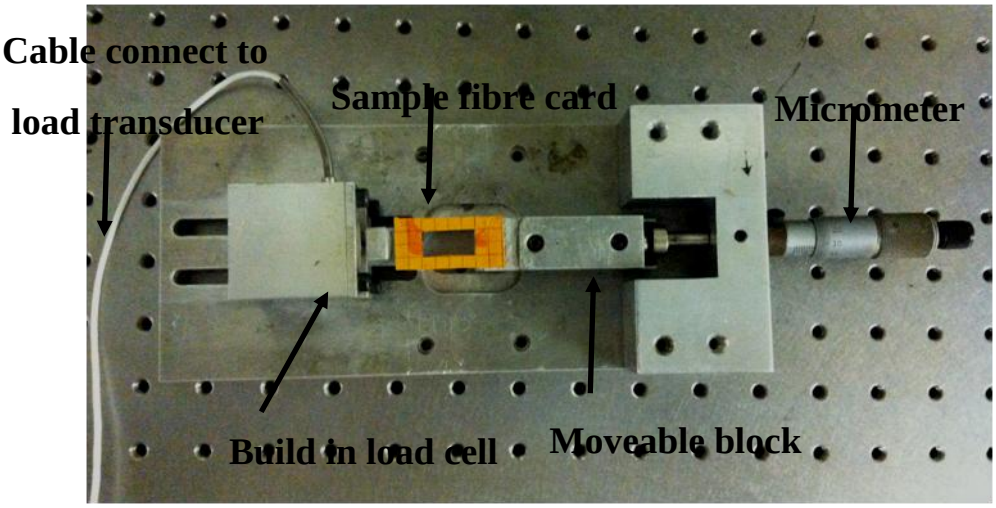

Figure 3.7 *Image of the fibre rig.*

The study follows by using the Raman shift and fibre stress or strain relations to detect the load transfer across the interface between the epoxy matrix and carbon fibre for different types of samples.

3.4.1.4 Raman band fitting

A Lorentzian function was used to fit the Raman spectra to determine the parameters of the bands. This function is given by the equation:

$$I(x) = \frac{1}{\pi}\frac{\frac{1}{2}\Gamma}{(x-x_0)^2+(\frac{1}{2}\Gamma)^2} \qquad (3.1)$$

where $I(x)$ is the intensity of the peak at any given wavenunmber x, x_0 is the peak position (in units of cm^{-1}), Γ is the full width at half maximum (FWHM) of the peak (Weisstein, 2012).

3.4.2 Optical Microscopy

Optical microscopy used in this study was performed using an Olympus BH2-UMA universal vertical illuminator. According to its user guide, the BH2 series of research-level microscope contains 160 millimetre tube length optics which are configured for Köhler illumination when coupled to LB series objectives and the extensive line of sub-

stage condensers. Auxiliary components for the microscope are composed of an automatic exposure photomicrography system, photo eyepieces, and a wide range of objectives covering the entire range of correction and magnification. Other equipment on this microscope involved 10× widefield high eyepoint eyepieces which have a field number of 20, precentered halogen lamps, aspherical collector lenses, and completely enclosed light paths designed to exclude dirt and dust. Additionally both circular and mechanical stages were provided, as were binocular and trinocular observation tubes. Contrast enhancing equipment included differential interference contrast, phase contrast, fluorescence, darkfield and polarized light were also available (Abramowitz, 1990).

3.4.3 Scanning Electron Microscopy (SEM)

As a type of electron microscopy, SEM images a sample by scanning it with an electron beam in a raster scan pattern. In this study, back scattered mode was used to characterise the samples. For a back scattered mode or secondary scattered mode, a number of interactions with atoms occur when a beam of electrons is scanned across a sample, this cause the emissions of electrons from the sample surface. Hence much significant information can be obtained including surface topography, composition and electrical conductivity by measuring the signals from these electrons (Lawes, 1987; Bindell, 1992).

A SEM is composed of three key components; these are the electron source, beam steering and the detector. First of all the electron gun column and sample chamber should be kept in a high vacuum state which is about ~1 Pa to allow the electrons to reach the detector without any further interaction. Then an electron beam with energy ranging from 0.2 KeV to 40 KeV is therminonically emitted from an electron gun installed with a tungsten filament cathode. Afterwards the electron beam is focused by two electromagnetic coils and goes through an aperture selector and the spot size about 0.4 nm to 5 nm in diameter is selected. Finally the electron beam passes through electromagnetic coils for focusing and scanning and is deflected in *x* and *y* axes; thus it can scan in a raster fashion over a specific area of the sample surface. A schematic diagram of SEM system is shown in Figure 3.8 (Bindell, 1992).

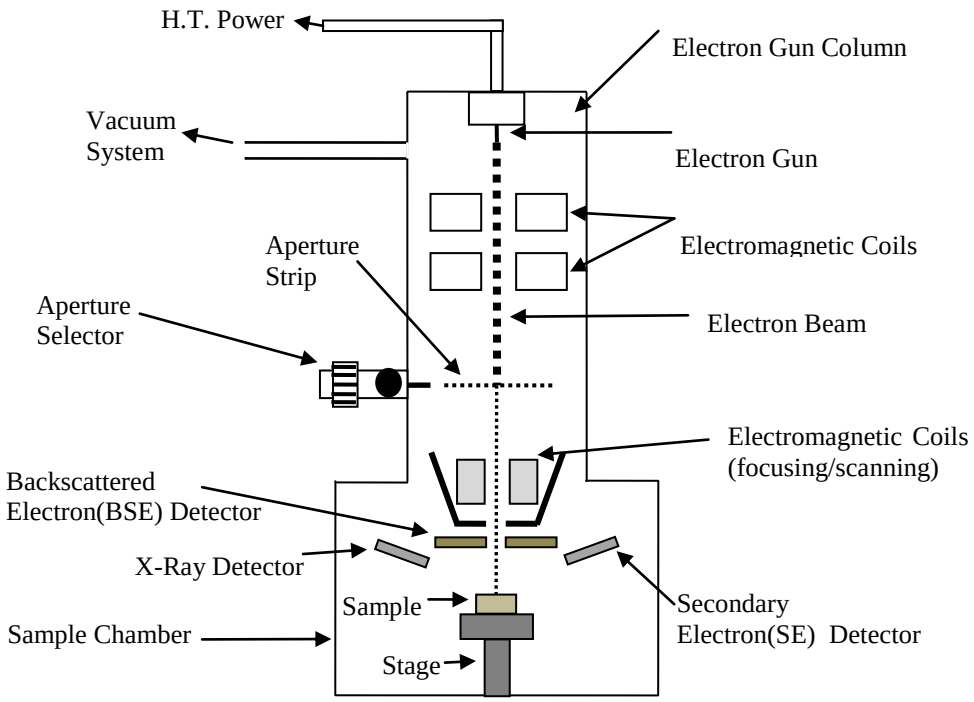

Figure 3.8 *A schematic diagram of SEM system (Stefane, 2010).*

There are three main ways that electrons interact with the sample as they are stated below (Lawes, 1987; Bindell, 1992):

a. Electrons traverse the sample unscattered especially when the sample is thin enough.
b. Electrons are scattered inelastically by the atomic electrons especially for materials with low atomic number. During the collision if sufficient energy is transferred to spray atomic electrons out, these electrons with energies < 50 eV are called secondary electron which mostly are detected within a few nm off the sample surface because further collisions will prevent their escape.
c. Electrons are scattered elastically in all directions together including back towards the source by the atomic nuclear, especially for the materials with high atomic number. Those electrons scattered from the sample are called back-scattered electrons (BSE). BSE signals are strongly related to the atomic number of the sample so they are able to offer information about the distribution of different elements in the specimen.

The detectors used in the SEM can be photomultiplier tubes or semiconductor detectors. Finally the intensity of the signal of detected electrons is scanned across a monitor generating a magnified image of the sample surface. The magnification is determined to be proportional to the image resolution and reciprocal to the beam diameter (Lawes, 1987).

For SEM, all samples must be electrically conductive or at least on the surface and in an appropriate size to fit in the specimen chamber. Non-conductive specimens will be charged if scanned by the electron beam, and especially in secondary electron imaging mode; this will result in scanning faults and other imaging distortions. Non-conducting samples can be coated with ultrathin layer of gold or carbon or other conducting material, ensuring that the topography is not changed through the coating process (Bindell, 1992).

It should be noted that the accelerating voltage plays a very important role in obtaining a better resolution image as the chromic aberration is reduced in the image when the accelerating voltage is higher. However a high accelerating voltage may damage the sample, so voltages are generally in the kV range (Lawes, 1987).

There are many factors that will affect the general resolution of a SEM image, as follows (Lawes, 1987):

a. Beam diameter: a larger spot size generates stronger signals but more noise at higher magnifications.
b. Accelerating voltage: a high voltage eases chromic aberration.
c. Working distance: a smaller distance between the sample and the final lens creates higher resolution if there is less beam divergence.
d. Scan speeds: a long scan speed increases the signal but does not amplify the noise, improving the signal to noise ratio (S/N).

All in all, carbon fibres have a good conductivity so do not need to be coated before imaging. However for samples in this study where an epoxy layer has been applied to the carbon fibre surface, a thorough coating is necessary. The SEM machine used in this project is Philips XL-30 Filed Emission Gun(FEG)-SEM. The operating conditions, such as Accelerating voltage, the magnification and the type of electrons (Secondary electrons or back scattered electrons) will be shown in each SEM images.

3.4.4 X-ray Diffraction

The apparatus used was a Philips Automatic Powder Diffractometer (APD), which has a 21 position automatic sample changer and operates in a θ-2θ (Bragg Brentano) configuration with a 2θ angle range from 5 °to 146 °. This machine is able to examine a variety of samples for phase identification, crystallite size and quantitative analysis by using a copper anode X-ray source with fixed optics a graphite monochromator and working under a high power of 50 kV and 40 mA.

Figure 3.9 shows schematic diagram of an X-ray Diffractometer. A specimen is fixed on a table that is free to rotate about its perpendicular axis. The X-rays are scattered from the sample and focused at the slit before entry to the detector.

A peak is expected when the Bragg condition is satisfied:

$$n\lambda = 2d \sin\theta \qquad (3.2)$$

where n is the order of the reflection, λ is the X-ray wavelength and d is the spacing between planes of given Miller indices h, k and l. In the cubic system, the plane spacing is related to the lattice constant a and the Miller indices by the following relation:

$$d = \frac{a}{\sqrt{h^2+k^2+l^2}} \qquad (3.3)$$

Combination the above two equations then we get:

$$(\frac{\lambda}{2a})^2 = \frac{(\sin\theta)^2}{h^2+k^2+l^2} \qquad (3.4)$$

As a result for all sets of Miller indices there will be an angle that will meet the Bragg condition such that the value of $\frac{\lambda}{2a}$ is a constant. The differences between the simple cubic (SC), body-centred cubic (BCC) and face-centred cubic (FCC) crystal structures can therefore be achieved by comparing the allowed Miller indices with those evaluated from the X-ray diffraction pattern. The value of the lattice constant follows straightforwardly from the X-ray wavelength, which is 1.54 Å for this experiment (Cullity and Stock, 2001).

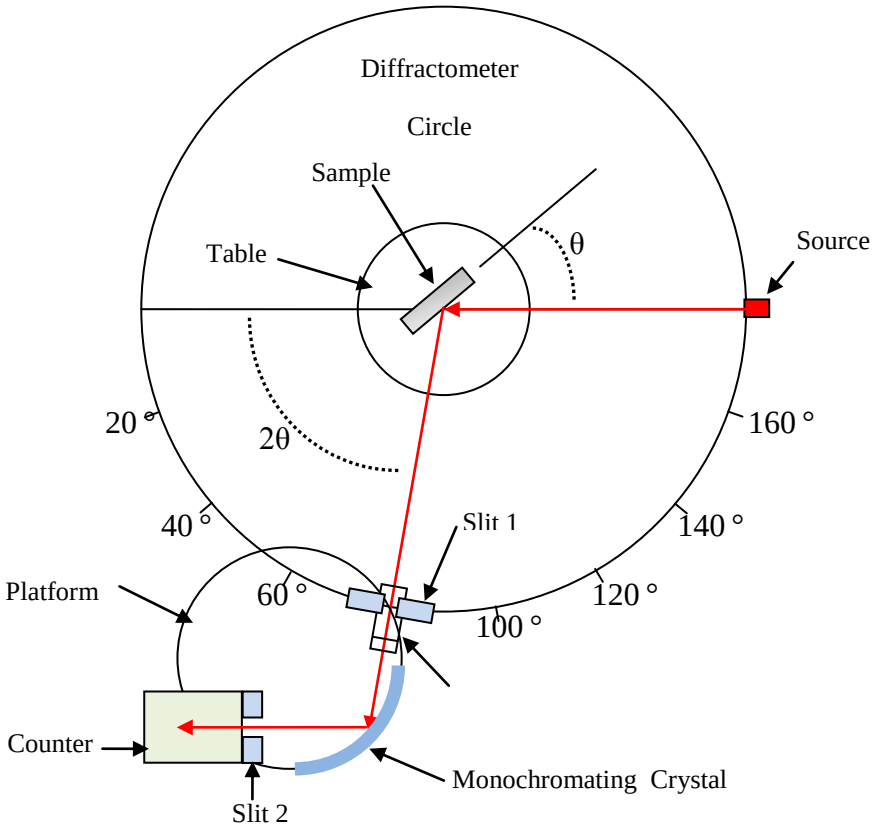

Figure 3.9 *Schematic of a typical X-ray diffractometer.*

The values of the Miller indices are calculated from the crystal structure factors $S(h,k,l)$, which are defined by the equation:

$$s(h,k,l) = \sum_m f_m \exp\left[-2\pi i(u_m h + v_m k + w_m l)\right] \qquad (3.5)$$

where f_m is the atomic scattering factor, (u,v,w) are the coefficients for the basis vectors of the atoms in the unit cell of the crystal structure. It can be determined that for the FCC structure, the Miller indices must be all even or all odd or else the structure factor is zero. Only nonzero $S(h,k,l)$ values create diffraction peaks as only these need be considered; same rules are valid for the SC and BCC structures (Whiston, 1987).

3.4.5 Atomic Force Microscopy (AFM)

In AFM, a sharpened tip is applied to scan across a surface to measure to measure topography. By evaluating forces between a sharp probe (<10nm) which is fitted on a adaptable cantilever and surface, AFM is able to provide a 3D nanoscale profile of a

sample surface. During a test, the probe will approach and gently touch the surface and record a small force between the probe and the surface. This method became achievable with the advent of semiconductor fabrication techniques which allow cantilevers to be made with low spring constants in order that the surface and probe bear minimal damage. The spring constants and resonant frequencies of cantilevers can be varied as they are made from different materials and in different shapes and sizes. Probes are usually produced from (silicon nitride (Si_3N_4), or silicon (Si) (Wilson, 2006).

Unlike SEM, an Atomic Force Microscope is able to image samples with non-conductive surfaces, including polymers, composites, ceramics, composites, glass, and biological samples.

A cantilever with a sharpened tip probe situated on the end can be considered as a spring. Thus the force between the probe and the sample is reliant on the spring constant, which also can be regarded as the stiffness of the cantilever and the distance between the cantilever and the sample surface. Hence the force can be determined by Hooke's Law:

$$F = -Kx \qquad (3.6)$$

where F is the force operated on the cantilever (typically in the range 10^{-9} nN to 10^{-6} μN in open air) K is the spring constant (usually ranging from ~0.1-1 N m^{-1}) and x is the cantilever deflection.

The movement of the probe across the surface is managed by using a feedback loop and piezoelectronic scanners. The deflection of the probe is normally calculated by a 'beam bounce' method, as shown in the schematic in Figure 3.10. A semiconductor diode laser is bounced off the back of the cantilever onto a position sensitive photodiode detector which evaluates the bending of the cantilever during the scanning of the tip across the sample. A map of the surface topography is finally created by measuring the cantilever deflections (Butt *et al*., 2005).

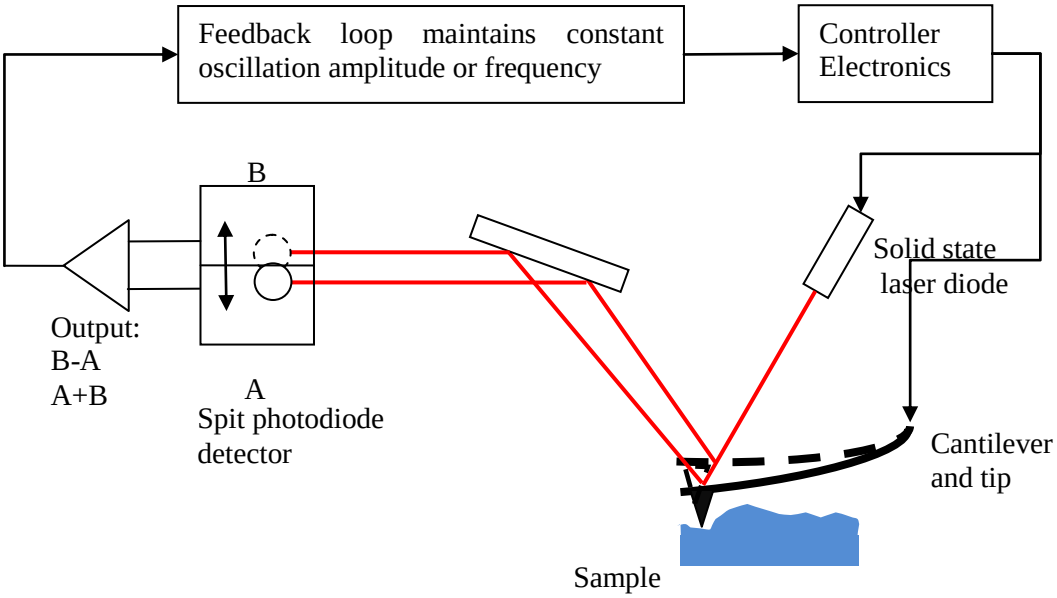

Figure 3.10 *A schematic diagram of AFM.*

AFM can be used to examine a wide range of samples, however it should be noted that there are limitations in reaching atomic resolution as the physical probe used in AFM imaging is not ideally sharp. Thus, an AFM image does not reveal the true sample topography but represents the interaction of the probe with the sample surface; this is called tip convolution as is shown in Figure 3.11 (Geisse, 2009).

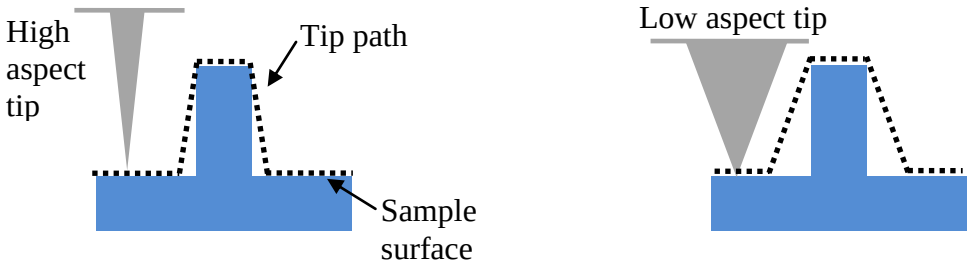

Figure 3.11 *A probe with a high aspect ratio will give a better resolution and the radius of the curvature of the probe results in tip convolution.*

3.4.6 Tensile Test

If a load is static or changes relatively slowly with time and is applied uniformly over a cross section or surface of a material, its mechanical behaviour may be ascertained by a

simple stress-strain test as shown in Figure 3.12. There are three principal ways in which a load may be applied: namely, tension, compression, and shear (Shackelford, 2008).

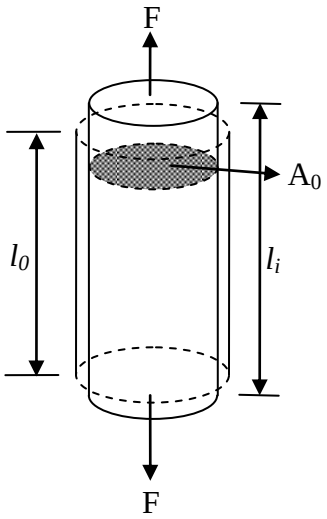

Figure 3.12 *A schematic diagram of tensile test.*

A tensile test can be used to ascertain several mechanical properties of materials that are important to the design process. A specimen is deformed, usually to fracture, with a gradually increasing tensile load that is applied uniaxially along the long axis of a specimen (Shackelford, 2008). The specimens were mounted by at their ends into the holding grips of the testing apparatus. The tensile testing machine as is shown in Figure 3.13 is designed to elongate the specimen at a constant rate, and to continuously and simultaneously measure the instantaneous applied load (with a load cell) and the resulting elongations (using an extensometer). In this study, an Instron™ 1120 test machine was used to perform the tensile test. A stress-strain test typically takes several minutes to perform and is destructive, where typically the test specimen is permanently deformed and usually fractured (Shackelford, 2008).

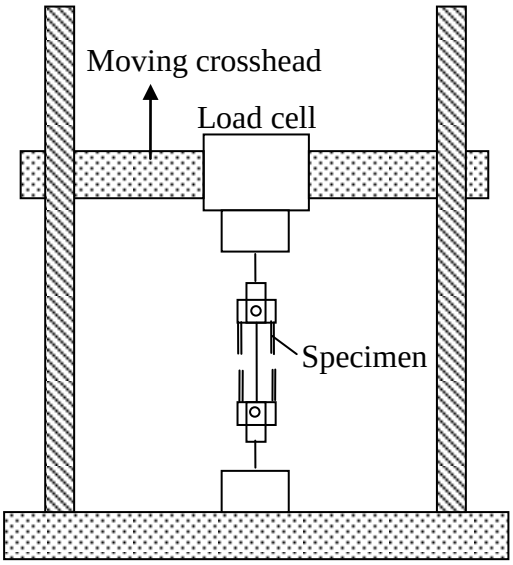

Figure 3.13 *Schematic of the tensile test machine.*

The output of such a tensile test is recorded on a strip chart (or by a computer) as load or force versus elongation (Shackelford, 2008). These load-deformation characteristics are dependent on the specimen size. For example, it will require twice the load to produce the same elongation if the cross-sectional area of the specimen is doubled. To minimize these geometrical factors, load and elongation are normalized to the respective parameters of engineering stress and engineering strain. Engineering stress σ is defined by the relationship

$$\sigma = \frac{\mathrm{F}}{\mathrm{A_0}} \tag{3.7}$$

in which F is the instantaneous load applied perpendicular to the specimen cross section, in units of Newtons (N), and A_0 is the original cross-sectional area before any load is applied (m^2). Engineering strain $\boldsymbol{\varepsilon}$ is defined according to the equation

$$\epsilon = \frac{l_i - l_0}{l_0} = \frac{\Delta l}{l_0} \tag{3.8}$$

in which l_0 is the original length before any load is applied, and l_i is the instantaneous length. Sometimes the quantity l_i - l_0 is denoted as Δl, and is the deformation elongation or change in length at some instant, as referenced to the original length. Engineering strain (subsequently called just strain) is unitless; the value of strain is obviously

independent of the unit system. Sometimes strain is also expressed as a percentage, in which the strain value is multiplied by 100 (Shackelford, 2008).

The degree to which a structure deforms or strains depends on the magnitude of an imposed stress. For some materials like metal that are stressed in tension and at relatively low levels, stress and strain are proportional to each other through the relationship

$$\sigma = E\varepsilon \tag{3.9}$$

This equation is derived from Hooke's law, and the constant of proportionality *E* (GPa or psi) is the modulus of elasticity, or Young's modulus. The standard unit for the modulus of elasticity is Pascals Pa (1GPa = 10^9N/m^2=10^3 MPa). For carbon fibres the magnitude of this modulus ranges between 200 GPa to 900 GPa (Chung, 1994).

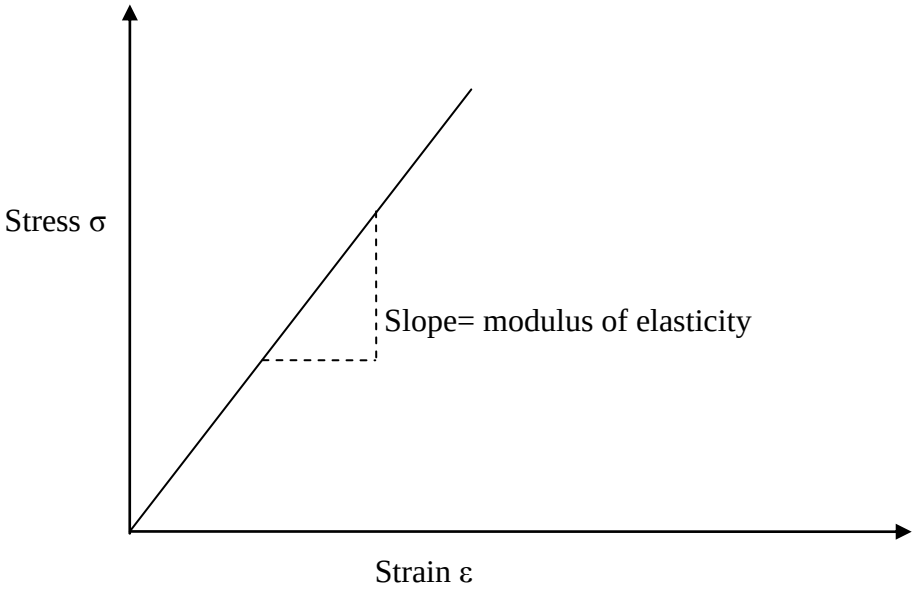

Figure 3.14 *A schematic stress-strain diagram showing linear elastic deformation.*

A plot of stress (ordinate) versus strain (abscissa) results in a linear relationship, as shown in Figure 3.14. For an elastic deformation, the slope of this linear segment corresponds to the modulus of elasticity *E*. This modulus can be regard as derived from stiffness or a material's resistance to elastic deformation (Shackelford, 2008). The greater the modulus, the stiffer the material, or the smaller the strain that results from

the application of a given stress. The modulus is an important design parameter used for computing elastic deflections. Elastic deformation is non-permanent, which means that when the applied load is released, the material returns to its original shape. Application of the load corresponds to moving from the origin up and along the straight line. Upon release of the load, the line is traversed in the opposite direction, back to the origin.

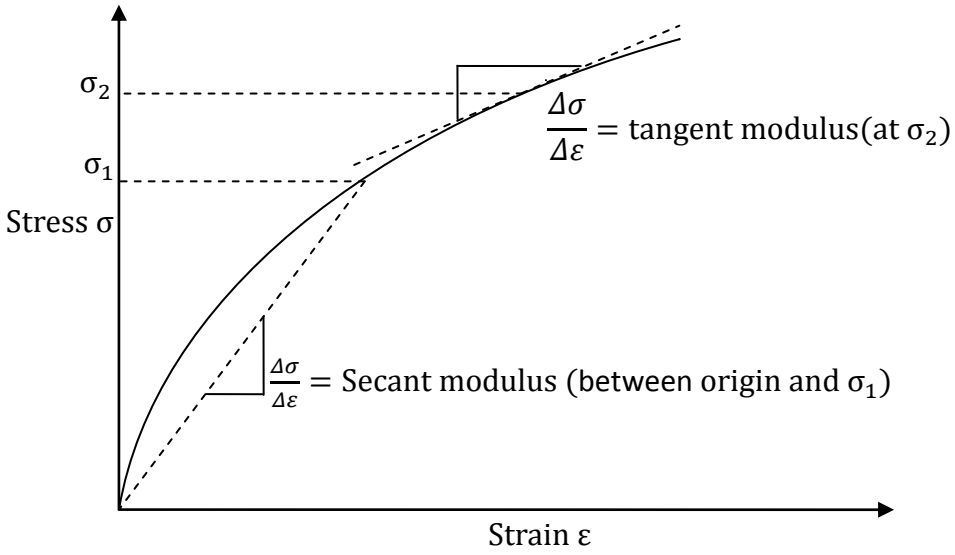

Figure 3.15 *A schematic stress-strain diagram showing non-linear elastic behaviour and how secant and tangent modulus are determined.*

For some polymer fibres and metals this initial elastic portion of the stress-strain curve is not linear (Figure 3.15) hence, it is not possible to determine a modulus of elasticity as described above. For this non-linear behaviour, either tangent or secant modulus is normally used (Shackelford, 2008). Tangent modulus is taken as the slope of the stress-strain curve at some specified level of stress, while secant modulus represents the slope of a secant drawn from the origin to some given point of the σ-ε curve. The determination of this modulus is illustrated in Figure 3.15.

References

Abramowitz, M. (1990) Reflected Light Microscopy: An Overview Olympus America. New York: Melville Inc., pp. 23.

Bindell, J.B. (1992) SEM, Scanning electron microscopy. In: Brundle, C.R., Evans, C.A., Wilson, S., editors, Encyclopaedia of materials characterization-surfaces, interfaces, thin films. Oxford: Elsevier, pp. 70-84.

Butt, H.J., Cappella, B. and Kappl, M. (2005) Force measurements with the atomic force microscope: Technique, interpretation and applications, *Surface Science Reports*, 59, pp. 7-9.

Cullity, B.D., and Stock, S.R. (2001) Elements of X-Ray Diffraction.2nd Ed. New Jersey: Prentice Hall.

Chung, D.D.L. (1994*) Carbon fibre composites*. Newton USA: Butterworth-Heinemann.

Eichhorn, S.J. and Young, R.J. (2004) Composite micromechanics of hemp fibres and epoxy resin microdroplets, *Composites Science and Technology*, *Science direct*, 64, pp. 767–772.

Formula Ten Technical Data, (2011) Ambersil. [online] Available at: http://nickersoneurope.co.uk/pdf_Technical/AMBT%20F10.pdf [Accessed 23 November 2011].

Geisse, N.A. (2009) AFM and combined optical techniques, *Materials today*, 12(7-8), pp. 40-45.

Halary, J., Cookson, P., Stanford, J.L., Lovell, A. and Young, R.J. (2004) Smart Nanostructured Polymeric Coating for Use as Remote Optical Strain Sensors. *Advanced Engineering Materials*, 6(9), pp. 729-733.

Huang, Y. and Young, R.J. (1995) Effect of fibre microstructure upon the modulus of PAN and Pitch based carbon fibres. *Carbon*, 33(2), pp. 97-107.

Kao, C.C. (2008) Study of the deformation of single-walled carbon nanotubes (SWNTs)/epoxy composites using Raman spectroscopy, PhD Thesis, University of Manchester.

Lawes, G. (1987) Scanning electron microscopy and x-ray microanalysis. Chichester: John Wiley and Sons.

Mitra, V.K., Risen, W.M. and Baughman, R.H. (1997) A laser Raman study of the stress dependence of vibrational frequencies of a monocrystalline polydiacetylene. *The Journal of Chemical Physics*, 66(6), pp. 2731-2736.

NanoIntegris, (2011) HiPCO SWNTs Technical Data. [Online] Available at: http://www.nanointegris.com/en/hipco [Accessed 10 December 2011]

PerkinElmer Inc, (2012). Raman spectroscopy. [Online] Available at: http://www.perkinelmer.com/raman [Accessed 17 July 2012].

Renishaw Raman Imaging Microscope WiRETM, User guide M/8012/1798/02, Wotton-under-Edge, Gloucestershire: Renishaw Plc Spectroscopy Products Division.

Robinson, I.M., Zakikhani, M., Day, R.J., Young, R.J. and Galiotis, C. (1987) Strain dependence of the Raman frequencies for different types of carbon fibres, *J. Mater. Sci. Left*, 6, pp. 1212-1214.

Robinson, I.M., Yeung, P.H.J., Galiotis, C., Young, R.J., Batchelder, D.N. (1986) Stress induced twinning of polydiacetylene single crystal fibres in composites. *J. Mater. Sci*, 21, pp. 3440-3444.

Stefane (2010) Diagram of a scanning electron microscope with English captions. Availablefrom:http://en.wikipedia.org/wiki/Scanning_electron_microscope [Accessed 27/01/2012].

Shackelford, J.F. (2008) Introduction to Materials Science for Engineers. 7th Edition. New Jersey: Prentice Hall.

Sigma-Aldrich Co. Ltd., (2011) COOH SWNTs Technical data. [Online] Available at: http://www.sigmaaldrich.com/catalog/product/aldrich/652490?lang=en&region=GB [Accessed 10 December 2011]

Weisstein, E.W., (2012). Lorentzian Function. from Math world-A Wolfram Web Resource.[online] Available at: http://mathworld.wolfram.Com/LorentzianFunction. html [Accessed 12 January 2012].

Whiston, C. (1987) X-Ray Methods, Analytical Chemistry by Open Learning, pp. 29-33

Wilson, R.A., and Bullen, H.A. (2006) Basic theory of AFM, Department of Chemistry, Northern Kentucky University.

Yusoff, R., Aroua, M.K., Nesbitt, A. and Day, R.J. (2007) Curing of polymeric composites using microwave resin transfer moulding (RTM). *Journal of Engineering Science and Technology*, 2(2), pp. 151-163.

Young, R.J. and Andrews, M.C. (1994) Deformation micromechanics in high-performance polymer fibres and composites. *Materials Science & Engineering A*, 184(2), pp. 197-205.

3-(2-Aminoethylamino)propyltrimethoxysilane Technical Data, (2011). Alfa Aesar, A Johnson Matthey Company.

CHAPTER 4 Material Characterization

4.1 General Introduction

The major materials used in this project are a high modulus carbon fibre, a low modulus carbon fibre, epoxy resin, HiPCO Single Walled Carbon Nanotubes (HiPCO-SWNTs) and Carboxylic acid modified functionalized Single Walled Carbon Nanotubes (COOH-SWNTs). A number of methods including Scanning Electron Microscopy (SEM), optical microscopy, Raman spectroscopy and X-ray diffraction have been used to determine the surface morphology and mechanical properties of these materials.

4.2 Carbon Fibre Morphology Characterization by Optical Microscopy

To examine the surface morphology by optical microscopy a single carbon fibre was firstly fixed on a paper card to secure it in place. The paper card has a window in the middle, and is the same as the sample used for the Raman spectroscopy and tensile testing studies. A schematic diagram of the sample can be seen in Chapter 3.The fibre card sample was then placed under the optical microscope to analyse the surface morphology and fibre diameter.

Figure 4.1 shows a typical optical micrograph of a model carbon fibre in the longitudinal direction. An objective lens of ×100 is used to record the image. It can be seen that the contrast of the micrograph is poor, with the edge of the carbon fibre hard to discern. Due to the wavelength of an electron is much smaller than that of visible light, the measurement of the fibre diameter by optical microscopy is not as accuracy as that measured by SEM.

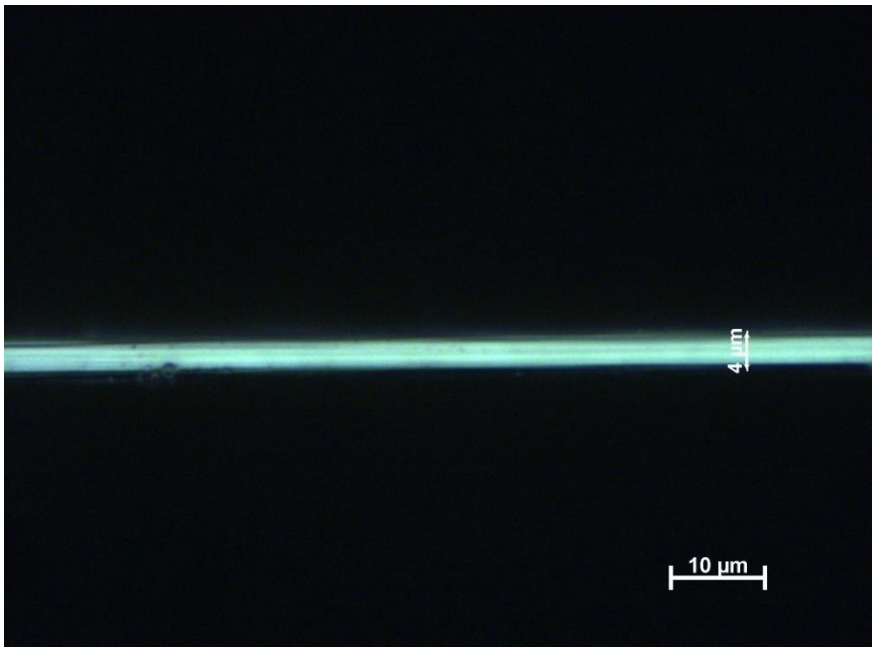

Figure 4.1 *Optical micrograph of a high modulus carbon fibre.*

4.3 Filaments Count for Commercial Carbon Fibres by Optical Microscopy

Both types of carbon fibres were provided by the manufacturers in a bundle form. The ends of these bundles have been imaged under the optical microscope. An example of this is shown in Fig.4.2 for the high modulus carbon fibres. Before the test bundles of high modulus carbon fibres and low modulus carbon fibres were embedded in polyester stubs separately. These stubs were then grinded until the end of each bundle of fibres was exposed at the top of the sample. The cross sectional area at the surface of each polyester stub was then polished in order to be observed clearly in an optical microscope. The average numbers of carbon fibre filaments in each bundle were 5900±200 and 11300 ±1000 for the high modulus carbon fibre and low modulus carbon fibres respectively. More importantly, as shown in Figure 4.2 it has confirmed the circular cross-section which is important for the next step of SEM analysis. The fibre diameter measured across the cross sections show their variability which are generally between 5 µm and 6 µm.

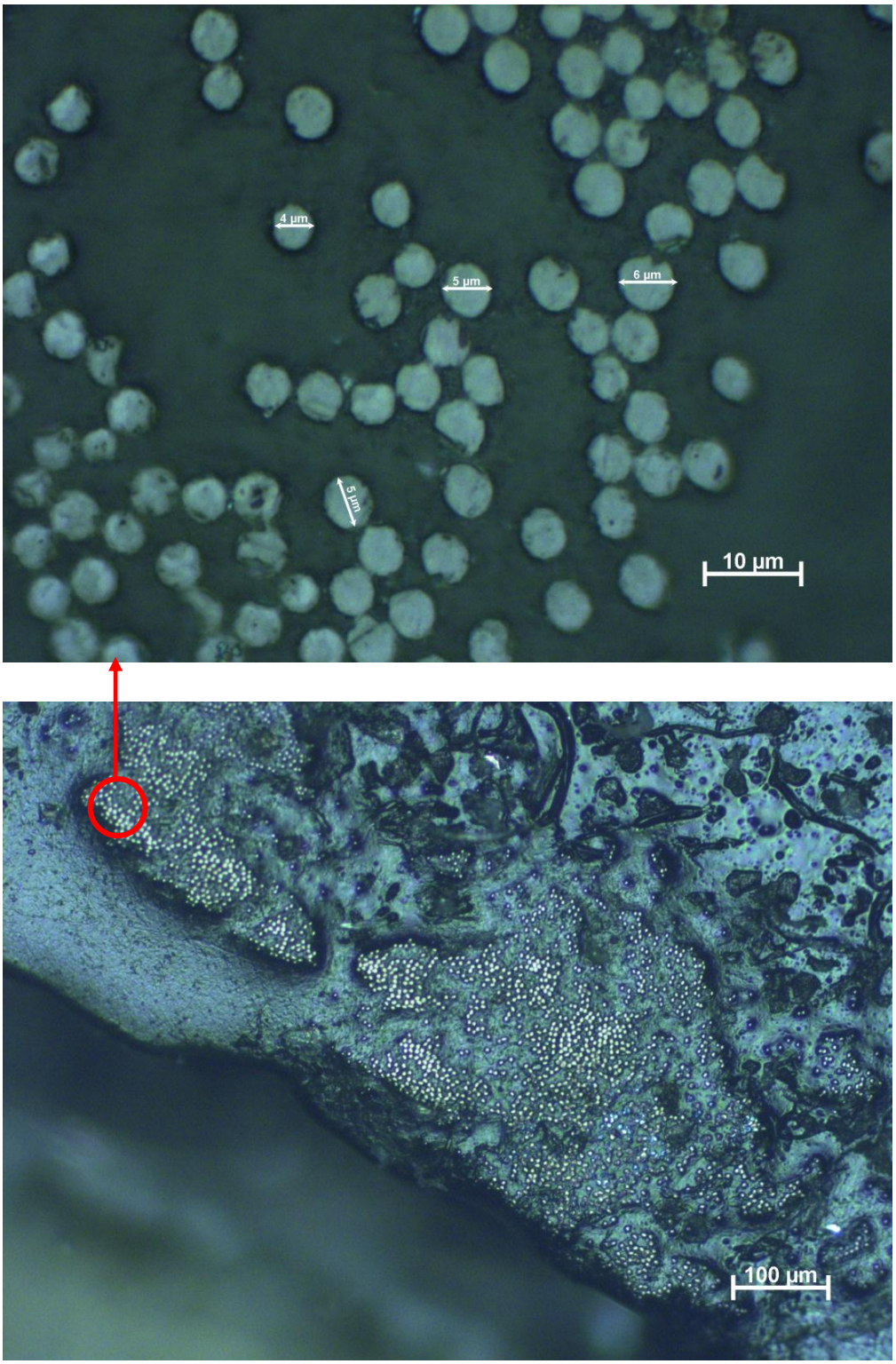

Figure 4.2 *Optical micrographs of aggregate commercial carbon fibres.*

4.4 Carbon Fibre Morphology Characterization by SEM

In this study both types of carbon fibres have been examined in the longitudinal direction, along the fibre surface. The cross section area was determined using Scanning Electron Microscopy (SEM), assuming a circular cross-section. Typical SEM micrographs are shown in Figure 4.3 and Figure 4.4.

According to Figure 4.3 there are no significant differences between the surface morphologies of the two types of fibres; both surfaces have some shallow 'furrows' present, parallel to the fibre axis. This could be due to the fact that both types of fibres are produced from a PAN precursor. These 'furrows' are thought to be created during the fibre spinning process (Smiley, 1993). In the literature these furrows are also described as wrinkled and distorted ribbons (Bascom and Drzal, 1987). Because they are considered to be defects on the carbon fibre surface and detrimental to the fibre strength, it is easy to understand that high strength carbon fibres have comparatively fewer furrows (Bascom and Drzal, 1987). The degree of surface roughness normally decreases with an increase in fibre modulus (Fitzer, 1990). Both types of carbon fibres have been surface treated with a sizing agent by the manufacturer. None of the sizing can however be observed in the SEM images.

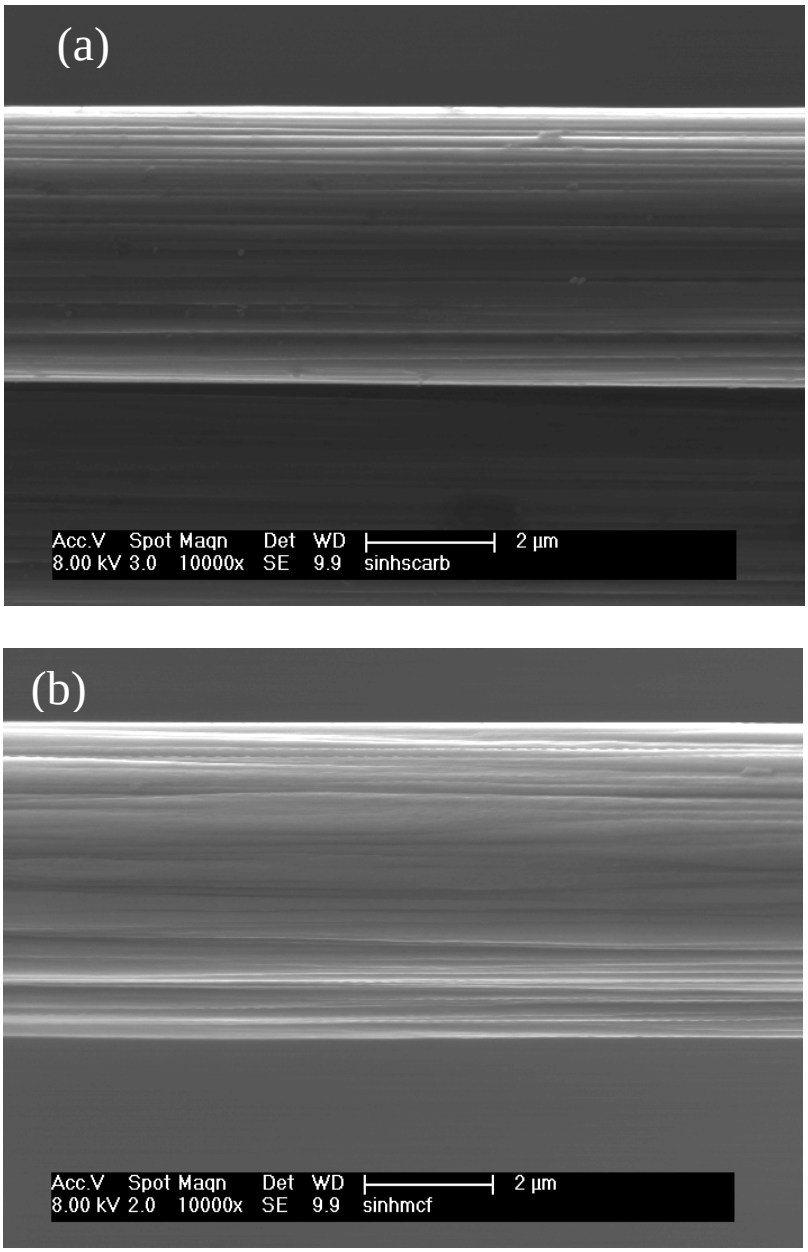

Figure 4.3 *SEM micrographs of (a) a low modulus carbon fibre and (b) a high modulus carbon fibre in the longitudinal direction.*

The cross section areas for fibres fractured during the tensile test have also been measured under SEM. According to Figure 4.4 both types of carbon fibre have mostly a circular cross section, but the low modulus carbon fibre exhibits a rather smooth fracture surface compared to the high modulus one which shows clearly a skin-core shape as the graphite basal planes are created turbostratically into a layered structure during the graphitization process (Diefendorf and Tokarsky, 1975). Furthermore it can be observed that the outer layers (skin) are more organized than the interior (core).

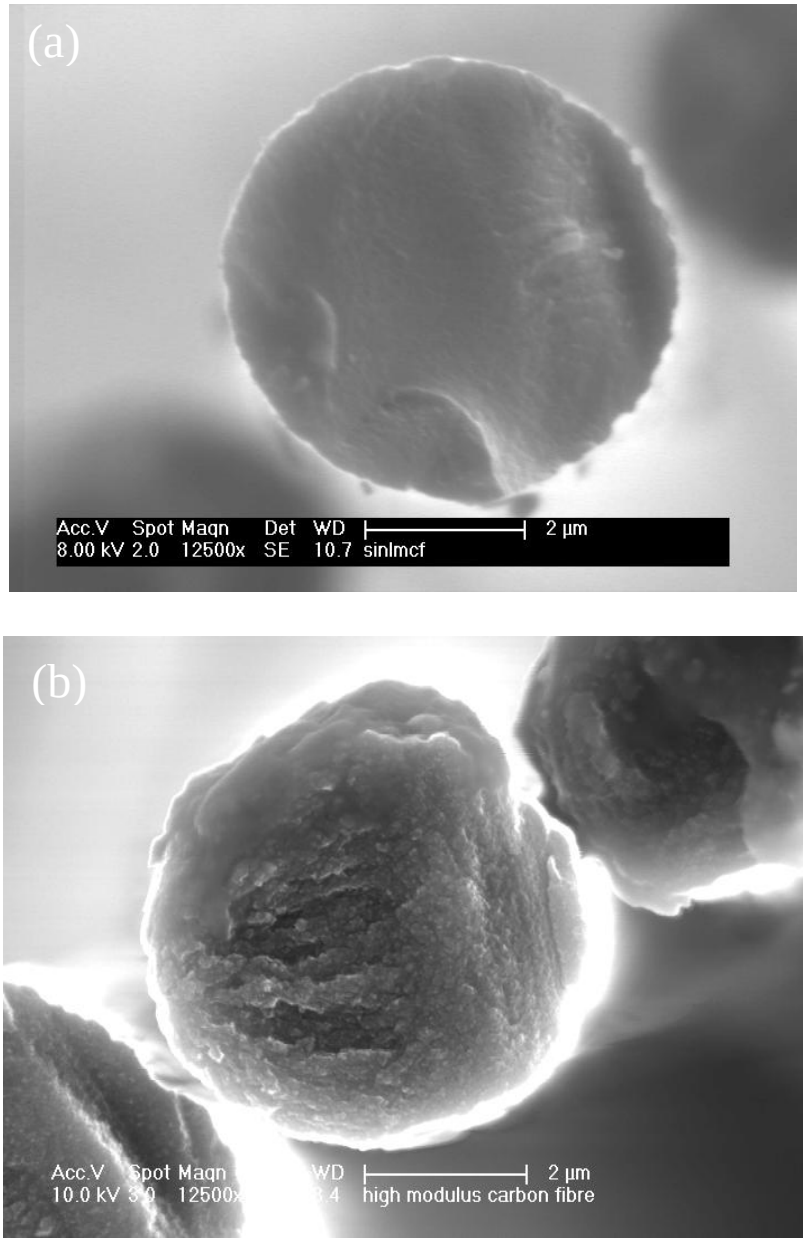

Figure 4.4 *SEM micrographs of the cross-sectional areas of (a) a low modulus carbon fibre and (b) a high modulus carbon fibre.*

Paris *et al.* (2001) indicated that PAN-based carbon fibres usually exhibit random cross sectional areas. The fundamental building block of carbon fibres are graphitic crystallites, which are generally made up from the layers of graphite basal planes. The size of the graphitic crystallites and their plane layers are highly reliant on the time and temperature conditions during the heat treatment procedure; larger planer graphitic basal planes and layered crystallites are created when the treatment time is longer and the

temperature is higher (Badami, 1967). These crystallites are generally parallel to the fibre axis in a filamentary or ribbon like morphology type (the 'furrows' discussed earlier). During manufacturing of the fibre, these crystallites become more parallel to the fibre axis if strain and higher temperatures are both applied. As a result of these mechanisms, the surface of high modulus carbon fibre tends to have more graphitic basal planes than the lower modulus carbon fibres which are produced in comparatively lower graphitization temperatures. This is why the cross section of high modulus carbon fibre indicates the presence of graphitic basal planes, and the low modulus fibres have a comparatively smoother cross section (Chuang, 1994).

Previous studies indicated that the properties of carbon fibres, such as tensile modulus, tensile strength, electrical resistivity, and thermal conductivity, are reliant on the microstructure of the fibre (Deurbergue and Oberlin, 1992; Melantis *et al*., 1996; Denison *et al*., 1985). The structural aspects that act as influences on the properties of fibres are as follows:

- the degree of crystallinity.
- the interlayer spacing(d_{002}).
- the crystallite sizes or more accurately, the coherent lengths perpendicular (L_c) and parallel (L_a) to the carbon layers.
- the texture (preferred orientation of carbon layers) parallel and perpendicular to the fibre axis.
- the transverse and longitudinal radius of curvature (r_t and r_l) of the carbon layers.
- the domain structure.
- the volume fraction, shape and orientation of micro voids.

A high modulus carbon fibre usually has a high degree of crystallinity. A high degree of crystallinity, large crystallite sizes, strong texture parallel to the fibre axis and low interlayer spacing and low density of in-plane defects normally contribute to a high modulus, low electricity resistivity and high thermal conductivity carbon fibre. Weak texture perpendicular to the fibre axis, a large amount of defects and distortions within a layer, small values of r_t and r_l, large value of L_c and a low volume fraction of micro voids result in a high tensile strength carbon fibre (Deurbergue and Oberlin, 1992).

A large value of L_c usually comes along with a reduction in side bonding between the stacks of carbon layers, thus decreasing the strength (Deurbergue and Oberlin, 1992). The microstructure of a carbon fibre is greatly reliant on the processing of the fibres, especially the heat treatment temperature and the ease of graphitization of the carbon fibre precursor (Deurbergue and Oberlin, 1992). It is noted that the structure of graphite layers for PAN based carbon fibres stays in a turbostratic form (no graphitic ABAB stacking of the graphite layers) even when the heat treatment temperature goes beyond 2000 ℃ (Chuang,1994).

The side expansion of graphitic crystals is predominately sensitive to the ultimate firing temperature (UFT), while crystallite orientation is dependent on a combination of drawing (pre-stretching and hot stretching) and UFT (Melanitis, 1996).

4.5 Carbon Fibre Characterization by X-ray Diffraction

The crystal structure of the fibres was examined using a Philips X'PERT APD powder X–ray diffractometer (λ = 1.54 Å, CuKα radiation). It can be seen from Figure 4.5 both carbon fibre samples have the same peaks but their intensities are different. According to XRD software, the peaks in both high and low modulus carbon fibre images matched perfectly with a database for carbon element, no other elements are indicated by these peaks for both types of carbon fibres. The average crystallite size can be calculated by using the Scherrer equation (Equation 4.1)

$$D = \frac{k\lambda}{\beta \cos\theta} \tag{4.1}$$

where D is the average crystallite size, k is scherrer algorithm with the value of 0.9, λ is the x-ray wavelength with the value of 1.542 for the operated system. θ is the Bragg angle. β can be obtained in equation 4.2 is the line broadening at half the maximum intensity (FWHM) after subtracting the instrumental line broadening in radians.

$$\beta = \frac{(\beta_{obs} - \beta_{std})\pi}{180} \tag{4.2}$$

In this study, the value of standard β_{std} is 0.136 ^{o}2 Theta, the obtained β_{obs} for the high modulus and low modulus carbon fibre are 2.13 ^{o}2 Theta and 2.15 ^{o}2 Theta respectively.

The bragg angle θ for the high modulus and low modulus carbon fibre are 26.13 ^{o}2 Theta and 26.18 ^{o}2 Theta respectively. Finally, average crystallite sizes for both high modulus and low modulus carbon fibre have been calculated to be 40 Å.

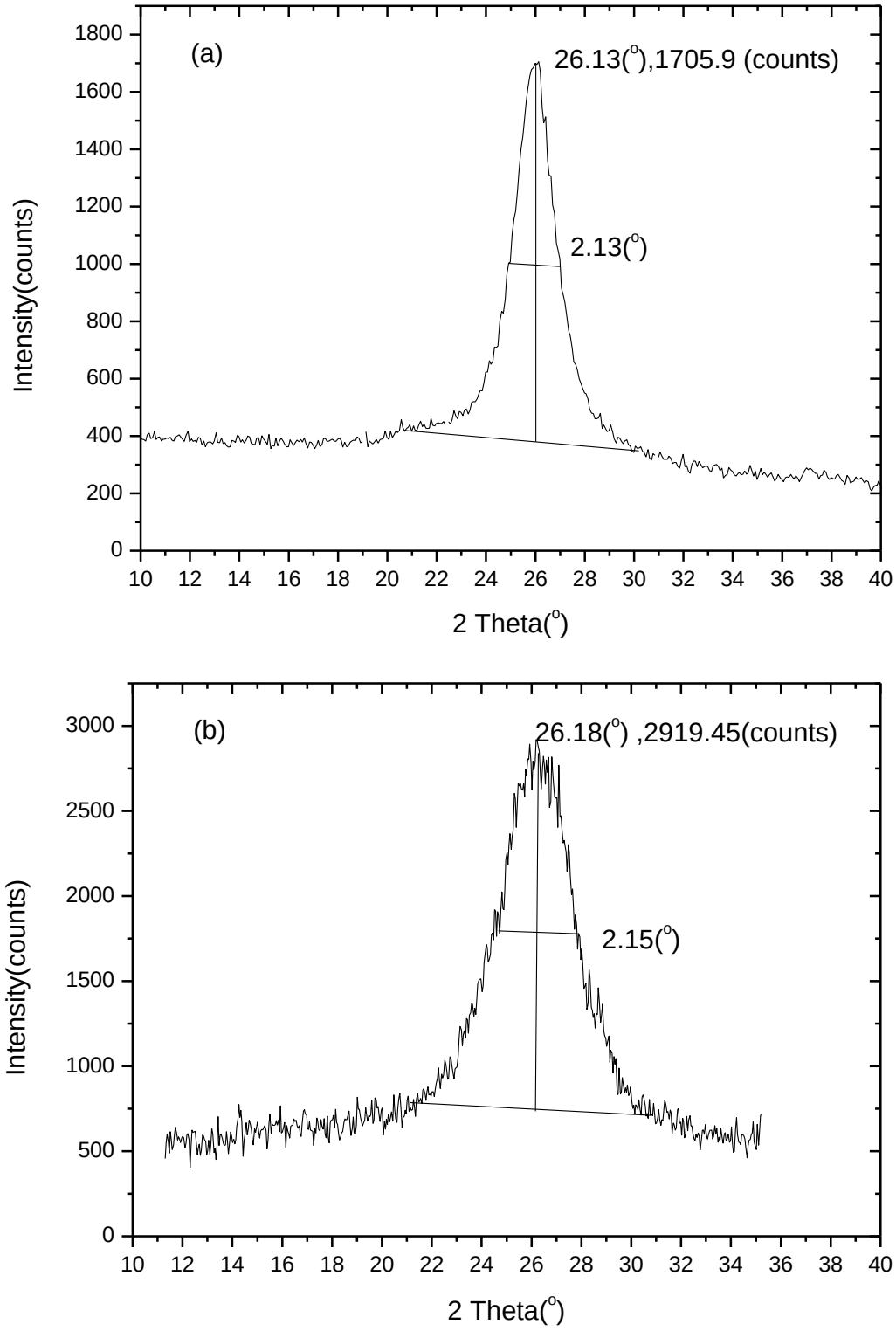

Figure 4.5 *X-ray diffractograms of (a) a high modulus carbon fibre and (b) a low modulus carbon fibre.*

4.6 Carbon Fibre Characterization by Atomic Force Microscopy

In this work AFM was used to characterise the surface morphology of carbon fibres. Figure 4.6 shows the surface morphology of the two types of carbon fibres; their surface roughness has been quantified as well. It can be seen that the shallow furrows which used to be detected from SEM images cannot be observed entirely clearly in the AFM image, this could be due to resolution limitation that a tip with higher aspect will give a better resolution and the radius of curvature of the probe results in different tip convolution, for which more details are provided in Chapter 3. However as the cantilever tip is able to touch the fibre surface, the depth of the shallow furrows can be determined through the line profile function as is shown in Figure 4.6. According to the crossed line profile the determined average roughness are 6.17nm and 9.32nm for the low modulus carbon fibre and high modulus carbon fibre respectively.

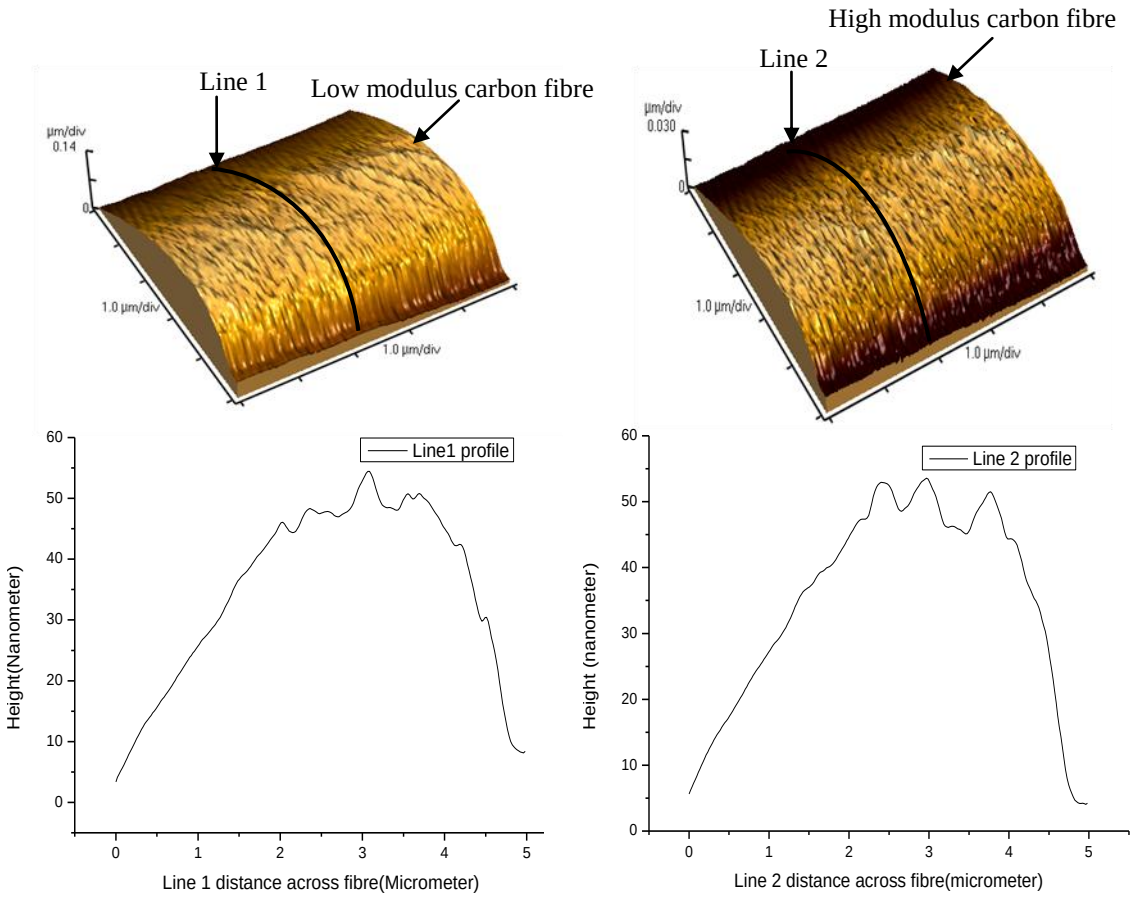

Figure 4.6 *The surface morphology micrograph of carbon fibre characterised by AFM.*

4.7 Carbon Fibre Diameter Measurement by SEM

In this work, the diameters of both the low and high modulus carbon fibres have been determined at the magnification of 7500, each type of carbon fibre have 20 samples to be measured. Due to the diameter along one single fibre could be varied, 10 different areas on the longitudinal direction of same fibre have been examined and the average value has been obtained. All results are showing in Table A.1 and Table A.2 in Appendix A, and finally the average diameter of 5.23 ± 0.25 μm and 5.35 ± 0.30 μm for the high modulus carbon fibre and low modulus fibre has been determined respectively.

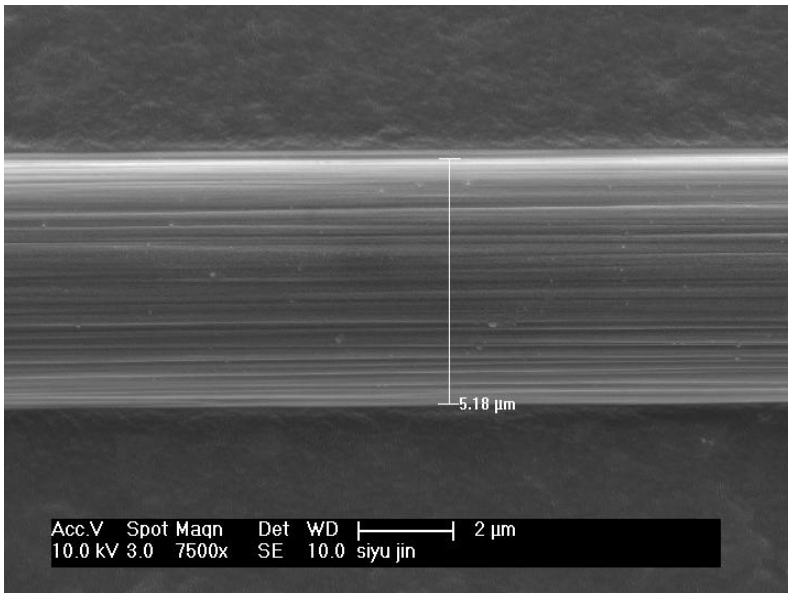

Figure 4.7 *Image of SEM for detecting the diameter of single carbon fibre.*

4.8 Characterization by Raman Spectroscopy

4.8.1 Raman Spectroscopy Calibration

A calibration is necessary before experiments can take place, in order to acquire consistent Raman band positions between experiments. A calibration is achieved by using a silicon standard. A very intense peak from this sample is located at a position of 520.20 cm^{-1}. To carry out a calibration, a static scan was carried out with the grating set at a central position of 520 cm^{-1}. The peak located close to this central position was then fitted and an offset correction was applied in order that is was consistently found at 520.20 cm^{-1}.

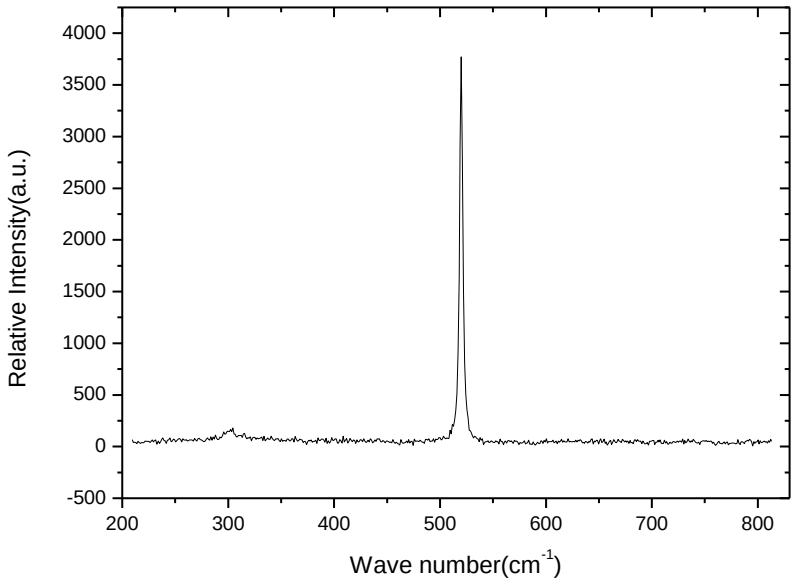

Figure 4.8 *Typical Raman spectra of a silicon sample for calibration.*

4.8.2 Raman Spectrum from Different Laser

Raman spectra from a high modulus carbon fibre have been obtained using different lasers; including 514 Argon, 633 HeNe-ion, 785 IR and 830 IR, the numbers here refer to laser wavelength which with the unit of nm. Since the laser power for all types of laser sources are impossible to be adjusted perfectly in the same value, they have been kept in the closest range at 1.0 ±0.2 mW. According to Figure 4.9 the 2D band intensity decreases with an increase in the laser wavelength; this band is completely absent from

the spectra obtained using a laser of wavelength 830 nm. The shifts that were recorded were mainly based on the 2D band, so a laser source with lower wavelength was deemed most suitable. However, a 633 nm HeNe-ion laser was selected, and was used for all Raman spectroscopy studies in this study, in order to compare the results with many previous researches as most of them use the 633 nm HeNe.

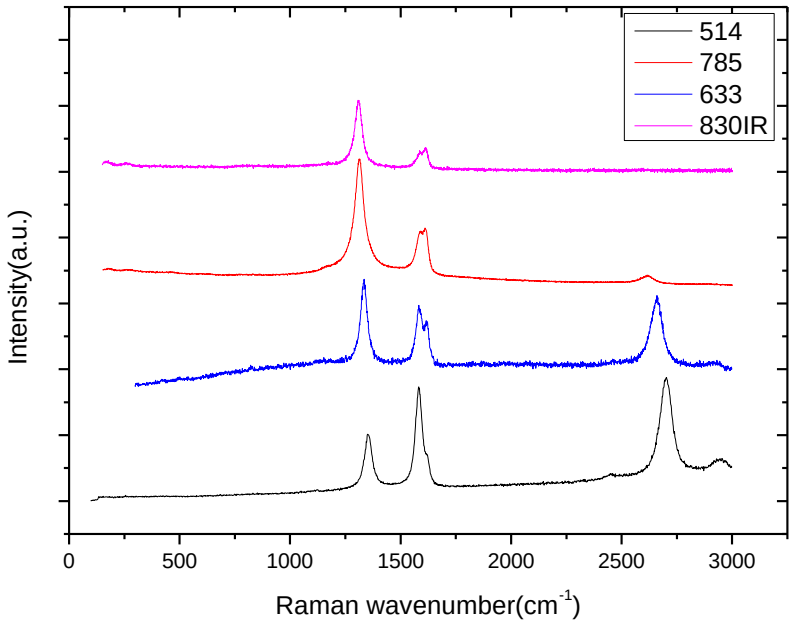

Figure 4.9 *Typical Raman spectra for a high modulus carbon fibre using different laser systems.*

4.8.3 Raman Spectrum of Carbon fibres

The Raman spectra for both types of carbon fibres have been recorded in the range 150 - 3000 cm^{-1} and are shown in Figure 4.10a and Figure 4.10b. The Raman spectra obtained from a high modulus carbon fibre were sharper and well-defined, and have a G'-band (2D band). Conversely, the spectra from low modulus carbon fibres exhibited a broad but weak Raman band in the region from 1000 cm^{-1} to 1700 cm^{-1}, which is also called the "first order" region. The region from 1700 cm^{-1} to 3300 cm^{-1} is called the "second order" region; this region is due to the overtone or combination frequencies of the scattering species (Tuinstra and Koenig, 1970).

It is well known from the literature that Raman spectra are fundamentally associated with the crystallite size, crystallite symmetry and the average orientation of the crystallite layer, and can provide exclusive information about the connection between microstructure and deformation in carbon fibres. There are straightforward ways to understand spectral differences between high and low modulus carbon fibres, as their crystallite sizes and orientations vary significantly.

According to previous studies, the general description of the Raman bands observed from carbon fibre are as follows (Young, 1995; Morita *et al*., 1986; Robinson *et al*., 1987; Huang and Young, 1993; Sakata, 1988): The D band at about 1360 cm^{-1} is considered to be due to the boundaries of the graphite crystal, and is only present in a poorly graphitized fibre. It tends to disappear when graphitization temperatures are higher. It will therefore not be present in single graphite crystals. The D band is attributed to the breakdown of the lattice symmetry of the graphite cell, and is assigned to the A_{1g} vibrational mode of the graphite plane, also owing to the small crystal size and structure disorder.

The G band at around 1580 cm^{-1} is related to the C-C in plane stretching mode of the graphite planes of an infinite crystal, and is presents in the for Raman spectra from single graphite crystals and all carbon fibres. This band is attributed to the vibrational mode E_{2g} of the graphite cell. Furthermore the intensity ratio of I_D/I_G is believed to be linked to the crystal size.

The D' band is only presents for non-graphitized fibres. It turns out to be strong at low annealing temperatures, but is detected as a shoulder peak to the G band at higher ultimate firing temperatures. It is attributed to disorder and small crystallite sizes and become attenuated when two dimensional ordering is established. Furthermore it is not present for well graphitized fibres.

The G' band at a position of ~2700 cm^{-1} , which about twice the wave number position of the 1360 cm^{-1} band is attributed to the overtone of the D band; the so-called 2D band. This band is present for crystalline graphite, and graphitized fibres and splits into two bands when samples are highly graphitized; if the ultimate firing temperature is increased above 3000 ℃. For PAN based carbon fibres this band only exits in spectra for high modulus fibres. It has to be noted that the position of the G' (2D) band is the most sensitive to deformation applied to fibres or graphene (Galiotis, 1988; Huang and

Young, 1995; Turrell, 1972; Nemanich, *et al*., 1977; Nemanich and Solin, 1979; Melanitis *et al*., 1996; Nakamizo *et al*., 1974; Tsu *et al*., 1978).

According to a previous study by Katagiri *et al.* (1998) the band width reflects the orientation of the graphite layer plane with respect to the fibre axis. The sharper the G band and 2D band, typically the higher the Young's modulus of the fibre and its surface crystallinity (Chieu *et al*., 1982; Menarch *et al*., 1984; Katagiri *et al*.,1984; Katagiri *et al*., 1988).

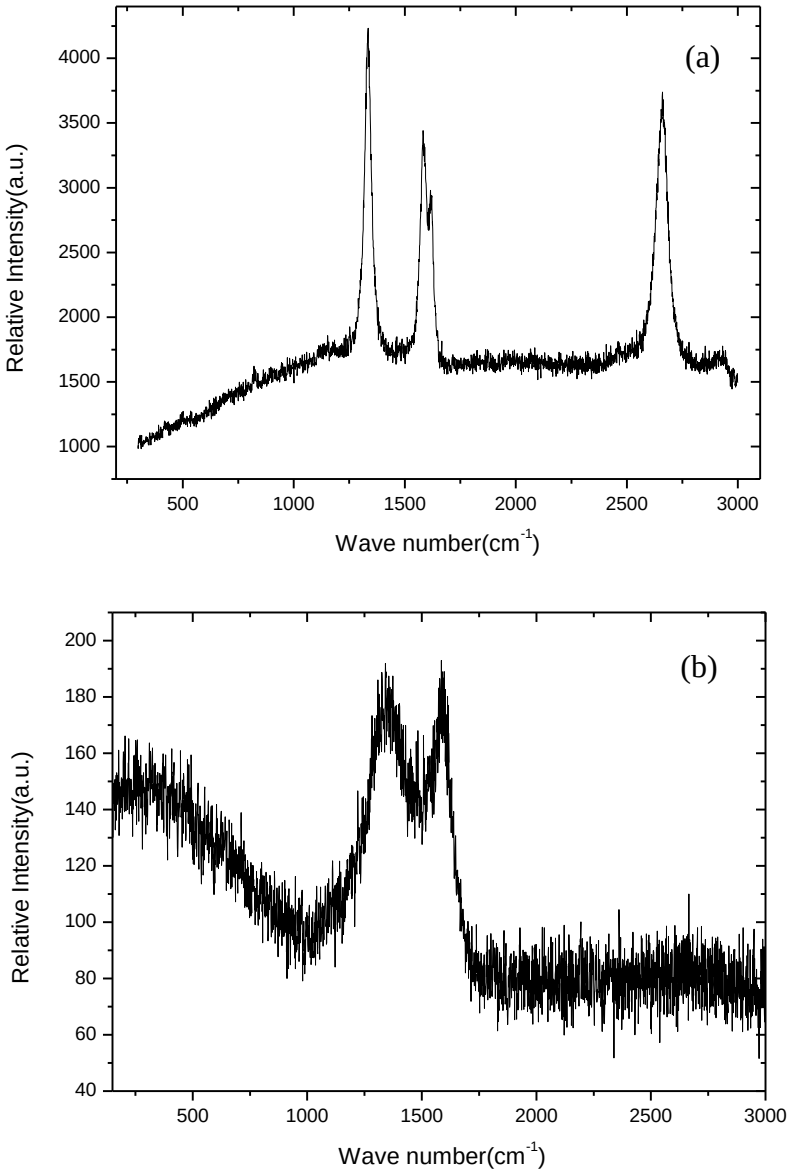

Figure 4.10 *Typical Raman spectra for (a) a high modulus carbon fibre and (b) a low modulus carbon fibre.*

4.8.4 Raman Spectrum of Carbon Nanotubes

Two types of Single Walled Carbon Nanotubes (SWNTs), HiPCO and carboxylic acid functionalised SWNTs have been characterized using Raman Spectroscopy. Typical spectra in the range of 150 - 3300 cm^{-1} are shown in Figs.4.11a and 4.11b respectively.

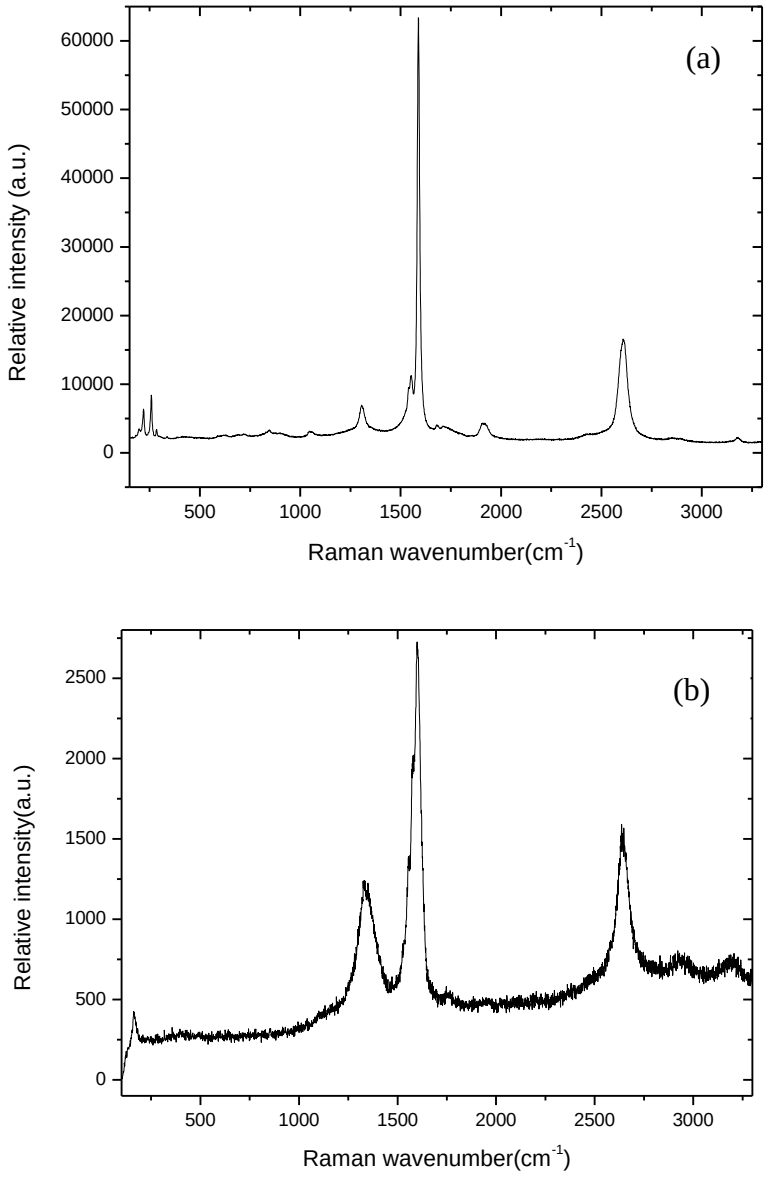

Figure 4.11 *Typical Raman spectra from HiPCO SWNTs (a) and COOH SWNTs (b).*

The spectra from carbon nanotubes are similar to carbon fibres as they consist of a D-band (Disorder-induced mode), a G-band (Tangential stretch mode or high energy mode) and a G' band (overtone of the D-band also named 2D-band). There are bands present at lower wavenumber positions called Radial Breathing Modes which are exclusive to carbon nanotubes, and cannot be observed in other carbon systems (Batra and Gupta,

2008). It is observed that the Raman spectrum of HiPCO SWNTS has more peaks in the RBM region than carboxylic acid functionalised samples. This is thought to be due to the fact that the HiPCO SWNTs are relatively smaller than the carboxylic acid functionalized SWNTs, and that they have a wider variety of diameters which will determine the positions of the RBMs. Moreover the functional group attached to the wall of tubes could have hindered the radial breathing oscillation motion (Peng *et al*., 2003).

Since there is a strong resonance enhancement of the scattering cross section and a photo selective response of the Radial Breathing Modes (RBM) related to tube diameters, Raman spectroscopy has been recognized as a powerful technique for the characterization of SWNTs (Kukovecz *et al*., 2002). The determined average band positions and diameters of HiPCO and COOH SWNTs are shown in Table 4.1.

Table 4.1 *Comparison of average band positions and diameters of HiPCO and COOH-SWNTs.*

Types of SWNTS	D band position(cm^{-1})	G band position(cm^{-1})	2D band position(cm^{-1})	Diameter(nm) from suppliers	Diameter(nm) calculated from RBM
HiPCO SWNTs	1554.5±0.8	1591.7±0.7	2609.2±0.6	0.8-1.2	0.9-1.0
COOH SWNTs	1329.6±1.9	1586.1±2.3	2645.1±2.9	1.3-1.5	1.4-1.7

4.9 Solubility of SWNTS

In this study, 2 mg COOH SWNTs and HiPCO SWNTs were dispersed in 200 mg of a range of solvents, and then sonicated for 10 hours. Afterwards their solubilities were qualitatively compared after 20 minutes and 20 days. The results suggest that ethanol has the best solubility than other types of solvent. Ethanol was therefore used to disperse SWNTs and later they will be mixed with epoxy or silane for different coating methods which will be used in Chapter 5.

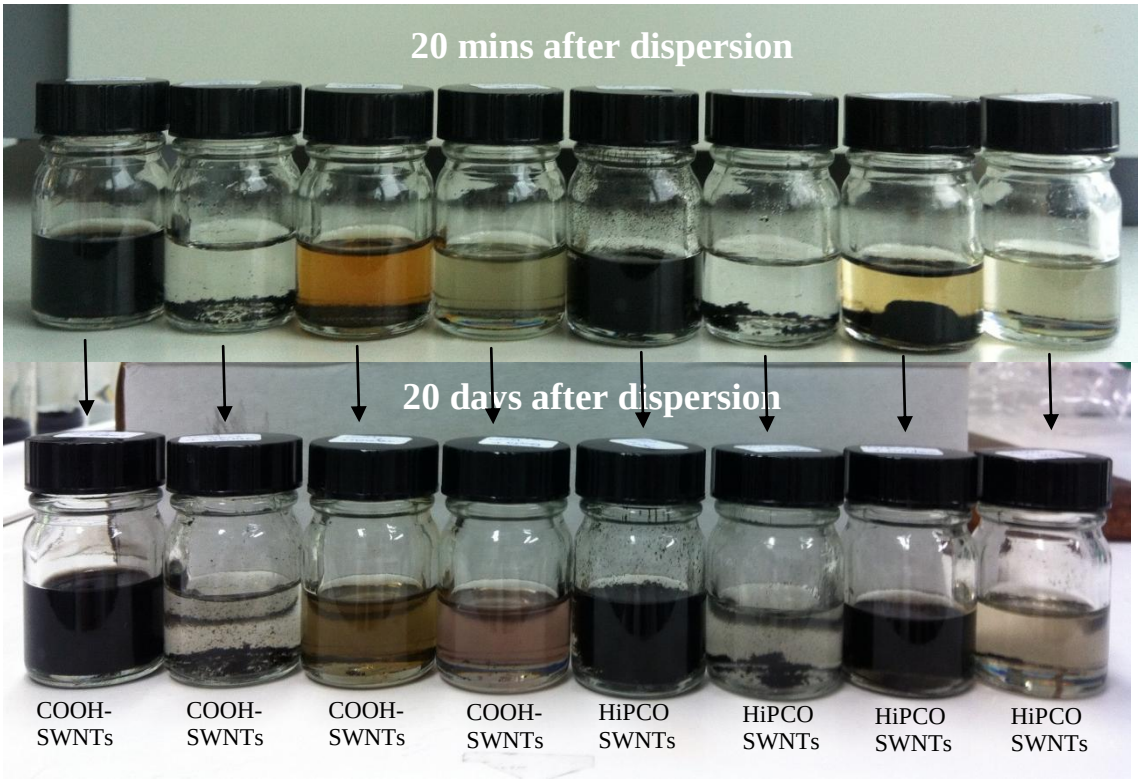

Figure 4.12 *Solubility of COOH SWNTs in ethanol, silane solution, hardener, epoxy and HiPCO SWNTs in ethanol, silane solution, hardener and epoxy from left to right. The upper picture shows the stability after 20 mins and the lower one is taken 20 days later.*

4.10 Mechanical Properties Characterization

In this study, the carbon fibres and epoxy dumbbell samples have been mechanically tested using an Instron^{TM} 1120 tensile testing machine.

4.10.1 Mechanical Properties of Carbon Fibre

A range of carbon fibres with gauge lengths of 10,20,30,50 and 100 mm were tested. The test load is 0.2 N for each specimen, and the cross head moving speed was 10% of the gauge length per minute. All results for the measured Young's modulus, breaking strength and strain are shown in Appendix B. Typical stress-strain curves for the high modulus carbon fibres and low modulus carbon fibre with the gauge length of 50mm are shown in Figure 4.13. These stress-strain curves exhibit a nearly linear deformation,

without a yield point until fibre fracture. Therefore, fibre modulus was obtained by using the slope of the linear fitted line. It should be noted that a secant modulus was used same as that of the manufacturers which is the slope value of the stress and strain curves from origin to the middle. In Figure 4.13, the values of modulus for the low and high modulus carbon fibres are found to be 260.2 ±1.1 GPa and 443.9 ± 1.3 GPa respectively.

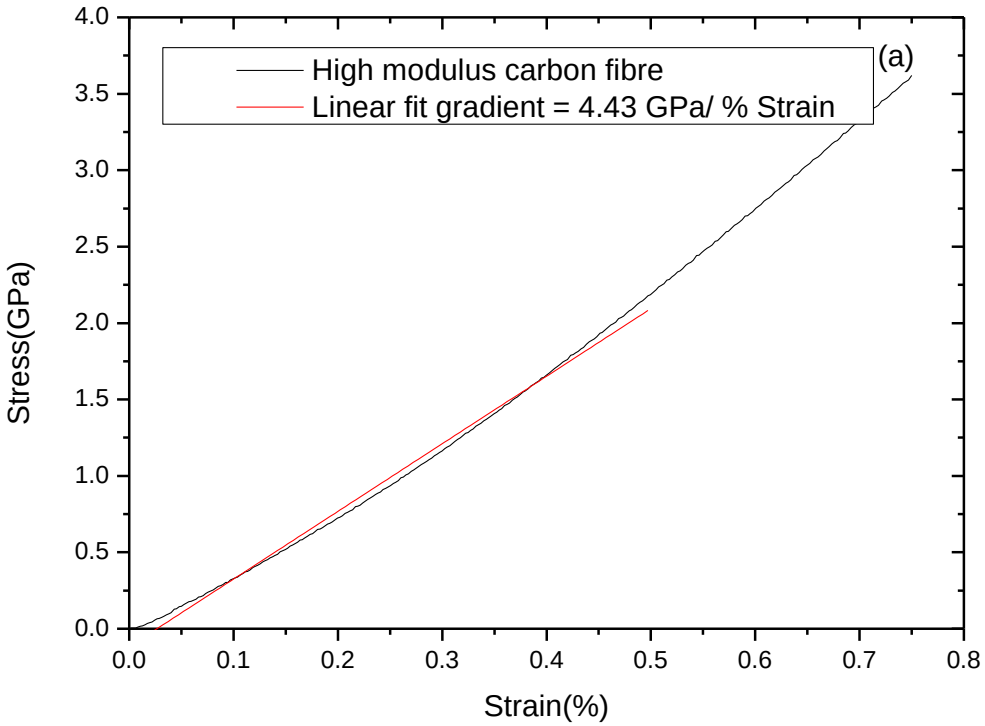

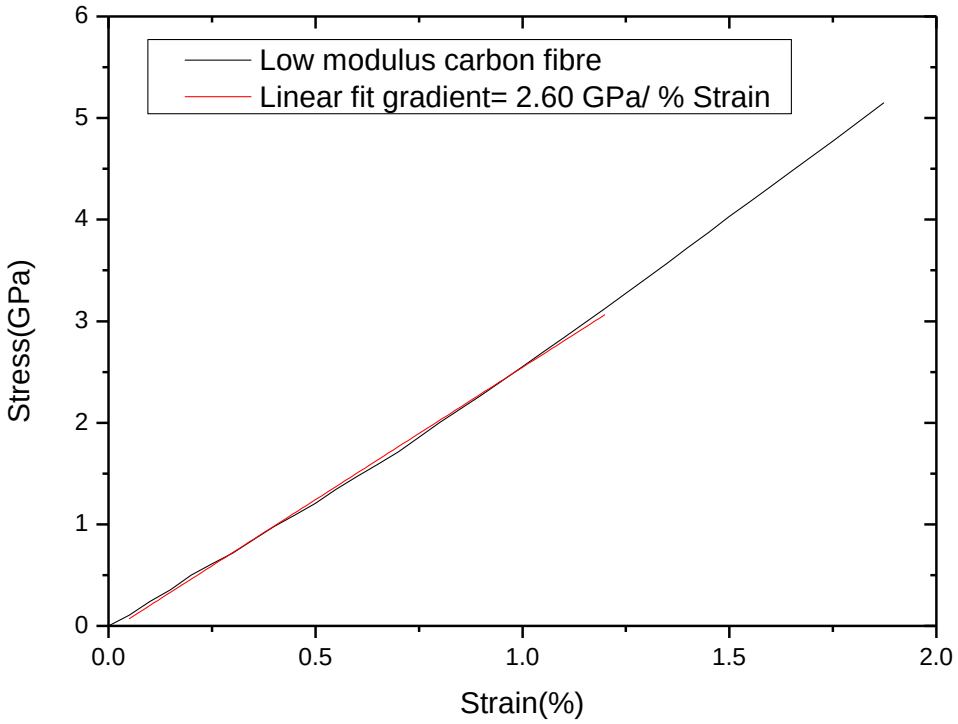

Figure 4.13 *Typical stress-strain curves for the high modulus carbon fibre (a) and low modulus carbon fibre (b).*

In order to detect the effects of gauge length on the tensile test data, both types of carbon fibres with 20 samples at each gauge length of 10, 20, 30, 40, 50 and 100 mm were tested, the results of which are displayed in the Figure 4.14, Figure 4.15 and Figure 4.16. Figure 4.14 shows that Young's modulus increases with an increase in the gauge length, the values become more stable when gauge lengths are higher. This effect has been discussed by Arridge *et al.* (1976), who indicated that Young's modulus from a short gauge length fibre could be underestimated. Since the load is preferentially transferred along the surface of the specimen leaving the regions close to the fibre axis comparatively undeformed, the Young's modulus therefore estimated by surface strain gauges or by movement of the points of the application of load will be lower than the true value. As the gauge length increases the load becomes more uniformly diffused across the entire cross-section, and then the effective modulus approaches the true value (Arridge *et al*., 1976). It should be noted that this gauge length dependence is not real, but an artefact of the test procedure. Modulus is intrinsic and only changes with gauge length due to end effects or the compliance of the machine.

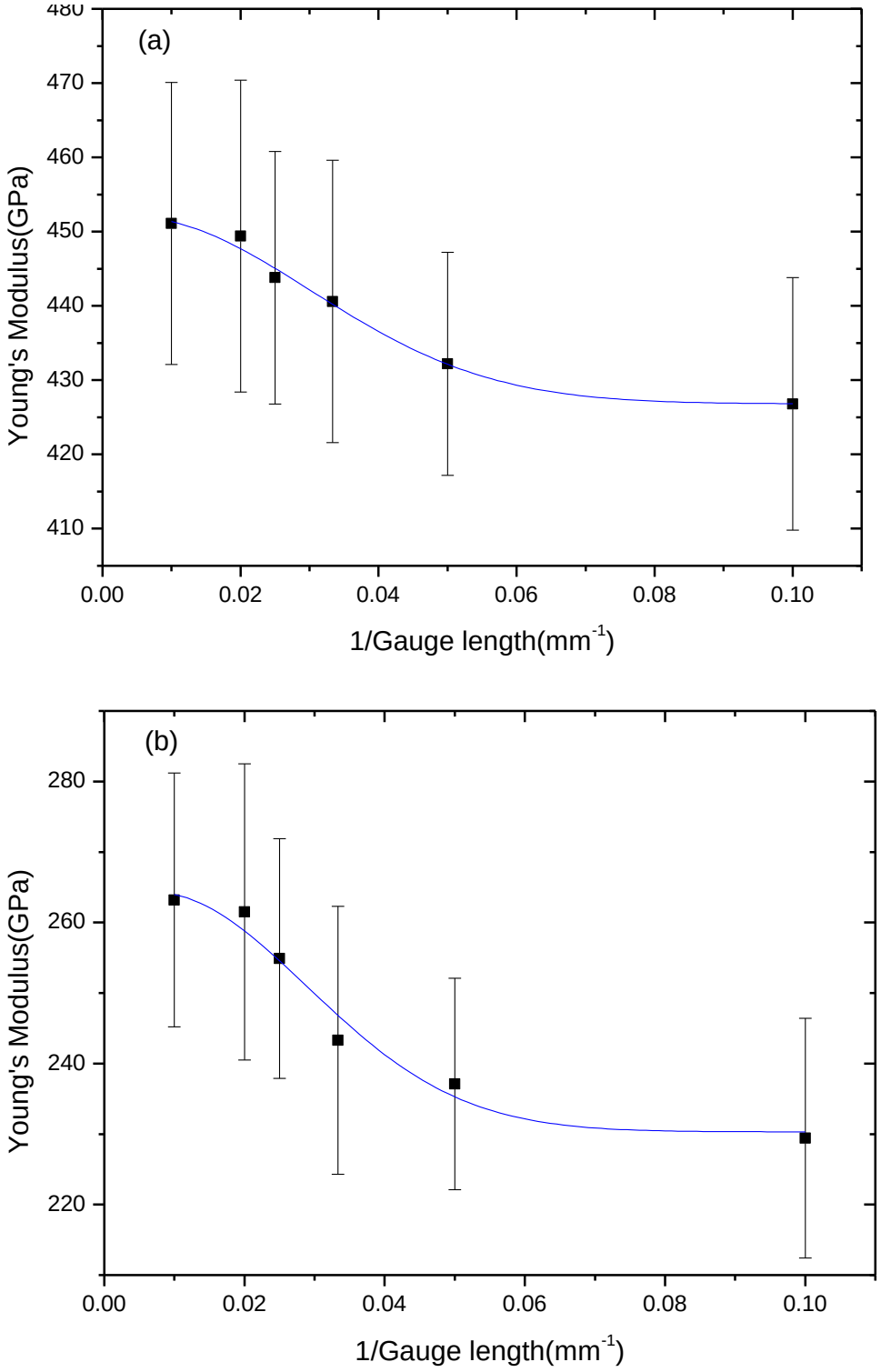

Figure 4.14 *Effect of gauge length on the Young's modulus of the samples for the high modulus carbon fibre (a) and low modulus carbon fibre (b).*

In addition, Figure 4.15 and Figure 4.16 also reveal that the breaking strength and strain will decrease with an increase in the fibre gauge length. This is because theoretically the

longer the gauge length, the more defects are statistically present, which negatively influences the strength of the fibre.

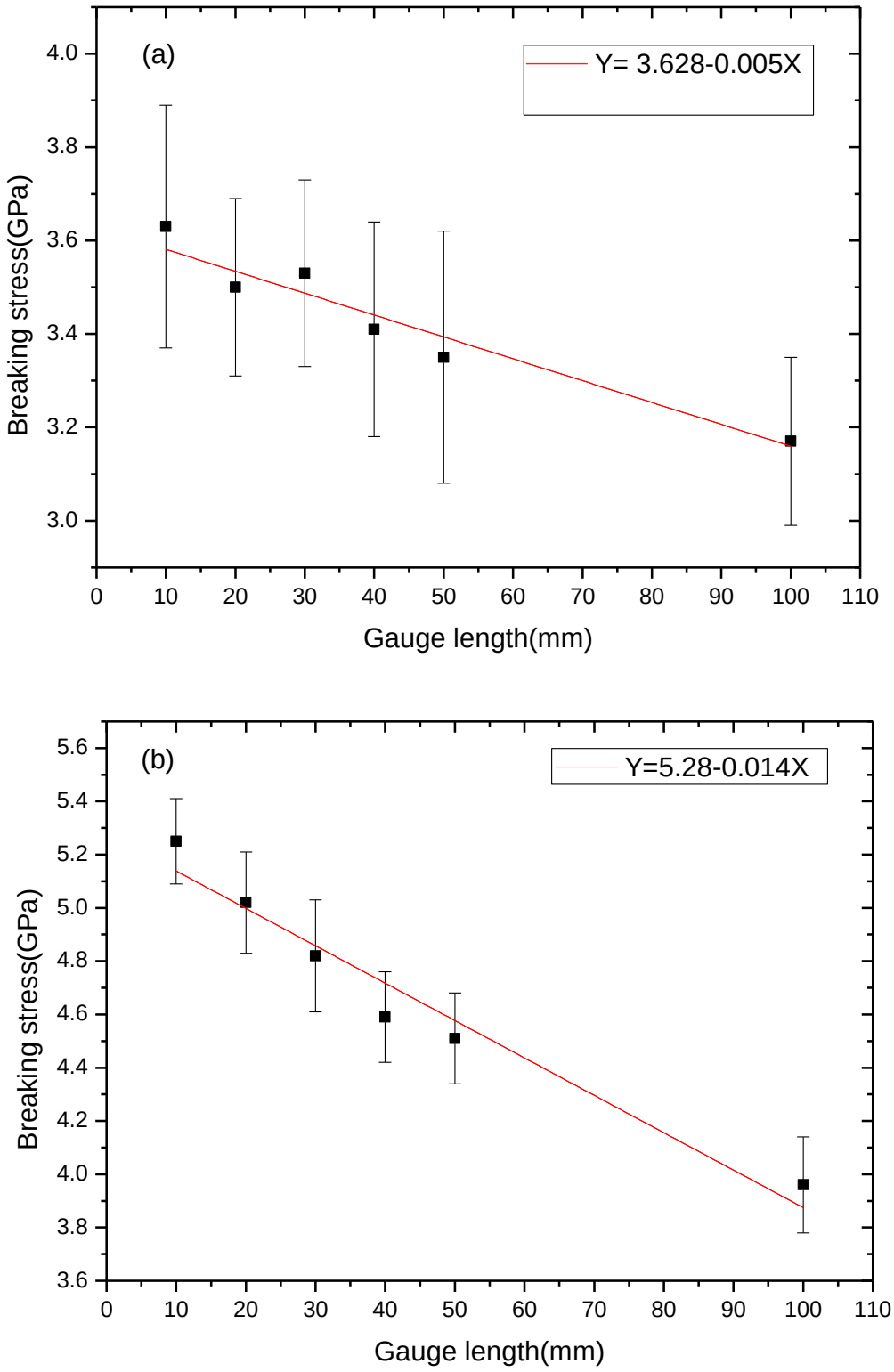

Figure 4.15 *The dependence of breaking strength on the gauge length of fibre samples for high modulus carbon fibre (a) and low modulus carbon fibre (b).*

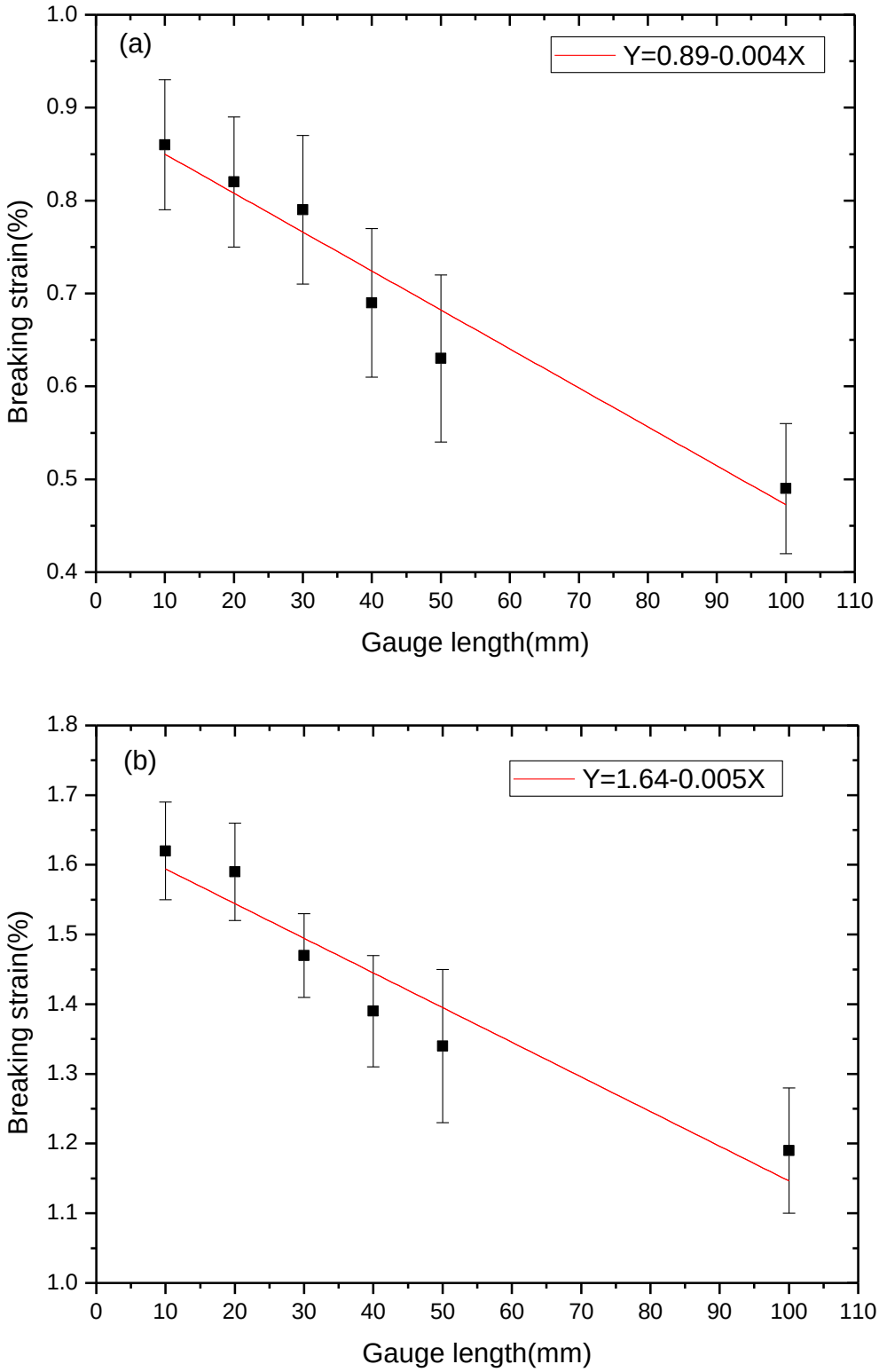

Figure 4.16 *The dependence of breaking strain on the gauge length of the samples for (a) a high modulus carbon fibre and (b) a low modulus carbon fibre.*

The "true modulus", from the extrapolation to infinite gauge length, for the high and low modulus carbon fibres are 451.1 ±0.7 GPa and 264.8 ± 0.4 GPa respectively. The

extrapolated breaking strengths arte 3.75±0.31 GPa and 5.47±0.27 GPa for the high and low modulus carbon fibres respectively. The extrapolated breaking strains are 0.95% ± 0.07%and 1.74% ±0.09% for the high and low modulus carbon fibres respectively.

4.10.2 Mechanical Properties of Epoxy Resin

In this study, 10 specimens of cold cured neat epoxy dumbbell shapes have been mechanically tested in an Instron 1121 tensile test machine. A typical stress and strain curve of this epoxy dumbbell specimen is shown in Figure 4.17. The value of Young's Modulus is by using the slope of the linear fitted line. The average dimension and detected Young's Modulus of the samples are shown in Table.4.2.

Table 4.2 *The average dimension of the epoxy specimens and Young's Modulus.*

	Gauge length(mm)	Thickness(mm)	Width(mm)	Young's Modulus (GPa)
Epoxy dumbbell specimen	34.99±0.05	1.92±0.10	8.07±0.08	2.63±0.28

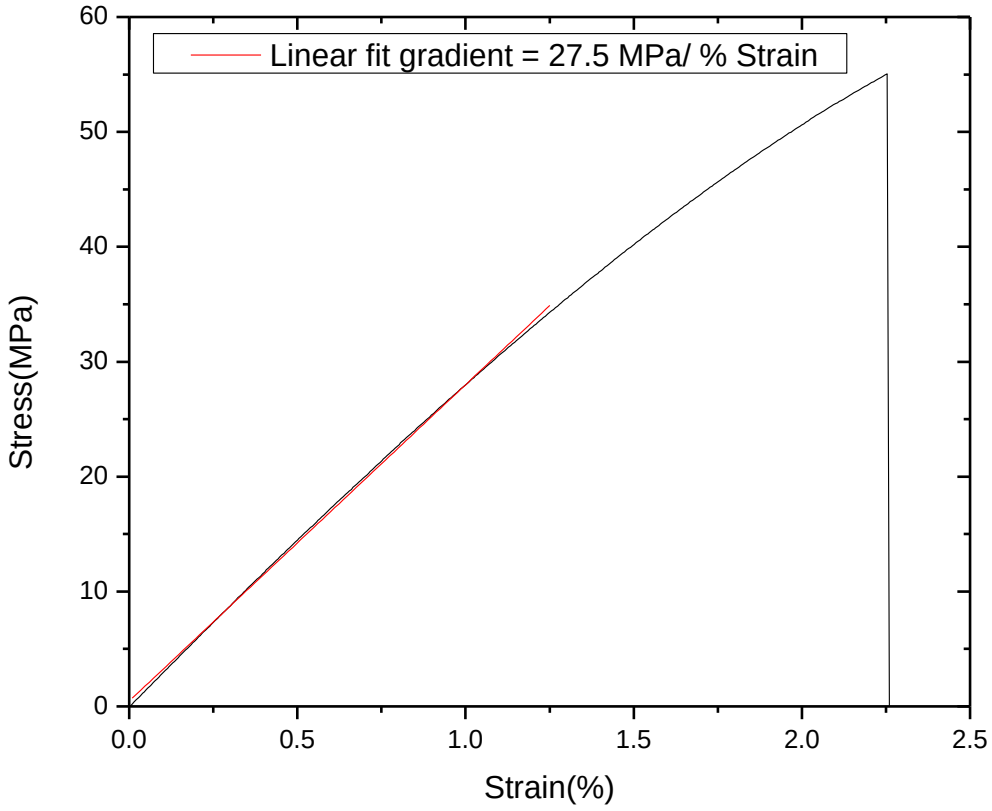

Figure 4.17 *A typical stress-strain curve for a neat epoxy dumbbell specimen.*

Reference

Arridge, R. Barham, P.J. and Farrell, C.J. (1976) Importance of End Effects in Measurement of Moduli of Highly Anisotropic Materials. *Journal of Materials Science*, 11(4), pp. 788-790.

Bascom, W.D., Drzal, L.T. (1987) *The surface properties of carbon fibre and their adhesion to Organic Polymers*. NASA Contractor Report 4084, pp. 35.

Badami, D. U., Joiner, J. C. and Jones, G. A. (1967) Microstructure of High Strength High Modulus Carbon Fibres, *Nature*, 215, pp. 386-387.

Batra, R.C., and Gupta, S. (2008) Wall thickness and radial breathing modes of single walled carbon nanotubes. *Journal of applied mechanics transactions of the ASME*, 75(6), 061010-1-6.

Chuang, D.D.L. (1994) *Carbon fibre composites*. Newton USA: Butterworth-Heinemann.

Chieu, T.C., Dresselhaus, M.S., and Endo, M. (1982) Raman study of benzene-derived graphite fibres. *Physical Review B,* 26, pp. 5867-5877.

Deuerbergue, A., and Oberlin, A. (1992) TEM Study of Some Recent High Modulus PAN-Based Carbon Fibres. *Carbon, 30*(7), pp. 981-987.

Denison, P., Jones, F.R. and Watts, J.F. (1985) X-ray Photoelectron Spectroscopic Analysis of Barium-Labelled Carbon Fibre Surfaces, *Journal of Material. Science,* 20, pp. 4647-4656.

Diefendorf, R.J. and Tokarsky, E. (1975) High Performance Carbon Fibres, *Polymer Engineering Science*, 15(3), pp. 150-159.

Fitzer, E. (1990) *Carbon Fibres Filaments and Composites*, edited by Figueredo, J.L., Bernardo, C.A., Baker, R.T.K. and Huttinger, K.J., Dordrecht: Kluwer Academic, pp. 405-439.

Galiotis, C., and Batchelder, D.N. (1988) Strain dependence of the first and second order Raman spectra of carbon fibres. *J.Mater.Sci.Lett*, 7(5), pp. 545-547.

Huang, Y., and Young, R. J. (1993) Nonlinear elasticity in carbon fibres. *Journal of Materials Science Letters*, 12(2), pp. 92-95.

Huang, Y., and Young, R.J. (1995) Effect of fibre microstructure upon the modulus of PAN and Pitch based carbon fibres. *Carbon*, 33(2), pp. 97-107.

Katagri, G., Ishida, H., AND Ishitani, A. (1984) *Proceedings of the 9th Conference on Raman Spectroscopy*, Tokyo, edited by ICORS, Tokyo, pp. 256.

Katagiri, G., Ishida, H., and Ishitani, A. (1988) Raman spectra of graphite edge planes. *Carbon*, 26(4), pp. 565-571.

Kukovecz, A., Kramberger, C., Georgakilas, V., Prato, M., and Kuzmany, H. (2002) A detailed Raman study on thin single-wall carbon nanotubes prepared by the HiPCO process. *European Physical Journal B*, 28, pp. 223-230.

Melanitis, N., Tetlow, P.L., and Galiotis, C. (1996) Characterization of PAN-based carbon fibres with laser Raman spectroscopy, *Journal of Materials Science*, 31, pp. 851-860.

Mernagh, T.P., Cooney, R.P., and Johnson, R.A. (1984) Raman spectra of graphon carbon-black. *Carbon*, 22(1), pp. 39-42.

Morita, K., Murata, Y., Ishitani, A., Murayama, K., Ono, T., and Nakajima, A. (1986) Characterization of commercially available PAN (Polyacrylonitrile)-based carbon fibres. *Pure Appl. Chem.*, 58, pp. 455-468.

Nakamizo, M., Kammereck, R., and Walker, P.L. (1974) Laser Raman studies on carbons. *Carbon*, 12(3), pp. 259-267.

Nemanich, R.J., Lukovsky, G., and Solin, S.A. (1977) Infrared active optical vibrations of graphite. *Solid State Commun*, 23(2), pp. 117-120.

Nemanich, R.J., and Solin, A. (1979) 1st order and 2nd order Raman scattering from finite-size crystals of graphite. *Phys. Rev*, 20(2), pp. 392-401.

Paris, O., Loidl, D., Muller, M., Lichtenegger, H., and Peterlik, H. (2001) *Cross sectional texture of carbon fibres analysed by scanning micro beam X-ray diffraction*, Journal of Applied Crystallography,34, pp. 473-479.

Peng, H.Q., Alemany, L.B., Margrave, J.L. and Khabashesku, V.N. (2003) Sidewall carboxylic acid fictionalization of single-walled carbon nanotubes. *Journal of the American Chemical Society*, 125(49), pp. 15174-15182.

Robinson, L.M., Zakikhani, M., Day, R.J., Young, R.J. and Galiotis, C. (1987) Strain dependence of the Raman frequencies for different types of carbon fibres. *Journal of Material Science*, 6(10), pp. 1212-1214.

Sakata, H., Dresselhaus, G., Dresselhaus, M.S., and Endo, M. (1988) Effect of uniaxial-stress on the Raman spectra of graphite fibres. *Journal of Applied Physics*, 63(8), pp. 2769-2772.

Smiley, R.J. and Delgass, W.N. (1993) AFM, SEM and XPS characterization of PAN-based carbon fibres etched in oxygen plasmas. *Journal of Materials Science*, 28, pp. 3601-3611.

Tuinstra, F., and Koenig, J. (1970) Raman Spectrum of Graphite. *Journal of Chemical Physics*. 53, pp. 1126-1130.

Tsu, R., Gonzalez, J.H., and Hernandez, C.I.(1978) Observation of splitting of E2G mode and 2-phonon spectrum in graphites. *Solid State Commun*, 27(5), pp. 507-510.

Turrell, G. (1972) *Infrared and Raman Spectra of Crystals*, London: Academic Press.

Young, R.J. (1995) Monitoring Deformation Processes in High-performance Fibres using Raman Spectroscopy. *Journal of the Textile Institute*, 86(2), pp. 360-381.

CHAPTER 5 Micromechanics of Single Carbon Fibres Using Raman Spectroscopy

5.1 General Introduction

It is well known from previous research by Robinson *et al.* (1987), that the position of Raman bands from carbon fibres are strain sensitive; these Raman bands shift to lower wavenumber positions, and for some fibres tend to broaden in peak width. As shown in Figure 5.1, the 2D band from the high modulus carbon fibre shifts towards a lower wavenumber position when fibre strain increases from 0% to 0.4%, and to 0.8%. On the other hand, the Raman band position is known to shift to a higher wavenumber position when the fibre is under compression (Amer and Schadler, 1996).

A study carried out by Huang and Young (1994) suggested that the rates of Raman band shift per unit strain are linearly related to Young's modulus of the fibres. Therefore the Raman shift can be used to determine the deformation of carbon fibres and thus analyze the interfacial properties for carbon fibre reinforced composites.

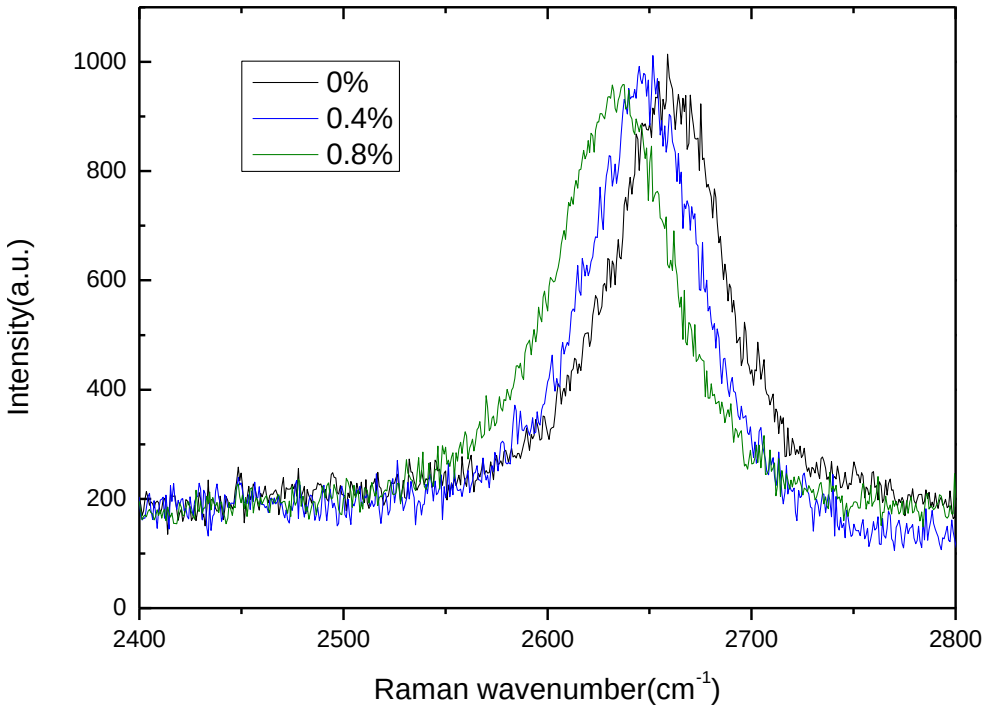

Figure 5.1 *The position of the 2D Raman band from a high modulus carbon fibre shifting towards a lower wavenumber position when deformed in tension at strain levels of 0 %, 0.4 % and 0.8 %.*

In this Chapter, the Raman 2D band shift rates for the high modulus carbon fibres will be investigated. Since there is no Raman 2D band can be observed from the low modulus carbon fibre, SWNTs will be used to coat on the fibre surface as a sensor. Therefore, the best coating method for SWNTs coating on a low modulus carbon fibre, to sense the applied deformation will be determined. The best coating method will be used to make carbon fibre reinforced model composites and analyse the interface between the fibres and the resin material (epoxy). Finally, SWNTs will also be coated on high modulus carbon fibre surface in order to compare Raman 2D band shift rates from SWNTs sensor and pure high modulus carbon fibre.

5.2 Deformation Micromechanics of a High Modulus Carbon Fibre using Raman Spectroscopy

Among all the Raman bands from the Raman spectra of high modulus carbon fibres the 2D band is the most sensitive to tensile deformation (Bowden and Gardiner *et al*., 1993).

Additionally, in the regions of the 2D band, no band from the epoxy resin is present (as shown in Figure 5.3). Therefore, when carbon fibres are embedded in an epoxy resin, there is no band from the resin interferes with the 2D band from the carbon fibre.

In this study, first of all the samples were prepared by fixing a single high modulus carbon fibre on a fibre card; these samples are the same as that used for mechanical tensile testing, as shown in Figure 3.12 in Chapter 3. Load was applied to the fibre to deform it to a certain strain level in increments of 0.1% until fibre fracture. This was carried out by using a load sensitive fibre rig, as shown in Figure 3.2. 2D Raman bands were recorded from five different areas on the fibre, using polarized laser configurations of VV and VN, at each strain level. Five samples were tested, and then these Raman bands were fitted by using a Lorenzian function. Finally the result is shown in Figure 5.2.

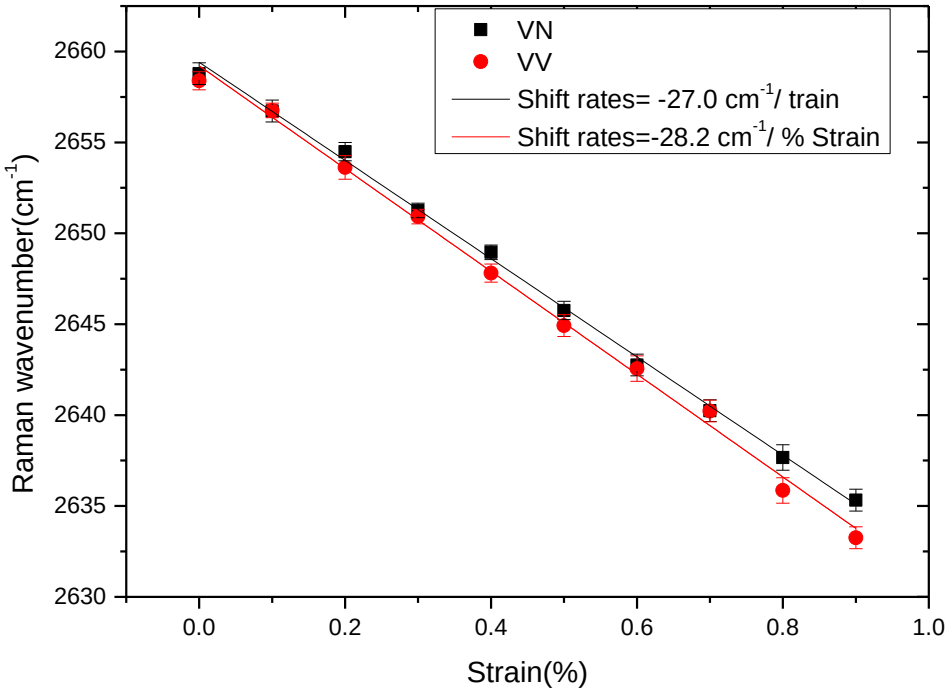

Figure 5.2 *Typical shifts in the position of the Raman 2D band for high modulus carbon fibres deformed in tension in different polarised laser configurations.*

It can be seen from Figure 5.2 that the 2D Raman band shifts in a linear fashion towards a lower wavenumber position with tensile deformation. Linear regressions have been applied to these data, and the slopes of these fitted curves have been found to be -

28.2 ±0.4 cm^{-1}/ % and -27.0 ±0.3 cm^{-1}/ % for the VV and VN polarized configuration respectively.

Since the band shift rate with respect to strain for the VV laser polarization configuration is higher than for VN, VV polarisation condition was used for all subsequent experiments on high modulus carbon fibres. The band shift rate with respect to strain was used to calibrate fibre strain, and to subsequently monitor the interface between a single carbon fibre and epoxy resin in Chapters 6, 7 and 8.

5.3 Micromechanics of a Low Modulus Carbon Fibre Using Raman Spectroscopy

Raman spectra from the low modulus carbon fibre, shown in Chapter 4 and Figure 4.10(b), are not well defined, with a low signal to noise ratio. A broad G and D Raman band are present, but no 2D Raman band. Without the presence of a 2D band it is hard to determine micromechanics of these fibres with any accuracy; using the weak and broad G or D Raman bands leads to inaccurate results. Furthermore, bands from epoxy resin interfere with both the G and D bands, as is shown in Figure 5.3. It is therefore impossible to determine the band positions from the low modulus carbon fibre when the fibre is embedded in an epoxy resin.

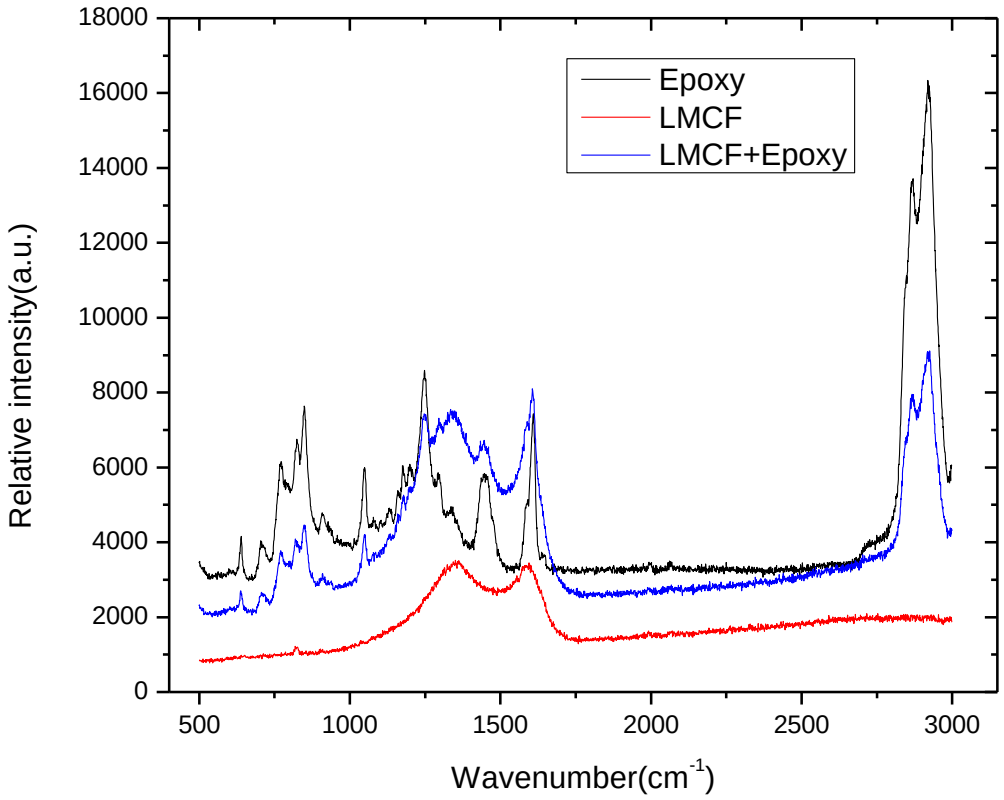

Figure 5.3 *Typical Raman spectra for low modulus carbon fibres and epoxy resin and their composites.*

To solve this problem single walled carbon nanotubes (SWNTs) were applied and coated on the fibre surface as a strain sensor, and the Raman 2D band obtained from SWNTs was then used to monitor fibre deformation. Similar work has been carried out

by Sureeyatanapas and Young (2009) where SWNTs were coated on a glass fibre to sense local strain and used to monitor the interface with an epoxy resin.

In this study, a number of different coating methods were used to prepare samples. The shift rates of the 2D Raman band were determined. It is assumed that the higher the shift rate with respect to strain of the 2D Raman band, the better the bonding between the SWNTs and the low modulus carbon fibres. Based on this criterion alone, the best preparation method was found by analysing the shift rates, and in addition, the distribution of SWNTs on the fibre surface. The best coating method was then used to prepare composite samples to monitor the interface between carbon fibres and epoxy resin.

5.4 Effect of Laser Power

According to previous research by Kao and Young (2004) the 2D Raman band from SWNTs tends to shift towards lower frequencies as the power of an incident laser beam is increased due to laser beam heating effects. Therefore a heat induced 2D band shift could affect the results from the single fibre deformation micromechanics.

In order to minimise the laser beam heating effects an appropriate laser power must be carefully chosen. The requirements for the laser power are as follows:

a. The laser power should be as low as possible to reduce the heat effects.
b. The 2D band obtained using this laser power should be intense enough with low noise to be adequate for sensing fibre strain.
c. The position of the 2D band should be within a consistent range within a small standard deviation.

COOH SWNTs were chosen to represent both types of carbon nanotubes. A range of laser power levels of 1%, 10%, 25% and 50% from the HeNe-ion laser source were applied (100% laser power on the sample is 2.4 mW). Raman spectra from COOH SWNTs were obtained at each laser power level, the result of which is shown in Figure 5.4. It can be seen from Figure 5.4 that as the laser power is increased, the intensity of the Raman bands also increases. When the laser power is 1%, the 2D band obtained is too weak and difficult to be observed. It is impossible to carry out micromechanical

investigations with such a low laser power. It can be seen that the 2D band is intense enough when the laser power increased to 10%. The position of the 2D Raman band was determined (spectra repeated ten times) at each laser power level, the results of which are shown in Figure 5.5. It was found that the 2D band position was not consistent when the laser power was increased to 50%; a large standard deviation is observed. The smallest standard deviation was detected when the laser power was 25%. To maximise intensity, but reduce variability, a 25% laser power was chosen to carry out the micromechanical studies.

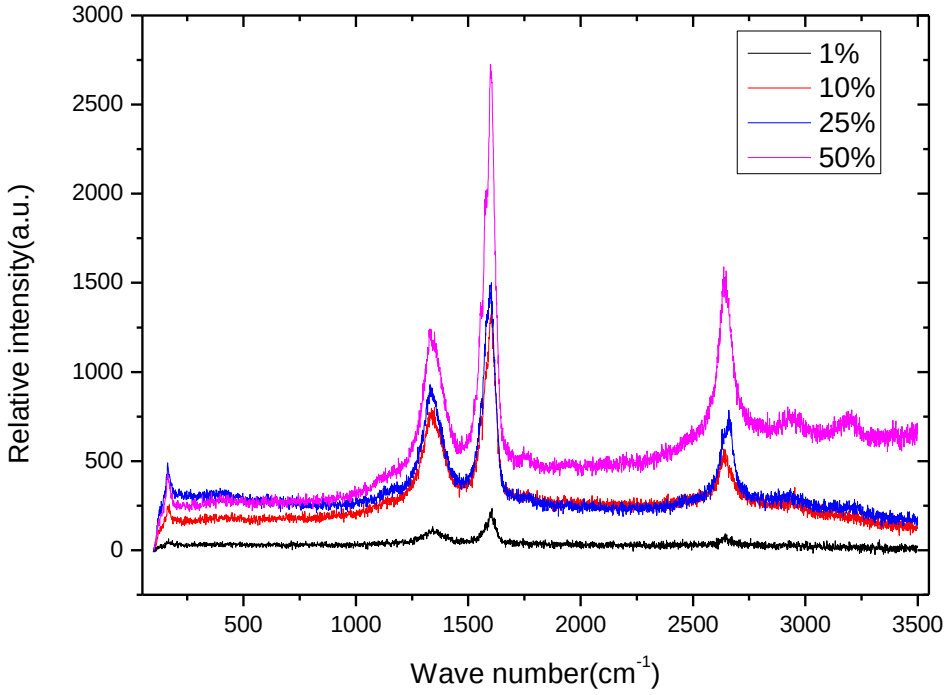

Figure 5.4 *Typical Raman spectra from COOH-SWNTs with different laser powers.*

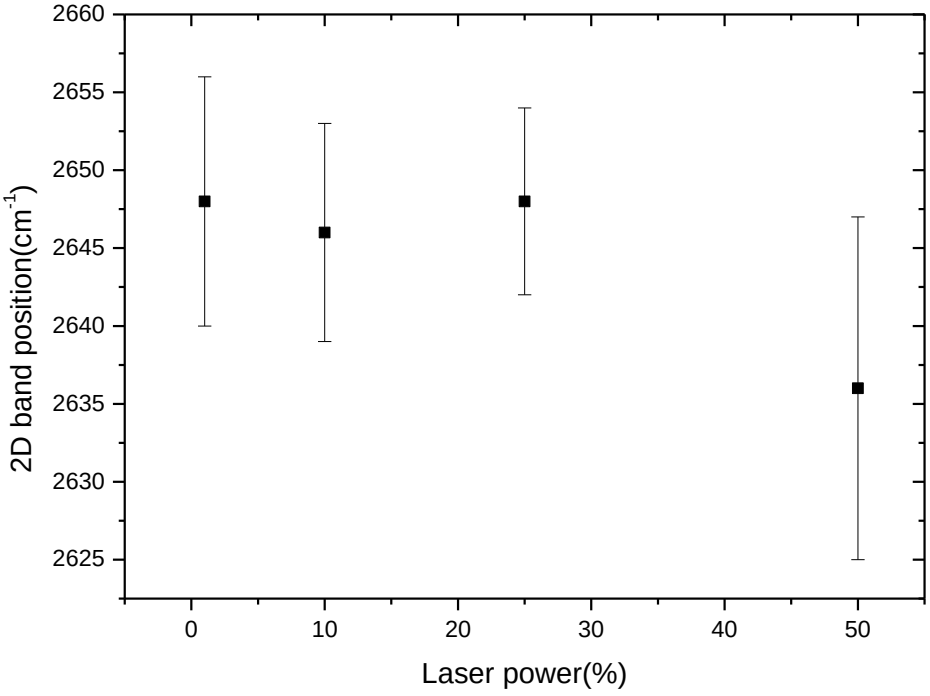

Figure 5.5 *The position of the 2D Raman band for different laser powers (10 times tested at each laser power).*

5.5 SWNTs Coating Methods

5.5.1 SWNTs in Epoxy Layer without Silane

The samples were prepared by firstly dispersing 0.05% by weight of SWNTs in an epoxy hardener, and sonicating for 4 hours. Then the hardener/SWNTs were mixed with epoxy resin in a volume ratio of 38/100. This mixture was then stirred magnetically for 30 minutes. Air bubbles were then removed from this mixture through vacuum pumping. Afterwards fibre card samples (the same as the specimens used to carry out tensile testing, as described in Chapter 3) were soaked in the epoxy resin and hardener with the SWNTs mixture for 5 minutes and then removed and placed against the wall of an angled Petri dish in order for the residual epoxy resin to flow off the single carbon fibre filament leaving a very thin layer on the fibre surface. Finally the samples inside the Petri dishes were either cold cured at room temperature for 7 days or hot cured at 120 ℃ for 2 hours. A schematic diagram of a prepared sample is shown in Figure 5.6.

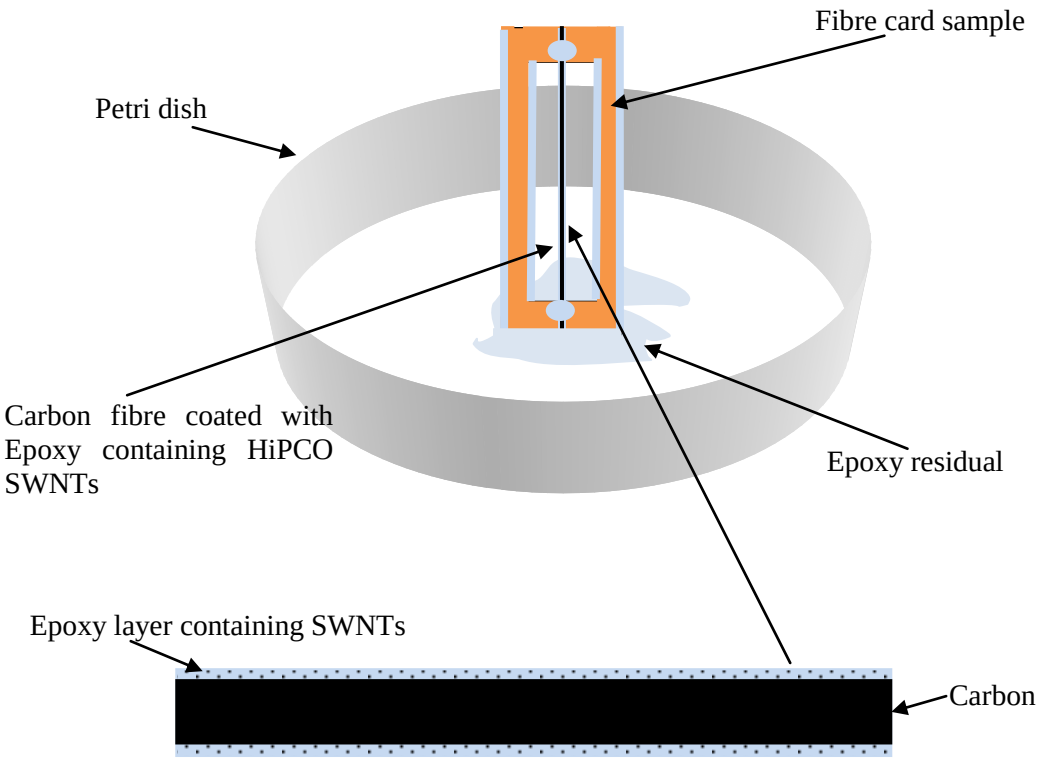

Figure 5.6 *Schematic of a prepared composite sample with a layer of SWNTs in an epoxy layer coated around a carbon fibre (without silane).*

5.5.2 SWNTs in Epoxy Layer with Silane

To prepare these samples, a 1.5% by volume silane solution was prepared, stirred and hydrolyzed for 15 minutes. Then the fibre card samples were immersed in the silane solution for about 20 minutes to ensure a thorough coating around the fibre surface. These fibre card samples were then heated at 120 ℃ for 2 hours in an oven in order for the silane to be cured and dried on the fibre surface. At the same time 0.05% by weight of SWNTs were dispersed and sonicated in epoxy hardener for 4 hours. Epoxy resin was then added in with the ratio of 38:100 by volume. This mixture was then stirred magnetically for 30 minutes. Air bubbles were removed from this mixture by using vacuum pumping. After that the fibre card samples with a silane layer on the fibre surface were soaked in the epoxy and hardener with the SWNTs mixture for 5 minutes and then removed and leant against the wall of a Petri dish. Finally the samples were either cold cured at room temperature for 7 days or hot cured at 120 ℃ for 2 hours in an oven. A schematic of the layer composition on the fibre surface is shown in Figure 5.7.

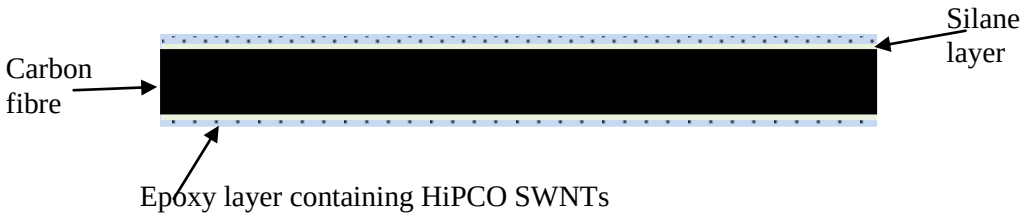

Figure 5.7 *Schematic of the layer composition of SWNTs in an epoxy resin layer on a carbon fibre.*

5.5.3 SWNTs in a Silane Layer

First of all a 0.1% by weight dispersion of SWNTs in ethanol was sonicated for 2 hours. A 1.5% by volume silane solution was also prepared, stirred and hydrolysed. These two solutions were mixed in the ratio of 1:1 and stirred magnetically for 30 minutes. After that the fibre card samples were soaked in this mixture for 20mins, and then removed and heated at a temperature of 120 ℃ for 2 hours. These samples then just had one single silane layer containing SWNTs, without the presence of an epoxy layer. However for the coating method that sample have epoxy layer, these samples were later placed in

the epoxy/hardener mixture for 5 min and hot cured afterwards. A schematic of the samples, with and without epoxy layer are shown in Figure 5.8.

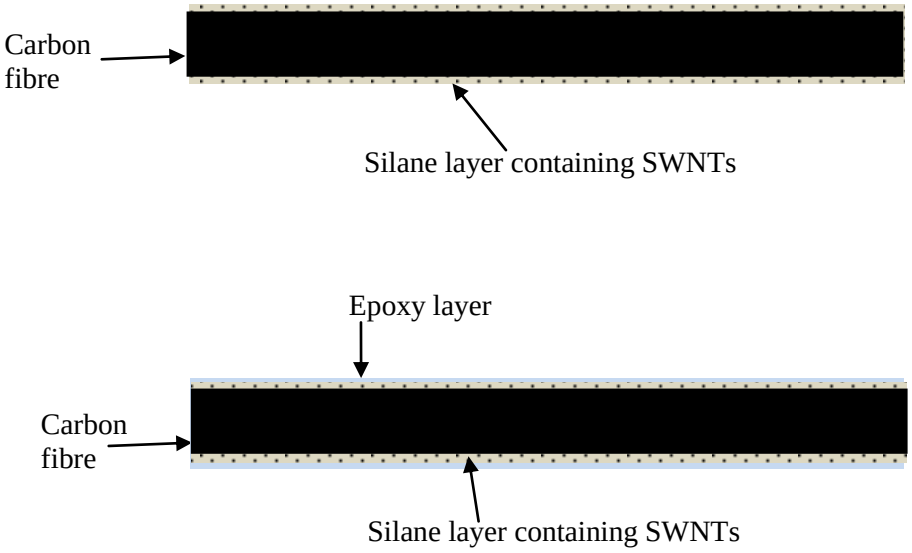

Figure 5.8 *Schematic of prepared sample with SWNTs in silane layer with epoxy layer (top) and without epoxy layer (below).*

5.6 SEM Characterization for the Samples Coated SWNTs

As shown in Figure 5.9, the sample with a coating method of just one silane layer containing SWNTs on the fibre surface clearly shows a thorough coating of tubes on the fibre surface. Figure 5.10 however shows, that if an epoxy resin layer was placed on the fibre surface, the SWNTs are not observed, and the surface of the fibre is very smooth; this is thought to be due to all SWNTs being embedded in the epoxy resin. Fibre diameters after epoxy layer coating have been measured as well but the average diameter has no significant change compared with the ones without coating.

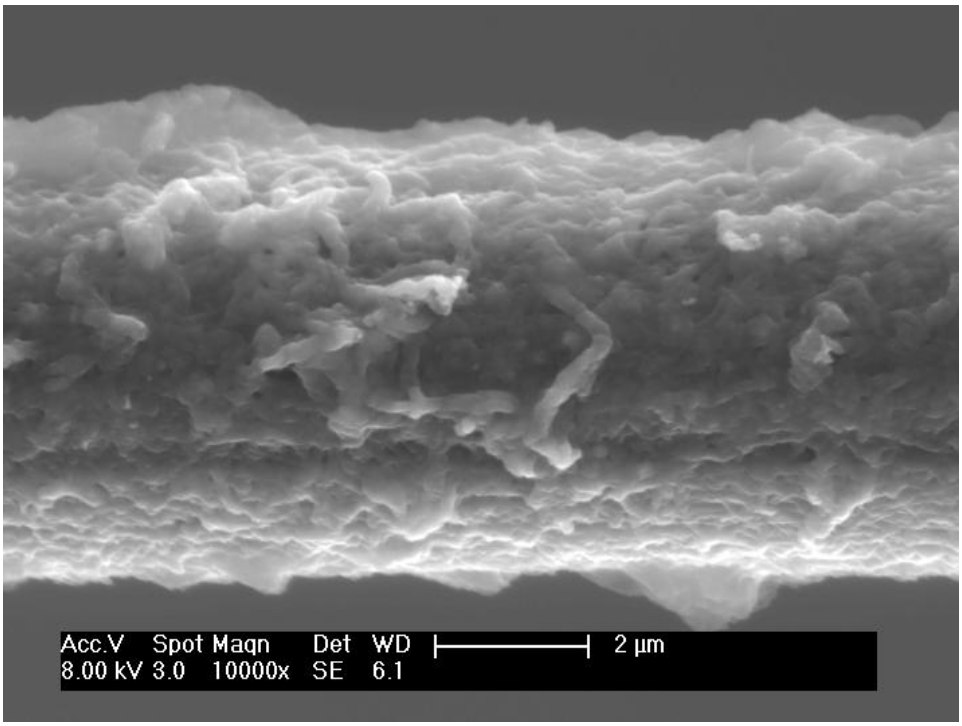

Figure 5.9 *SEM image of carbon fibre coated with HiPCO SWNTs.*

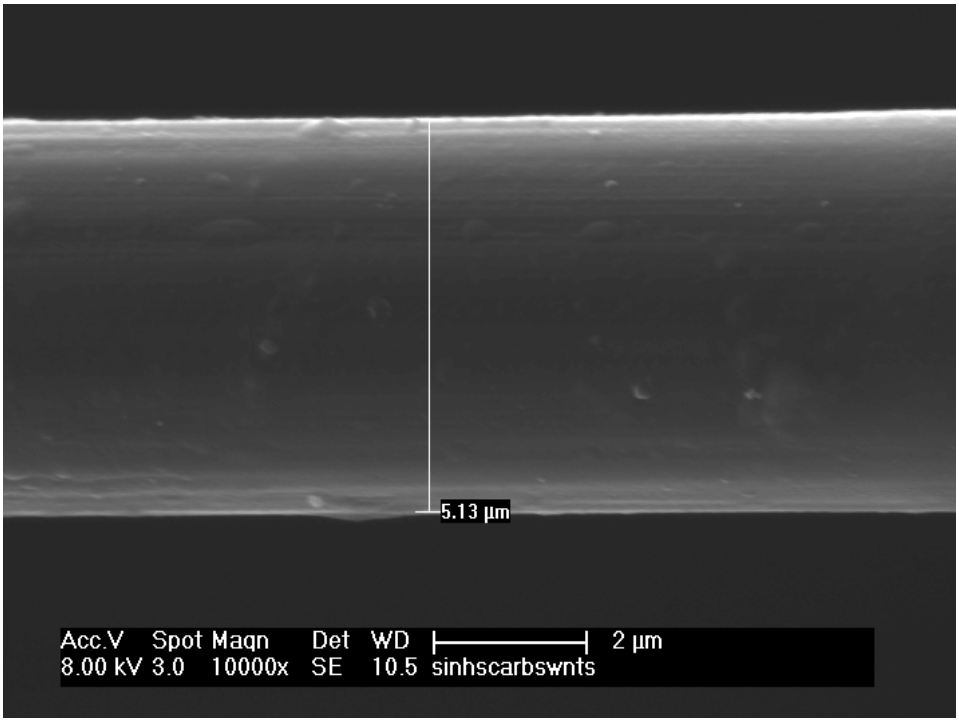

Figure 5.10 *SEM image of carbon fibre coated with HiPCO in epoxy layer.*

5.7 Effects of Laser Polarisation and Fibre Strain Axis Angle on Raman Band Shift Rates

5.7.1 Effect of Laser Polarization on 2D Band Shift Rates

According to previous research the stress induced Raman band shift rates for SWNTs coated fibres are highly dependent on the laser polarisation and the angle between the SWNTs axis and the fibre strain axis (Sureeyatanapas and Young, 2009; Deng and Young, 2010).

In this study HiPCO SWNTs were chosen. The low modulus carbon fibre card samples coated with SWNTs in a silane layer, without an epoxy layer, were used. The Raman polarisation configurations of VV, VH and VN were applied, and spectra containing the Raman 2D band from the SWNTs were obtained from 5 different areas along the fibre at each strain level. The Raman shift rates were determined and compared, as shown in Figure 5.11. It can be seen that the value of shift rate obtained using a VV configuration is higher than that obtained from VN configuration; the VH configuration gave the lowest shift rate of 1.2 cm^{-1}/ % strain.

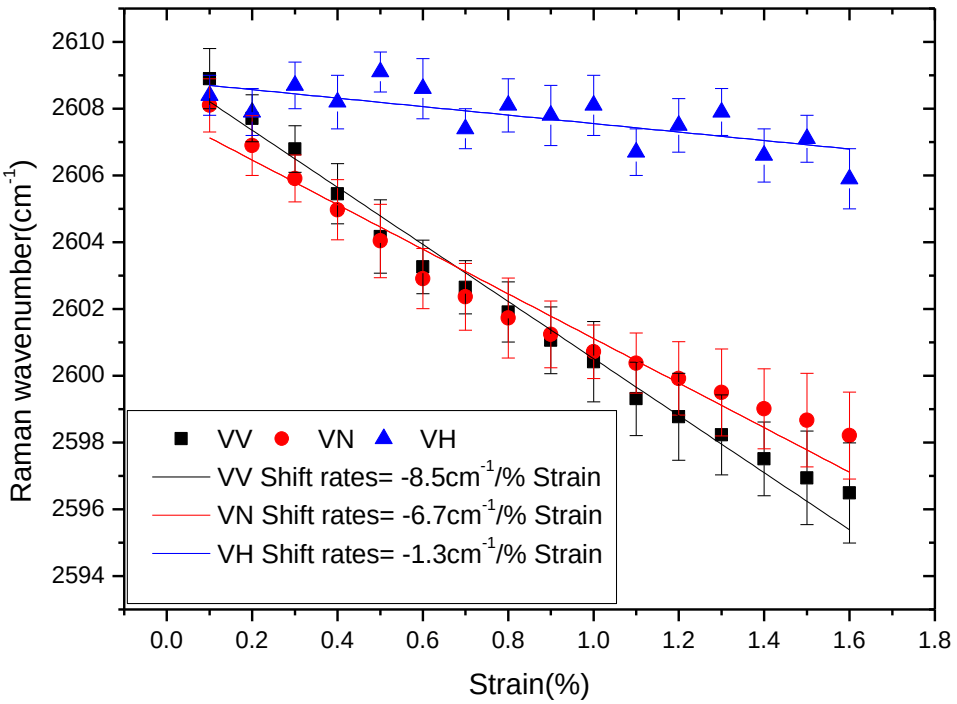

Figure 5.11 *Raman 2D band shift rates with respect to strain for HiPCO SWNTs in silane layer, without epoxy resin, for different types of laser polarized configuration.*

5.7.2 Model analysis of Angle Effects on Raman 2D Band Shift Rates

A detailed study was carried out to determine and explain the effects of the different angles between the direction of laser polarisation and the fibre axis (φ) and the SWNTs axis (α) on the stress-induced band shift rates for SWNTs coated on carbon fibres. The angle θ is defined as the angle between fibre axis and the SWNTs axis as shown in the schematic diagram of Figure 5.12.

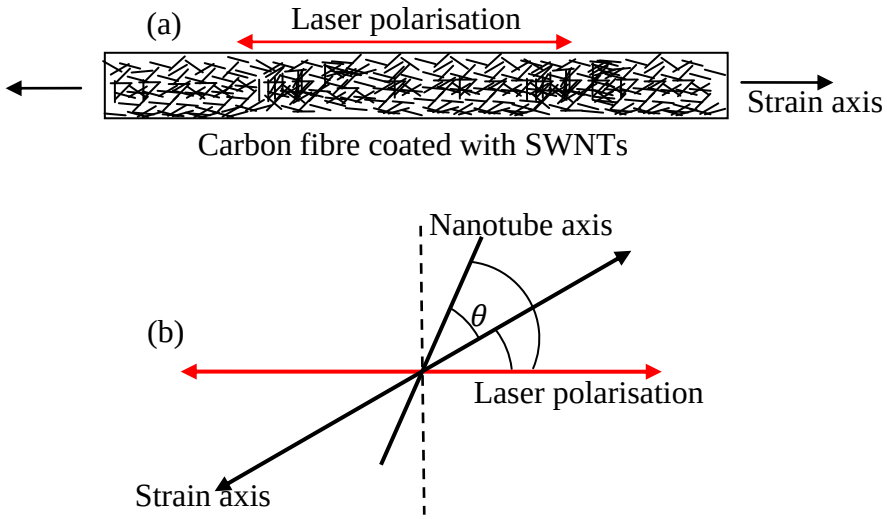

Figure 5.12 *Schematic of a sample with the strain axis parallel to the polarized laser (a) and different angles between nanotube axis, strain axis and direction of laser polarization (b).*

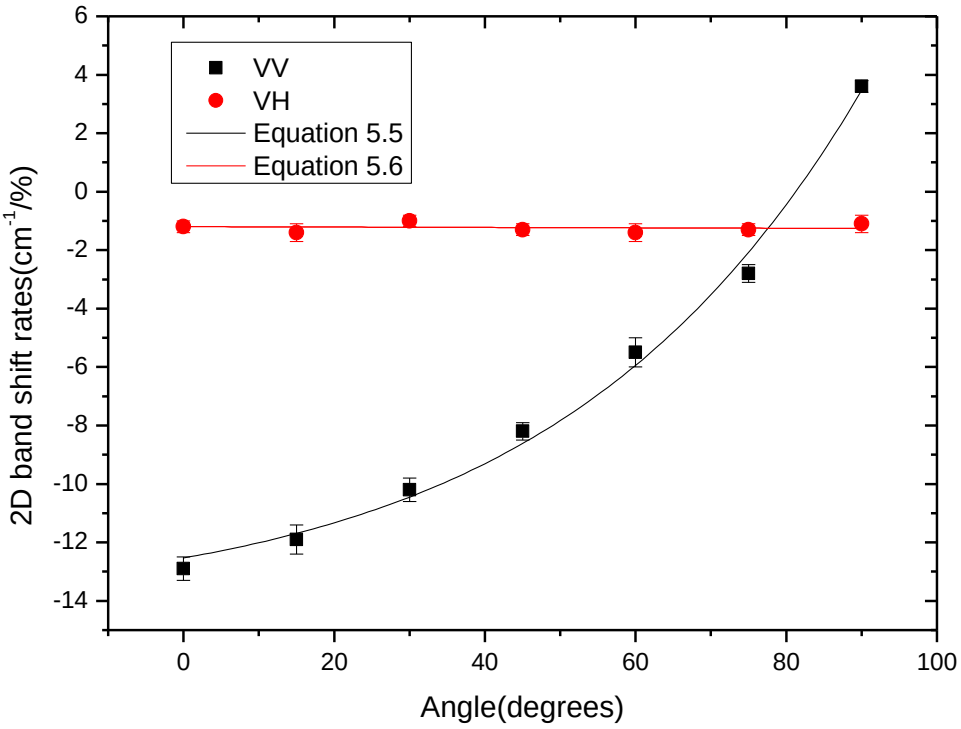

Figure 5.13 *Raman 2D band shift rate with respect to strain and its dependence on the angles between the fibre strain axis and the direction of the polarised laser for the low modulus carbon fibre samples coated with SWNTs in a silane layer with an epoxy coating layer.*

The differences in Raman band shift rates for different polarized laser configurations can be explained by the following. As the SWNTs coated on the carbon fibre surface are dispersed randomly in all directions, the Raman band intensity is a contribution of SWNTs lying at all directions corresponding to the direction of laser polarization. If we suppose the proportion of SWNTs lying within an infinitesimal angle range ($\mathrm{d}\alpha$) regarding the polarisation direction ($\frac{1}{\pi}\mathrm{d}\alpha$),the Raman band intensities of different polarized configurations can be calculate using the functions (Huang *et al*.,2000; Gommans *et al*,2000):

$$I_{VV}(\alpha) = \frac{1}{\pi}\int_0^{\pi} I_0 \cos^4\alpha \, d\alpha \qquad (5.1)$$

$$I_{VH}(\alpha) = \frac{1}{\pi}\int_0^{\pi} I_0 \cos^2\alpha \, \sin^2\alpha \, d\alpha \qquad (5.2)$$

At any certain given angle φ, the intensity for VV and VH configurations can be obtained using the equations

$$I_{VV}(\varphi) = \frac{1}{\pi}\int_0^{\pi} I_0 \cos^4(\theta + \varphi)\, d\theta \qquad (5.3)$$

$$I_{VH}(\varphi) = \frac{1}{\pi}\int_0^{\pi} I_0 \cos^2(\theta + \varphi)\ \sin^2(\theta + \varphi)\, d\theta \qquad (5.4)$$

where I_0 is the parameter that give maximum intensity for each configuration.

Since the Raman band is due to the involvement of all SWNTs, the stress induced band shift is also an involvement of band shifts for all SWNTs. The overall band shift can be calculated as an intensity-weighted average of band shift for SWNTs lying at all angles (Deng, 2010). As only a small fraction of SWNTs has been dispersed in the coating layer, so the distribution of SWNTs can be considered in two dimensions. As a result, for SWNTs distributed randomly in the coating layer, the overall shift rates for the two different polarization configurations, VV and VH, based on the given angle φ can be calculated using the equations

$$S_{VV}(\varphi) = \frac{\frac{1}{\pi}\int_0^{\pi} I_0 \cos^4(\theta+\varphi)\times[S_0(cos^2\,\theta - v\ sin^2\,\theta)]d\theta}{\frac{1}{\pi}\int_0^{\pi} I_0 \cos^4(\theta+\varphi)\, d\theta} \qquad (5.5)$$

$$S_{VH}(\varphi) = \frac{\frac{1}{\pi}\int_0^{\pi} I_0 [\cos^2(\theta+\varphi)\sin^2(\theta+\varphi)]\times[S_0(cos^2\,\theta - v\ sin^2\,\theta)]d\theta}{\frac{1}{\pi}\int_0^{\pi} I_0 [\cos^2(\theta+\varphi)\ \sin^2(\theta+\varphi)]d\theta} \qquad (5.6)$$

where the Poisson's ratio v was taken as 0.2 (Popov and Van Doren, 2000). Equations 5.5 and 5.6 were evaluated using Mathematical and least-squares fits of these equations to the experimental data give S_0= -12.8 cm^{-1}/% for the VV configuration and -1.3 cm^{-1}/% for the VH configuration respectively.

5.7.3 Conclusion

A higher band shift rate and stronger band intensities will give more accuracy and reliable calibration results when SWNTs are used to sense the strain from the carbon fibres embedded in a composite. The conclusion is drawn that the fibre samples should always be placed to parallel the direction of the polarisation of the incident laser, and a VV laser polarization configuration was used for further studies.

5.8 Effects of SWNTs Coating Method on Raman 2D Band Shift Rates

In this study low modulus carbon fibres coated with COOH SWNTs were chosen to represent both types of carbon fibres and SWNTs samples. The shifts in the 2D Raman band as a function of fibre strain were recorded from samples prepared using each coating method as described in Chapter 5.4. 2D Raman band shift rates with respect to strain were then calculated by fitting linear regressions to the shift data. A higher band shift rate indicates better bonding between the carbon fibre and SWNTs. Finally the best coating method was obtained and was used to prepare composites samples and subsequently to monitor composite interfaces.

5.8.1 SWNTs in Epoxy layer

5.8.1.1 Effect of the Existence of Silane Layer

In this section, all samples have SWNTs been homogenously dispersed into epoxy layer. There are two types of samples, with and without the presence of a silane layer, were prepared by following the coating methods described in Sections 5.4.1and 5.4.2 respectively. All samples were placed into an oven with the temperature of 120 ^{o}C for 2 hours to have epoxy layer to be hot cured. Five samples were tested for either type using Raman spectroscopy, and the positions of the 2D band were obtained at each strain level, the results of which are reported in Figure 5.14.

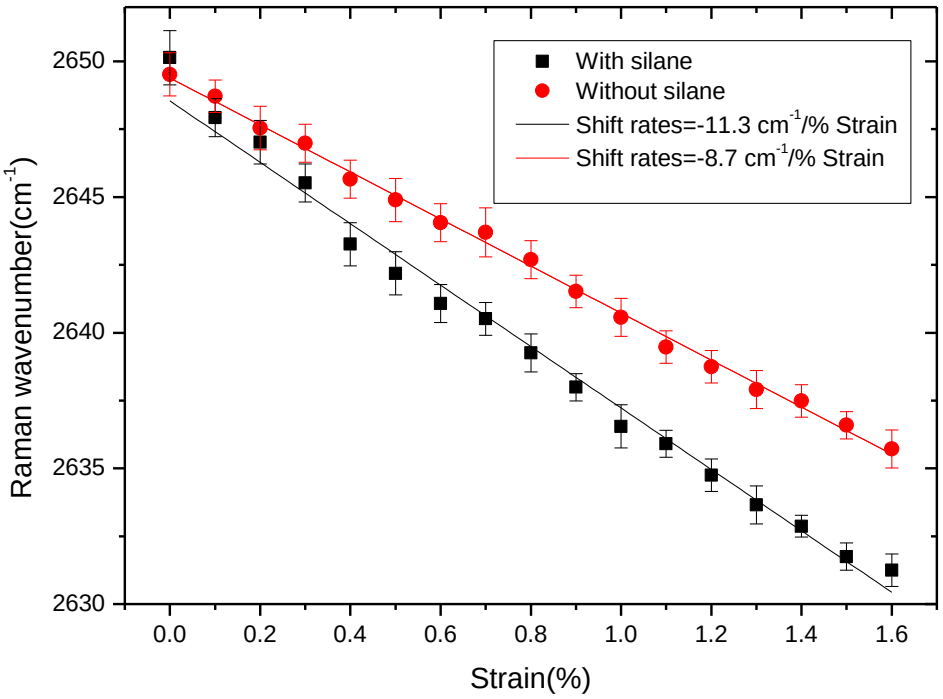

Figure 5.14 *Raman 2D band shift rates for a low modulus carbon fibre coated with COOH SWNTs in an epoxy layer with and without the presence of a silane layer.*

It can be seen from Figure 5.14 that samples with a silane layer between the carbon fibre and the epoxy layer have a higher shift rate. This means that the presence of silane appears to improve the bonding between the carbon fibre and the epoxy resin.

5.8.1.2 Effect of Epoxy Layer Preparation Method

As the epoxy resin has a high viscosity, it is very difficult to disperse SWNTs homogeneously in it. One method to overcome this is to disperse a certain ratio of the SWNTs in the hardener then to mix the hardener and epoxy together. This method has been described in Section 5.7.1.2. Another method which has been used by Sureeyatanapas *et al.* (2009) was to disperse SWNTs in ethanol first; it can be seen from Figure 4.12 that SWNTs have a really high solubility in ethanol. This was carried out, and then the ethanol solution and epoxy were mixed in a ratio of 1:1 and stirred magnetically for an hour before the hardener was added. This method reduces the viscosity of the epoxy resin and makes the dispersion of SWNTs in epoxy easier and homogeneous. The ethanol contained in the epoxy may however not be able to be fully evaporated when the samples are cold cured at room temperature. The existence of ethanol in the epoxy layer may weaken the bonding between the carbon fibre and epoxy.

The 2D Raman band shift rates with respect to strain for these two different methods were also determined and the results are shown in Figure 5.15. The epoxy layers for both types of samples were hot cured and the ethanol solvent in the epoxy layer is assumed to be removed during the hot curing process. The results show that the Raman 2D band shift rates for the samples where the SWNTs were dispersed in ethanol first is lower than for the other type of sample Although ethanol has been removed during the hot curing process, it is true that the existence of ethanol during the sample fabrication has possibly weakened bonding between the epoxy resin and the carbon fibre.

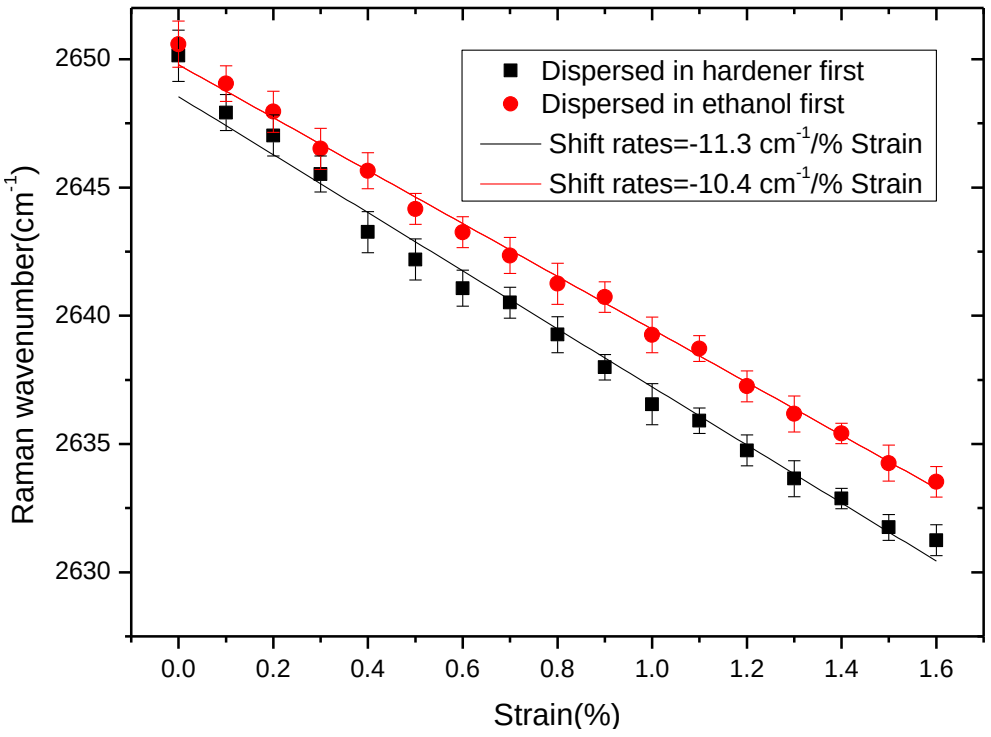

Figure 5.15 *Raman 2D band shift rates with respect to strain for low modulus carbon fibre samples coated with COOH SWNTs dispersed in an epoxy resin layer using two different methods. Both samples produced with silane.*

5.8.2 SWNTs in a Silane Layer

5.8.2.1 Effect of the Existence of an Epoxy Layer

In this study COOH SWNTs and low modulus carbon fibres were chosen to represent both types of carbon nanotubes and fibres. Samples were prepared with COOH SWNTs in a silane layer with and without the presence of an epoxy layer were prepared by following the steps described in Section 5.4.3. Samples with an epoxy layers were hot

cured. Finally Raman 2D band shift rates were determined and compared for these two types of samples as the results are shown in Figure 5.16.

Figure 5.16 show that the samples with an epoxy layer have a higher 2D Raman band shift rate with respect to strain. The existence of epoxy layer could help prevent the slippage of SWNTs when the carbon fibre is being deformed.

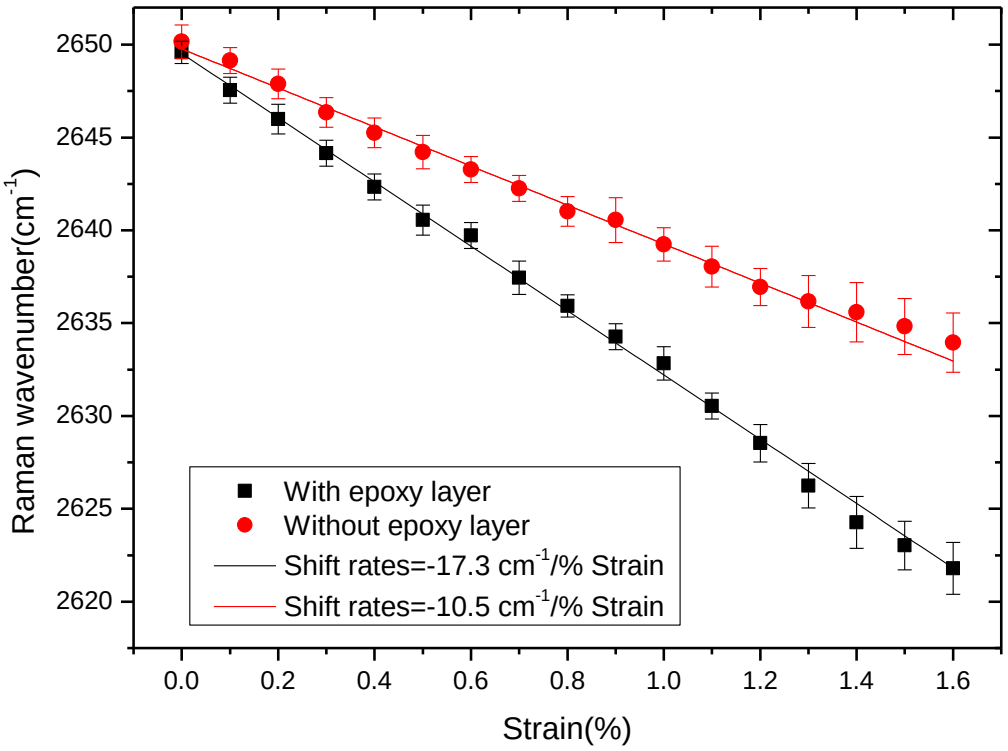

Figure 5.16 *Raman 2D band shift rates for low modulus carbon fibres coated with COOH SWNTs in a silane layer, with and without the presence of an epoxy layer.*

5.8.2.2 Effect of Epoxy Curing Process

In this section the effect of different epoxy curing processes on the 2D Raman band shift rates with respect to strain have been determined. The epoxy layer coated onto the fibre after silane sizing, were either hot cured at a temperature of 120 ℃ for 2 hours or cold cured at room temperature for 7 days. The 2D band shift rates for these two types of sample have been investigated and the results are shown in Figure 5.17

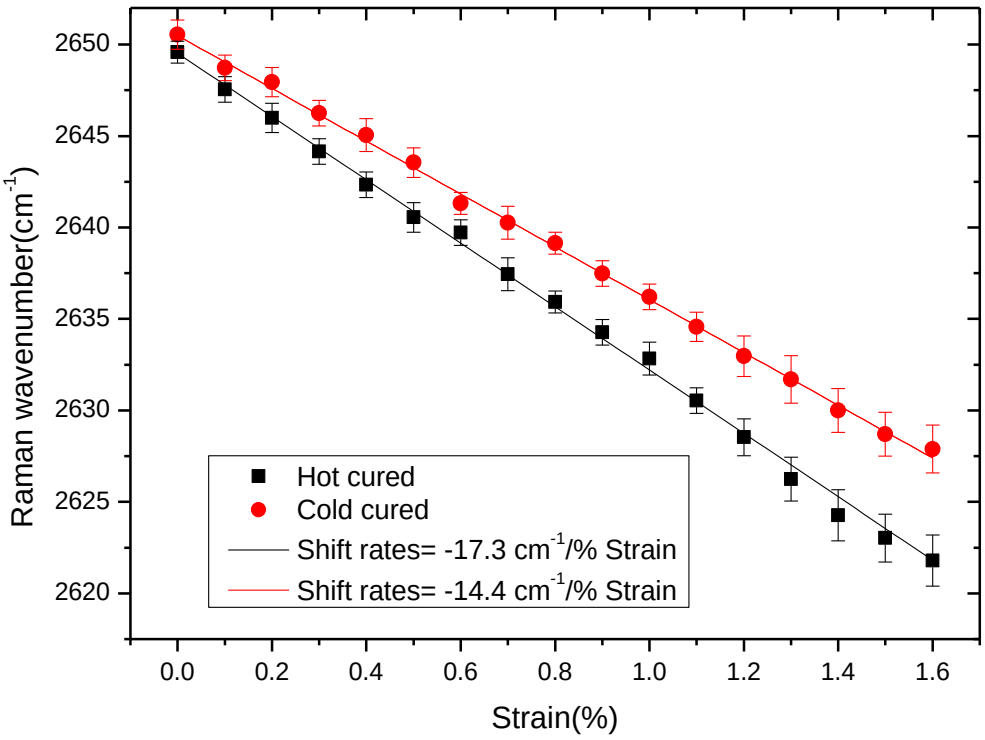

Figure 5.17 *2D Raman band shift rates for a low modulus carbon fibre coated with COOH SWNTs in a silane layer, with a subsequent epoxy layer which was either hot cured or cold cured.*

The results show that the samples that were hot cured have a higher 2D Raman band shift rate with respect to strain. This difference could be explained by the existence of a radial pressure at the interface resulting from thermal expansion coefficient mismatch between the fibre and the epoxy resin during the curing process. The hot cured samples have higher thermal residual pressure on the fibre and therefore result in the contraction of SWNTs in the silane layer. So when the same strain applied on carbon fibres the SWNTs from hot cured samples have higher deformation which causes a higher 2D band shift rates. A hot curing will normally cause shrinkage of epoxy resin and a better consolidation of the interface between fibre and epoxy can be achieved.

5.9 Effect of the Concentration of SWNTs

Differences in the SWNTs concentration within the silane layer may also affect interfacial bonding and thus result in a variation of the 2D Raman band shift rates with respect to strain.

Samples were prepared with SWNTs in silane layer, followed by an epoxy coating which was then hot cured. The ratio of SWNTs dispersed in ethanol was varied. The 2D Raman band shift rates for two types of SWNTs, as a function of the concentration of SWNTs dispersed in ethanol are shown in Figure 5.18.

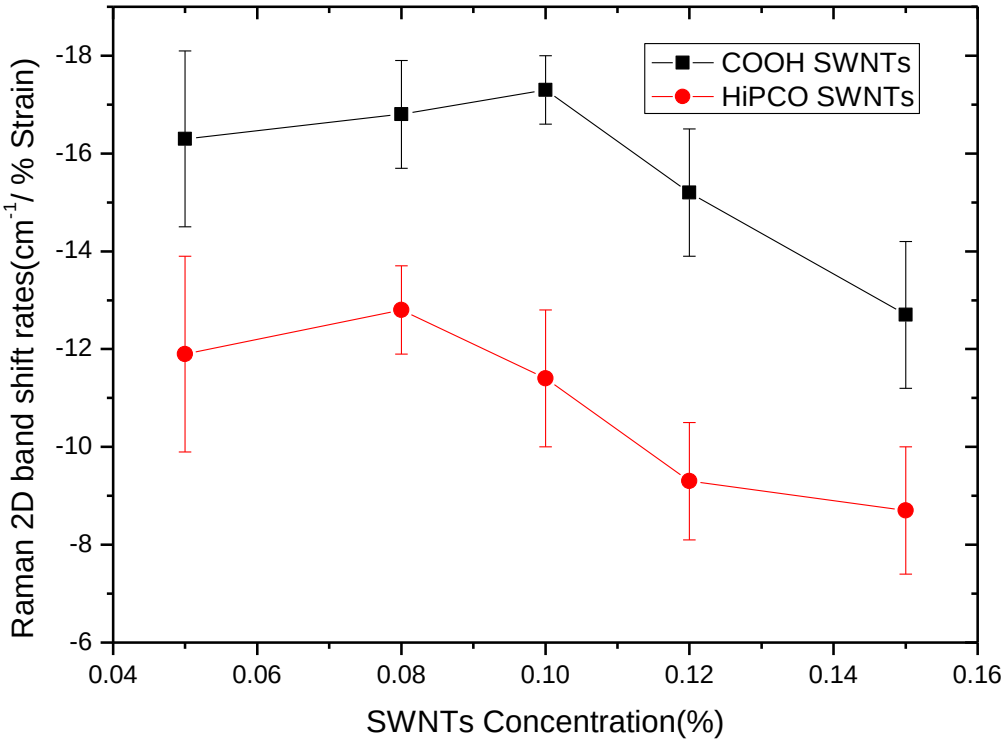

Figure 5.18 *Raman 2D band shift rates dependent on the concentration of COOH and HiPCO SWNTs.*

It has been found that the highest 2D band shift rates with respect to strain are found for samples coated with HiPCO or COOH SWNTs are at concentrations of 0.08% and 0.1% respectively. The variation of 2D Raman band shift rates could be explained as that SWNTs have not dispersed homogenously on the fibre surface leaving some areas uncoated (see the SEM image in Figure 5.19) when the concentration of SWNTs is low.

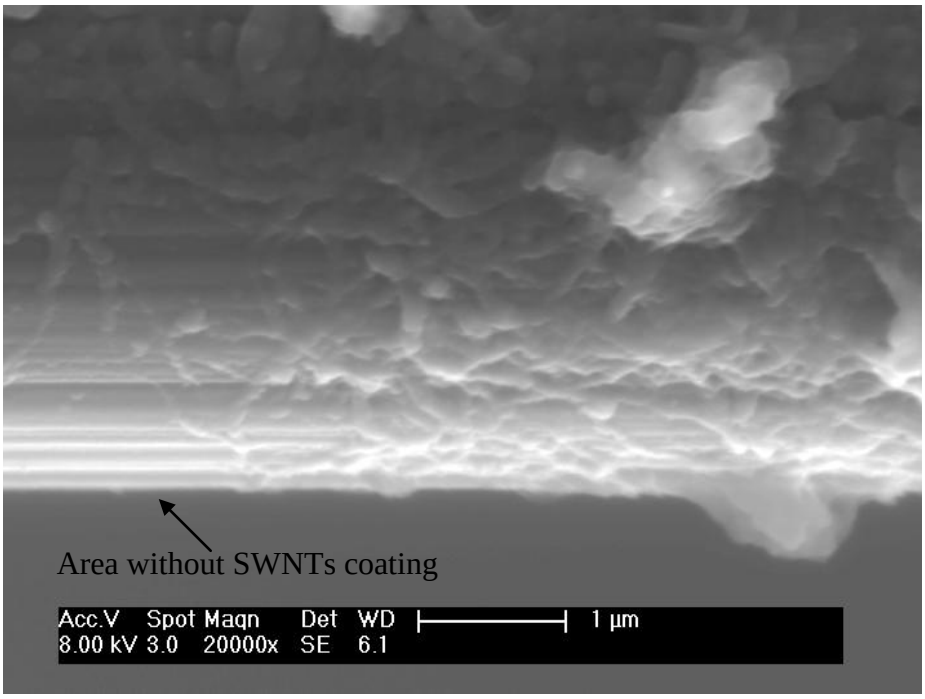

Figure 5.19 *SEM image of an uncoated area on a HiPCO SWNTs coated low modulus carbon fibre.*

5.10 Effect of Different Types of SWNTs

Both HiPCO SWNTs and COOH SWNTs have been used as a strain sensor to determine stress transfer across the interface of carbon fibre and epoxy resin by using Raman spectroscopy. To analyse the effect of the different types of SWNTs on interfacial bonding, the 2D Raman band shift rates with respect to strain of the low modulus carbon fibre samples coated with these two different SWNTs in a silane layer, followed by an epoxy coating have been investigated. The best average band shift rates for HiPCO SWNTs and COOH SWNTs samples were found to be -12.8±0.9 and -17.3±0.7 cm^{-1}/ %. The reasons for the different band shift rates for different types of SWNT-coated samples can be explained as follows:

a. Compared with HiPCO SWNTs the COOH SWNTs have covalent attachment of COOH functional groups on the wall of the tubes. There are many chemical reactions could occur between the COOH group, epoxy resin and amino silane as shown by the reaction equations 5.7-5.9. These reactions will result in a greater adhesive bonding between COOH SWNTs, carbon fibre, epoxy, silane

coupling agent and Bisphenol A on the fibre surface leading to higher 2D band shift rates.

b. As the carboxylic functional groups have polarity, this causes the COOH SWNTs to more easily disperse in ethanol or epoxy hardener, as is shown in Figure.4.12. This higher level of dispersion could help the homogeneous dispersion of SWNTs on the fibre surface, leading to a higher 2D Raman band shift rate with respect to strain.

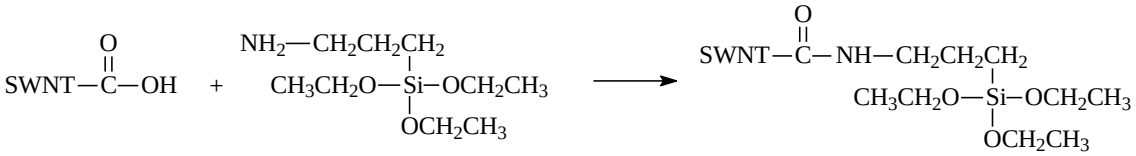

(5.7)

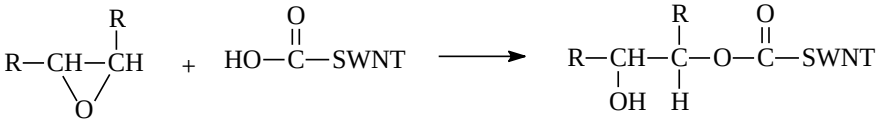

(5.8)

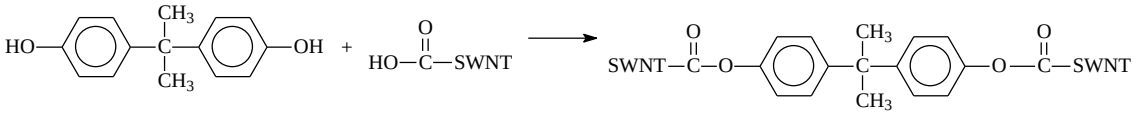

(5.9)

5.11 High Modulus Carbon Fibre with SWNTs Coating

5.11.1 Raman Spectra Study

The 2D Raman band can be obtained from both the high modulus carbon fibre and SWNTs separately. Therefore, for the high modulus carbon fibre samples coated with SWNTs, there are potentially two expected 2D Raman bands. According to the previously obtained Raman spectra the 2D band positions for an unstressed high modulus carbon fibre, HiPCO SWNTs and COOH SWNTs are located at about 2660 cm^{-1}, 2609 cm^{-1} and 2645 cm^{-1} respectively. So for this sample the two 2D bands, from fibre and SWNTs may interfere with each other as their band positions are very close. Raman spectra for these samples have been recorded and are shown in Figure 5.20 and Figure 5.21. The obtained Raman spectra reveal that only one 2D Raman band can be observed from the carbon fibre coated with SWNTs. It is thought that because the

Raman intensity from carbon nanotubes is considerably stronger than the underlying carbon fibre, it has 'over shadowed' the spectra from high modulus carbon fibre.

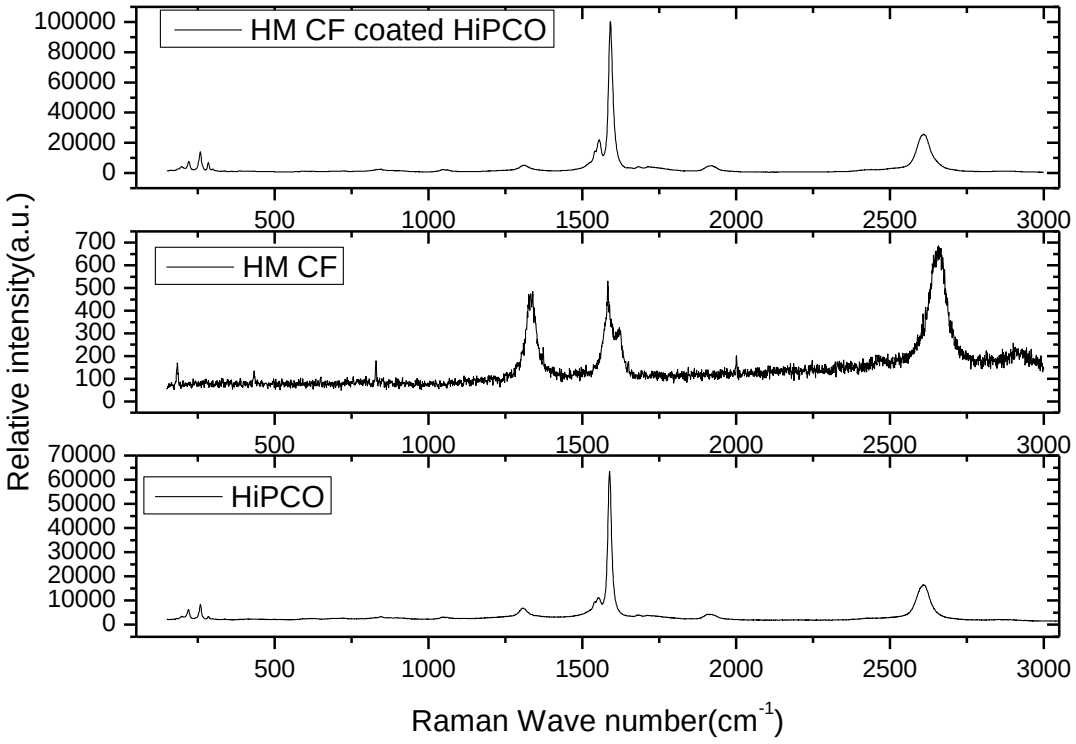

Figure 5.20 *Typical Raman spectra from a high modulus carbon fibre, HiPCO SWNTs and a high modulus carbon fibre coated with HiPCO SWNTs.*

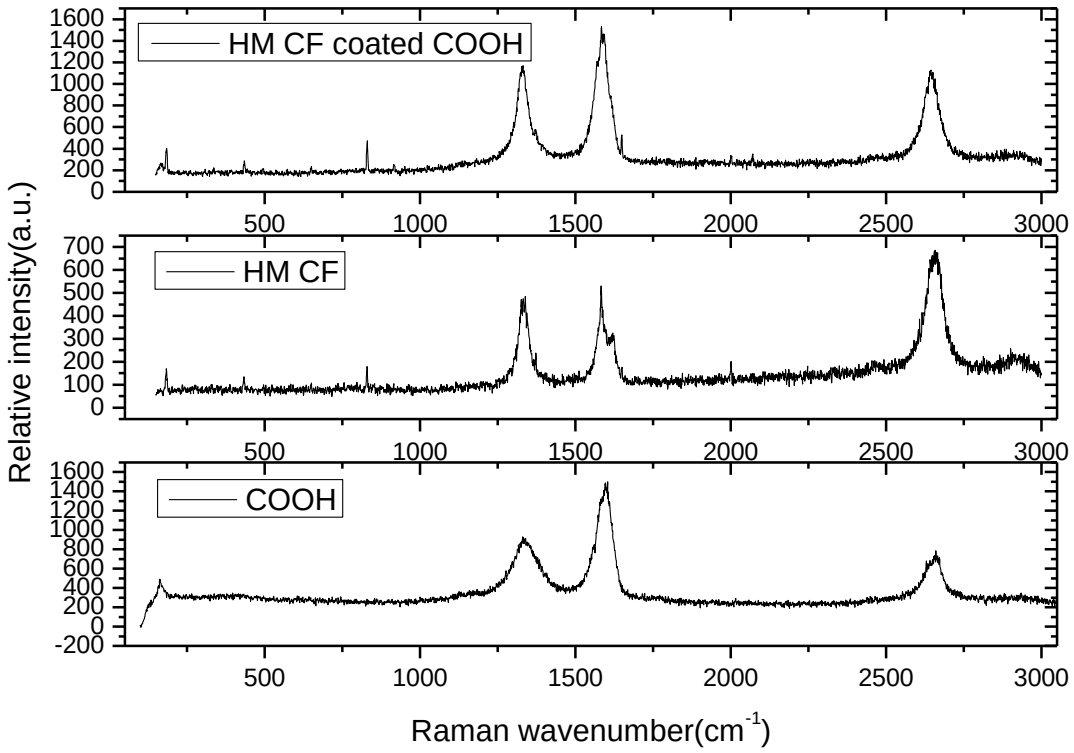

Figure 5.21 *Typical Raman spectra from a high modulus carbon fibre, COOH SWNTs and a high modulus carbon fibre coated with COOH SWNTs.*

5.11.2 Comparing the 2D Raman Band Shift Rates with Respect to Strain from a High Modulus Carbon Fibre Coated with/without SWNTs

Since the shift rate with respect for the 2D Raman band depends on the level of deformation, it is meaningful to compare this parameter from the fibre itself and the SWNTS coated on the surface. Samples were prepared by coating half of the high modulus carbon fibre with SWNTs, using the best coating method determined in the previous study. A schematic of this sample is shown in Figure 5.22.

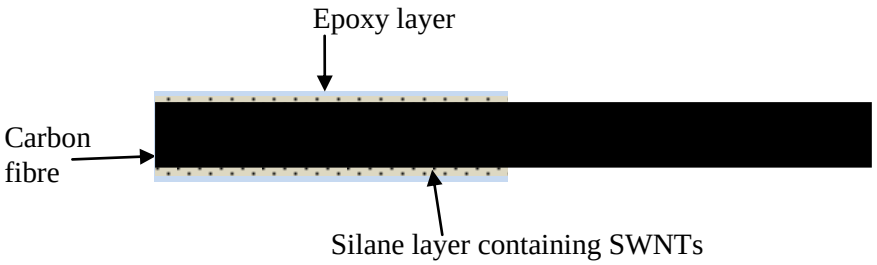

Figure 5.22 *Schematic diagram of a high modulus carbon fibre half coated with SWNTs in a silane layer and surrounded by an epoxy layer.*

This fibre was then deformed until fracture occurred with a strain increment of 0.1%. The 2D Raman band was recorded from five different areas, and either from the uncoated region of the fibre or the SWNTs coated region. A relationship between the 2D Raman band position and the fibre strain is shown in Figure 5.23. It can be seen that the highest shift rate with respect to strain is found from the uncoated region of the fibre. The shift rate with respect to strain obtained from COOH SWNTs is higher than that from HiPCO SWNTs.

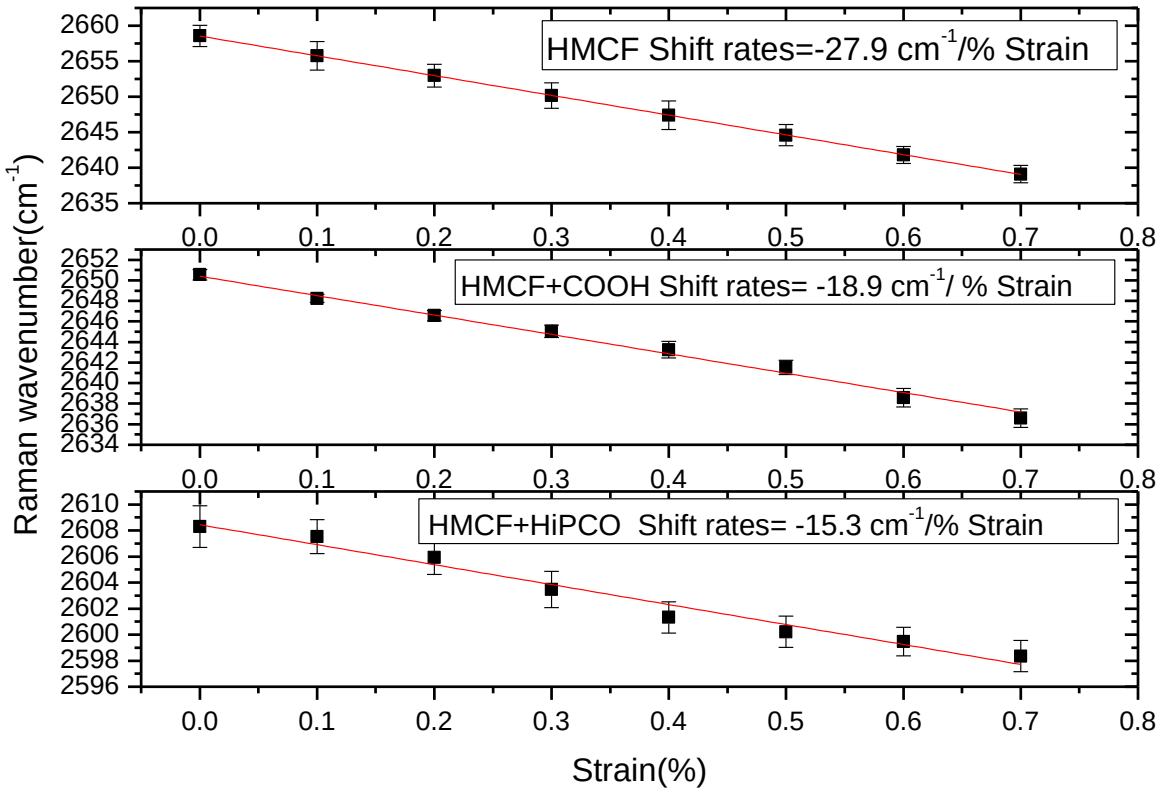

Figure 5.23 *Comparison of Raman 2D band shift rates for high modulus carbon fibre, high modulus carbon fibre coated with COOH SWNTs and high modulus carbon fibre coated with HiPCO SWNTs.*

5.12 Conclusion

Overall in this chapter, the 2D band shift rates for a range of samples were determined and are shown in Table 5.1.

Table 5.1 *Raman 2D band shift rates for all types of samples based on the specific laser polarised configuration.*

Sample type	SWNTs coating method		Laser Polarisation	2D band shift rates(cm^{-1}/ % Strain)	SD
Low modulus carbon fibre	HiPCO SWNTS in silane layer without epoxy		VV	-8.5	±0.8
			VN	-6.7	±1.0
			VH	-1.3	±0.4
	COOH SWNTs in epoxy layer without silane		VV	-8.7	±1.2
	COOH SWNTs in epoxy layer with silane	SWNTs dispersed in hardener first	VV	-11.3	±1.4
		SWNTs dispersed in ethanol first	VV	-10.4	±1.7
	COOH SWNTs in silane layer with epoxy	Epoxy hot cured	VV	-17.3	±0.7
		Epoxy cold cured	VV	-14.4	±0.8
	COOH SWNTs in silane layer without epoxy		VV	-10.5	±1.0
	HiPCO SWNTs in silane layer		VV	-12.8	±0.9

	with epoxy hot cured			
High modulus carbon fibre	No coating	VN	-27.0	±0.6
		VV	-28.2	±0.4
	HiPCO SWNTs in silane layer with epoxy hot cured	VV	-15.3	±0.9
	COOH SWNTs in silane layer with epoxy hot cured	VV	-18.9	±0.7

Because the low modulus carbon fibre does not have any Raman bands which are able to sense the strain applied on the fibre, the method of using SWNTs as strain sensor was developed. Different coating processes have been investigated in order to find the best one to sense the interface between a low modulus carbon fibre and an epoxy resin. A method whereby SWNTs were dispersed in a silane layer followed by epoxy coating and hot curing was found to be the best approach for strain mapping; giving the highest 2D Raman band shift rates with respect to strain. This sample preparation method was found to be the most effective for both types of SWNTs. It was however found the concentration of SWNTs in the silane layer also affected the Raman band shift rates When dispersed in ethanol the HiPCO SWNTs and the COOH SWNTs with concentrations of about 0.08% and 1.00%achieved the highest 2D band shift rates respectively. It was also shown that a higher band shift rate was obtained when using a polarised laser in a VV configuration.

5.13 References

Amer, M.S. and Schadler, L.S. (1996) Stress concentration phenomenon in graphite/epoxy composites: tension/compression effects. *Composites Science and Technology*, 57, pp. 1129-1137.

Bowden, M., Gardiner, D.J, Southall, J.M. and Gerrard, D.J. (1993) Determination of band shifts as a function of strain in carbon fibres using Raman microcline focus spectrometry. *Carbon*, 31(7), pp. 1057-1060.

Deng, L., Eichhorn, S.J., Kao, C.C. and Young, R.J. (2011) The effective of Young's Modulus of Carbon nanotubes in composites. *ACS Applied Materials and Interfaces*, 3, pp.433-440.

Deng, L. (2010) Raman spectroscopic studies of carbon nanotube composite fibres. Unpublished thesis (PhD), University of Manchester.

Gommans, H.H., Alldredge, J.W., Tashiro, H., Park, J., Magnuson, J. and Rinzler, A.G. (2000) Fibres of aligned single-walled carbon nanotubes: Polarized Raman spectroscopy. *Journal of Applied Physics*, 88(5), pp. 2509-2514.

Hwang, J., Gommans, H.H., Ugawa, A., Tashiro, H., Haggenmueller, R., Winey, K.I., Fischer, J.E., Tanner, D.B. and Rinzler, A.G. (2000) Polarized spectroscopy of aligned single-wall carbon nanotubes. *Physical Review B*, 62(20), pp. R13310-R13313.

Huang, Y. and Young, R.J. (1994) Effect of fibre microstructure upon the modulus of PAN and Pitch based carbon fibre. *Carbon*, 33(2/1995), pp. 97-107.

Jorio, A. , Souza Filho, A.G., Brar, V.W., Swan, A.K., Unlu, M.S., Goldberg, B.B., Righi, A., Hafner., J.H., Lieber, C.M., Saito, R., Dresselhaus, G. and Dresselhaus, M.S. (2002) Polarized resonant Raman study of isolated single-wall carbon nanotubes: Symmetry selection rules, dipolar and multipolar antenna effects. *Physical Review B*, 65, pp. R1214021-R1214024.

Kao, C.C. and Young, R.J. (2004) A Raman spectroscopic investigation of heating effects and the deformation behaviour of epoxy/SWNT composites. *Composites Science and Technology*, 64, pp. 2291-2295.

Popov, V.N. and Van Doren, V.E. (2000) Elastic properties of single-walled carbon nanotubes. *Physical Review B*, 61(4), pp. 3078-3084.

Robinson, I.M., Zakikhani, M., Day, R.J., Young, R.J. and Galiotis, C. (1987) Strain dependence of the Raman frequencies for different types of carbon fibres. *Journal of Materials Science Letters*, 6, pp. 1212-1214.

Sureeyatanapas, P. and Young, R.J. (2009) SWNT composite coating as strain sensor on glass fibre in model epoxy composites. *Composites Science and Technology*, 69, pp. 1547-1552.

Sureeyatanapas, P. (2009) Carbon nanotubes as strain sensors for glass fibres/epoxy model composites. Unpublished thesis (PhD), University of Manchester.

CHAPTER 6 Epoxy Resin Microdroplet Model

6.1 Introduction

According to the literature, many model composite geometries have been used to analyse the interfacial micromechanical properties of carbon fibre and epoxy resin systems using Raman spectroscopy; these include fragmentation, microbond, pull out and push in tests (Young, 1997). In recent years, an alternative geometry of a microdroplet on a single fibre, which is very similar to the geometry of microbond test but without a restraint, has been investigated, again using Raman spectroscopy (Eichhorn and Young, 2003; Mottershead and Eichhorn, 2007; Bennett *et al*, 2006; Cen *et al*, 2006). No report for using this approach for a carbon fibre and epoxy resin system has so far been found. In this chapter this approach is reported, and the interfacial micromechanical properties between a carbon fibre and an epoxy microdroplet investigated. High modulus carbon fibres were chosen for this study as they exhibit a strong 2D band. It is shown that the geometrical shape of the microdroplet has a significant effect on the interfacial shear stress (ISS), in agreement with previous findings of epoxy microdroplet composites with other fibres systems. Therefore this geometry has not been used any further to determine the interfacial behaviour between a low modulus carbon fibre and epoxy resin.

6.2 Experimental Methodology and Sample Preparation

The shifts in the position of the 2D Raman band are an indication of the local strain in the carbon fibres with a spatial resolution of about 2μm. Raman 2D bands were obtained using an exposure time of 20s with 2 accumulations at each scanning point. Each spectrum was taken from the carbon fibre at the interface with an epoxy resin droplet using an incremental distance of 0.01 mm along the free fibre length. After each spectrum along the fibre through the microdroplet was recorded, the strain on the carbon fibre was increased to the next level and the scanning process was repeated. The deformation levels applied were 0%, 0.3%, 0.5% and 0.7% strain; the high modulus carbon fibres normally fractured above a strain level of about 0.8%.

Using single fibre deformation results reported in Chapter 5, these shifts in the 2D Raman band can be converted to the local fibre strain. Since the stress-strain behaviour

of the carbon fibres were determined using tensile testing (the results are given in Chapter 4) these data were used to convert the local fibre strain to stress. Subsequently a map of stress as a function of the distance along the interfacial area can be obtained. A schematic of the geometry of the microdroplet specimen, which is similar to the more established micro-bond test specimen, is shown in Figure 6.1. Local stress σ_f depends on the distance along the interfacial area can be obtained by using the equation

$$\sigma_f = \sigma_{app} \frac{\cosh\left(\frac{nx}{r_f}\right)}{\cosh\left(\frac{nL}{r_f}\right)} \qquad (6.1)$$

where σ_{app} is the fibre stress outside the droplet, L is the droplet size, n is a fitting parameter, x is the distance along the fibre across the interfacial area and r_f is the fibre radius. The interfacial shear stress τ can be calculated by taking the first derivative of equation 6.1 ($d\sigma/dx$) leading to the equation

$$\tau = \sigma_{app} \frac{n \sinh\left(\frac{nx}{r_f}\right)}{2\cosh\left(\frac{nL}{r_f}\right)} \qquad (6.2)$$

It should be noted however that Equation 6.1 is not generally found to be applicable for all the droplets systems as other interfacial failure can occur, such as debonding. This debonding is identified by a linearization of the Raman data (where the ISS is constant). Matrix yielding can also occur where ISS drops to a value close to that when the interface is intact. In this situation the data can be fitted using the equation (Mottershead and Eichhorn, 2007)

$$\sigma_f = -\frac{2\tau}{r_f}x + \sigma_0 \qquad (6.3)$$

where σ_0 is a constant and is the stress ahead of the debonded region.

Another equation, derived from a force balance approach (McCrum and Buckley *et al*, 1997), can be used to calculate the interfacial shear stress, as

$$\tau = \frac{r_f}{2}\frac{d\sigma_f}{dx} \qquad (6.4)$$

This equation is only used when the stress distribution profile has already been determined, and so the ISS τ will be calculated from the deviation of stress upon distance along the interface.

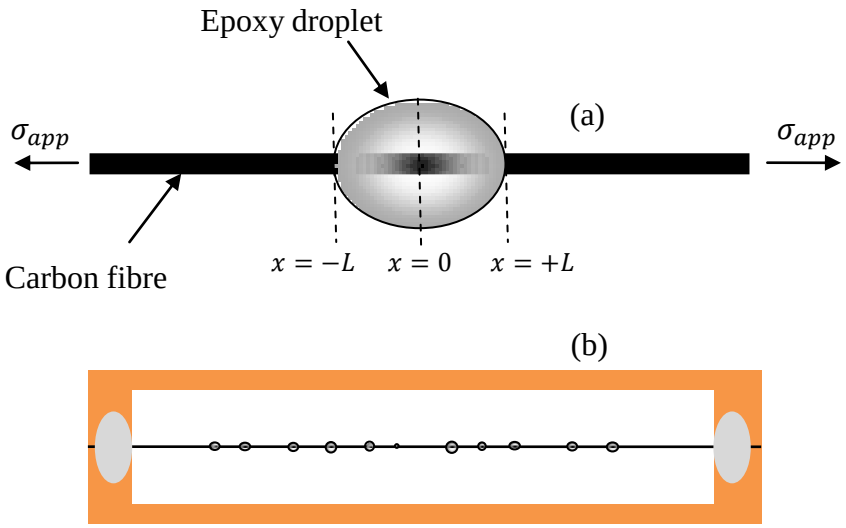

Figure 6.1 *Schematic geometry of the microdroplet specimen (a) and a general view of the whole sample (b).*

The same specimens (see Figure 3.12) as those for tensile testing were used for the following experiments, with a range of micro droplets placed along the gauge length by dipping the ends of a pair of tweezers into epoxy resin (LY5052/HY5052) and then slowly opening them on the surface of carbon fibres along the gauge length. This approach was used by Eichhorn and Young (2003). These droplets were then cured for about 7 days at room temperature before testing. A schematic of the sample is shown in Figure 6.1b.

6.3 Microdroplets Characterization by Optical Microscopy

The microdroplets on the carbon fibres suitable for interfacial analysis were selected using optical microscopy. Figure 6.2 shows that the epoxy microdroplets have significantly different morphologies, with a variety of sizes and shapes. The carbon fibres also pass through the microdroplets at different positions. The position where the carbon fibre goes through the microdroplets could play a very important role and affect the interfacial behaviour. As shown in Figure 6.2a this carbon fibre just touches the droplet and is not deeply embedded. In this situation debonding could easily occur when the carbon fibre is deformed in tension. Nevertheless, if the carbon fibre does not travel through the droplet from its centre (see Figure 6.2b), the embedded area is very difficult to distinguish and focus on due to total internal reflection, typified by the dark areas observed at the edges of the microdroplet using the optical microscope of the Raman spectroscometer. Therefore samples were carefully selected and those with carbon fibres travelling right through the centre of the microdroplets were chosen (see Figures 6.2c and 6.2d). Then the embedded lengths of the selected samples were measured using optical microscopy and image analysis. Since the droplet sizes may affect interfacial behaviour and in order to make the determined interfacial shear stresses more comparable for different samples, the samples with embedded lengths of around 200 ± 20 μm were chosen and these specific droplets were marked to have their interfaces monitored using Raman spectroscopy.

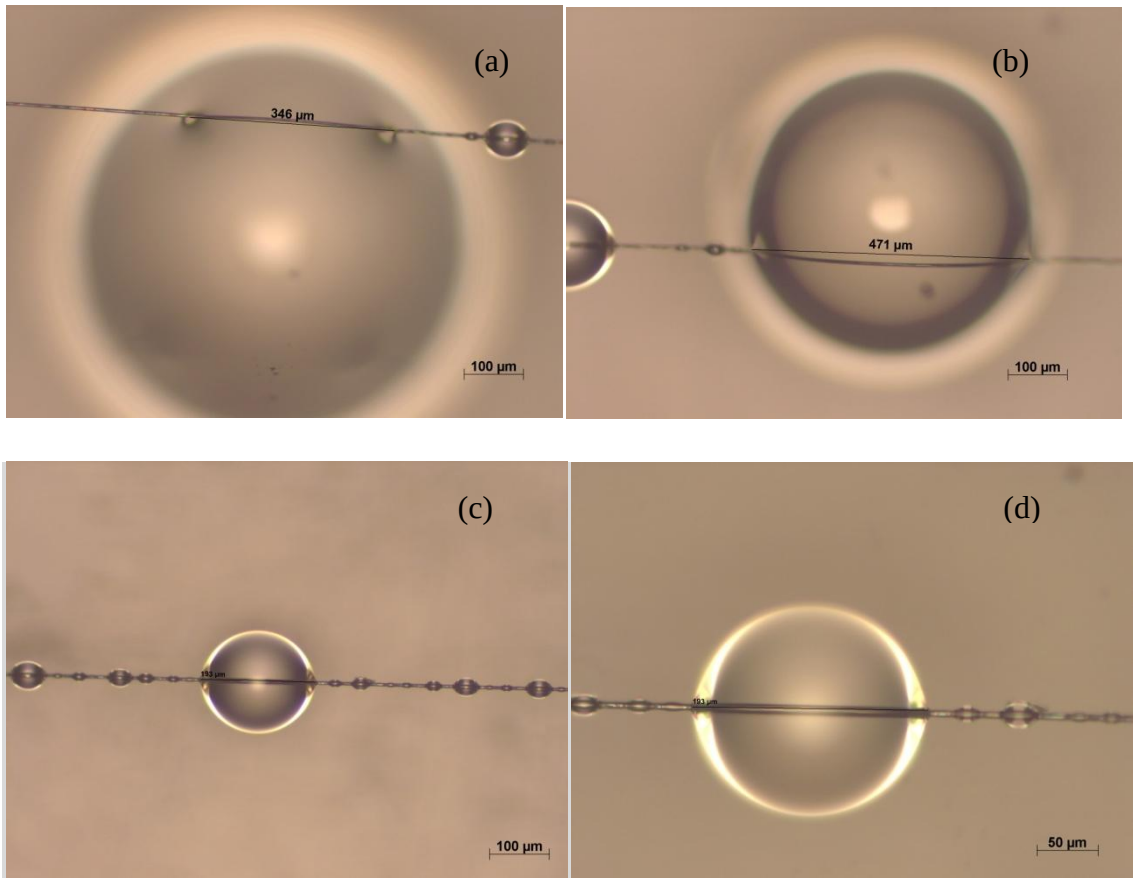

Figure 6.2 *Examples of typical light microscope images of different contact positions of epoxy resin microdroplets on carbon fibres used for the evaluation of embedded length by optical microscopy; Carbon fibre just touching a microdroplet (a); Carbon fibre not passing through the centre of a microdroplet (b); Carbon fibre passing through the centre of a microdroplet (c) & (d).*

6.4 Stress Mapping By Raman Spectroscopy

In this study, a typical example of the 2D Raman band positions as a function of the distance along the interfacial area between a carbon fibre and an epoxy microdroplet is shown in Figure 6.3. It can be seen that Raman spectra cannot be obtained from the regions 10-30 μm from the edge of the microdroplet where the carbon fibre enters and exits.

The Raman shift data obtained from the scanning of the microdroplet-fibre system were converted to stress by using the calibration obtained from Chapter 5. Typical plots of local tensile stress as a function of the distance along the fibre both inside and outside the microdroplet are shown in Figure 6.4. The vertical solid lines indicate the edges of the microdroplet. It is clearly observed that when there is no stress applied on the fibre a small region inside the microdroplet is in compression. This is evidence of shrinkage of the epoxy droplet and a possible thermal residual stress was generated during the curing of the epoxy matrix, even though it was cold cured. These thermal residual effects could be possibly caused by the resin's exothermal reaction during its curing process.

Figure 6.4 suggests that the stress decreases significantly at both edges of the droplet. This drop in local stress at the edges of the microdroplet has also been observed in previous studies of other epoxy microdroplet composites systems but with different fibres such as hemp fibres (Eichhorn and Young, 2003), regenerated cellulose (Mottershead and Eichhorn, 2007), and aramid fibres (Cen *et al*, 2006). This drop in stress is attributed to that the extension of fibre has been restricted by the droplet as the deeper the fibre enters into microdroplet the stronger it is restricted by the matrix. This decay of stress is also in agreement with the prediction of the stress distribution across the interface according to Equation 6.1. It was however found that was an increase and a drop in stress (the so-called "hump region") in the central region of the stress profile. This effect is thought to be caused by the compression of fibres in the centre of the microdroplet, and has been explained by Eichhorn and Young (2003) for epoxy microdroplets on hemp fibres. They found it was due to the surface tension effects at the edge of droplet placing the fibre under compression. The refraction of the laser by the microdroplet should also be considered, as it will lead to the data to be recorded in a different area of the sample. As the epoxy droplet tends to contract during loading, the

'hump region' tends to become more flattened; this observation is in agreement with the findings of Mottershead and Eichhorn (2006).

Due to the presence of the 'hump region' in the stress profile, the distribution of stress data across the interface cannot be fitted exactly by Equation 6.1. These data were therefore fitted using a 4th order polynomial. It should be noted that the stress profile of the 0.7% strain level indicates there is neither a drop in stress when the fibre enters the resin, nor a "hump region" in the middle of the microdroplet. This suggested that the debonding occurs all across the interfacial length or the epoxy matrix yield has occurred.

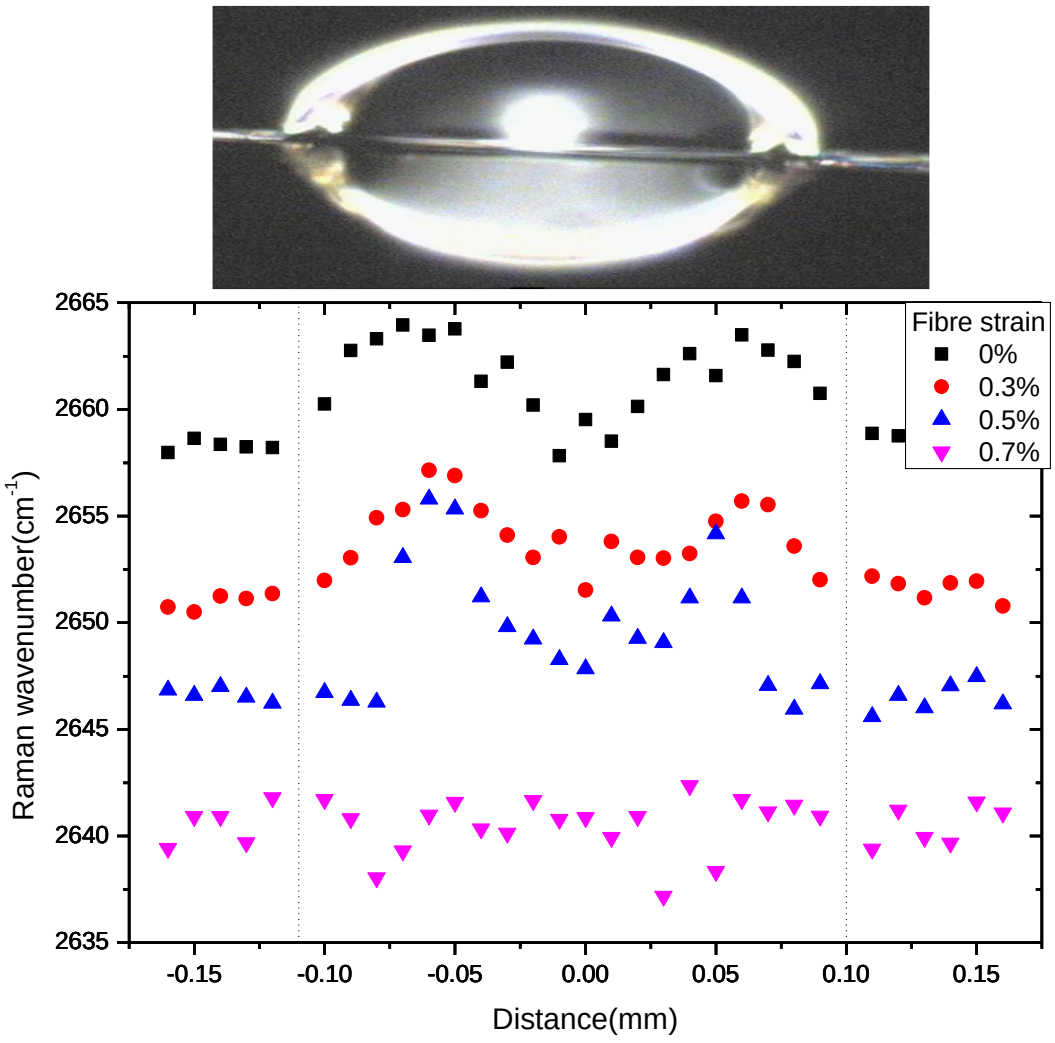

Figure 6.3 *Typical shifts in the position of the 2D Raman band as a function of the distance along the interface inside and outside of a microdroplet at elevated strain; vertical dotted lines indicate the edges of microdroplet.*

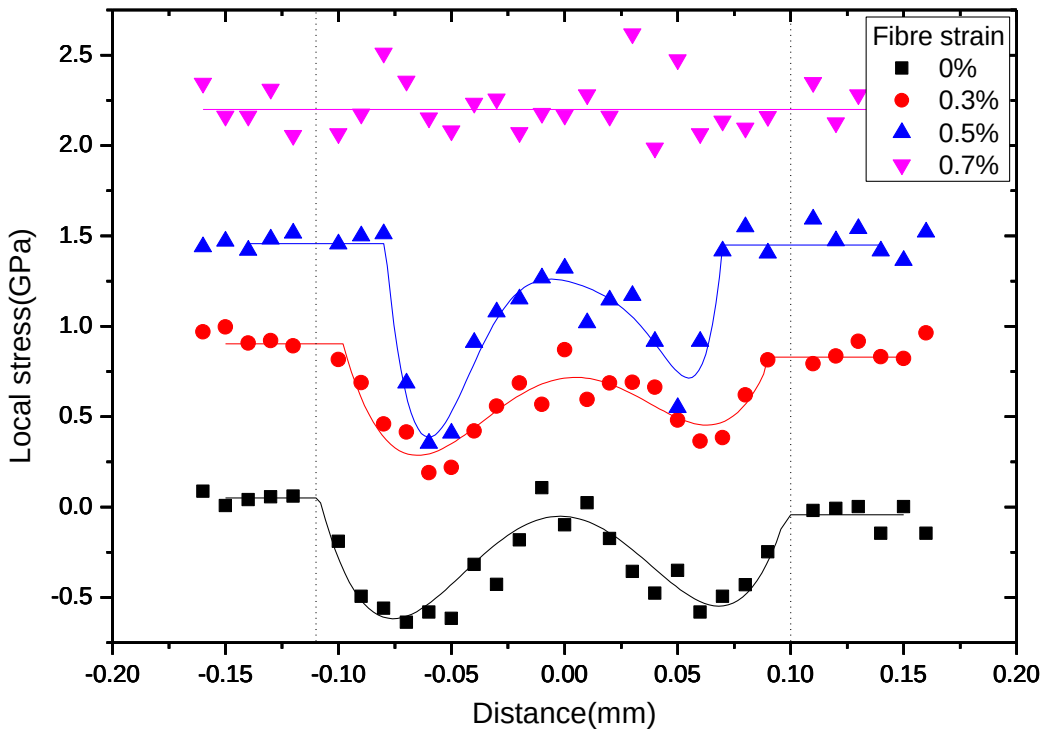

Figure 6.4 *Typical stress profile calibrated from the shifts in the 2D Raman band along the interface between a microdroplet and a high modulus carbon fibre at elevated strain; a polynomial equation was used to fit the data, vertical dotted lines indicate the edges of microdroplet.*

6.5 Interfacial Shear Stress (ISS) Profile Characterization

By using Equation 6.4 and differentiation of the fitted polynomial equation the interfacial shear stress can be derived, as shown in Figure 6.5. It is obvious, according to Equation 6.4, that the higher the rate of change of stress with respect to distance ($\mathrm{d}\sigma/\mathrm{d}x$) along the interface, the greater the ISS; the maxima of ISS are near the edges of the droplet. It can be seen from Figure 6.5, the ISS is zero at the centre of droplet. The 'sharp spikes' observed near the edges of the droplet suggest that the shear stress is not constant in this region; where the elastic stress transfer between the fibre and the matrix is thought to occur. The continuous curve in the centre indicates that the interface is intact, and the horizontal line at the edge of droplet could possibly means interfacial crack between fibre and droplet occurred at these areas thus ISS of zero was obtained. A maximum ISS of around 110 MPa for this sample was detected. This value is too high for a reasonable ISS for a carbon fibre/epoxy resin interface. This could be due to the rapid drop of stress when the fibre enters the droplet. An interfacial study by

Mottershead and Eichhorn (2006) using the same geometrical microdroplet sample but with a cellulose fibre also reported similar ISS values. They suggested that the constraint at the interface, which may due to surface tension forces at the resin meniscus, could also provide a rise to such a high value of ISS. However after the region where fibre enters the droplet, the maximum ISS obtained was about 30MPa, which is a typical value for the interfacial shear stress for epoxy and carbon fibre systems.

Overall, this ISS profile in Figure 6.5 shows four main stages of interfacial micromechanical behaviour of a single high modulus carbon fibre/ epoxy microdroplet system. They are as follows:

I. High modulus carbon fibre and epoxy microdroplet were perfectly bonded together, all deformation in system were elastic (strain in specimen were below 0.3%).
II. Debonding started to occur at the edge of droplets where stresses concentrated on, it will continued propagation from both ends of the microdroplet to its centre as the increasing of strain in the sample(strain in specimen were between 0.3% and 0.7%).
III. Debonding reached all length of interfacial area or matrix yield occurred (strain in specimen was about 0.7%).
IV. Stretched fibre was finally broken outside or inside the microdroplet (strain in specimen was 0.8% or above).

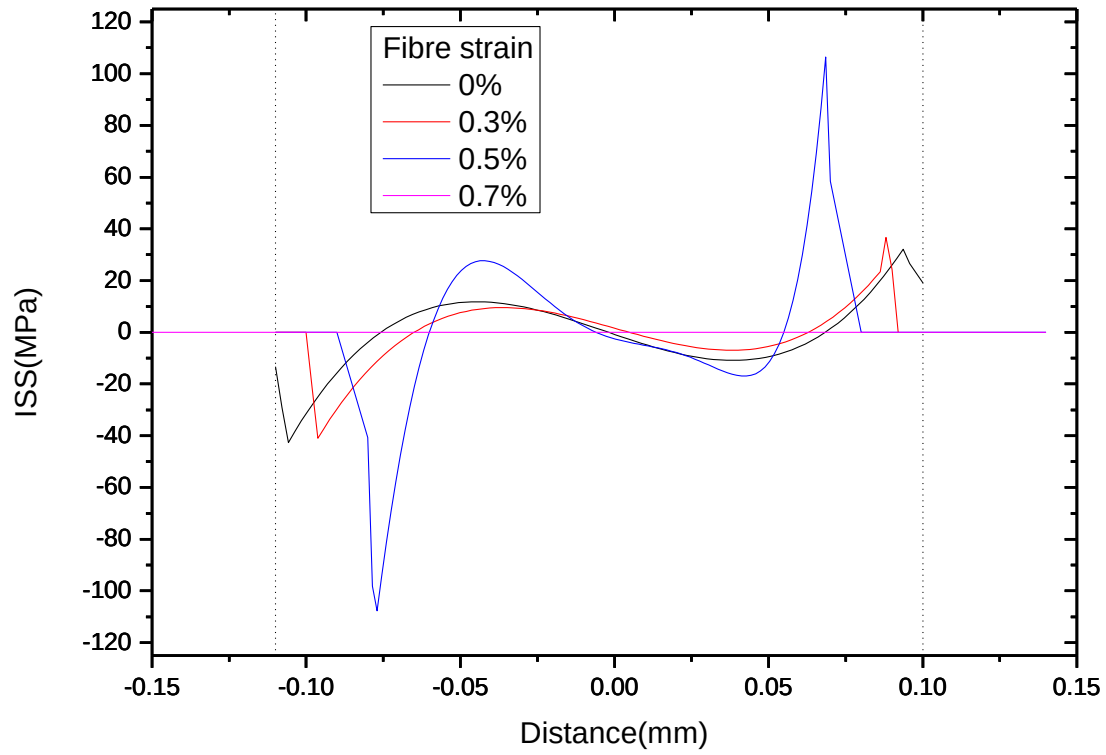

Figure 6.5 *Interfacial shear stress (ISS) along the interfacial area between a carbon fibre and an epoxy resin microdroplet. Vertical dotted lines indicate the edge of microdroplet.*

All experiments were repeated three times. The maximum ISS values obtained were 142.7 ±3.8 MPa, 108.6 ±2.9MPa and 87.9 ±3.1MPa. The reason for this variation will be discussed in Section 6.6.

6.6 Results Affected by Geometrical Characteristics of Microdroplet

In this study the effect of the microdroplet shape on the interfacial behaviour has been investigated. The shape of the microdroplet is characterized by the interfacial edge angle θ, which is defined as the slope of the microdroplet at the interfacial end point where the fibre enters the droplet, as shown in Figure 6.6a. The magnitude of the interfacial edge angle θ is given by the equation

$$\theta = \tan^{-1}(h/D) \qquad (6.5)$$

where *D* is the fibre diameter and *h* is the height of the microdroplet at a distance *D* from the edge of the microdroplet (see Figure 6.6b). An optical microscope was used to determine the value of *h*.

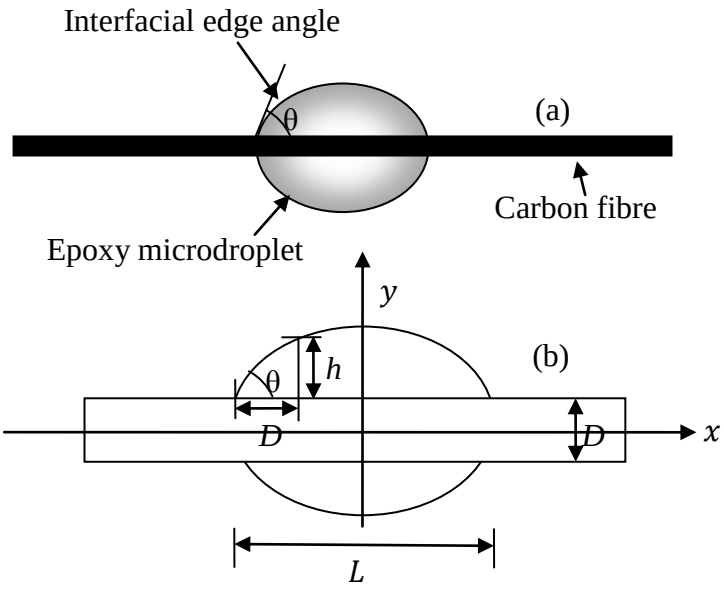

Figure 6.6 *Schematic of geometrical interfacial angle θ (a) and its geometrical definition (b).*

Table 6.1 *The geometrical characteristics of the microdroplets from three samples and their ISS values.*

Samples	Interfacial edge angle, θ (°)	Interfacial length(mm)	ISS(MPa)
Sample A	79	0.20 ±0.04	142.7 ±3.8
Sample B	64	0.21 ±0.03	108.6 ±2.9
Sample C	43	0.20 ±0.03	87.9 ±3.1

Figure 6.7 shows the local stress in the fibre for the three samples. The first five data points where the fibre enters the microdroplet are displayed and the external fibre strain on all three samples was 0.3%. It is found that the stress distribution is affected significantly by the interfacial edge contact angle. It is noted that the stress at the entry

point of the fibre for all samples was about 0.8GPa. The fibre stress in the microdroplets decreased more rapidly when the interfacial contact angle is larger. The reasons for this can be explained by considering the stress transfer length.

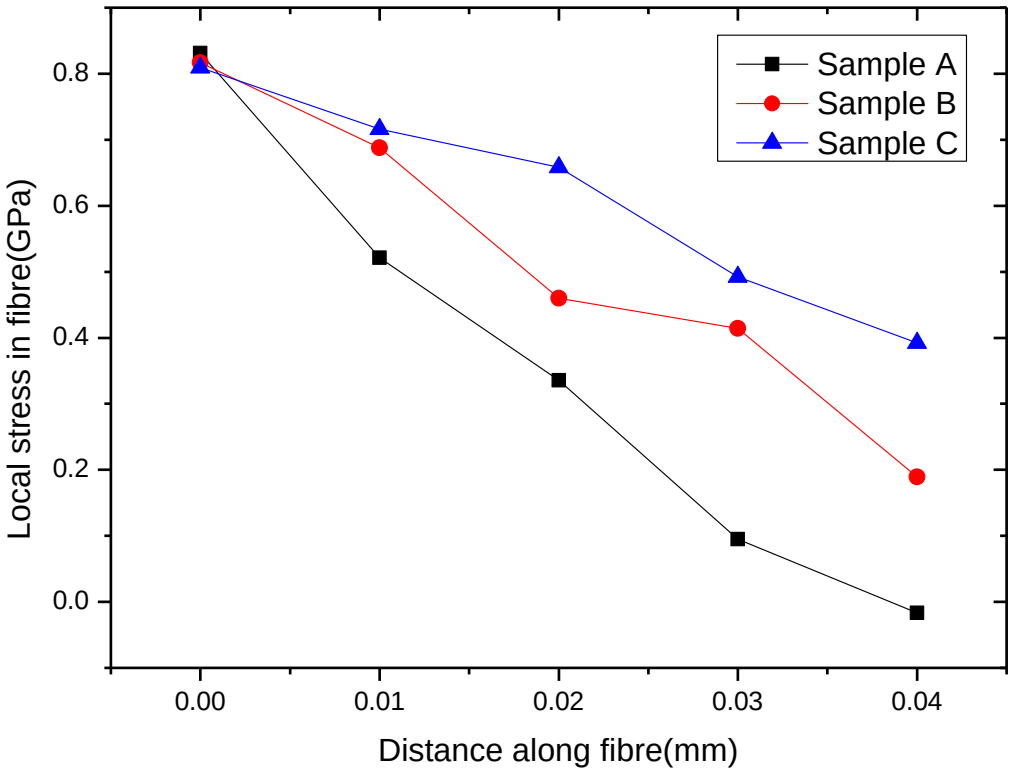

Figure 6.7 *Stress distributions for three samples with different interfacial edge angles for the first five points when the fibre enters the microdroplet (Fibre strain level = 0.3%).*

In the studying of interfacial mechanisms, the stress transfer length is one of the most important parameters characterizing the interfacial properties, and it means the fibre axial distance from the edge of microdroplet to the location where the fibre stress decreased to zero. In this work, the stress transfer length for Sample A could be measured from Figure 6.7 and it is about 0.04mm. As can be seen the gradient of stress profiles in Figure 6.7 are in the order of $G_{Sample\ A} > G_{Sample\ B} > G_{Sample\ C}$, therefore the length that for the stress of each sample to reach zero is in this order: $L_{Sample\ A} < L_{Sample\ B} < L_{Sample\ C}$, which is also the order of stress transfer length. In order to analyse the geometry effects on the stress transfer length numerically, a two dimensional investigation of the microdroplet has been set up(see Figure 6.6 b). The volume of the microdroplet can be express in Equation 6.6.

$$V = 2\pi \int_{-\frac{L}{2}}^{\frac{L}{2}} \{[y(x)]^2 - (\frac{D}{2})^2\} dx \quad (6.6)$$

Where L is the embedded length, in this study L= 200±20 μm. For the volume at the edge of the microdroplet, Equation 6.6 can be stated like this:

$$V_{edge} = 2\pi \int_{-\frac{L}{2}}^{x} \{[y(x)]^2 - (\frac{D}{2})^2\} dx \quad (6.7)$$

For the stress profile shown in Figure 6.7, where $-\frac{L}{2} < x < 0.04$mm, and in this region $y(x)$ could be expressed roughly as:

$$y(x) \approx \left(x - \frac{L}{2}\right) \tan\theta \quad (6.8)$$

At a specific given embedded region, x is a constant, thus $y(x)$ is rely on the contact angle θ(0°< θ <90°), according to Equation 6.8 a larger θ will result in a higher value of $y(x)$, and then a greater calculated volume of this specific region at the edge of microdroplet(according to Equation 6.7). Finally a higher matrix volume fraction in comparison with carbon fibre for this micro composite system will be obtained. As the study by Jang *et al.* (1993) for a single fibre pull-out test suggested that when the volume fraction of fibre V_f is above a critical value (Volume fraction of matrix V_m below a critical value), the decrease of V_f (increase of V_m) will result in a shorter stress transfer length from fibre and higher ISS concentration at the region where fibre enters matrix. This rule can still be valid for such a small epoxy microdroplet and carbon fibre micro-composite system, as V_m at the edge of the microdroplet should be under the critical value. Therefore it can be understand why stress drops more sharply and the stress transfer length became shorter during the increasing of microdroplet edge angle θ for this epoxy microdroplet composite system.

6.7 Discussion and Conclusion

It is obvious that Raman spectroscopy has been applied successfully in obtaining comprehensive information for the interface between epoxy droplet and carbon fibre due to its high sensitivity, high spatial resolution, point to point measurement, non-destructive and non-contact measurement. The interfacial shear stress has been

determined for this epoxy microdroplet and high modulus carbon fibre system, but the obtained results varied significantly for different samples. Subsequently the study found that the microdroplet geometry shape by means of edge contact angle has dominant effect on the interfacial properties, as a larger interfacial edge angle of microdroplet is normally equivalent to a shorter stress transfer length and sharper decreases in fibre stress at the edge of microdroplet, thus generates higher interfacial shear stress concentrated at the interfacial end point. This also means a greater possibility of interfacial failure and breakage will occur at the place. The reasons for this geometry effect have also been investigated numerically in a 2D dimensional model.

Due to the ISS determined for this epoxy microdroplet model is inaccurate to some extent and the experimental hardship for applying the SWNTs on low modulus carbon fibre as strain sensor together with epoxy microdroplet, the interface between low modulus carbon fibre and epoxy was not studied in this epoxy microdroplet model. However, these interfaces will be investigated in the epoxy film method and fragmentation in the following two chapters.

6.8 References

Cen, H., Kang, Y., Lei, Z., Qin, Q. and Qiu, W.(2006) Micromechanics analysis of Kevlar-29 aramid fibre and epoxy resin microdroplet composite by Micro-Raman spectroscopy. *Composite structures*, 75, pp. 532-538.

Day, R.J. and Cauich Rodrigez, J.V. (1997) Investigation of the micromechanics of the microbond test. *Composites and Science Technology*, 58, pp. 907-914.

Dai, Y. and Ji, X. (1995) Elastic analysis of a cylindrical interface crack. *ACAT Mechanica Solida Sinica*, 8, pp. 573-669.

Eichhorn, S.J., Bennett, J.A., Shyng, Y.T., Young, R.J. and Davies, R.J. (2006) Analysis of interfacial micromechanics in microdroplet model composites using synchrotron microfocus X-ray diffraction. *Composites Science and Technology*, 66, pp. 2197-2205.

Eichhorn, S.J. and Young, R.J. (2004) Composite micromechanics of hemp fibres and epoxy resin microdroplets. *Composites Science and Technology*, 64, pp. 767-772.

Guar, U. and Miller, B. (1989) Microbond method for determination of the shear strength of a fibre/resin interface: Evaluation of experimental parameters. *Composites and Science Technology*, 34, pp. 35-51.

Jang, K.K., Zhou, L., Bryan, S.J. and Mai, Y.W. (1993) Effects of fibre volume fraction on the stress transfer in fibre pull-out tests. Composites, 25(7), pp. 470-475.

Kang, Y.L. and Pan, X.J. (2000) Experimental study of the strain field of the biomaterial interface. 2000SEM IX international congress on experimental mechanics, Orlando Florida USA, pp. 688-690.

McCrum, N.G., Buckley, C.P. and Bucknall, C.B. (1997) Principles of polymer engineering. Oxford: Oxford University Press.

Motterhead, B. and Eichhorn, S.J. (2007) Deformation micromechanics of model regenerated cellulose fibre-epoxy/polyester composites. *Composites Science and Technology*, 67, pp. 2150-2159.

Wu, X. (2006) Droplet on a fibre: Geometrical shape and contact angle. *Acta Mechanica*, 185, pp. 215-225.

Young, R.J. (1996) Evaluation of composite interface using Raman spectroscopy. *Key Engineering Materials*, 116-117, pp. 173-192.

CHAPTER 7 Epoxy Film Model

7.1 Introduction

Since the interfacial properties determined in Chapter 6 for the epoxy microdroplet model system vary significantly, another alternative geometry model comprising an epoxy film encapsulating carbon fibre filaments have are reported in this chapter. For this epoxy film model system, the stress was also transferred from the carbon fibre to the epoxy resin matrix, as for the epoxy microdroplet model system.

The interfacial properties of this epoxy film model system were investigated using point-to-point stress mapping with a Raman spectrometer. Interfacial shear stresses (ISS) were calculated using a similar approach to that reported in Chapter 6. Epoxy films containing high and low modulus carbon fibres are reported compared in this Chapter. Both HiPCO SWNTs and COOH SWNTs have been coated on the low modulus carbon fibre to assist the sensing of the local stress, as low intensity Raman bands are obtained from these fibre samples. These types of SWNTs were also coated on the high modulus carbon fibre to compare properties. Furthermore, model composites comprising an epoxy film/ and a high modulus carbon fibre with and without a SWNT coating were compared to see if the interfacial adhesion is affected by their presence.

7.2 Experimental Methodology and Sample Preparation

The methodology used to investigate the interfacial properties of the epoxy film model composites is similar to the droplet model system in that the stress across the interfacial area was also mapped using shifts in the position of the 2D Raman band. These point-to-point measurements were carried out using an exposure time of 20s and 2 accumulations at each scanning point from high modulus carbon fibre. The exposure time was reduced to 10s for the samples coated with SWNTs as 2D Raman bands of high intensity were expected given the resonant properties of nanotubes. Since the epoxy film specimens are comparatively much longer in length than the microdroplets, and as the carbon fibre embedded length was ~18 mm, the distance between each scanning point varied when more detail was required at the edge of the epoxy film where debonding was typically initiated. Therefore the scanning distance between each point was 10 μm within the edge region, which is about 1 mm along the fibre from where it enters the epoxy film. On the other hand, in the central region of the epoxy film, the scanning distance was 100 μm, where the interfaces were expected to be remaining intact. After each scan across the interface finished, the specimen was extended to the next strain level and the scanning process repeated until the fibre fractured. The strain levels applied on the epoxy film with a high modulus carbon fibre were 0%, 0.3%, 0.5% and 0.7%, where the determined stresses applied on the sample are approximately equal to 0, 1.1, 2.1 and 3.1 GPa respectively, the same as for the epoxy microdroplet-high modulus carbon fibre system described in Chapter 6. On the other hand, due to the higher breaking strain of low modulus carbon fibre, a different set of strain levels were applied to the epoxy film with a low modulus carbon fibre as they were 0%, 0.3%, 0.6%, 0.9% and 1.2%, where the determined stresses applied on the sample are approximately equal to 0, 0.8, 1.6, 2.4 and 3.2 GPa. By using the calibration with fibre stress, as reported in Chapter 5 for each specific sample, these peak positions of the 2D Raman band were converted to fibre local stress.

The local stress as a function of the distance along the fibre/matrix interface can be fitted using the following equation (Mottershead and Eichhorn, 2007)

$$\sigma_f = \sigma_{app} \frac{\cosh(nx/r_{\mathrm{f}})}{\cosh(nL/r_{\mathrm{f}})} \qquad (7.1)$$

where L is half length of the epoxy film (in this study L = 9mm), σ_{app} is the applied stress on the fibre, r_{f} is radius of the fibre, and

$$n^2 = \frac{E_{\mathrm{m}}}{E_{\mathrm{f}}(1+v_{\mathrm{m}})\ln(R/r_{\mathrm{f}})} \qquad (7.2)$$

where E_{m} and E_{f} are Young's moduli of the matrix and fibre respectively, v_{m} is the Poission's ratio of the matrix and R is the radius of the resin block, $\ln(R/r_{\mathrm{f}})$ can be regarded as a volume fraction parameter (Bannister *et al*, 1995). In this case the interfacial shear stress can be calculated using the equation

$$\tau = -\sigma_{\mathrm{app}} \frac{n\ \sinh(nx/r_{\mathrm{f}})}{2\cosh(nL/r_{\mathrm{f}})} \qquad (7.3)$$

In the case that the stress distributions along the interface have been determined, the interfacial shear stress can be calculated from the equilibrium of forces exerted on a differential fibre element stress $d\sigma_{\mathrm{f}}$ on the length dx, giving the equation

$$\tau = E_{\mathrm{f}} \frac{r_{\mathrm{f}} d\sigma_{\mathrm{f}}}{2dx} \qquad (7.4)$$

The samples were produced by firstly cutting paper card into the shape as shown in Figure 7.1. Then a single carbon fibre filament was fixed on this paper card by using two drops of Araldite™ precision epoxy adhesive at the edges of the window. A glass slide was placed below the fibre in the middle of paper card window, supported by two strips to prevent them from applying load to the fibre before testing or rotating during mechanical deformation. It was ensured that the fibre was run centrally across the glass slide. After that a small droplet of epoxy resin was applied to the surface of glass slide and another glass slide was placed on top of the first one, sandwiching the fibre between the two. Adjustments were also made to the position of the slides so that they were in line with each other as much as possible to overcome edge effects (Mottershead and Eichhorn, 2007). These model composites were placed in a room with a controlled environment (temperature of 23 ℃ and 50% humidity) for 7 days to make sure they were fully cured.

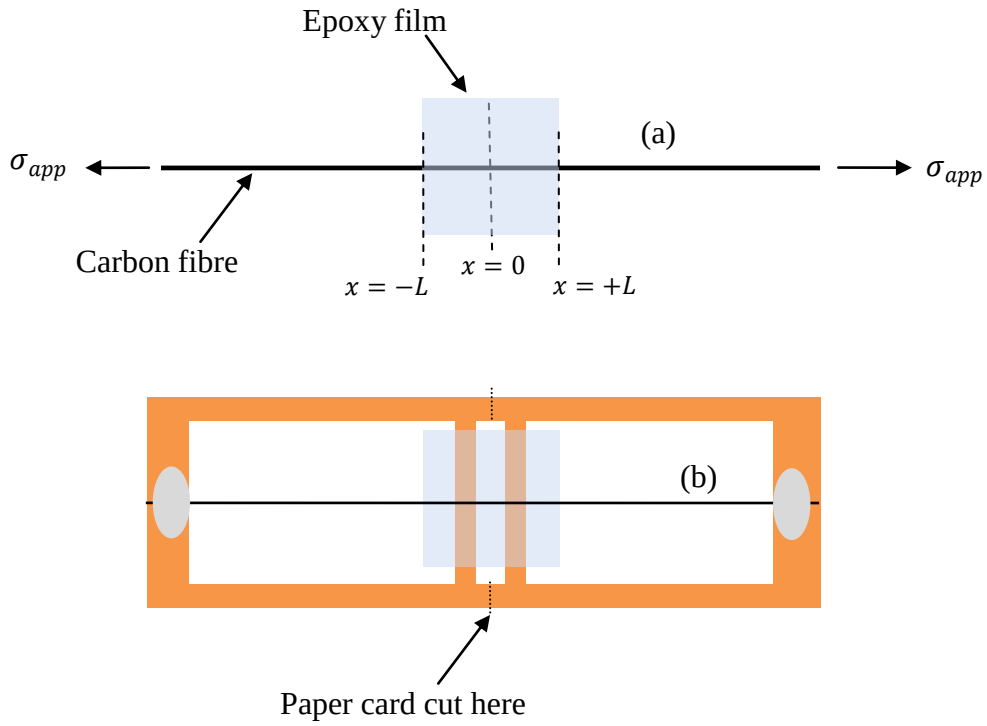

Figure 7.1 *Schematic geometry of the epoxy-carbon fibre composite film specimen (a) and a general view of the whole sample (b).*

7.3 Thickness of Epoxy Film Characterization by Optical Microscopy

It was expected that the thickness of the epoxy film may have an effect on the interface with a carbon fibre. The thicknesses of 20 epoxy films of high modulus carbon fibre system were measured using an optical microscope, the results of which are reported in Table C.1 in Appendix C. The thicknesses were found to be in the range of ~200-240 μm; average thickness is 223.06 ± 0.17 μm.

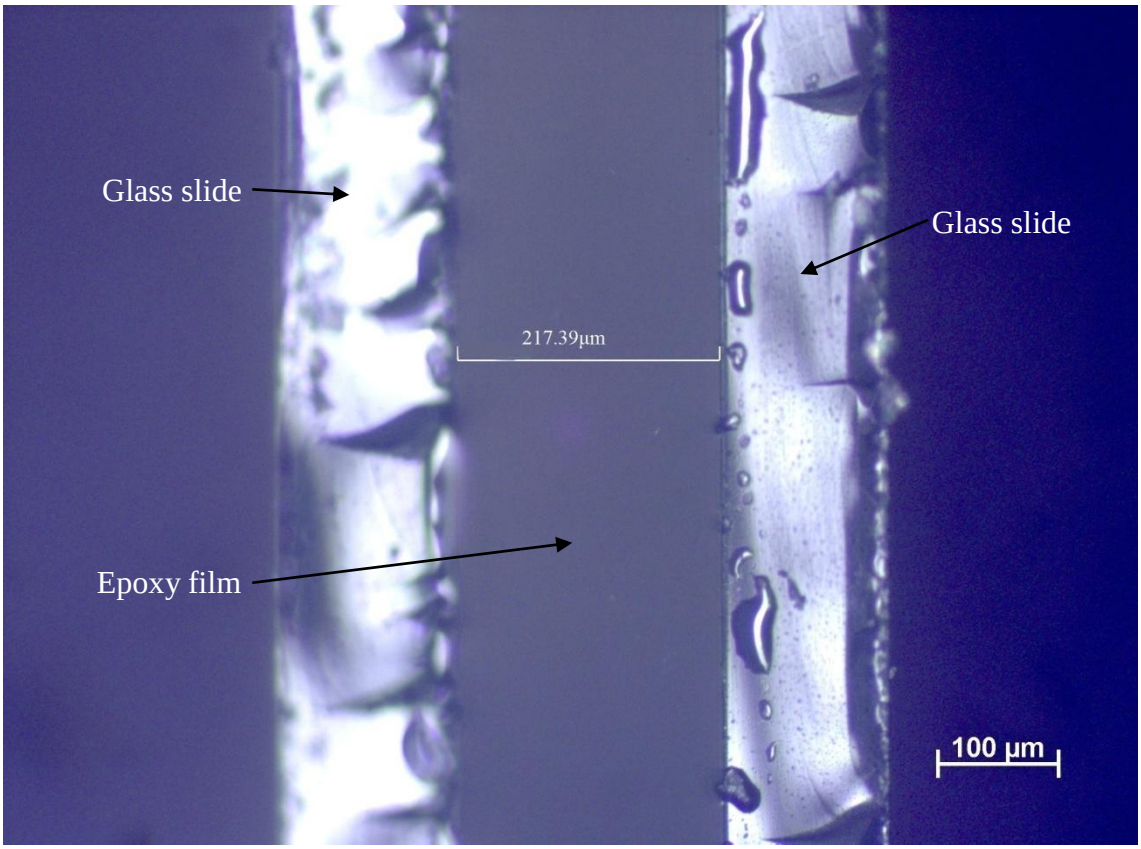

Figure 7.2 *A typical cross section of an epoxy film sandwiched between two glass slides.*

Five different epoxy films and carbon fibres were used to determine interfacial shear stress profiles using Raman spectroscopy. The results show that the interfaces between the fibre and epoxy are no significant difference among these samples as their ISS profiles were shown in Appendix D.

7.4 High Modulus Carbon Fibre with Epoxy Film System

7.4.1 Stress Mapping by Raman Spectroscopy

The 2D Raman band shift position as a function of the distance along the fibre both inside and outside the epoxy film is shown in Figure 7.3. The 2D Raman band can be obtained along the whole interfacial region, including the edge areas. This is different to the microdroplet model composite, where refraction of the laser due to the spherical nature of the droplet gave rise to inaccessible regions.

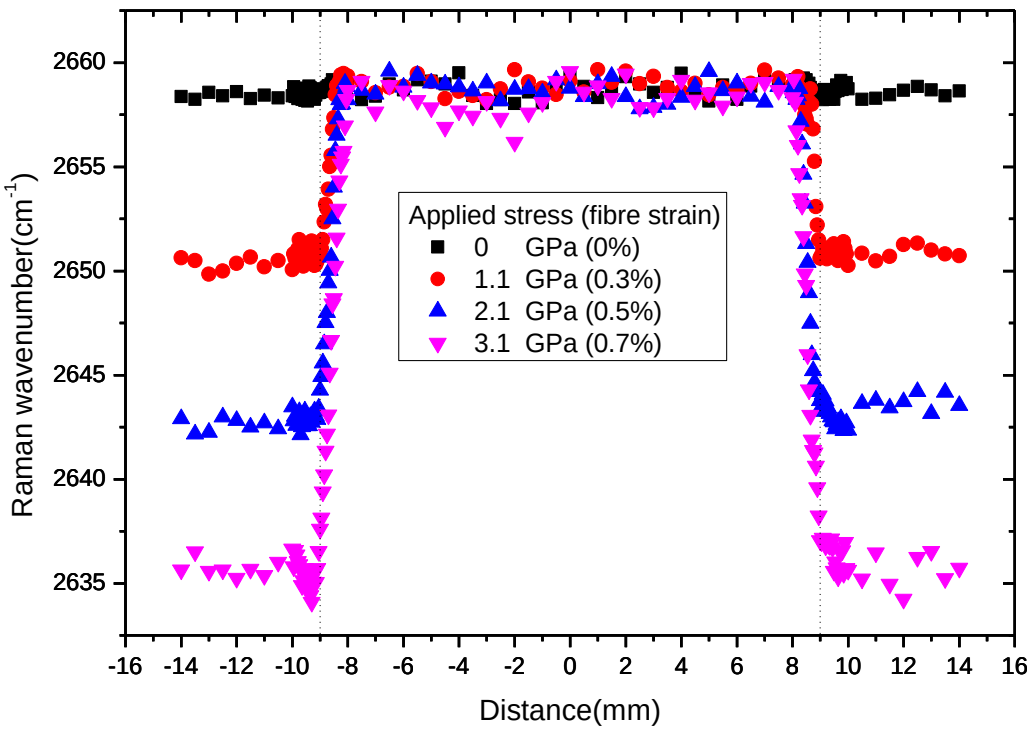

Figure 7.3 *Typical positions of the Raman 2D band with respect to the distance along a high modulus carbon fibre, both inside and outside an epoxy film; the vertical dotted lines indicate the edge of the epoxy film.*

The Raman 2D band positions were converted to local stresses (see Figure 7.4) by using the calibration result reported in Chapter 5. The stress profile was then fitted using Equation 7.1.

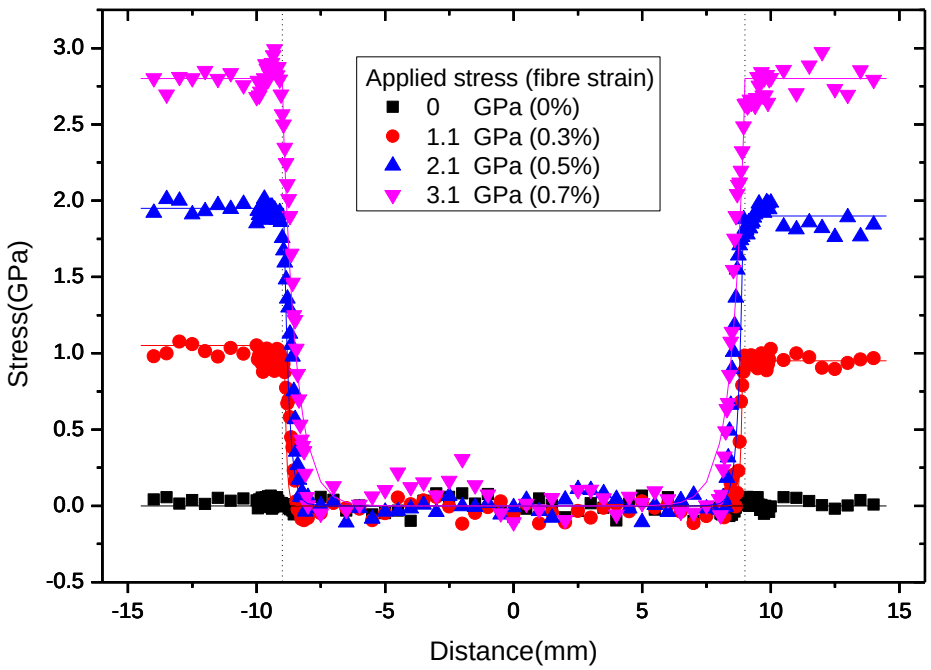

Figure 7.4 *Typical stress profile converted from Raman 2D band positions along the interface of epoxy film and a high modulus carbon fibre at elevated strain; Vertical dotted lines indicated the edges of the epoxy film.*

First of all it can be clearly observed from the stress profile that the central region of the flat film remained unstressed even when the exterior deformation applied on the sample increases. As the debonding region could not reach all length of fibre due to the long embedded length, this epoxy film model test can be generally regarded as two typical pull-out test (in early stages before fibre was pulled out) from both sides of the epoxy film. No residual compressive stress was found. It is therefore thought that in the microdroplet model composite system the rapid decay of fibre stress when the fibre first enters the matrix is not caused by thermal residual stresses, and is mainly due to the distortion of the laser by the curvature of the microdroplet itself. Furthermore, no 'hump region' is observed at the centre of the stress profile for the epoxy film model composite system, which could be due to the fact that there is no optical distortion for the flat film samples.

Since there is a dramatic change in stress occurring at the edge region of the epoxy film, where the fibre enters the matrix, and a relatively larger number of data points were recorded in this region, the stress profile in this region has been magnified, as shown in Figure 7.5.

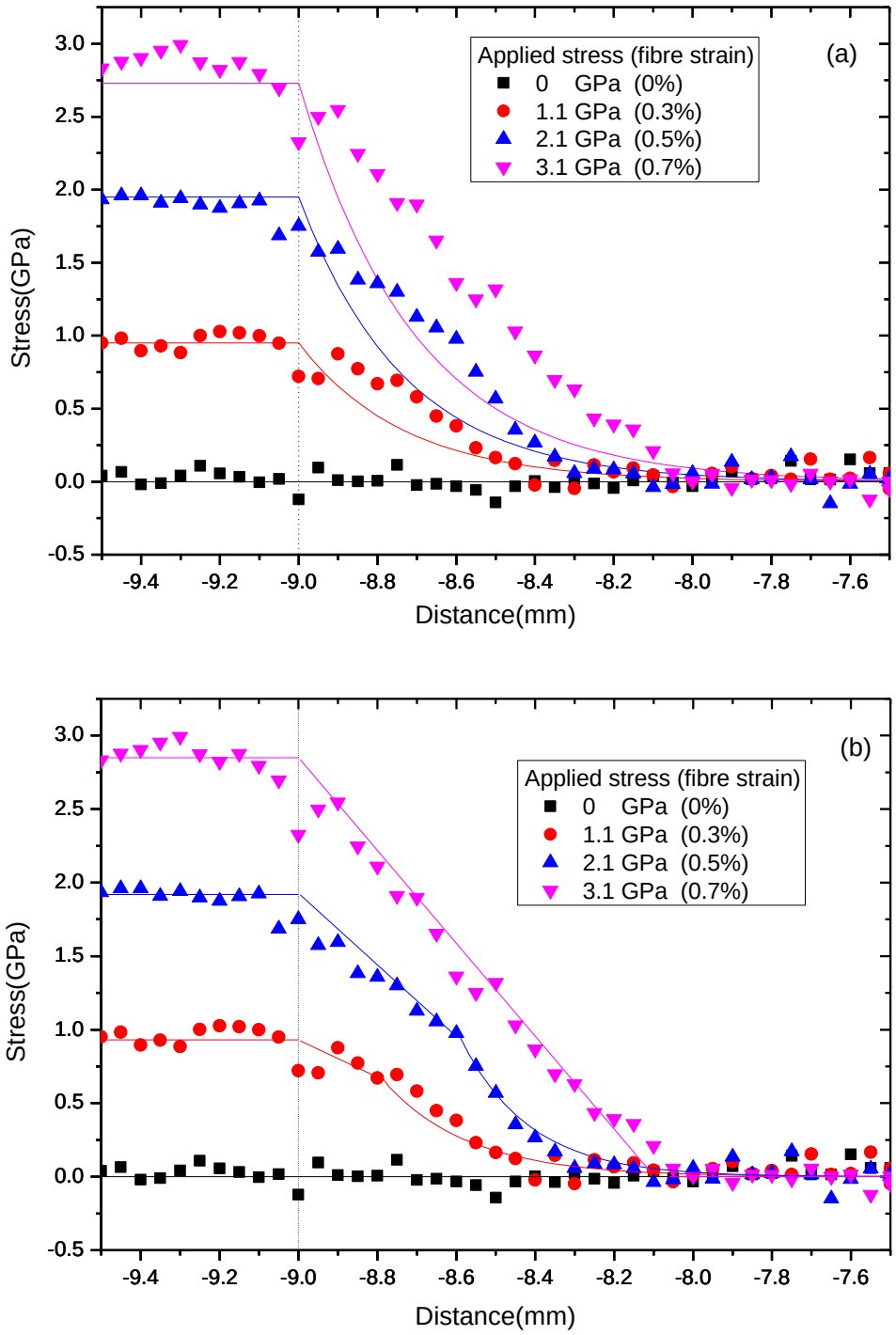

Figure 7.5 *Typical stress profile at the edge of a film model composite; where (a) the data are fitted using Equation 7.1 and (b) they are fitted with a combination of a linear line and Equation 7.1.*

The data in Figure 7.5 are similar in profile to a pull-out test where the fibre stress decreases from the maximum value from where the fibre enters the resin down to zero at a distance of about 1 mm along the fibre inside the epoxy film. It should be noted that

as the epoxy film was not fixed and may move slightly when the sample is deformed during the test. Therefore the vertical bold line at the position of -9 mm cannot be ensured as the edge of the film and is only reported as a reference point. Discontinuous stress distribution data are observed at the point where the fibre enters the epoxy matrix; this has been observed in a previous study of pull-out tests (Patrikis *et al*, 1994). These discontinuities develop during deformation and can be the source of a stress concentration at the edge of the interface due to a sudden change in material properties which will usually results in interfacial failure.

Equation 7.1 was initially used to fit these stress distribution data, however, large quantities of data were in disagreement with the fitted curve, especially for that of higher applied strain levels (see Figure 7.5a). Since Equation 7.1 was based on the assumption that the fibre and matrix is assumed to be elastic and perfectly bonded together (Gu *et al*, 1995), the disagreement between the stress distribution data and the fitted curve means the interface between high modulus carbon fibre and epoxy matrix was not perfectly bonded together and the stresses transfer from fibre to matrix were not fully elastic. Furthermore, debonding could have occurred at the edge region which was about 1±0.05 mm from the edge of the epoxy film. Finally the stress distributions were fitted by a combination of a linear line and Equation 7.1, good agreement was achieved as shown in Figure 7.5b.

Mottershead and Eichhorn (2007) reported the presence of stress concentrations at the edges of this model composite system, however with cellulose fibres rather than carbon. These stress concentrations were thought to be due to the slides compressing the fibre, and were found to depend on the film thickness. In the present study the film thicknesses were in a narrow range of ~200-240 μm, and so the effect of film thickness could not be considered. There could be less of an effect of thickness due to the relatively high transverse stiffness of carbon fibres, although this would have to be studied further. The stiffer the fibre is, the less compliant it will be to any effect of external deformation. For this reason, thermal residual stress from the resin curing procedure will generate far less compression of a fibre of high stiffness than low stiffness.

7.4.2 Interfacial Shear Stress (ISS)

The calculation of the interfacial shear stress for epoxy film model composite was carried out using Equation 7.4. A typical ISS profile for a high modulus carbon fibre and an epoxy film system is shown in Figure 7.6, and it was based on the differentiation of the stress distribution profiles in Figure 7.5(b).

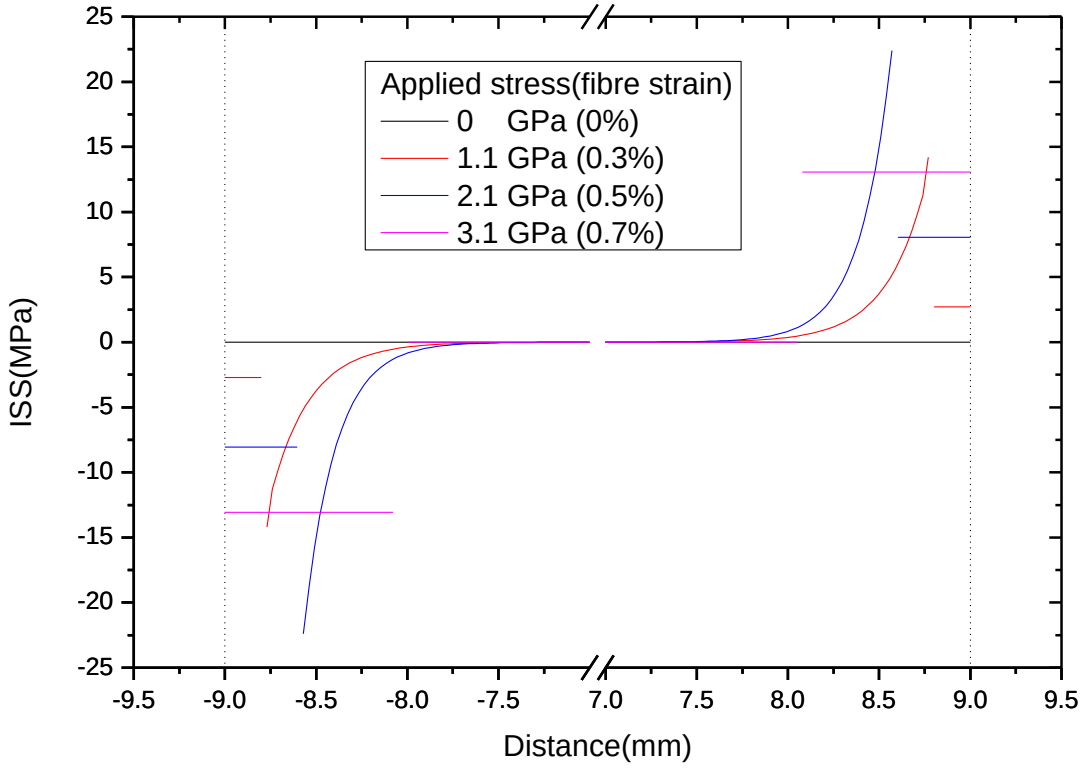

Figure 7.6 *Typical ISS profile for the high modulus carbon fibre and epoxy film model system.*

It can be seen the maximum ISS obtained at the region close to the edge of the epoxy film was around 22.5 ± 0.16 MPa, which is a reasonable value for the epoxy resin and carbon fibre system, and this value is also close to the ISS determined from the microdroplet model system with the area after the region where fibre enters the microdroplet. This is evidence that the true value of ISS for the epoxy microdroplet system was not appeared at the edge of droplet where an excessively high value was obtained. It is obviously that according to the ISS profile the debonding length (where the ISS is stable) was within ~1.0 mm from the edge of the epoxy film and it becomes longer during the increase of strain on the sample. It could be observed from the ISS profile that as higher the strain applied on the sample, the maximum ISS obtained was

more close to the centre of epoxy film. When the applied strain increased to 0.7% the edge region was fully debonded and the debonding length increased to ~0.9 mm, the maximum ISS decreased to 12.7 ± 0.4 MPa (the stable ISS at the debonding region). Finally, as the applied stress increased above 3.1 GPa (0.7% fibre strain) the high modulus carbon fibre fractured outside of the epoxy film.

This test has been repeated five times to investigate whether the variance of the thickness of epoxy film has affected the interface; no such effect was found as described in Section 7.3. The maximum ISS determined for each test are 22.5 ± 0.16MPa, 21.9 ± 0.14MPa, 23.1 ± 0.18MPa, 22.1 ± 0.14 MPa and 19.9 ± 0.17MPa, it can be noted the results are in a small range with low deviation rather than that determined from epoxy microdroplet system. This means the interfacial micromechanical properties determined from the epoxy film model system was more accuracy than that from the epoxy microdroplet model system. Therefore the interfacial properties for low modulus carbon fibre and epoxy have been analysed as well by using this epoxy film model.

7.5 Low Modulus Carbon Fibre with Epoxy Film System

In this section the interfacial behaviour for the low modulus carbon fibre and an epoxy resin film have been investigated. Single walled carbon nanotubes have been coated on the low modulus carbon fibre surface as a strain sensor. The coating of SWNTs was optimised to provide the highest 2D band shift rates obtained from single fibre deformation reported in Chapter 5. Both HiPCO and COOH SWNTs were used in order two analyse the influence of different SWNTs on the interfacial properties. After SWNTs were coated onto the carbon fibres, epoxy film samples were produced by using the process described in Section 7.2. These model composites were deformed under the Raman spectrometer to analyse interfacial properties.

7.5.1 Stress Mapping by Raman Spectroscopy

The scanning procedure using Raman spectroscopy was the same as that for the high modulus carbon fibre and the epoxy film model samples, but the exposure time at each scanning point was reduced to 10 seconds as the signal from the SWNTs was strong enough to obtain a high intensity 2D band. The fibre axis was kept parallel to the

direction of the laser polarisation, which was adjusted to the VV configuration. Since the low modulus carbon fibre has a higher breaking strain than the high modulus sample, strain levels of 0%, 0.3%, 0.6%, 0.9% and 1.2% were possible; the fibres normally fractured at a strain level greater than 1.2%. Figures 7.7a and 7.7b report the position of the Raman 2D band as a function of the distance along the fibre along the interfacial area for the HiPCO SWNTs and COOH SWNTs coated samples respectively.

It can be seen from Figure 7.7 that both HiPCO and COOH SWNTs have been successfully applied to a low modulus carbon fibre to sense the local fibre stress. Both types of SWNTs were thoroughly distributed along the embedded length as the Raman 2D band was observable along the whole interface region.

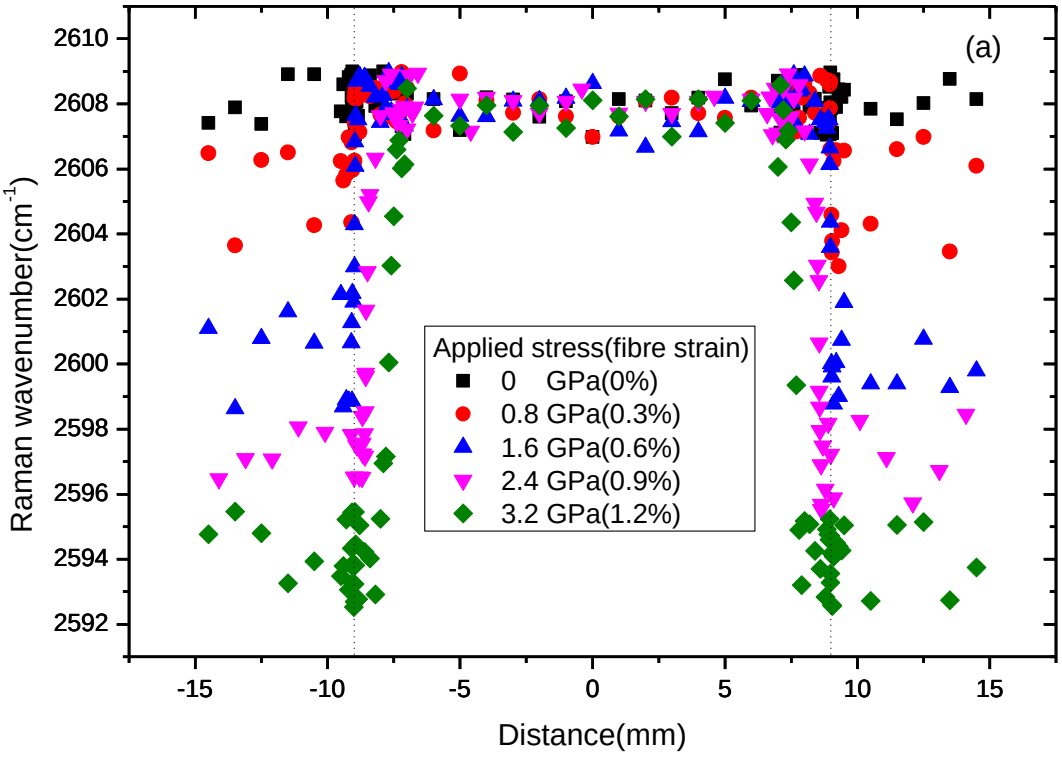

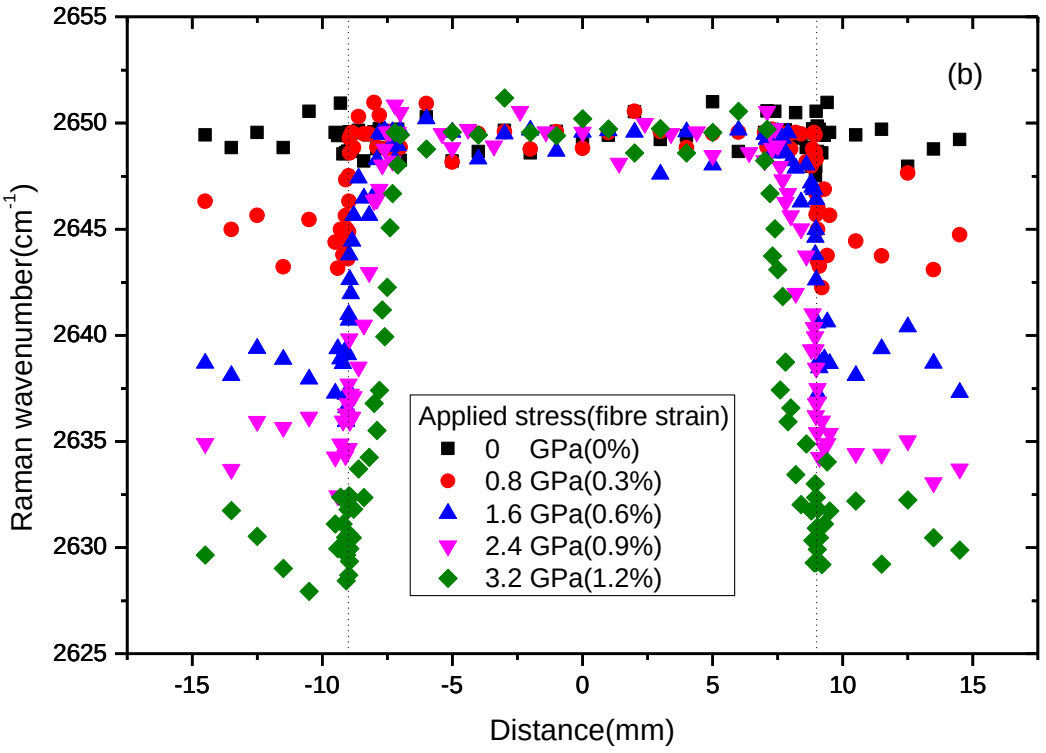

Figure 7.7 *Typical 2D Raman band positions with respect to the distance along a low modulus carbon fibre both inside and outside an epoxy film model composite sensed by coating the fibre with HiPCO SWNTs (a) and COOH SWNTs (b). Vertical dotted lines indicate the edge of the epoxy film.*

Since the intensity of the 2D Raman band is an indication of the concentration of SWNTs this has been plotted for both types of SWNTs along a fibre as shown in Figure 7.8. These data show that the intensities obtained from both HiPCO SWNTs and COOH SWNTs are within narrow ranges of ~10000-10800 and ~725-875 (arbitrary units) respectively. This indicates that the SWNTs are homogenously distributed along the matrix-fibre interface. Lower intensities inside the epoxy film are observed because the Raman scattering intensities have been reduced by the presence of the epoxy film.

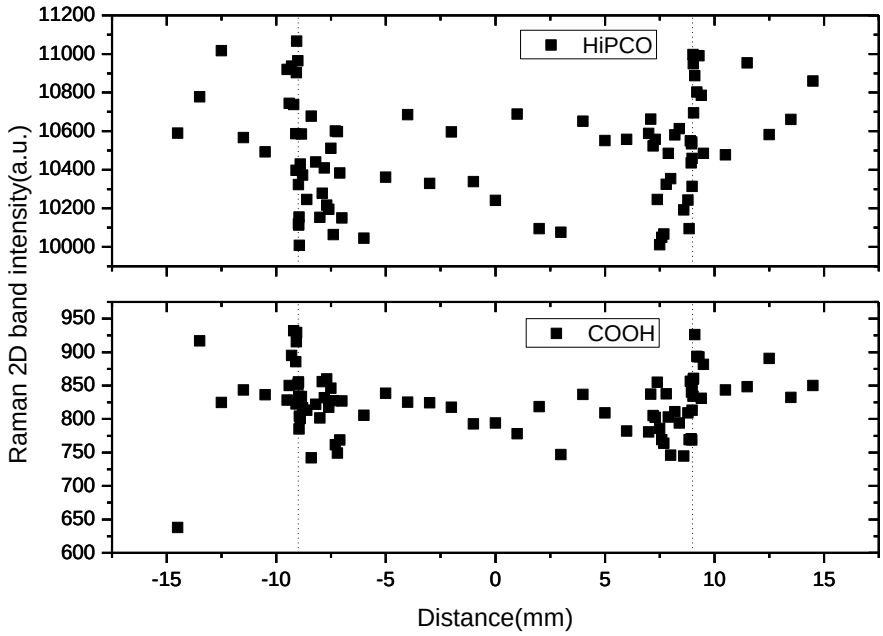

Figure 7.8 *2D Raman band intensity as a function of the distance along the low modulus carbon fibre with inside and outside epoxy film model composite sensed by HiPCO and COOH SWNTs respectively. No external deformation was applied to the sample.*

Raman 2D band positions were converted to local fibre stress by using the calibration from single fibre deformation test results; on samples where HiPCO and COOH SWNTs were coated on the low modulus carbon fibre surface as strain sensors. These stress profiles were then fitted by using the model Equation 7.1. The determined stress profiles are shown in Figure 7.9a and 7.9b, as sensed by HiPCO and COOH SWNTs respectively.

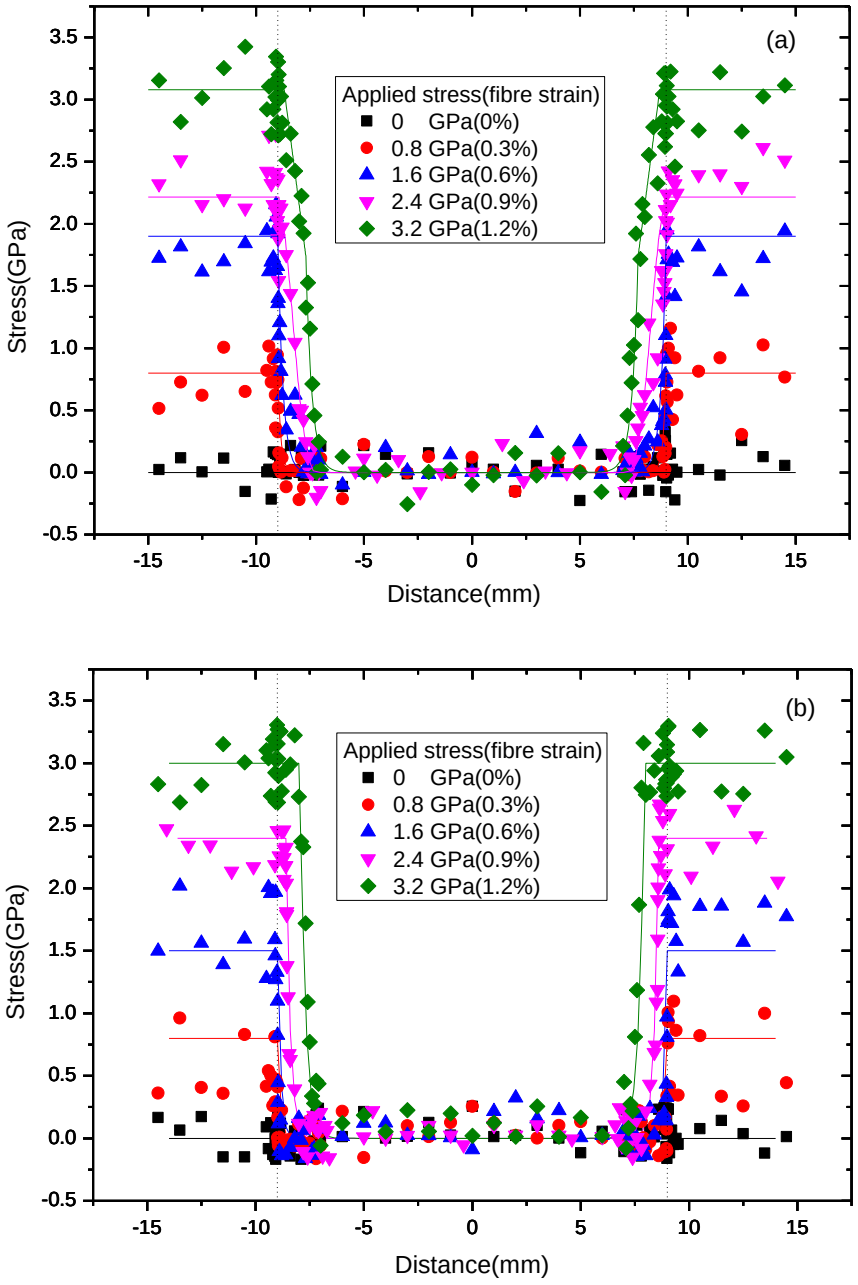

Figure 7.9 *Typical stress profiles for the low modulus carbon fibre and epoxy film model composites with HiPCO SWNTs (a) and COOH SWNTs (b) as strain sensors.*

It can be seen for both stress profiles in low stress levels ($\sigma_{app} < 2.4$ GPa) there is good agreement between the experiment data and the shear-lag model describe by Equation 7.1. Again the stress profile seems like that of two pull out tests (in early stages before fibre was pulled out) which the fibres were being symmetrically pulling out from two sides of epoxy film, however due to the long embedded length and good interfacial bonding between fibre and epoxy matrix, interfacial debonding cannot reach all the embed length and carbon fibre was not able to be pulled out from the epoxy film. The

low modulus carbon fibre remains unstressed at the central region of the epoxy film for different deformation levels of the specimen. On the other hand the stresses change dramatically within the edge regions located at both sides of the epoxy film where fibre enters and exits because stress is transferred from fibre to the resin. Therefore further investigation was carried out and the stress profiles at the edge region have been magnified and displayed in Figure 7.10.

It can be seen when the applied strain $\sigma_{app} \geq 2.4$ GPa, the situation becomes more complicated and the simple shear-lag model becomes inadequate to model the equivalent stress distributions. It is obvious from Figure 7.10 that interfacial failure occurs at the edge region for both samples. The debonding theories proposed by Piggott (1980) propose a constant interfacial shear stress in the debonded zone, which in other words means a linear changing in stress in such a region. So the stress decreases linearly in the deboned region. This was observed for the stress distribution sensed using COOH SWNTs. For samples sensed using HiPCO SWNTs, the stress profiles indicates interfacial failure caused by total interfacial cracking. For this partial debonding model, the stress distribution has been fitted in two distinct zones. In the interfacial cracking or debonding zones, the stress profiles have been fitted linearly; in the totally bonded region, the modified shear-lag Equation 7.5 from Equation 7.3 has been used to fit the stress distribution plots; namely

$$\sigma_f = \sigma_{app} \frac{\cosh[n(x - l_d)/r_f]}{\cosh(nL/r_f)} \qquad (7.5)$$

where l_d is the interfacial debonding or cracking length.

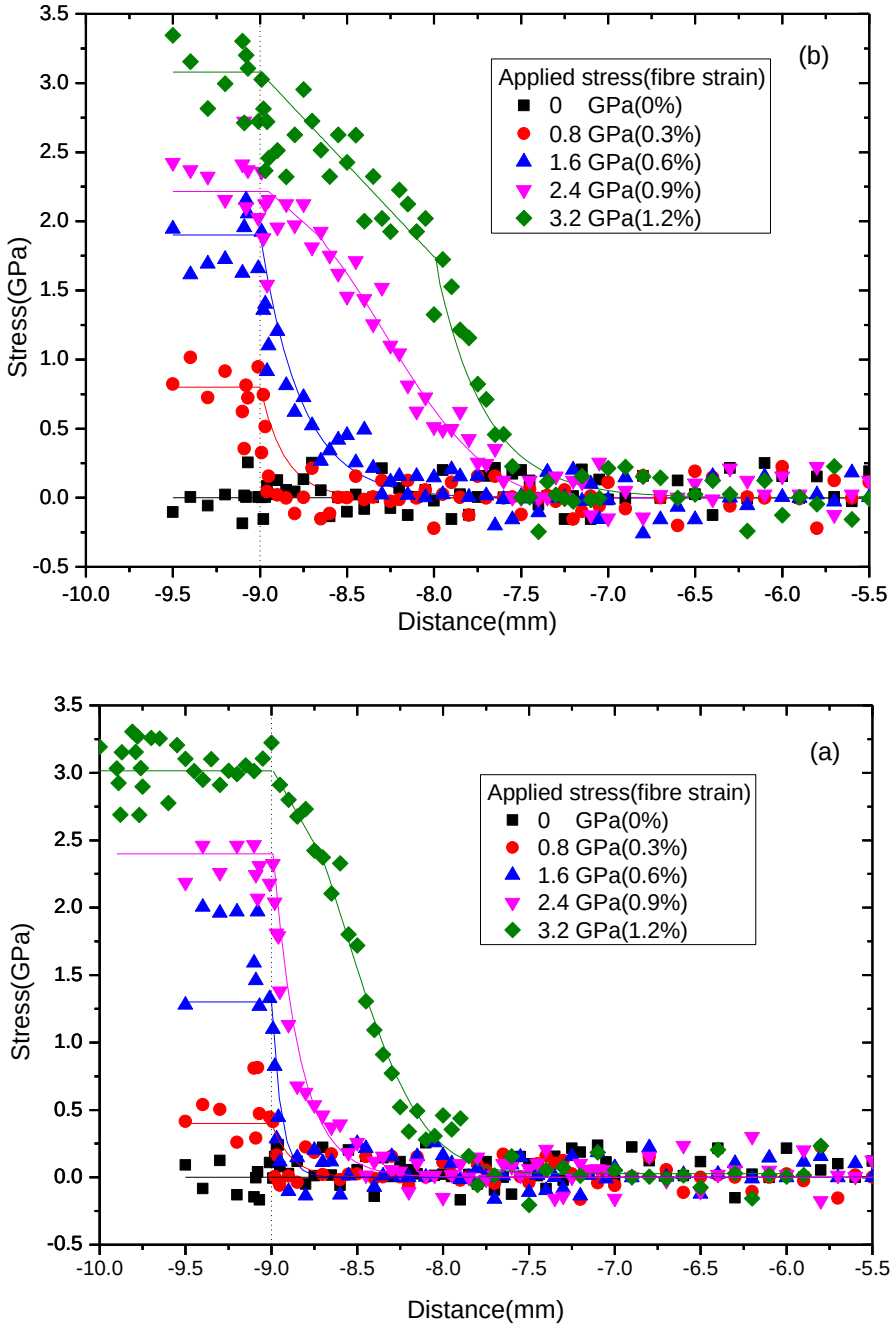

Figure 7.10 *Typical stress profiles at the edge region for the low modulus carbon fibre epoxy film model composite with HiPCO SWNTs (a) and COOH SWNTs (b) as strain sensors.*

It was found that the stress profiles at the edge region were different for the samples sensed using HiPCO SWNTs and COOH SWNTs. For the sample that used HiPCO SWNTs as strain sensors, interfacial failure were determined at the edge area where the fibre local stress were determined decreased linearly from the edge of film to the centre. The debond length of 0.50 ± 0.05mm along the fibre, from the edge of the model

composite, was found when the strain level was increased to 0.9%. This fragment length propagated to 1.25±0.10 mm when the strain was increased to 1.2%. However for the samples that sensed by the COOH SWNTs, the stress distribution shows that the interface is remain intact with elastic deformation model at the edge region when applied strain level increased to 0.9%. It shows linearization at the edge region when the applied stress levels were increased to 1.2%. The debonded zone was observed with lengths of 0.62 ±0.10 mm for strain level of 1.2%.

It should be noted that when compared with the stress profile of the epoxy film model system with high modulus carbon fibres, both stress profiles of low modulus carbon fibres system sensed by HiPCO SWNTs and COOH SWNTs were not observed discontinuous at the verge of the epoxy film, for this reason the discontinuity can be attributed to the unique of each sample. This is in agreement with the report by Patrikis *et al.* (1994) for the single fibre pull out test of aramid fibres. Furthermore, it should be emphasised that due to the elongation properties of carbon fibres itself, high modulus carbon fibre will be normally fractured outside of the epoxy film when the applied stress was around 0.8%. So the exterior strain levels applied on the epoxy film model system with high modulus carbon fibre specimens were not as high as that for the low modulus carbon fibre system specimens, this could be the main reason that there was no such interfacial failure behaviour as that for low modus carbon fibre system samples been observed for the high modulus carbon fibre and epoxy film model samples.

7.5.2 Interfacial Shear Stress (ISS)

The ISS distributions along the low modulus carbon fibre inside the epoxy film have been determined by using the force balance approach and Equation 7.4. These data for a low modulus carbon fibre coated using HiPCO SWNTs and COOH SWNTs are shown in Figure 7.11a and 7.11b respectively. The similarities and differences between the two systems sensed by these two types of SWNTs as are now summarised:

Similarity:

1. When the applied strain $\varepsilon_{app} \leq 0.6\%$, there were mainly elastic stress transfer at the interface for epoxy model system sensed by both types of SWNTs. In this

case, rapid decrease of stress from the point where fibre enters the matrix and this resulted in a high ISS at the edge of epoxy film were determined. Additionally, the maximum ISS increase as the increasing of applied strain levels.

2. When the exterior applied strain level was 0.6%, the epoxy film model system sensed by both types of SWNTs show considerably higher interfacial shear stresses with the values very close to the maximum ISS determined for both systems. This could be due to the stress concentration on the edge region where fibre enters epoxy film. Since no obvious debonding was observed at this strain level, plus interfacial failure started to occur from the point where fibre enters epoxy film for both systems when $\sigma_{app} > 0.6\%$, it is easily to understand why comparatively high interfacial shear stresses were generated for both systems. This is in agreement with the debonding theory that the highest interfacial shear stresses were usually created in prior of debonding (Li and Grubb, 1994).
3. Due to the long embedded length, the central region of the epoxy film for both type of samples were remain not affected by the exterior applied strain.
4. Interfacial debonding occurred for the epoxy film model system sensed by both types of SWNTs when the applied strain level reached 1.2%.

Difference:

1. The maximum ISS observed from the samples sensed by COOH SWNTs was 51.1 ± 0.18MPa, which is comparatively higher than that of 39.8 ± 0.12 MPa observed from samples sensed by HiPCO SWNTs.
2. The ISS distributions were more complicated for epoxy film model system sensed by both types of SWNTs when the applied strain $\varepsilon_{app} > 0.6\%$. For the epoxy film model system sensed by HiPCO SWNTs, the interfacial shear stresses remains constant at the distance of 0.5 ± 0.05mm and 1.25 ± 0.10mm to the edge of epoxy film when the applied strain levels were 0.9% and 1.2% respectively. This is caused by the interfacial debonding and it propagated during the increase of applied strain level. After the interfacial cracking region, the interface between the low modulus carbon fibre and epoxy film matrix was remain intact and the maximum ISS decreased with the value of 14.3 ± 0.31MPa at applied strain level of 0.9%. When the applied strain level increased to 1.2%,

the length of interfacial cracking increased from the edge and ISS distribution curves becomes broader but the determined maximum ISS increased with the value of 39.4±0.19 MPa. This mean after the debonding region the interface between the low modulus carbon fibre and epoxy matrix was remain intact and the stress turned out to be highly concentrated at the border area. For the epoxy film model system sensed by COOH SWNTs, when ε_{app}= 0.9%, the interfacial shear stresses reached its maximum value of 51.1±0.18MPa When the applied strain ε_{app} = 1.2%, it can be observed ISS was constant with the value of 21.7±0.21 MPa with the small length of 0.62 ± 0.10 mm from the edge of epoxy film caused by interfacial debonding at the edge area.

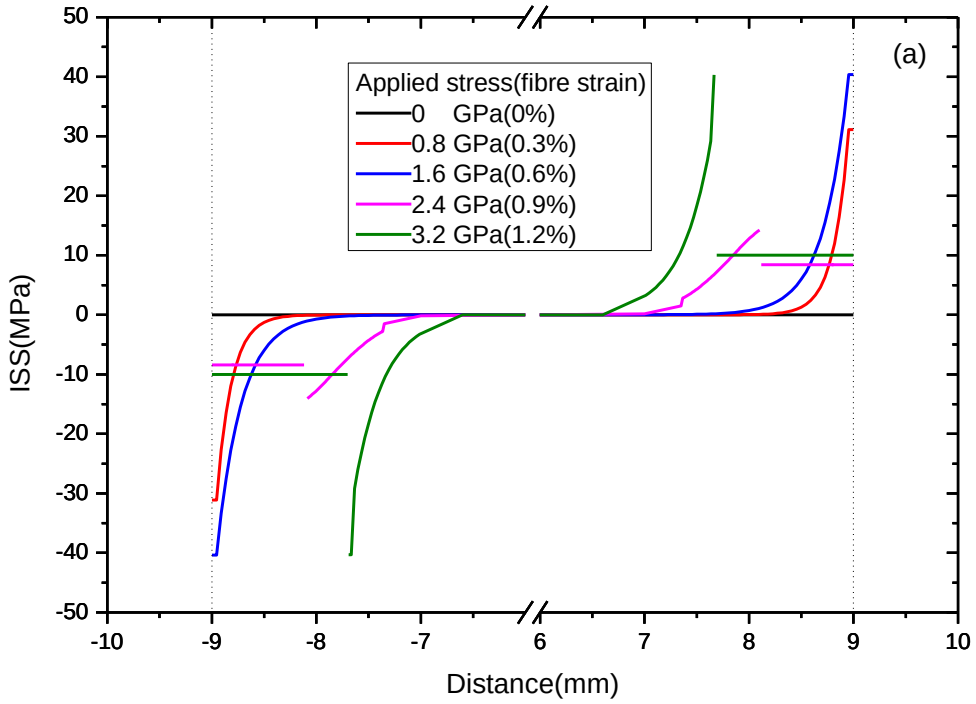

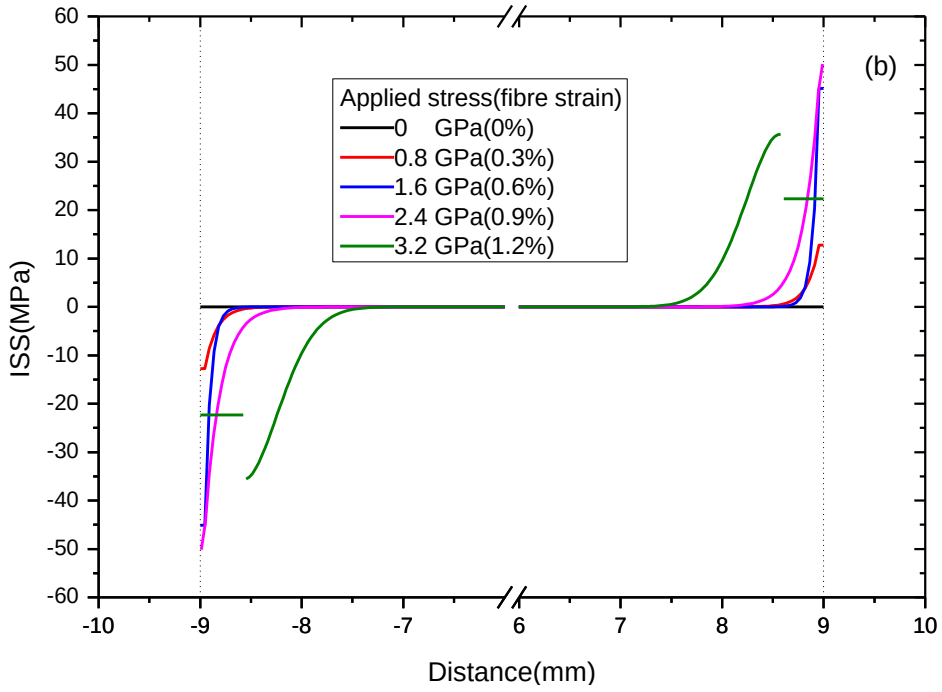

Figure 7.11 *Typical ISS profile for the low modulus carbon fibre epoxy film model system with HiPCO SWNTs (a) and COOH SWNTs (b) as strain sensors.*

The maximum interfacial shear stresses for both types of SWNTs sensed system regard each strain level applied on the system are shown in Figure 7.12. It can be seen that for both system the determined maximum ISS were in the range of 40~55MPa, which was very close to the epoxy matrix yield stress (Mottershead and Eichhorn, 2007). More importantly, after that maximum ISS observed for both systems, the maximum ISS obtained from next higher strain level decreased, this is a strong evidence that matrix yield could possibly occurred at the place where the previous maximum ISS obtained.

Finally it can be concluded that the changes of interfacial properties during the increase of strain levels applied on the epoxy film model system with low modulus carbon fibre are in the following steps:

1. Elastic stress transfer at interface in the edge region of epoxy film ($\varepsilon_{app} \leq$ 0.6%).
2. Interfacial debonding occurred. This happened at the edge region when $\varepsilon_{app} \geq$ 0.9% for the system sensed by HiPCO SWNTs and when $\varepsilon_{app} = 1.2\%$ for the system sensed by COOH SWNTs.

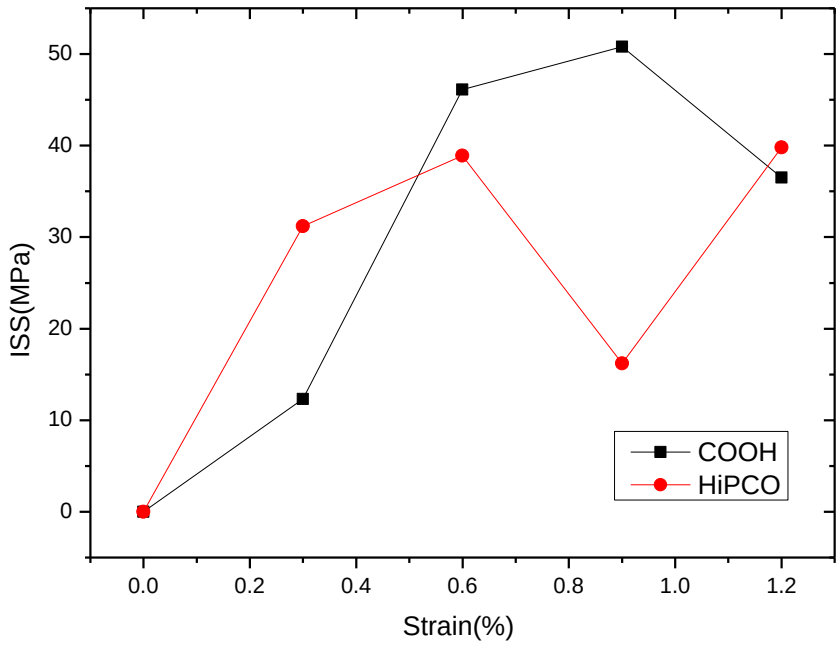

Figure 7.12 *The variation of determined maximum ISS at different strain levels for the epoxy film model system sample sensed by HiPCO and COOH SWNTs.*

It should be noted that the low point discovered for the samples coated with HiPCO SWNTs is caused by matrix fracture which occurred at the edge area of this sample. Since this is not found for the sample systems sensed by using COOH SWNTs, it could presume that COOH SWNTs have better reinforcement to epoxy matrix than that using HiPCO SWNTs. Further study on the reinforcement of SWNTs on epoxy matrix was carried out and will be explained in section 8.5.1.3.

Moreover, inelastic deformation may have happened for both microcomposite systems, however it have not been detected due to the setting of applied strain levels. As inelastic deformation usually happened before interfacial debonding taken place, for the sample system sensed by HiPCO SWNTs inelastic deformation may occurred when $0.6\% < \varepsilon_{app} < 0.9\%$, and for the sample system sensed by COOH SWNTs it could possibly occurred when $0.9\% < \varepsilon_{app} < 1.2\%$.

7.6 High Modulus Carbon Fibre and Epoxy Film System with SWNTs as Strain Sensor

In order to analyse the effects of SWNTs on the interfacial properties between carbon fibre and epoxy resin, SWNTs have also been coated on the high modulus carbon fibre and the interfacial shear stress for the high modulus carbon fibre and epoxy film model system with both HiPCO and COOH SWNTs as strain sensors have been investigated. The determined interfacial properties for this system will be compared with the interfacial properties of high modulus carbon fibre and epoxy film model system without SWNTs which has been described in Section 7.4.

7.6.1 Stress Mapping by Raman Spectroscopy

The coating of SWNTs on high modulus carbon fibre was in exactly the same process as that for the low modulus carbon fibre. However, the samples were more difficult to prepare as the high modulus carbon fibre is stiffer and more fragile, and it was easier to break during the sample preparation. The Raman scanning process was also the same as that for the epoxy film model system with low modulus carbon fibre but the applied strain level on the samples were 0%, 0.3%, 0.5% and 0.7%. The determined Raman 2D band frequencies form both types of SWNTs across the interface were shown in Figure 7.13.

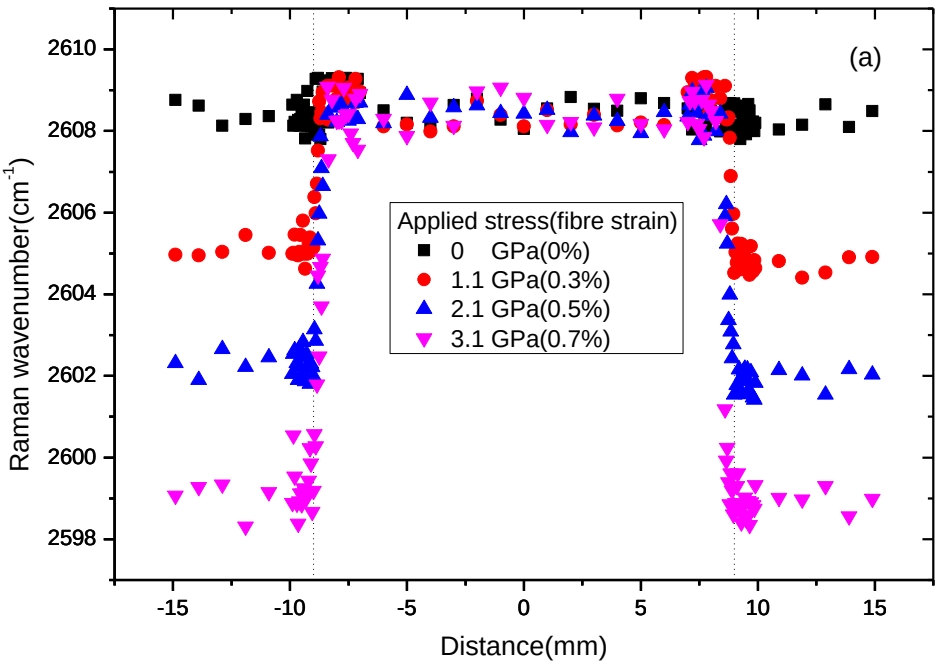

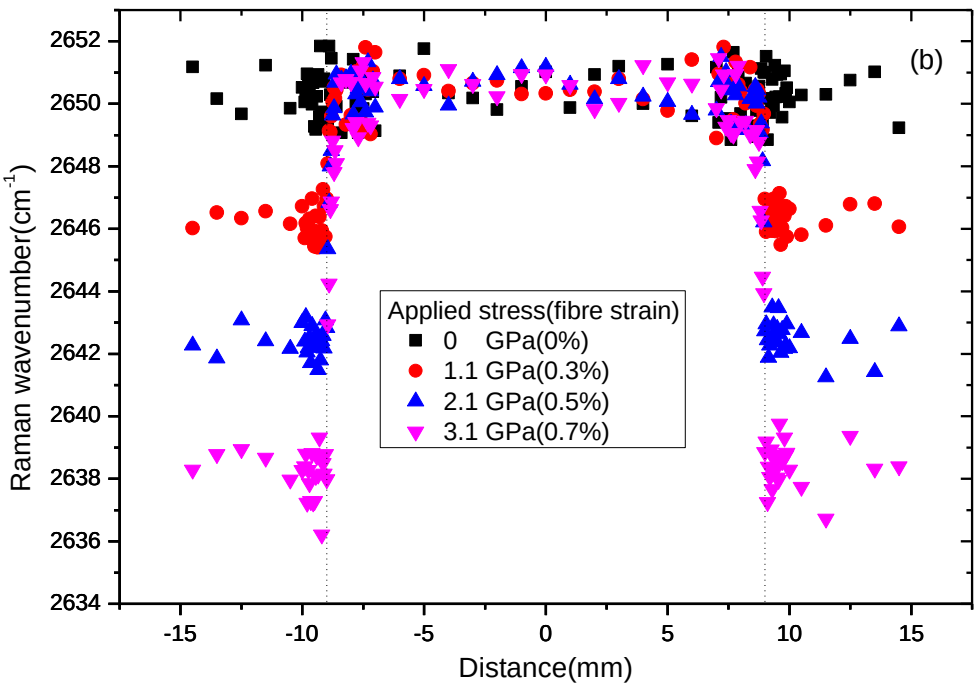

Figure 7.13 *Typical Raman 2D band frequencies related to the distance along the high modulus carbon fibre with inside and outside the epoxy film model composite sensed by HiPCO SWNTs (a) and COOH SWNTs (b).*

It can be seen the determined 2D band frequencies across the interface for the samples sensed by both types of SWNTs were clearly following the changes of strain levels applied on the sample and in small stable range of deviation. This means the SWNTs have been dispersed homogeneously and the local fibre strains were well sensed by both types of SWNTs.

The 2D band frequencies were then converted to the local fibre stress by using the calibration determined through single fibre deformation test as described in Chapter 5, and the converted stress profiles were shown in Figure 14(a) and (b) for that sensed by HiPCO and COOH SWNTs respectively.

There is no doubt that the whole stress profiles displayed in Figure 7.14 were in similar shape as that for the epoxy film model for the low modulus carbon fibre or high modulus carbon fibre system without SWNTs, the dramatically change of stresses on the fibre were happened at the edge of epoxy film and fibre at the middle region of epoxy film were non-stretched.

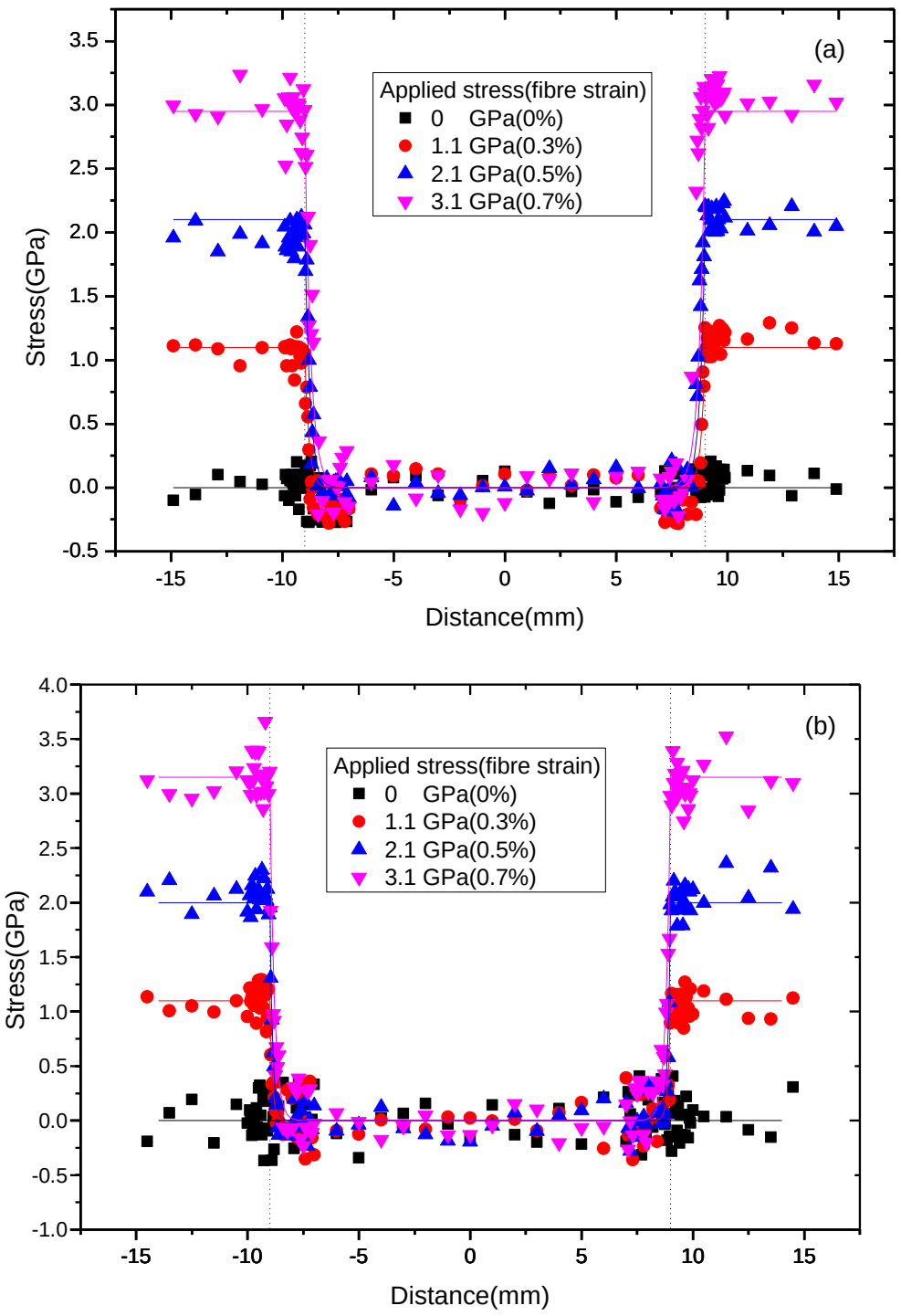

Figure 7.14 *Typical stress profiles for the high modulus carbon fibre and epoxy film model composites with HiPCO SWNTs (a) and COOH SWNTs (b) as strain sensors.*

Due to the overlay of large quantities of data obtained across the interface for all the applied strain levels, the most important change of stresses and fitted curves at the edge region were not shown distinctly. Furthermore, as stresses were symmetrically

distributed at both of the edge regions, one edge region has been magnified and analysed in Figure 7.15.

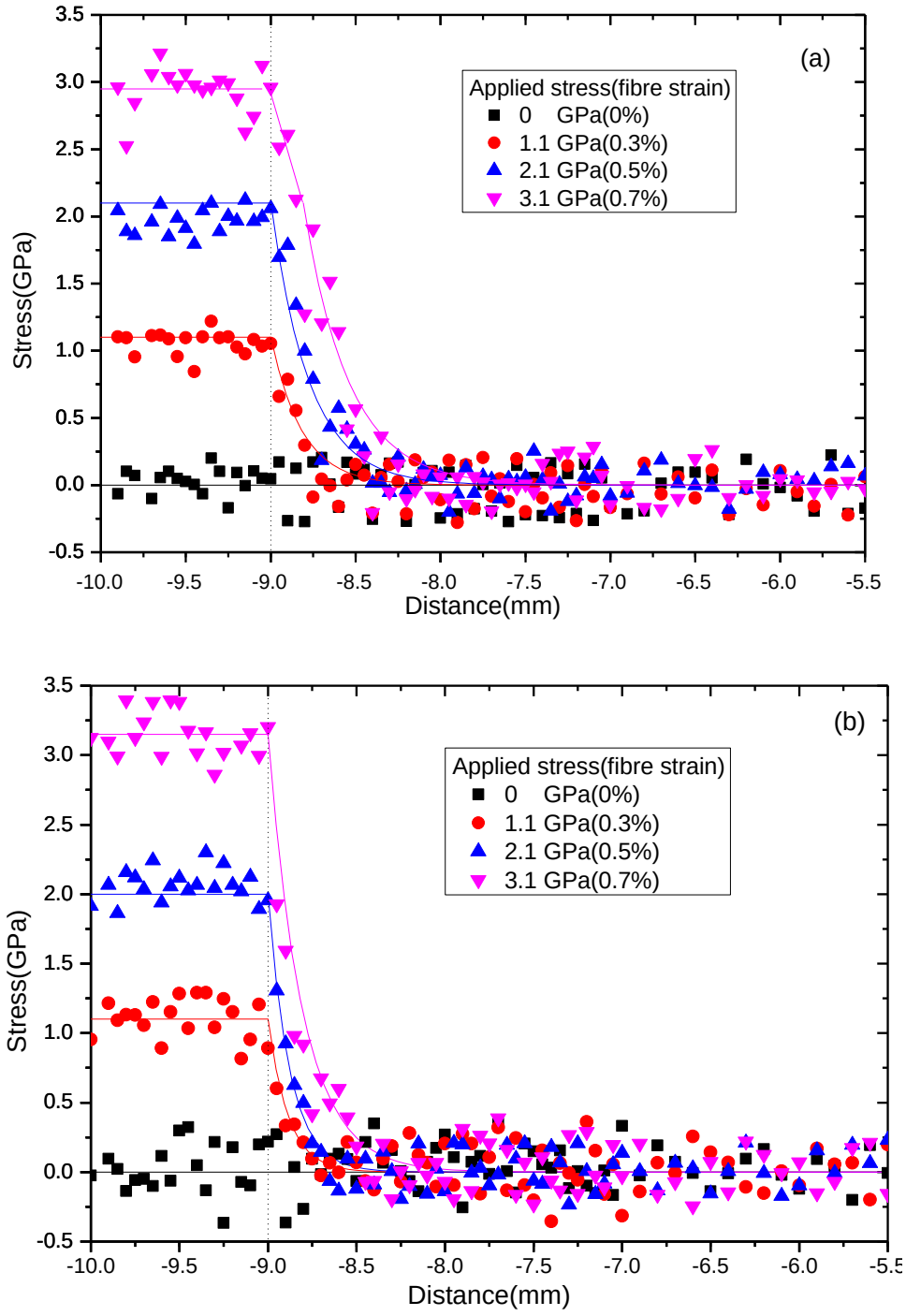

Figure 7.15 *Typical stress profiles at the edge region for the low modulus carbon fibre epoxy film model composite with HiPCO SWNTs (a) and COOH SWNTs (b) as strain sensors.*

It was found for the systems sensed by both types of SWNTs, the interfaces were perfectly bonded together and the stress distribution data were well fitted by the elastic shear-lag model of Equation 7.1 which was proposed by Chua and Piggott (1985). This was of significant difference with the epoxy film model system with high modulus carbon fibre without SWNTs, which debonding has occurred and the stress distributions were failed to be fitted by using Equation 7.1.

When the interfacial properties were analysed by means of tress transfer length, it can be seen that the stress transfer length for the system sensed by HiPCO SWNTs (see Figure 7.15(a)) was very close to that system without SWNTs sensors (see Figure 7.5). However, according to Figure 7.15(b), the system sensed by COOH SWNTs has greatly reduced the stress transfer length. It can also be seen that at the applied strain level of 0.7%, the system sensed by HiPCO SWNTs shows a minor interface debonding occurred within a short distance of 0.2 ± 0.05 from the edge of epoxy film, this was not found in the systems sensed by COOH SWNTs.

The whole information suggested that the existence of SWNTs have improved the interfacial bonding between the fibre and epoxy, and the interfaces sensed by COOH SWNTs have even better improvement. This could be due to the carboxylic group grafted on each SWNT which could react with epoxy matrix and the sizing agent on carbon fibre surface.

7.6.2 Interfacial Shear Stress (ISS)

The interfacial shear stresses were then calculated for both systems based on the differentiation of the fitted stress distribution profiles, as the ISS profiles were shown in Figure 7.16. It can be seen the maximum ISS determined for the epoxy film model system sensed by HiPCO and COOH SWNTs were 30.7 ± 0.09MPa and 38.4 ± 0.07 MPa. Both of them are higher than the maximum ISS obtained from the system without SWNTs which was 24.3 ±0.11MPa. As have mentioned previously the coated SWNTs on the carbon fibre surface could have strengthened the interface. Obviously for both systems the highest ISS of all applied strain levels were obtained at the edge region of the epoxy film. For the system sensed by COOH SWWNTs, the interface was perfectly bonded and it remain elastic even when the gradually increased applied strain reached the highest level of 0.7% and after that the high modulus carbon fibre fractured outside of the epoxy film. For the system sensed by HiPCO SWNTs, when the applied strain

increased to 0.7%, interface debonding occurred and ISS dropped to 23.2 ± 0.12 MPa from the maximum value at the edge region. As the maximum interfacial shear stresses for both systems were below 40 MPa, epoxy matrix yielding was not supposed to occur here (Mottershead and Eichhorn, 2007).

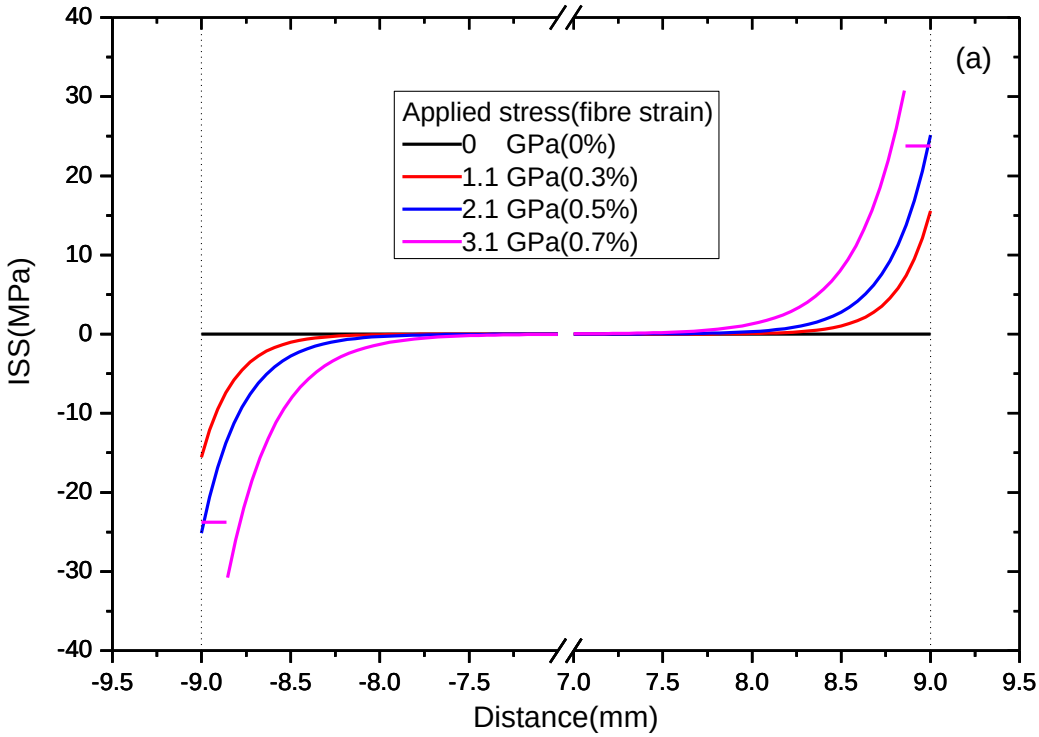

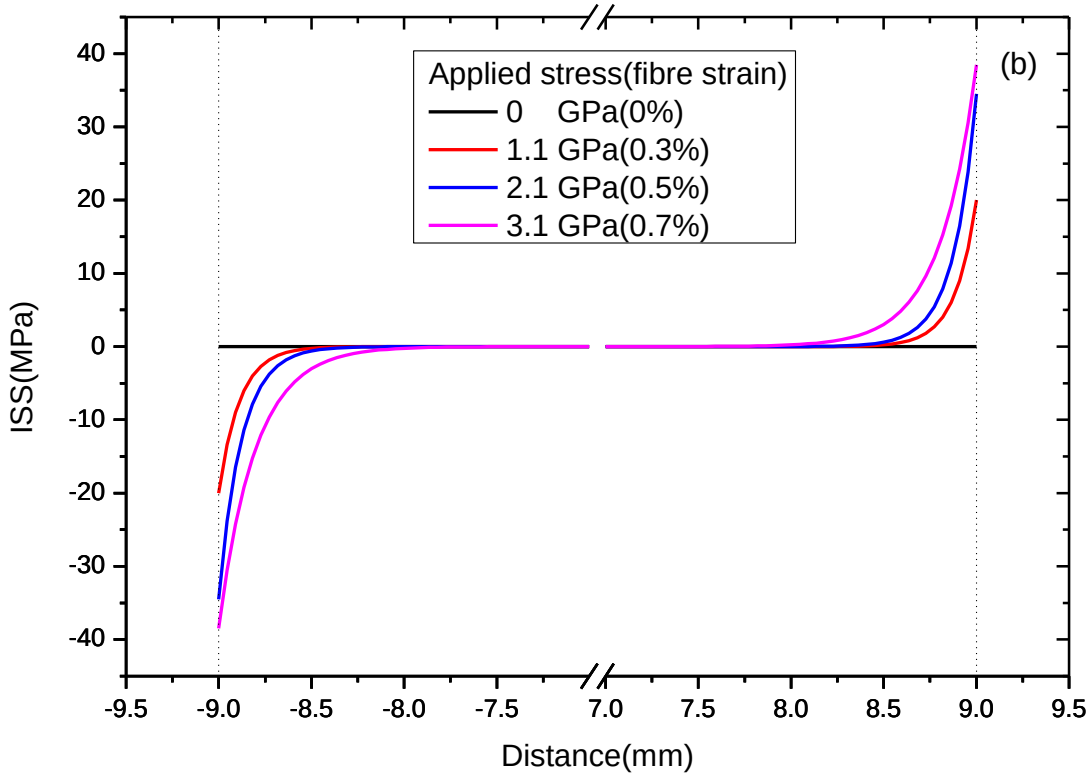

Figure 7.16 *Typical ISS profiles for the high modulus carbon fibre epoxy film model system with HiPCO SWNTs (a) and COOH SWNTs (b) as strain sensors.*

7.7 Reasons why SWNTs have Improved the Interface

Since the existence of SWNTs on the surface of carbon fibre improved the interfacial properties have been determined in the previous study, in this section the reasons for this have been investigated.

The studies carried out by Puglia *et al*. (2003) have analysed the cure reaction of SWNTs and epoxy resin by the way of thermal analysis and Raman spectroscopy, it was found that the SWNTs act as a strong catalyst on the cure reaction of a diglycidyl ether of bisphenol A based epoxy resin. In this project, the applied epoxy resin of LY5052 and hardener HY5052 system contains a high concentration of butanediol diglycidyl ether (Yusoff *et al*, 2007). Furthermore, both the high modulus and low modulus carbon fibre used in this study were sized with the agent including bisphenol A by their manufacturer (Toray industry inc., 2011). Therefore, it can draw a conclusion that the coated SWNTs on the carbon fibre surface have improved the interface in the way of helping the chemical bonding between epoxy resin and carbon fibre.

For the COOH SWNTs among the interfaces, the studies by Zhu *et al*. (2004) suggested that strong covalent interfacial bonding were formed as that the COOH SWNTs have involved in the reaction at the fibre/matrix interface. A typical integration of COOH SWNTs into the covalent bonding is shown in Figure 7.17.

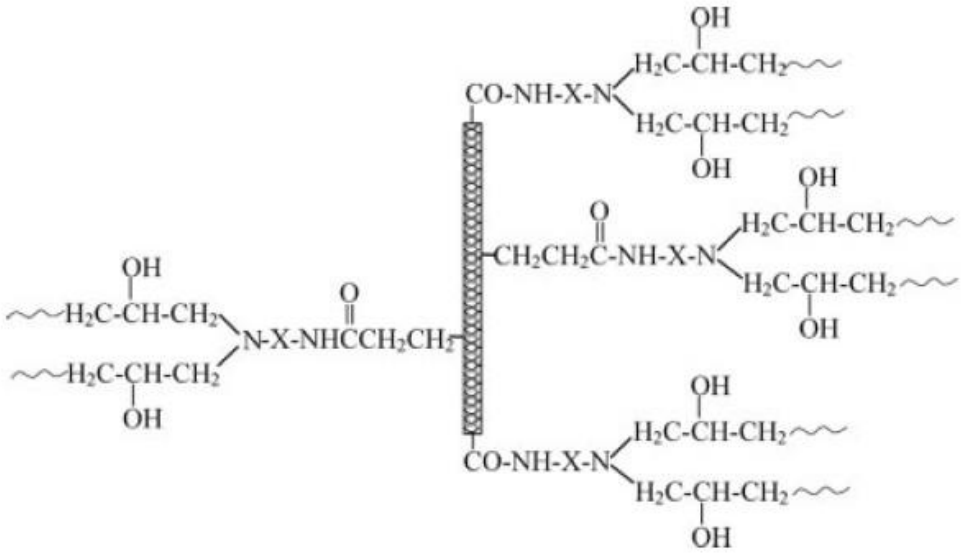

Figure 7.17 *Typical integration of COOH SWNTs into the covalent interfacial bonding at the fibre/matrix interface (Zhu et al. 2004).*

In this study, the carboxylic group from COOH SWNTs could have involved in the chemical reaction with the amino group from silane or epoxy (Isophorone diamine and cyclohexylamine), the hydroxy group from carbon fibre (Bisphenol A) and epoxy in the interface. Therefore, it can well understand that the epoxy film model system sensed by COOH SWNTs have the best interfacial bonding and better than of the system sensed by HiPCO SWNTs.

7.8 Conclusion

In this chapter, the determined maximum ISS for the epoxy film model system with both high modulus and low modulus carbon fibre, the system with and without SWNTs and with both HiPCO and COOH SWNTs were shown in Table 7.1. For the epoxy film model with low modulus carbon fibre, the systems sensed by both types of SWNTs were found interfacial debonding occurred at the edge region when the applied strains were above 0.9% and SWNTs have been proved to be great tool to provide the strain sensitive 2D Raman band and characterise the interface. However, the applied strain level can only reach the maximum level of 0.7% for the epoxy film model of high modulus carbon fibre systems; this could be a very important reason that such interfacial debonding performance of corresponding applied strain level of 0.9% and 1.2% for the low modulus carbon fibre system cannot be found for the high modulus carbon fibre systems.

Table 7.1 *The determined maximum ISS for each epoxy film model system.*

Epoxy film model system		Maximum ISS (MPa)
High modulus carbon fibre	Without SWNTs	22.5 ±0.16
	With HiPCO SWNTs	30.7±0.09
	With COOH SWNTs	38.4±0.07
Low modulus carbon fibre	With HiPCO SWNTs	39.8±0.12
	With COOH SWNTs	51.1±0.18

For the epoxy film model with high modulus carbon fibre, the system without SWNTs was found interfacial debonding occurred at the edge region even when the applied strain was as low as 0.3%. However, the added of SWNTs on the high modulus carbon fibre surface has notably improved the interface, especially for that of COOH SWNTs.

The reasons that SWNTs improve the interface have been investigated and the SWNTs at the interface between carbon fibre and epoxy resin could act as a strong catalyst

(Puglia *et al*, 2002), which will significantly benefit for the chemical bonding between epoxy resin and the bisphenol A sized carbon fibre(Toray industry inc., 2011). The carboxylic group grown on the COOH SWNTs could involve into the chemical reaction in the interfacial area and improve the interfacial bonding even better.

7.9 References

Bannister, D.J., Andrews, M.C., Cervenka, A.J. and Young, R.J. (1995) Analysis of the single-fibre pull-out test by means of Raman spectroscopy: Part 2: Micromechanics of deformation for an aramid/epoxy system. *Composite Science and Technology*, 53, pp. 411-421.

Chua, P.S. and Piggott, M.R. (1985) The glass fibre-polymer interface: 1-Theoretical consideration for single fibre pull-out tests. *Composite Science and Technology*, 22, pp. 33-42.

Gu, X.H., Young, R.J. and Day, R.J.(1995) Deformation micromechanics in model carbon fibre-reinforced composites Part 1 the single-fibre pull-out test. *Journal of Materials Science*, 30, pp. 1409-1419.

Li, Z.F. and Grubb, T. (1994) Single fibre polymer composites. Part 1: Interfacial shear strength and stress distribution in the pull-out test. *Journal of Material Science*, 29, pp.189-202.

Mottershead, B. and Eichhorn, S.J. (2007) Deformation micromechanics of model regenerated cellulose fibre-epoxy/polyester composites. *Composites Science and Technology*, 67, pp. 2150-2159.

Patrikis, A.K., Andrews, M.C. and Young, R.J. (1994) Analysis of the single-fibre pull-out test by the use of Raman spectroscopy. Part 1: pull-out of aramid fibres from an epoxy resin. *Composite Science and Technology*, 52, pp. 387-396.

Piggott, M.R. (1980) *Load Bearing Fibre Composites*. Pergamon Press. Oxford. UK, pp. 83-89.

Puglia, D., Valentini, L. and Kenny, J.M. (2002) Analysis of the cure reaction of carbon nanotubes/epoxy resin composites through thermal analysis and Raman spectroscopy. *Journal of Applied Polymer Science*, 88, pp. 452-458.

Puglia, D., Valentini, L., Armentano, I. and Kenny, J.M. (2003) Effects of single-walled carbon nanotue incorporation on the cure reaction of epoxy resin and its detection by Raman spectroscopy. *Diamond and Related Materials*, 12, pp. 827-832.

Toray Industry Inc. (2012) Translation form fibre to composites. [online] Available at: http://www.torayca.com/en/techref/index.html [Accessed 10 April 2011].

Yusoff, Y., Aroua, M.K., Nesbitt, A. and Day, R.J. (2007) Curing of polymeric composites using microwave resin transfer moulding (RTM). *Journal of Engineering Science and Technology*, 2(2), pp. 151-163.

Zhu, J., Peng, H. Macias, F.R., Margrave, J.L., Khabashesku, V.N., Iman, A.M., Lozano, K. and Barrera, E. (2004) Reinforcing epoxy polymer composites through covalent integration of functionalized nanotubes. *Advanced Functional Materials*, 14(7), pp. 643-648.

CHAPTER 8 Fragmentation

8.1 Introduction

In the previous two Chapters, the interface between a carbon fibre and an epoxy resin matrix has been analysed in microdroplet and film geometries. The micromechanical tests for both model systems are based on the performance of load transfer from the carbon fibre to the epoxy resin matrix. However, for real industrial composites, the load is normally transferred from the matrix to the fibre. The fragmentation test can fulfil this load transfer condition and also helps to confirm the interfacial properties of the systems investigated. Over the past two decades conventional fragmentation tests combining carbon fibres and epoxy resin matrix systems have been studied extensively (Netravali *et al*, 1989; Herrera-Franco and Drzal, 1991). It has been found to be the most appropriate micromechanical test for carbon fibre composite systems due to the severe brittleness (Huang and Young, 1994). Raman spectroscopy has been used to analyse stress transfer from an epoxy resin matrix to a high modulus carbon fibre in a fragmentation test by Huang and Young (1994). It was demonstrated that the Raman spectroscopy approach can provide much more detail than the conventional fragmentation test. However, for low modulus carbon fibres, due to reduced Raman band position sensitivity to stress and the weak and broad Raman bands obtained for these fibres (see Figure 4.10) there is no report of such a system undergoing fragmentation. Highly strain sensitive SWNTs have been coated on the low modulus carbon fibres to act as sensors. High modulus carbon fibre and epoxy resin with and without the presences of SWNTs were also investigated in order to compare the results. The conventional fragmentation test for each type of sample was also carried out and the determined interfacial shear stresses were compared to that using the Raman technique.

8.2 Experimental Methodology and Sample Preparation

The conventional fragmentation test is an experimental procedure which involves fully embedding a single fibre along the centreline of a comparatively large dumbbell shaped specimen of matrix material. Load is then applied to deform the specimen at incremental strain levels uniaxially along the fibre axis. It should be noted that the matrix material should have a higher failure strain than the fibre. The fibre is then found to break at frequent intervals along its length with increasing strain. After numerous breaks then at some point, the fibre fragments become too short that the stress transfer along the fragment lengths can no longer accumulate enough tensile stress to trigger any further failures with an increase in deformation of the composites. The test is then finished and the composites are analysed using optical microscopy to determine the fragment lengths (Netravali *et al*, 1989). For the fragmentation test carried out by using Raman spectroscopy, the laser is applied to scan point-to-point along the fibre embedded in the matrix at each applied strain level and a detailed variation of fibre strain can be determined (Huang and Young, 1994).

The interfacial shear stress can be determined from a force balance micromechanical model (Kelly and Tyson, 1965) as given by the equation

$$\tau = \frac{\sigma_{\text{fra}} r}{l_{\text{c}}} \qquad 8.1$$

where σ_{fra} is the fibre fracture stress which is taken as a constant and in this study was determined in the single fibre tensile test. r is the diameter of the fibre and l_{c} is the critical fragment length. Equation 8.1 is based on the ideal micromechanical model that the matrix is a rigid-perfectly elastic material, the stresses on the fibre fragments build up linearly from zero at either end of the fragment to the applied stress, so the interfacial shear stress is constant along the fragment and is the same for each fragment.

When the applied stress σ_{app} approaches the fracture stress σ_{fra}, the fibre will break instantaneously into shorter and shorter pieces until the remaining fragments are not long enough for the linear stress build up from either end to exceed σ_{fra} anywhere along the fibre lengths. The critical length l_{c} is defined as the length of fibre where the stress build up from the two ends yields a stress exactly equal to σ_{fra} at its centre. Therefore, any fragment having a length marginally exceeding l_{c} will break in two yielding, at the

conclusion of a fragmentation test, fragment lengths which are randomly distributed between $l_c/2$ and l_c.Correspondingly the peak stress in these fibre fragments varies from a minimum value of $\sigma_{fra}/2$ to a maximum of σ_{fra} yielding a mean peak stress which is somewhat less than the fibre fracture stress σ_{fra}.

A typical ideal stress distribution of stress profiles in a fragmentation process is shown in Figure 8.1.

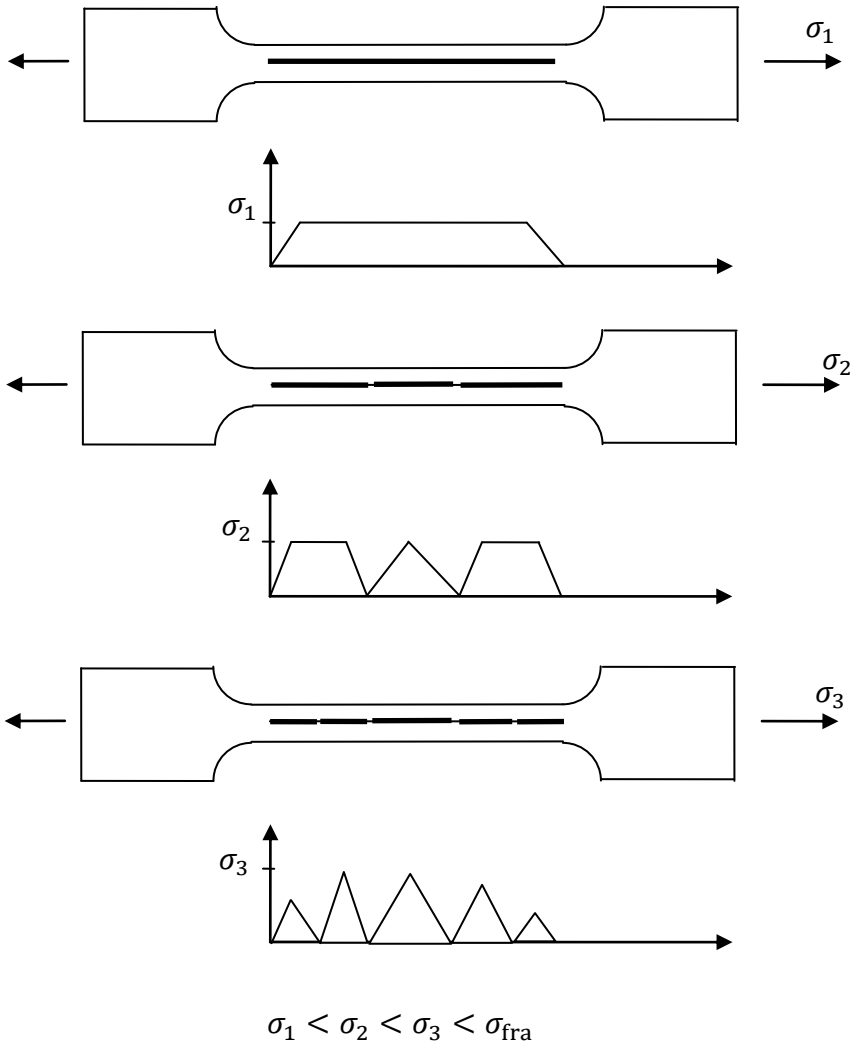

Figure 8.1 *Typical stress distribution profiles for an ideal fragmentation process(Huang and Young, 1994).*

The critical length can be determined using the equation

$$l_c = \frac{4}{3} l_f \qquad 8.2$$

where l_f is the average fragment length determined at the saturation level. Equation 8.2 was firstly proposed by Ohsawa *et al* (1978) for composites of glass fibre reinforced thermosetting resins and later was used by Huang and Young (1994) in the analysis of the fragmentation test of high modulus carbon fibre and epoxy model composites.

Then the interfacial shear stress can be expressed in Equation 8.3, which is the integration of equation 8.1 and 8.2 as

$$\tau = \frac{3\sigma_{fra} r}{4 l_f} \qquad 8.3$$

For the fragmentation test carried out by using the Raman technique, the interfacial shear stress can be determined from a force balance using Equation 8.4, which is based on the differentiation of the strain distribution profiles along the embedded fibre as

$$\tau = E_f \frac{r d\varepsilon_f}{2dx} \qquad 8.4$$

where ε_f is the fibre local strain and $d\varepsilon_f/dx$ is the rate of change of strain with position along the fibre (McCrum *et al*, 1997). After the distribution of strains along the fragments were determined using Raman spectroscopy they were then fitted by using a proper function which will be discussed in section 8.3.1.1, the interfacial shear stress τ was then determined.

In this study the samples were prepared by pouring about 1/3 of the total degassed LY5052/HY5052 epoxy resin mixture into a dumbbell shape mould (see Figure 8.2) into which the release agent had been sprayed. After about 1 hour when it was been partially solid, a single carbon fibre with a length of 18mm was placed at the central region and was adjusted to parallel to the centreline of the dumbbell mould. An embedded length of 18mm was chosen as it is the same length used for the epoxy film model composite and so made the results between the two systems comparable. Afterwards, the remaining 2/3 of the epoxy resin was poured into mould and the system was hot cured in an oven at a temperature of 120 ℃ for 2 hours. Finally the samples

were removed from the mould, and then grinded and polished. This made the thickness of samples to be 2.05 ± 0.02 mm and more importantly ensured that they had a smooth and transparent surface in order to be analysed by transmission optical microscopy and Raman spectroscopy.

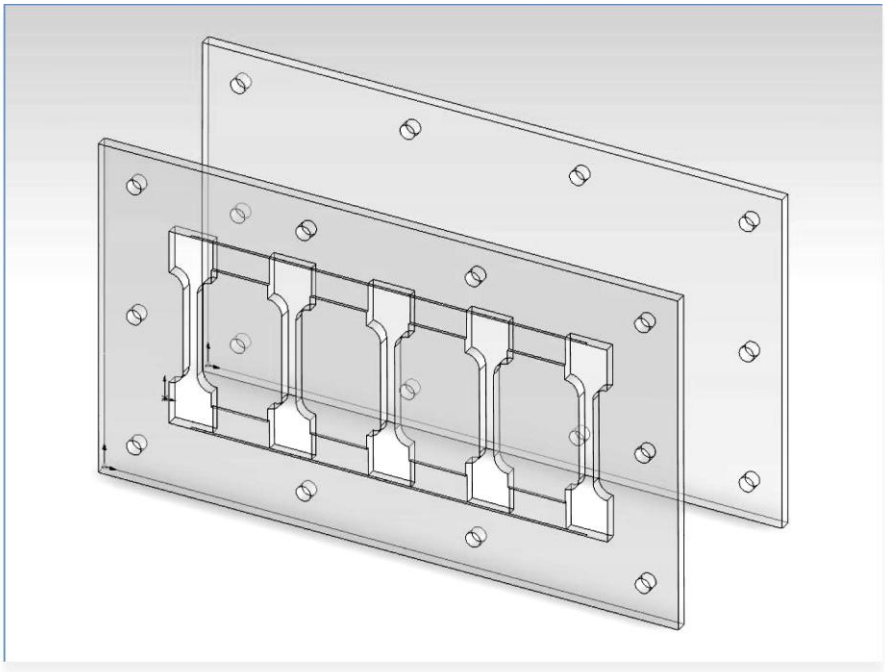

Figure 8.2 *Schematic diagram of dumbbell shaped mould.*

At this point, the samples were ready for a conventional fragmentation test. However, for the samples to be analysed using Raman spectroscopy, in order to monitor the deformation on the sample, a strain gauge was carefully attached on each sample surface using cyanoacrylate adhesive. Two tin wires were then soldered on the strain gauge and connected to a transducer.

To apply deformation to the samples, the epoxy dumbbell sample was fixed on the fragmentation rig by using two screws on both ends as shown in Figure 8.3. By rotating the bar on the fragmentation rig clockwise, deformation can be applied on the sample. Compression can be made by rotating the bar anticlockwise. The live strain on the sample was sensed by the strain gauge and can be calculated from the transducer.

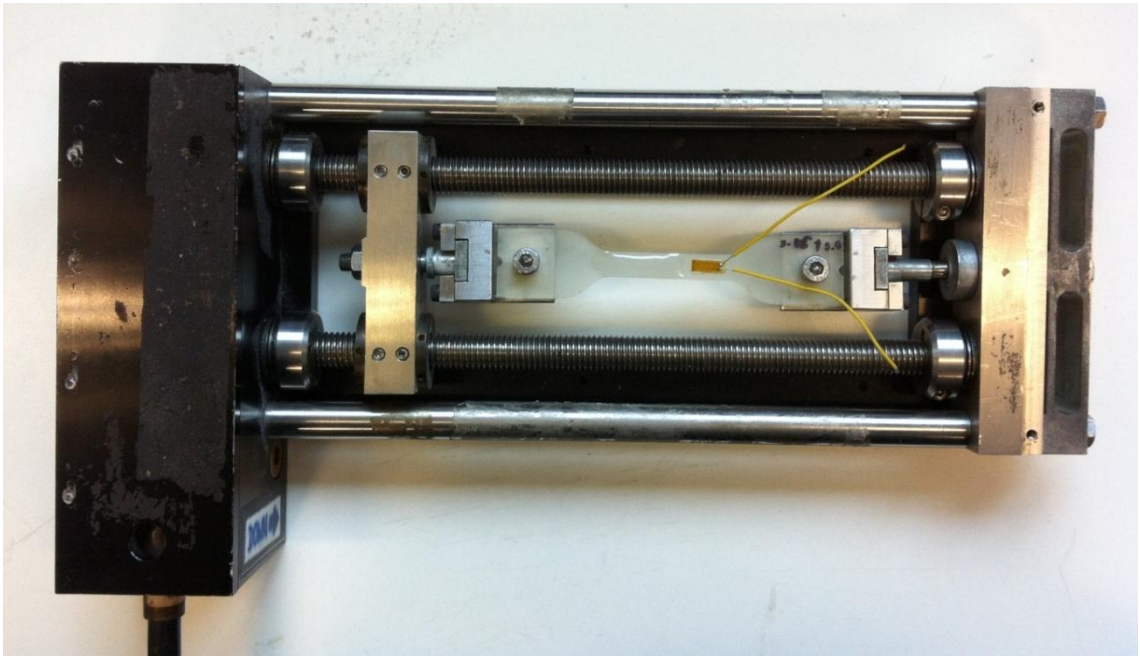

Figure 8.3 *MINIMAT fragmentation rig.*

Raman spectroscopy was carried out using the Renishaw 1000 system and a He-Ne laser. A ×50 objective lens of an Olympus BH-2 optical microscope was employed to focus the laser beam on the specimen to a spot size of ~1-2 μm and to collect the scattered radiation. Static scans centred on the 2D band, which is found at ~2660 cm^{-1}, were recorded using an exposure time of 20s, and then analysed. The intensity, width and position of this band were obtained using by curve fitting a mixed Gaussian-Lorentzian function.

8.3 High Modulus Carbon Fibre Microcomposite System

8.3.1 Fragmentation Test by Using Raman Spectroscopy

8.3.1.1 Strain/Stress Mapping by Using Raman Spectroscopy

In this study, the samples with an embedded high modulus carbon fibre were analysed and Raman spectroscopy was used to scan along the fibre length point to point at each applied strain level. The distance between each scanning point was 0.05 mm and the strain levels applied on the microcomposite samples were 0%, 0.3%, 0.6%, 0.9%, 1.2%, 1.5% and 1.8%. The 2D band wavenumber positions from the high modulus carbon fibre with respect to the distance along the interface at different strain levels is shown in Figure 8.4. The shift in the 2D Raman band position was determined to an experimental error of ±0.8 cm^{-1}; this converted to the local fibre strain and stress were ±0.02% and ±0.10 GPa respectively.

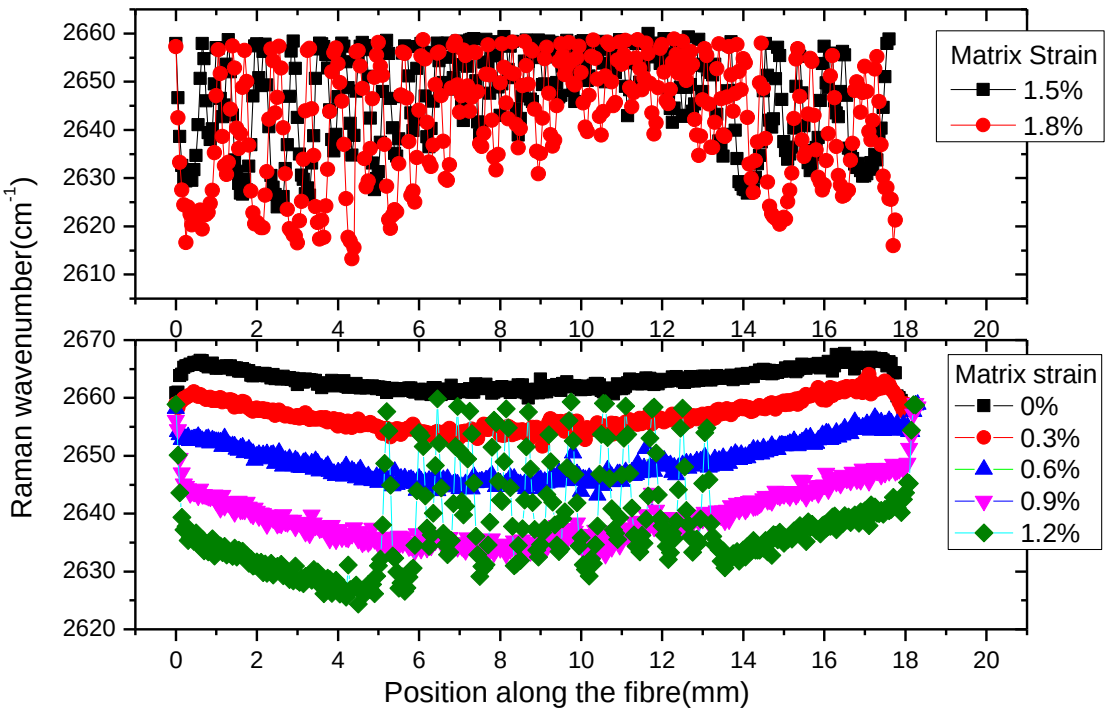

Figure 8.4 *Typical Raman 2D frequencies with respect to the distance along a high modulus carbon fibre at elevated strain levels.*

It can be seen from Figure 8.4, there is a pronounced shift of the 2D Raman band to a lower wavenumber position at increasing strain levels. As it has been analysed in the single fibre deformation test in Chapter 5, the linear relationship between the position of

the 2D Raman band and fibre strain (and stress) can be expressed empirically by Equation 8.5 and Equation 8.6 respectively. The 2D Raman band shift rates with respect to strain and stress were determined to be -28.2 ±0.7 cm^{-1}/ % strain and -5.8 ± 0.2 cm^{-1}/GPa.

$$y_{\text{Raman}} = -28.2\, x_{\text{strain}} + 2658.7 \qquad (8.5)$$

$$y_{\text{Raman}} = -5.8\, x_{\text{stress}} + 2659.2 \qquad (8.6)$$

The high modulus carbon fibre started to break from the central region when the applied strain went above 1.2%. When the applied strain reached 1.5%, the whole carbon fibre was found to have been broken into many fragments. Since large quantities of data at different matrix strain levels were obtained the strain levels of 1.5% and 1.8% have been displayed separately as shown in Figure 8.4.

The 2D Raman band positions were then converted to the local fibre strains (see Figure 8.5) and stresses (see Figure 8.6) using Equations 8.5 and 8.6.

According to Figure 8.5, when there was no exterior strain applied on the sample ($\varepsilon_{\text{app}} = 0\%$), the local fibre strain along the interface was below zero, this indicates that the high modulus carbon fibre was in compression due to the compressive thermal residual stress generated from the hot curing process. In this study, when $\varepsilon_{\text{app}} = 0\%$, it is observed that the strain at both fibre ends approaches zero but does not reach zero due to residual compressive stresses. These findings are in agreement with Huang and Young (1995) for a hot cured high modulus pitch based carbon fibre and an epoxy resin system. Furthermore, it was found that the fibre local stain distribution along the interface varied continuously with the strain higher in the centre and close to the matrix strain, this may due to less residual compressive stress suffered in the central region of the fibre. When the strain $\varepsilon_{\text{app}} = 0.3\%$, it can be seen the strain distribution along the fibre fluctuated around zero, this means the strain is approximately balancing the residual thermal compressive strain in the high modulus carbon fibre.

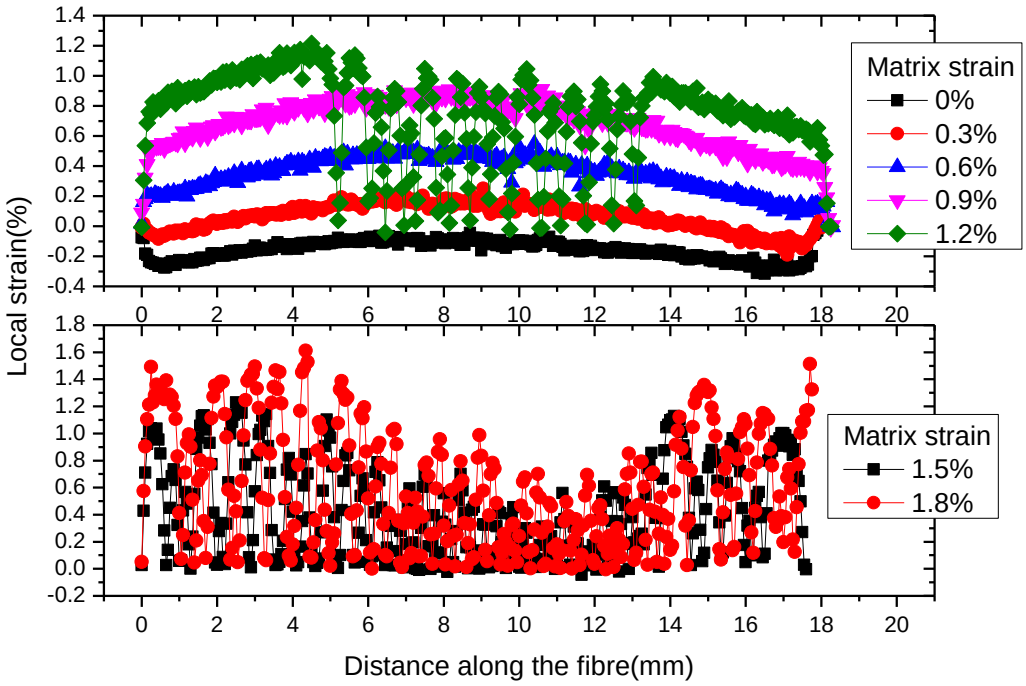

Figure 8.5 *Typical local fibre strain profiles along the fibre length with increasing strain levels applied to a high modulus carbon fibre/epoxy resin composite.*

Since the stress and strain behaviour for the high modulus carbon fibre is a near linear relationship, there is almost no difference in the shape of the strain and stress profiles shown in Figures 8.5 and 8.6.

In this study the stress distribution profiles were not like the predicted ideal ones (see Figure 8.1) for the fragmentation test, as stress distribution determined have higher values in the central region of the fibre and this continue exist as the increasing of applied strain levels on matrix until the high modulus carbon fibre started to break from this central region when applied matrix strain reached 1.2%. This could be due to marginal difference.

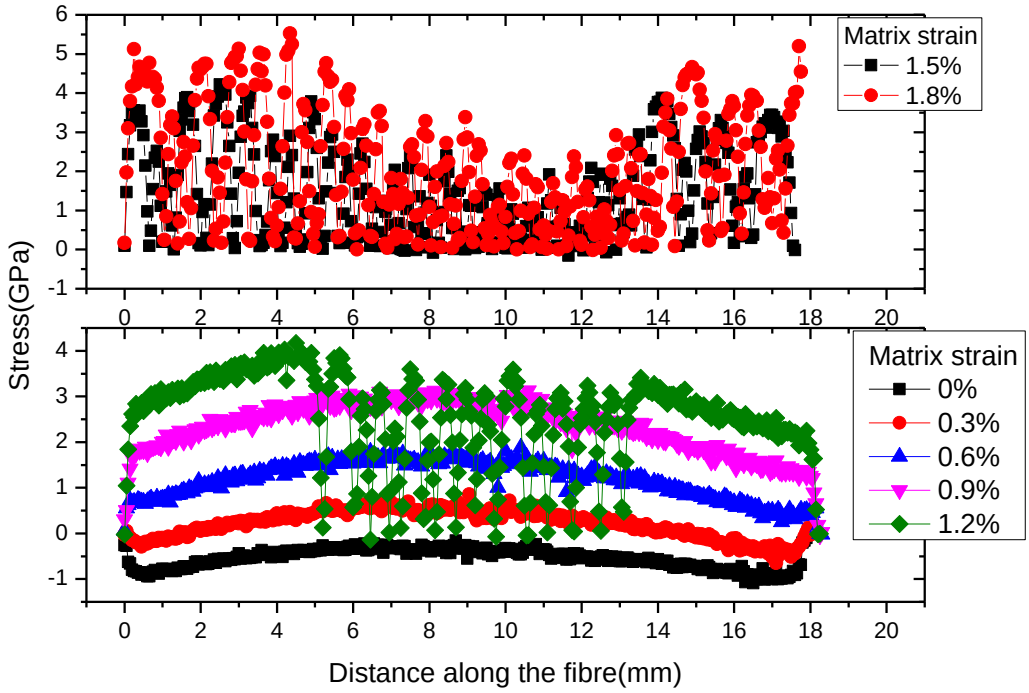

Figure 8.6 *Typical local fibre stress profiles across the interface at elevated strain levels for a high modulus carbon fibre/epoxy resin composite.*

The shear-lag model proposed by Nairn (1997) based on the theory of a single fibre reinforced infinite matrix as expressed in Equation 8.7 was used to fit the strain distribution profiles along the high modulus carbon fibre at the interface. This model assumes that the bonding between the fibre and matrix is perfect and the system deforms elastically. Nairn's shear-lag model was proved to be more accurate than Cox (1952) in the work of Sureeyatanapas *et al* (2010) for the fragmentation test of a SWNT coated glass fibre and an epoxy matrix composite system by using Raman spectroscopy.

$$\varepsilon_f = \varepsilon_m \left[1 - \frac{\cosh \beta (\frac{l}{2} - x)}{\cosh \beta \frac{l}{2}} \right] \tag{8.7}$$

In considering the relationship between the strain and stress, the stress distribution profiles can be fitted by using the equation

$$\sigma_{\mathrm{f}} = E_{\mathrm{f}}\varepsilon_{\mathrm{m}}\left[1 - \frac{\cosh\beta(\frac{l}{2} - x)}{\cosh\beta\frac{l}{2}}\right] \tag{8.8}$$

where ε_m is matrix strain and x is the distance along the fibre. β is shear-lag parameter and can be calculated using Equation 8.9.

$$\beta = \left\{\frac{2}{r_1^2 E_{\mathrm{f}} E_{\mathrm{m}}}\left[\frac{E_{\mathrm{f}}V_{\mathrm{f}} + E_{\mathrm{m}}V_{\mathrm{m}}}{\frac{V_{\mathrm{m}}}{4G_{\mathrm{f}}} + \frac{1}{2G_{\mathrm{m}}}(\left(\frac{1}{V_{\mathrm{m}}}\right)\ln\left(\frac{1}{V_{\mathrm{f}}}\right) - 1 - \frac{V_{\mathrm{m}}}{2}}\right]\right\}^{\frac{1}{2}} \tag{8.9}$$

where r_1 is the fibre radius, E_{f} and E_{m} are the Young's modulus of the fibre and matrix respectively, V_{f} and V_{m} are the volume fraction of the fibre and matrix respectively and they are expressed in the equations

$$V_{\mathrm{f}} = \frac{r_1^2}{r_2^2} \tag{8.10}$$

$$V_{\mathrm{m}} = \frac{r_2^2 - r_1^2}{r_2^2} \tag{8.11}$$

G_{f} and G_{m} are the shear modulus of the fibre and matrix respectively, G_{m} is defined by the equation

$$G_{\mathrm{m}} = \frac{E_{\mathrm{m}}}{2(1+v)} \tag{8.12}$$

where v is Poisson's ratio of the matrix.

However, in this study it was found that a curve described by Equation 8.7 was not in good agreement with data from the lower matrix strain levels ($\varepsilon_{app} \leq 1.2\%$). This was because the strain distribution predicted by the shear-lag analysis suggested that the data should plateau at the central region of the fibre. The strain data did not however exhibit a flat and plateau in the central region due to a residual compressive stress which did not distribute uniformly on the fibre leading to a higher stress. Therefore, the strain distribution profiles were modified by subtracting the thermal residual compressive strain which was defined as the strain across the fibre without applying external matrix strain. The modified strain profiles were found to be in good agreement with Nairn's

model as shown in Figure 8.7 (Nairn, 1997). The strain distribution profiles in Figure 8.7 were also converted to stress profiles (Figure 8.8) by using the calibration of fibre stress and strain behaviour obtained by tensile testing. The stress profiles, as shown in Figure 8.9, can also be well fitted by Nairn's shear lag model.

It can be seen that when the applied matrix strain reached 1.2%, the middle region of the fibre breaks into many small fragments. The two fragments close to both ends of the fibre are considerably longer than other fragments. More importantly, the maximum strain for the fragment close to the left end was significant higher than that of the right end; with the left hand fragment's maximum strain was closer to the matrix strain of 1.2%. This obviously indicates that the fibre length at the left end is comparatively longer than the others and there is good interfacial bonding between fibre and epoxy matrix at the left end. Later the longer of fragments detected in this region when the applied matrix strain increased to 1.5% and 1.8% again. When the applied matrix level reached 1.5% and 1.8%, a debonding model proposed by Piggott (1980) was applied to the debonded fragments which are mostly located at the central region as the triangle fitting line shown in Figure 8.7(b) and Figure 8.8(b).

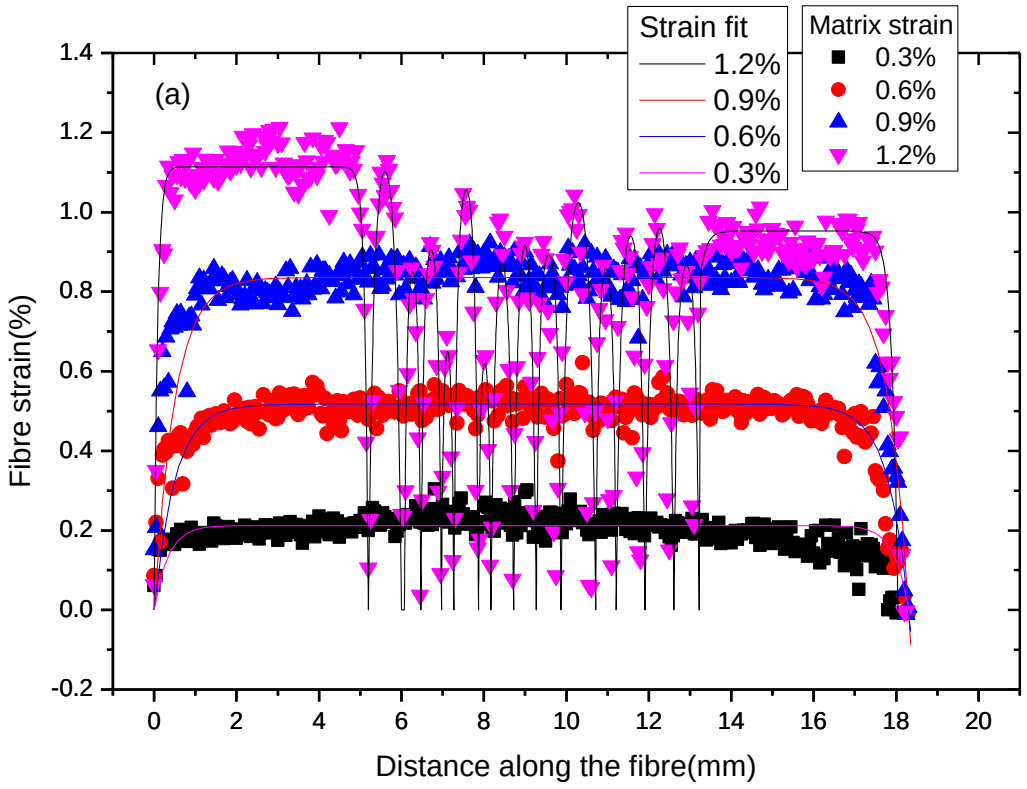

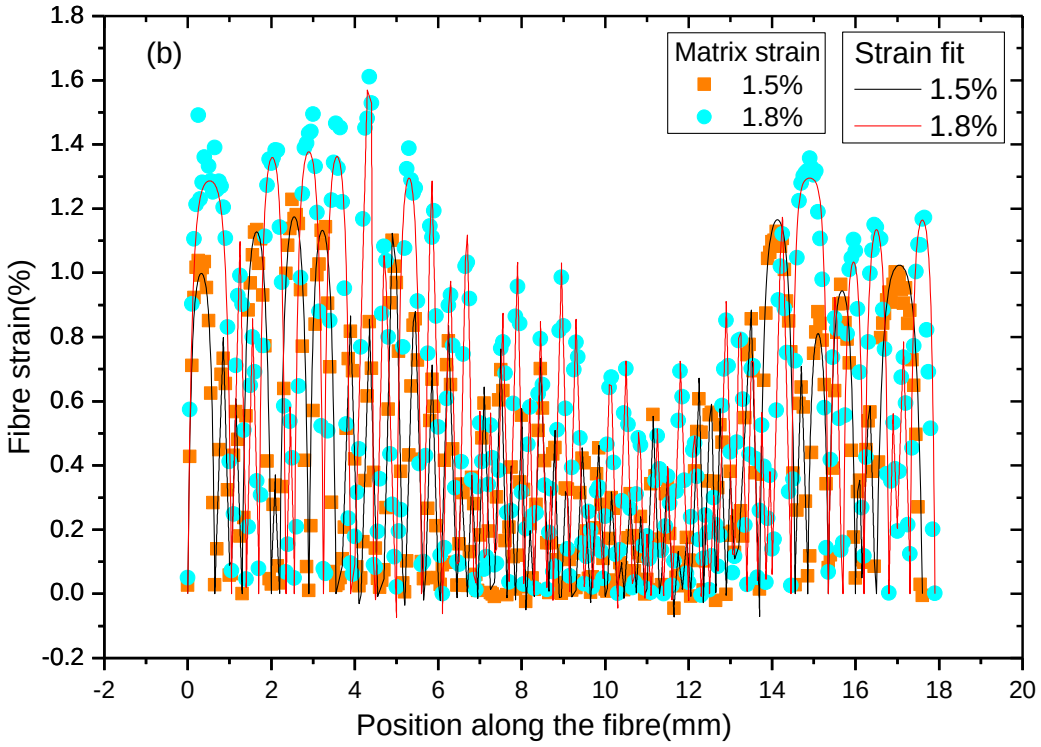

Figure 8.7 *Fibre strain distribution with fitted curves at different matrix strain levels; (a) matrix strain levels below 1.5%; (b) matrix strain levels of 1.5% and 1.8%.*

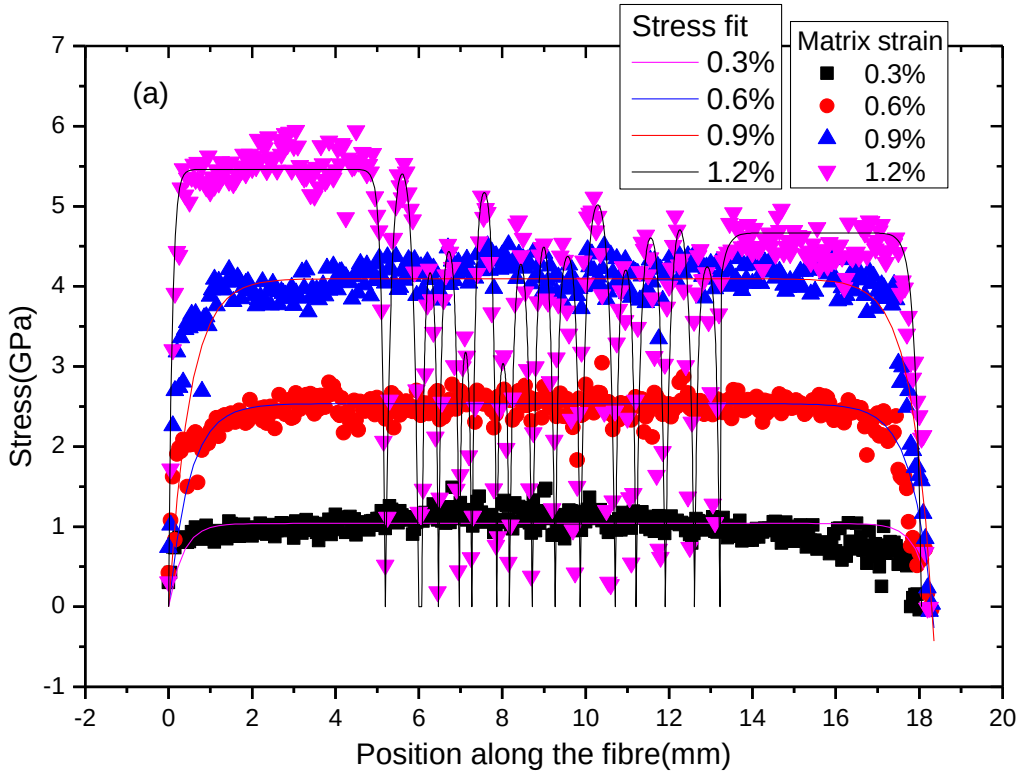

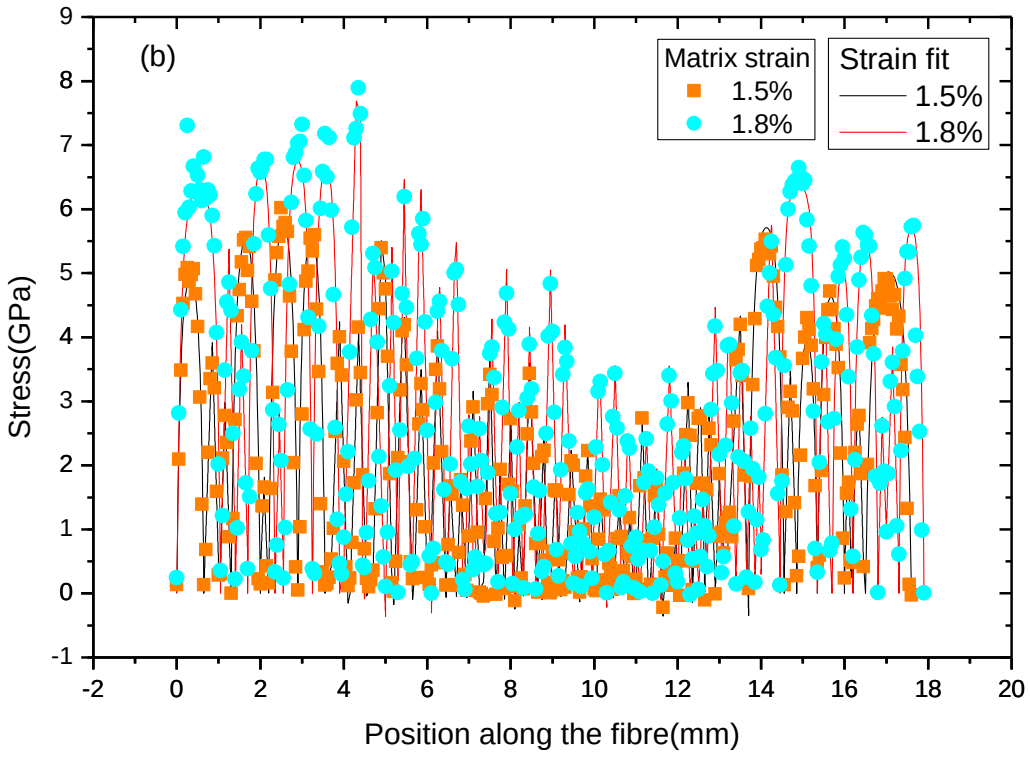

Figure 8.8 *Fibre stress distribution with fitted curves at different matrix strain levels; (a) matrix strain levels below 1.5%; (b) matrix strain levels of 1.5% and 1.8%.*

Since the high modulus carbon fibres broke into large quantities of small fragments each strain distribution cannot be clearly observed. Therefore the strain distributions in a region from 5 mm to 10 mm along the length of the fibre at matrix strain levels of 1.2%, 1.5% and 1.8% have been magnified as shown in Figure 8.9. It can be seen that the same as the theoretical prediction, every strain distribution peak represents a fragment with the highest strain determined in the middle region of each fragment with the strain normally decreasing to zero at both ends. The width of each peak is assumed to be equal to the length of each fragment. The maximum strain at the centre of each fragment is well below the applied matrix strain. Figure 8.9 also suggests that the fragments were longer when the matrix strain was 1.2% and that they continue to fracture during an increase in matrix strain. When the applied matrix strain was 1.5%, the fragmentation reached a saturation stage because the length of each fragment did not change at higher strain levels as shown in Figure 8.9.

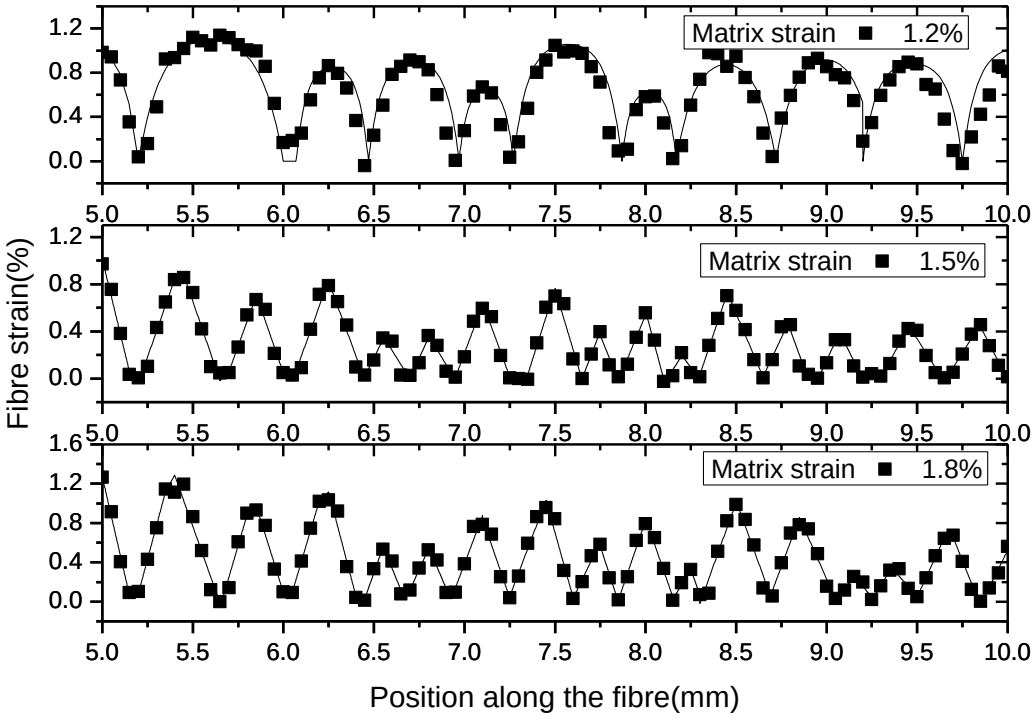

Figure 8.9 *Typical local magnified fibre strain distributions for fragments in the range of 5-10 mm along the length of a single high modulus carbon fibre embedded in a composite at epoxy matrix strain levels of 1.2%, 1.5% and 1.8%.*

The theory of ineffective transfer length δ which is defined as the fibre length necessary to build up a maximum stress is typically used to evaluate the efficiency of stress transfer across an interface (Kim, 1997). However in this study only the ineffective stress transfer length obtained from lower matrix strain levels of 0.3%, 0.6% and 0.9% were compared, as shown in Figure 8.10. The reason for this is that only the ineffective transfer lengths of intact fibres of same length are comparable and the fibre had not started to break at low strain levels. Obviously the ineffective stress transfer length is highly dependent on the elastic properties of the matrix and fibre, and more importantly the interfacial bonding. In Figure 8.10, the ineffective stress transfer length was calculated from the left end of the fibre to the vertical dotted line which was drawn when the fitted data beginning to plateau and the results are shown in Table 8.1. For the same fibre and matrix composite sample, when the embedded length of fibre is the same, a smaller the value of ineffective transfer length means better interfacial bonding between the fibre and matrix.

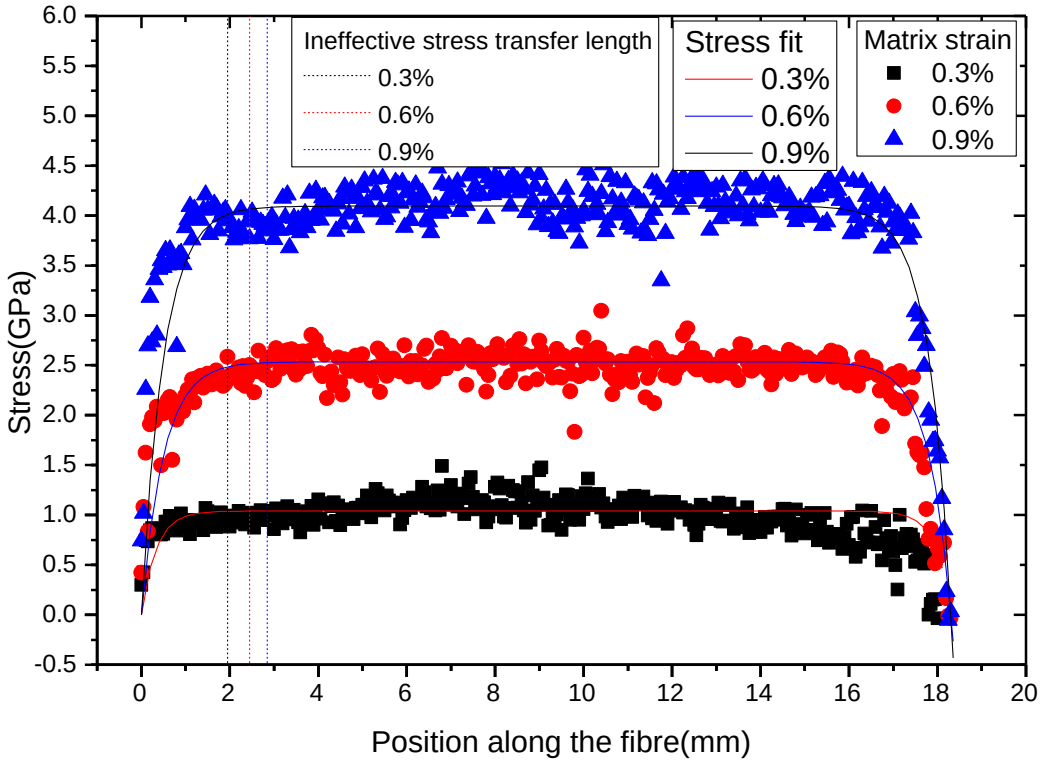

Figure 8.10 *Ineffective stress transfer length measurement at matrix strain level of 0.3%, 0.9% and 1.2%.*

Table 8.1 *The determined ineffective stress transfer lengths at different matrix strain levels.*

Matrix strain level	Ineffective stress transfer length(mm)
0.3%	1.95±0.06
0.6%	2.45±0.05
0.9%	2.85±0.05

8.3.1.2 Interfacial Shear Stress (ISS) Determination

The strain distribution profiles were converted to interfacial shear stress profiles using Equation 8.4. The determined ISS profiles at different matrix strain levels are shown in Figure 8.11. Similar to that predicted by the elastic shear-lag model (Nairn, 1997), the maximum interfacial shear stress is observed at the fibre end or fragment end and it falls to zero in the central region of the fibre or fragment. Figure 8.11(a) indicates that when matrix strain $\varepsilon_{app} \leq 1.2\%$, the stress transfer at the fibre/matrix interface is in elastic shear-lag model. It can be seen when the matrix strain is 1.2%, the maximum interfacial shear stress at the fibre left end was higher than that of the right end, this is due to that the length of fragment at left end is higher than that of the one at right end.

Furthermore, there appears to be a really good adhesion between the fibre and matrix at the left end of the fibre. The ISS at this fibre end continues to increase with an increase in the strain. Figure 8.12 is an optical microscope (using the Raman microscope) image of the left hand end of the fibre, taken when the matrix strain was 1.8%. It shows good adhesion between the fibre and matrix as well since the matrix was following the contraction of the fibre. The dark lines from the fibre end indicated that matrix was slightly cracked at the fibre end. However, in opposite the determined ISS at the middle area of this fibre show fully debonding occurred for most fragments(from 1.2% to 1.8%), the ISS even dropped at the region with the distance of 10mm to13mm along the fibre due to debonding occurred. At the applied matrix strain of 1.8%, as shown in Figure 8.11(c) the fragments at the position of 1.8mm and 14.5 mm shows partly debonding occurred. A final maximum ISS was obtained of 52.81±0.22 MPa at the position of 3.2 mm when $\varepsilon_{app} = 1.8\%$, it shows an inelastic deformation with matrix fracture, this is very close to a reasonable matrix fracture stress(40-50 MPa).

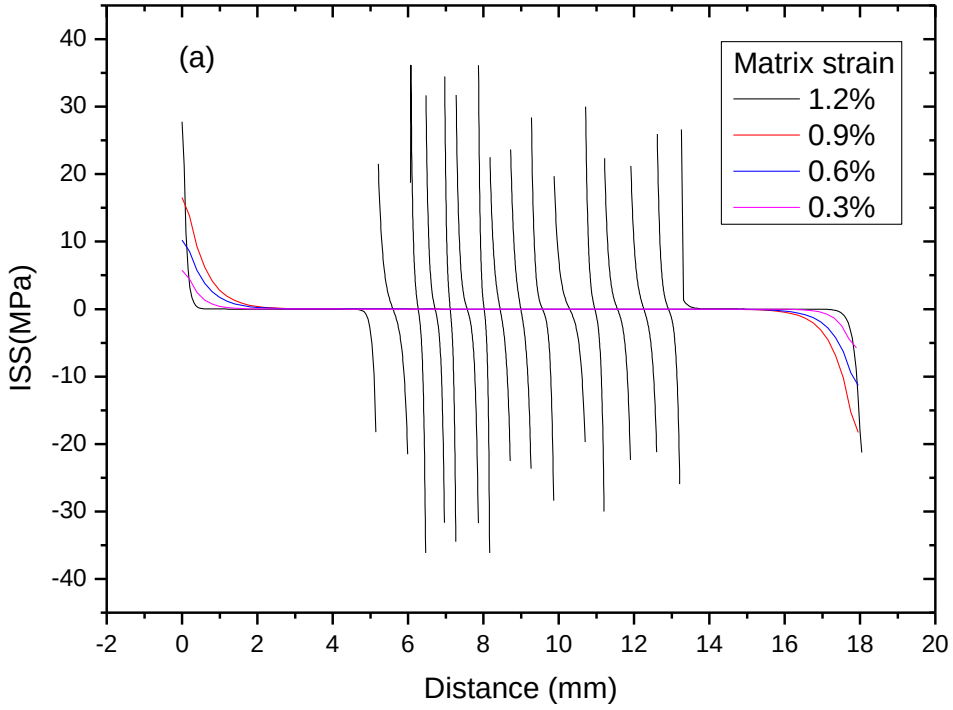
(a)
Matrix strain
1.2%
0.9%
0.6%
0.3%
ISS(MPa)
Distance (mm)

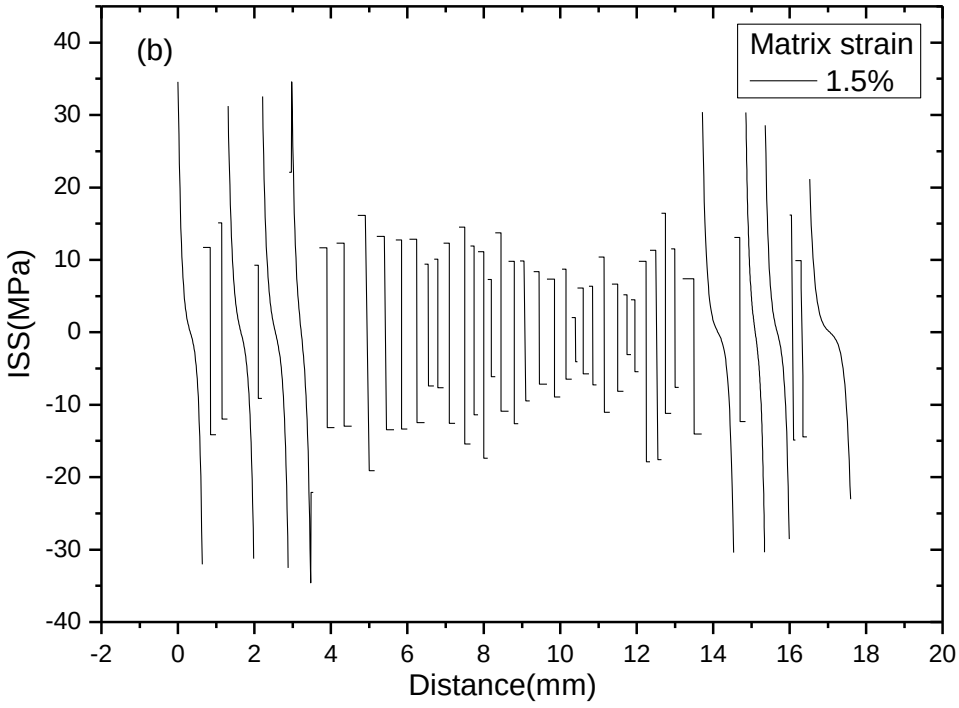
(b)
Matrix strain
1.5%
ISS(MPa)
Distance(mm)

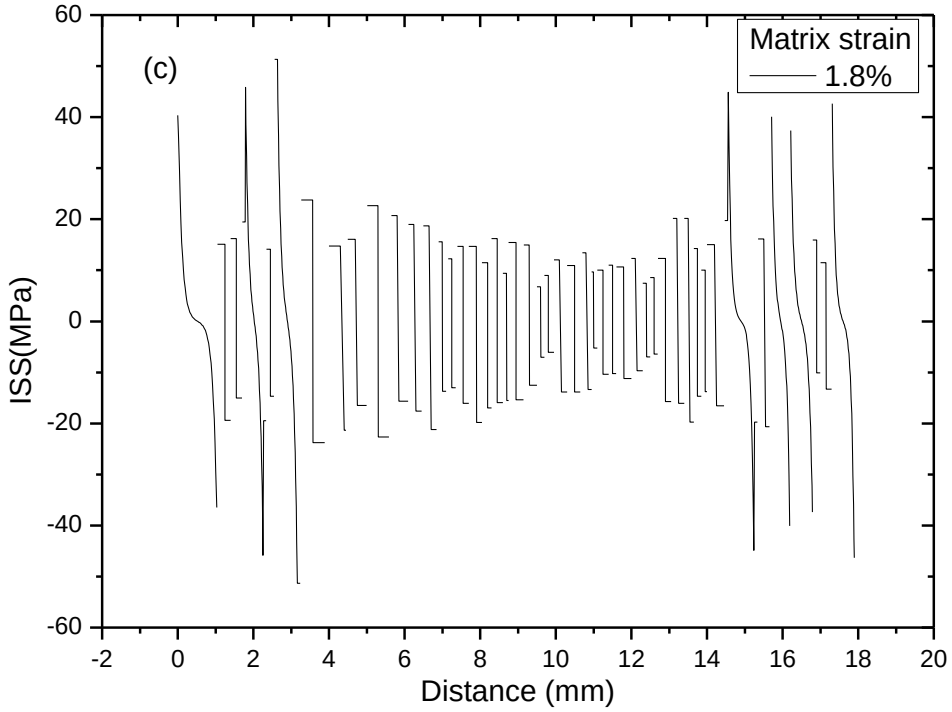

Figure 8.11 *Interfacial shear stress distribution for the high modulus carbon fibre and epoxy resin system at different matrix strain levels;(a) matrix strain levels of 0.3%,0.6%,0.9% and 1.2%;(b) matrix strain of 1.5%;(c)matrix strain of 1.8%.*

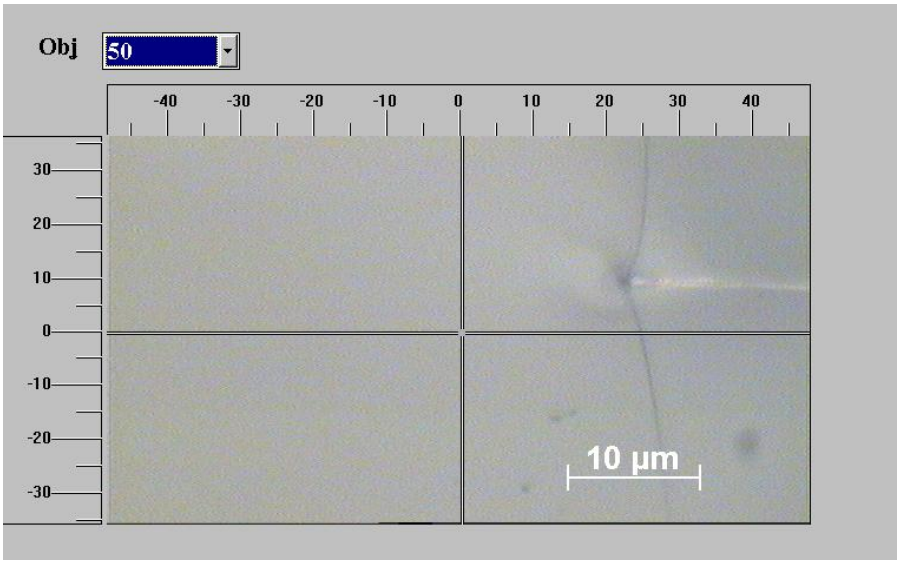

Figure 8.12 *Left end of high modulus carbon fibre taken from the optical microscope of Raman system ($\varepsilon_{app} = 1.8\%$).*

Overall the test suggested that there is a very good adhesion between this high modulus carbon fibre and the epoxy resin. It should be noted that the maximum ISS determined from this fragmentation test (52.81±0.22 MPa) is much higher than that obtained from the previous epoxy film model test (24.32±0.11MPa). The reason for the difference could be that when the stress is transferred from matrix to the fibre for the fragmentation test, the fibre can be stretched into ultimate stage since the higher elongation property of epoxy matrix than the fibre, the test continues even if the fibre fractured into pieces. However, for the epoxy film model test, it usually stops once the fibre breaks and this normally occurs outside of the film. Therefore, the fragmentation test could be the better micromechanical test method to investigate the interface of carbon fibre and epoxy composite system comparatively.

8.3.2 Conventional Fragmentation Test

As well as determining the interfacial shear stress by using Raman technique, it was also calculated in the conventional way. As is shown in Figure 8.13, a fibre breaking point can be clearly observed using the optical microscope of Raman system. Therefore, by turning the micrometre mounted on the microscope stage, all the breaking nodes were captured and the length of each fragment was measured by using the micrometer with an accuracy of 5μm. The numbers of fragments as a function of the matrix strain are shown in Figure 8.14. It can be seen that when the matrix strain was 1.8%, the number of fragments reached a saturation stage.

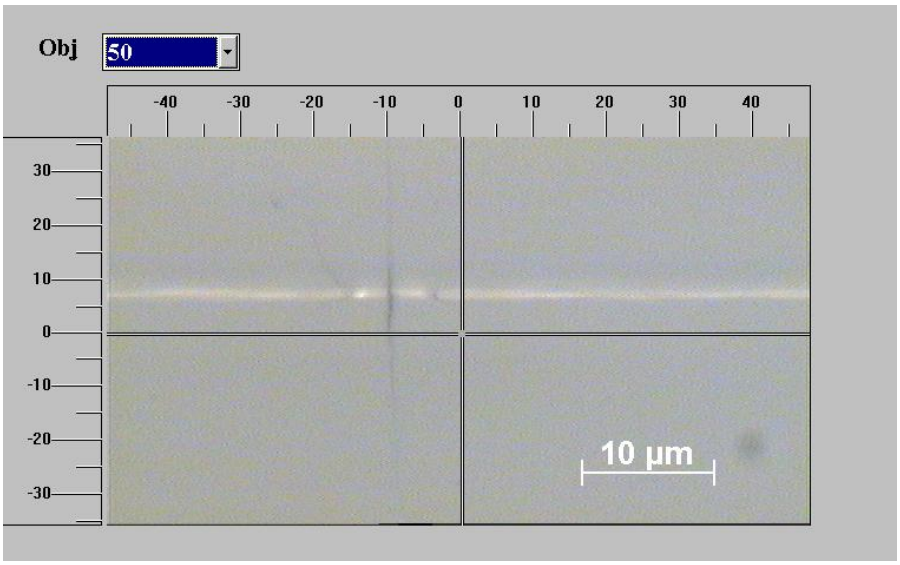

Figure 8.13 *Typical fibre breaking node observed from an optical microscope of Raman system.*

The interfacial shear stress was calculated using Equation 8.1, which depends on the critical length l_c of the fibre; l_c is related to the measured average fragment length in the saturation state and was calculated by using Equation 8.2. The average fragment length was determined to be 0.40±0.01 mm at a matrix strain of 1.8%. The measured fragment lengths of this high modulus carbon fibre at a matrix strain of 1.8% are shown in Table E.1 of Appendix E. The fibre fracture stress σ_{fra} for the high modulus carbon was determined using tensile testing (Section 4.10.1) to be 3.75±0.31GPa. An interfacial shear strength of 36.83±0.25 MPa was calculated. All data, including average fragment length, critical fragment length, IFSS determined by using the conventional method and the Raman method are summarised in Table 8.2.

It can be seen the IFSS determined using the conventional method is lower than the value determined using the Raman technique. The results are in agreement with the findings of Huang and Young (1994) wherein the value of interfacial shear strength determined by the conventional fragmentation test was always lower than the maximum values of interfacial shear stress obtained using Raman technique. This is due to the reason that the value determined using conventional method is just a single value but the value obtained using Raman technique is a maximum one from many fragments 'peaks'.

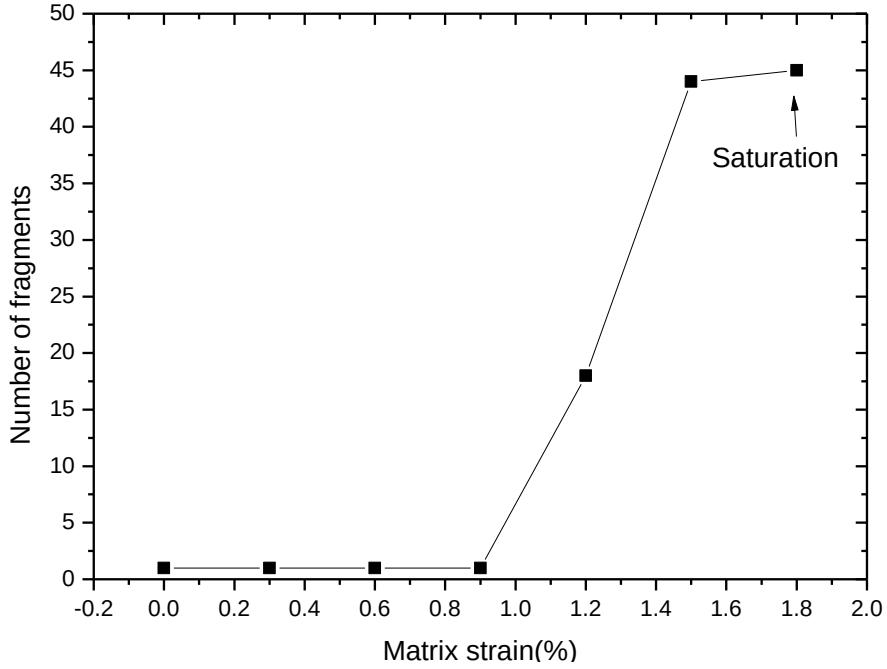

Figure 8.14 *Numbers of fragments regard matrix strain applied on the sample.*

Table 8.2 *The determined average fragment length, critical length, IFSS obtained in conventional method and Raman method.*

Sample system	$l_f(mm)$	$l_c(mm)$	$\tau_c(MPa)$	$\tau_{R_{max}}(MPa)$
HMCF/Epoxy	0.40 ±0.01	0.53 ±0.01	36.83 ±0.25	52.81 ±0.22

8.4 Low Modulus Carbon Fibre Microcomposites System

Both HiPCO SWNTs and COOH SWNTs were firstly coated on a low modulus carbon fibre surface separately in order to sense the strain distribution on the fibre according to their Raman 2D band positions during the fragmentation test. Again, the fragmentation of both model systems was analysed by using Raman technique and the conventional approach.

8.4.1 Fragmentation Test Analysed by Using Raman Technique

8.4.1.1 Strain/Stress Mapping by Using Raman Spectroscopy

The experimental process was almost the same as that for the high modulus carbon fibre model system, but the scanning time at each point was reduced to 10s due to the high intensity and easily obtained 2D band from single walled carbon nanotubes. Furthermore, the samples were deformed to a matrix strain of 2.3% which was significantly higher than that of 1.8% for the high modulus carbon fibre model systems in order for the numbers of the low modulus carbon fibre fragments to reach a saturation stage and the matrix of epoxy dumbbell samples usually fractured when the strain was increased above 2.3%. The determined Raman 2D band shift frequencies from the HiPCO and COOH SWNTs along the low modulus carbon fibre are shown in Figure 8.15(a) and 8.15(b) respectively. First of all, these data again proved that both types of SWNTs can be successfully sized onto the carbon fibre surface, and they also enable point to point strain mapping.

Due to the SWNTs being highly Raman active materials, the 2D band frequencies obtained along the fibre at elevated matrix strain levels were genuinely continuous with less variation than that from the pure high modulus carbon fibre. Secondly, it can be seen from Figure 8.15(a) and Figure 8.15(b) that for the samples sensed by both types of nanotube the low modulus carbon fibre started to break when the matrix strain increased to 1.8%. As shown in Figure 8.15(b), for the samples that used COOH as strain sensors, the number of peaks reached a maximum value when the matrix strain was 2.1% and it was then reached saturation when the matrix strain increased to 2.3%. However, for the samples which use HiPCO SWNTs as strain sensors, the number of fragments was still increasing even when the matrix strain reached 2.3%, as shown in Figure 8.15(a). The reasons for this different behaviour will be explained in more detail with the strain

mapping figures shown in Figure 8.16. Thirdly, it also can be seen that from Figure 8.15(a), when the matrix strain increased from 2.1% to 2.3%, some peaks were observed to move, which could mean that some carbon fibre fragments were 'drifting' during the deformation of the epoxy resin matrix. However, this was not the case for the samples made using COOH SWNTs as strain sensors. Therefore, it could be inferred that the fibres sized with COOH SWNTs have better bonding at the interface.

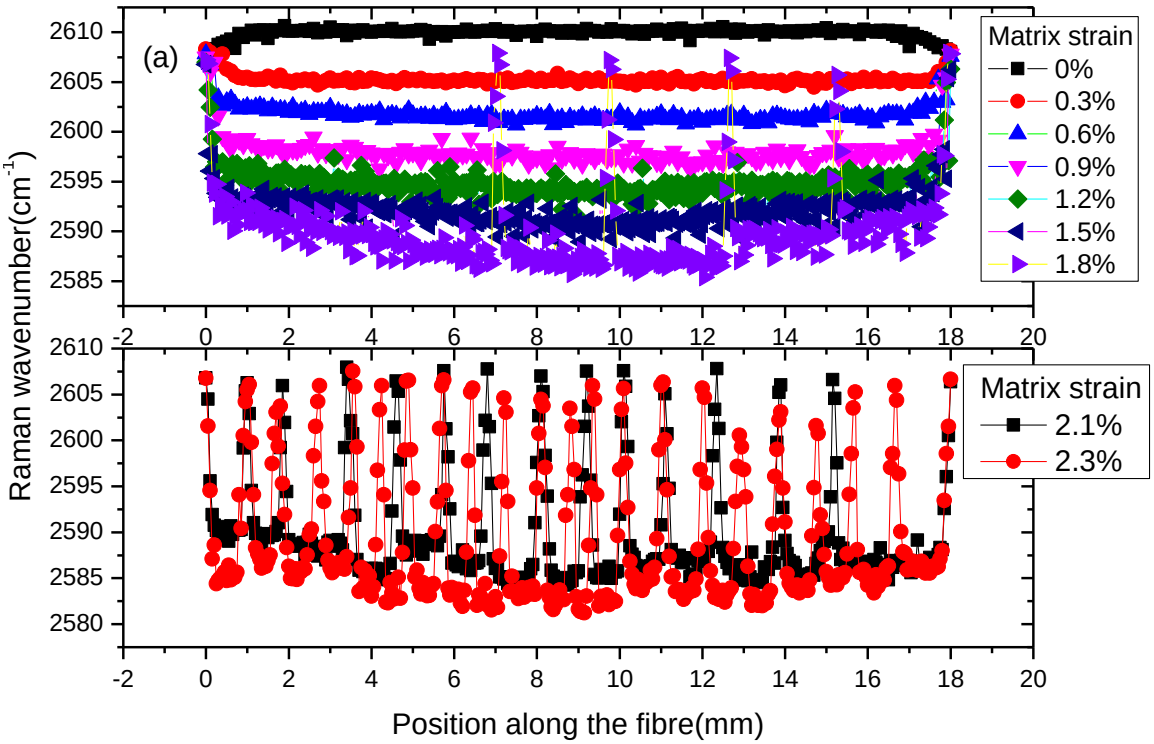

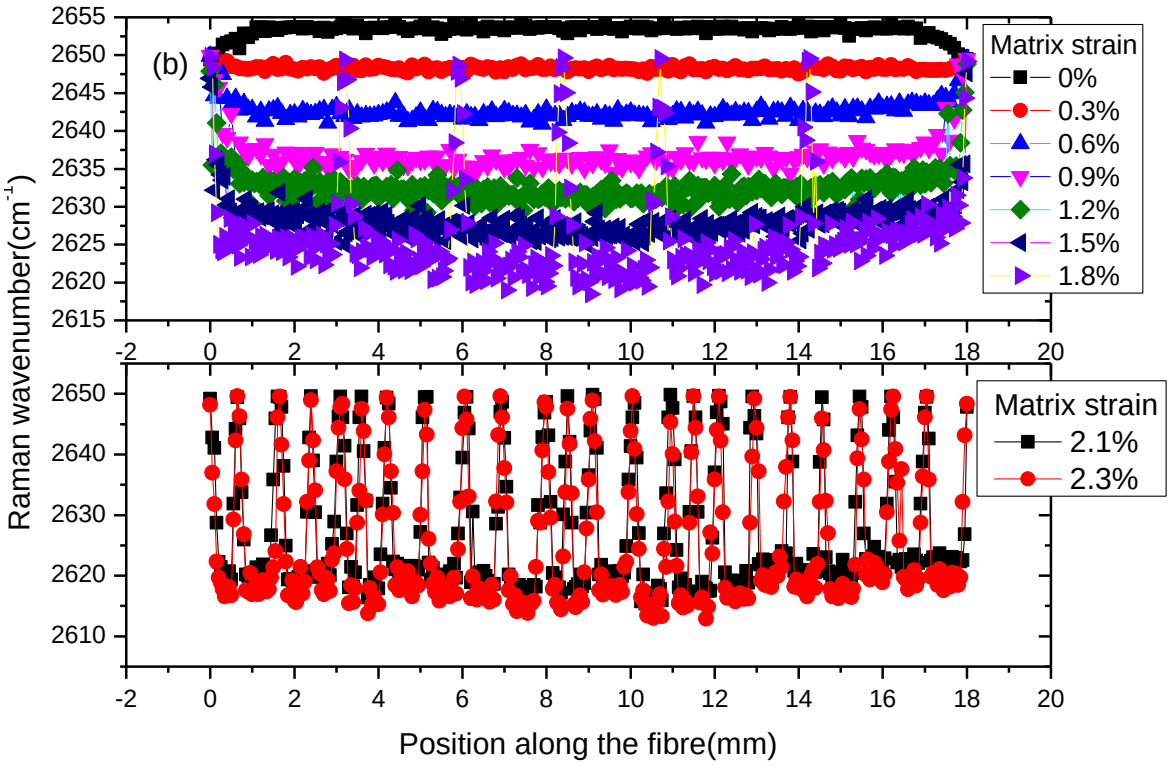

Figure 8.15 *Typical Raman 2D band wavenumber positions from HiPCO SWNTs (a) and COOH SWNTs (b) related to the distance along a low modulus carbon fibre at elevated matrix strain.*

Again the obtained Raman shift wavenumber positions along the fibre with their relevant applied matrix strain levels were converted into local fibre strain and stress by using the calibration determined from a single fibre deformation test. The strain mapping and stress mapping with respect to distance along a low modulus carbon fibre at elevated matrix strain levels are displayed in Figure 8.16 and Figure 8.17 respectively. Since all samples were hot cured, the fibres were in compression when there was no load applied, this demonstrated in the strain or stress mapping figures were that when matrix strain was 0% ($\varepsilon_{app} = 0\%$), the fibre strain or stress were below zero at the central region of the fibre and they were approaching zero at both fibre ends. Due to thermal axial compressive stresses, local fibre strains were slightly lower than each applied matrix strain level. More importantly, it can be seen from Figure 8.17, for both types of samples, the residual compressive stresses were uniformly distributed along the fibre with less fluctuation, this resulted in the local fibre stresses at each matrix strain level were continuously distributed with less variation, the stress or strain

profiles($\varepsilon_{app} > 0\%$) shaped perfectly as plateau. The strain and stress maps can be fitted by using Nairn's shear-lag model expressed in Equations 8.7 and 8.8 respectively (Nairn, 1997). When $\varepsilon_{app} = 0\%$, the average fibre strain in the central region was -0.19±0.07% and -0.23±0.06% for the composite systems sensed using HiPCO and COOH SWNTs respectively. When $\varepsilon_{app} = 1.8\%$, the low modulus carbon fibres exhibited fragmentation for both nanotube coating systems. The sample made using COOH SWNTs in the sizing layer had more homogeneously broken fragments, as shown in see Figure 8.16(b). It can be seen from Figure 8.16(a) that the system sensed using HiPCO SWNTs has a fragment at the left hand side with a length of about 7mm; this is significantly longer than any of the other fragments. The possible reasons for this are that the compressive residual stress was not homogenously distributed along the fibre and left the left side more compressed.

It was found that the system with COOH SWNTs at the interface have more regular breaking points distributed along the length of the fibre. This again was a sign that the interface with the existence of COOH SWNTs could have better bonding between low modulus carbon fibre and epoxy resin matrix.

It can be clearly observed that as the applied matrix strain increased above 2 % the low modulus carbon fibres underwent extensive fragmentation, with fragment lengths of around 1mm. It should be noted that for both types of sample there were differences between the applied matrix strain $\varepsilon_{\mathrm{app}}$ and the obtained highest fragment strain. When $\varepsilon_{\mathrm{app}} = 2.1\%$, the average differences were calculated to be 0.35±0.02 % and 0.31±0.02 % for the samples sensed using HiPCO and COOH SWNTs respectively. When $\varepsilon_{\mathrm{app}} = 2.3\%$, these differences were 0.37±0.02% and 0.35±0.01% respectively. There are two factors that could cause the unequal of the matrix strain and fragment strain. One has been mentioned previously that it is the thermal compressive stress resulted from the hot curing of samples; however, according to the study beforehand, it was determined that the average gaps caused by thermal compressive stress were only -0.19 ±0.07% and -0.23±0.06% for the sample system sensed by HiPCO and COOH SWNTs respectively. Therefore, there must be the second factor which was that the length of fragments is below the critical length. As the increasing of matrix strain, the fibre broke into many short length fragments, the shorter the fragment the harder for the stress to be built up on. When the applied matrix strain $\varepsilon_{app} > 2.1\%$, the fragments were too short for the

shear stress to be built up on, then debonding occurred and it shows a linearization of stress distribution of data.

As shown in Figure 8.17, Raman 2D band shift peak positions along the low modulus carbon fibre for both types of systems were converted into fibre local stress using the standard calibration used previously. It can be seen than when the matrix strain $\varepsilon_{app} =$ 1.8%, the low modulus carbon fibre started to break with the highest local fibre stress being about 4.5 GPa; this is close to the average value of the fibre breaking strength determined from tensile testing. The highest local fibre stress determined in this test was 5.64±0.06 GPa at a matrix strain of 2.3%.

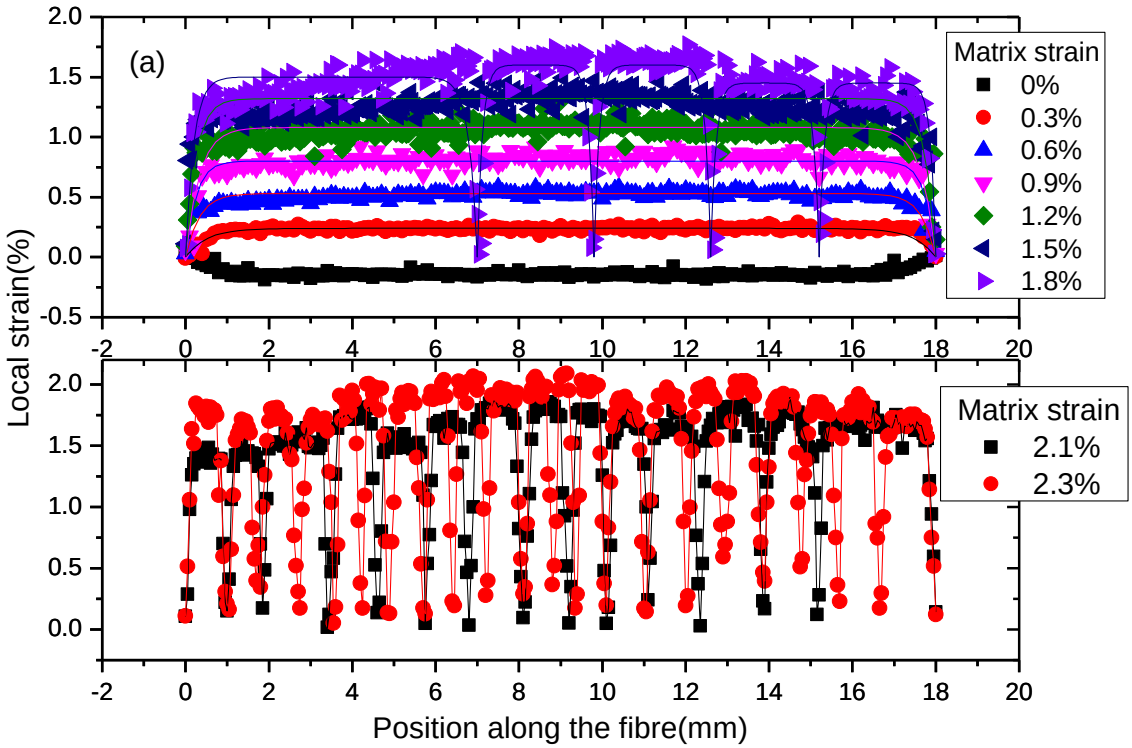

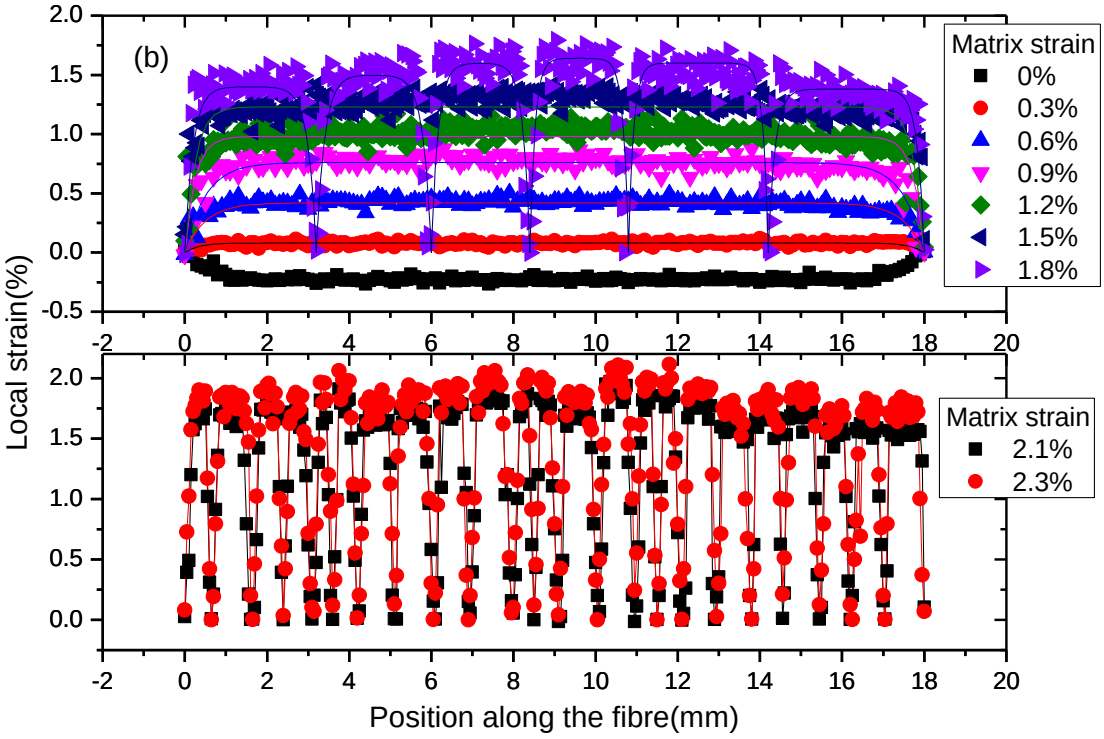

Figure 8.16 *Typical fibre local strain with respect to the distance along low modulus carbon fibre at an elevated matrix strain level with a coating of HiPCO SWNTs (a) and COOH SWNTs (b) as strain sensors.*

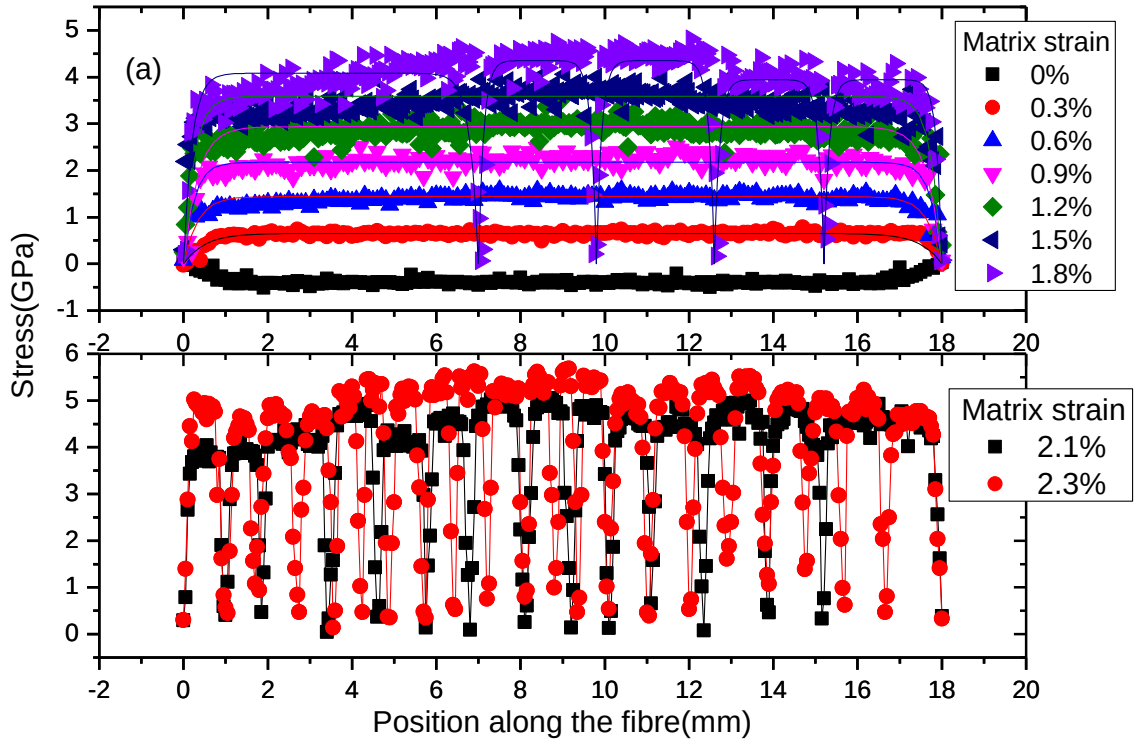

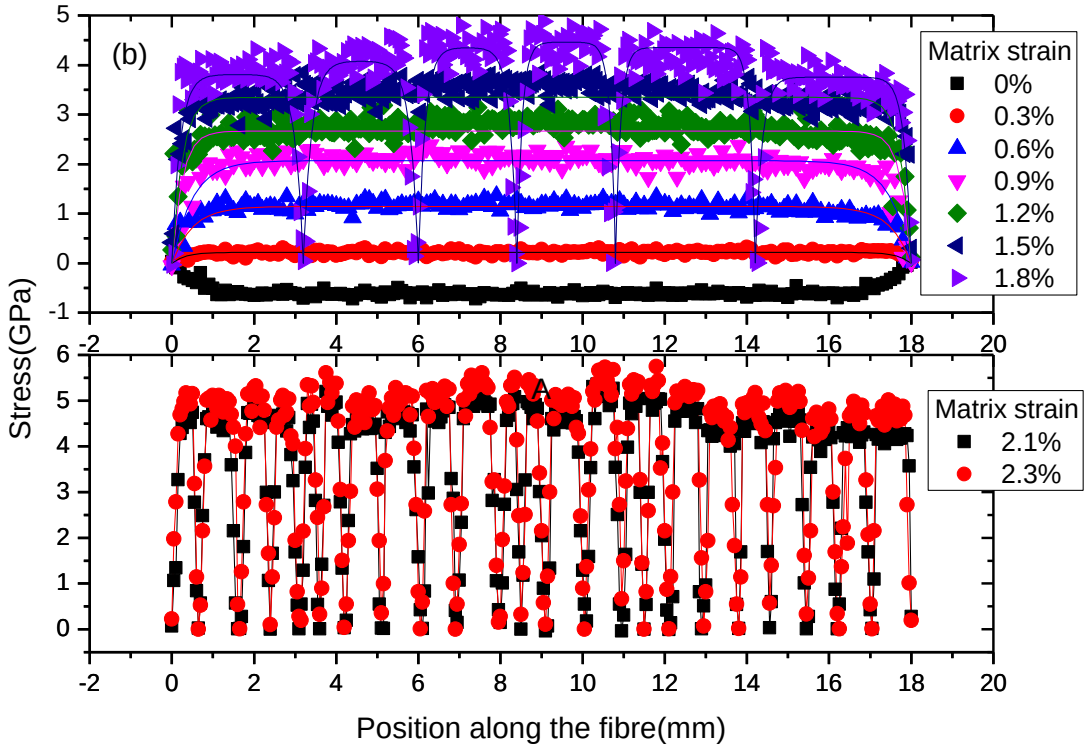

Figure 8.17 *Typical fibre local stress with respect to the distance along a low modulus carbon fibre at elevated matrix strain levels with HiPCO SWNTs (a) or COOH SWNTs (b) as strain sensors.*

The ineffective stress transfer lengths for both systems were also analysed as shown in Figure 8.18. As the ineffective stress transfer lengths are only comparable if the sample fibre length are the same, the ineffective stress transfer length of both types of sample systems at matrix strain levels of 0.3%, 0.6%, 0.9%, 1.2% and 1.5% have been analysed where low modulus carbon fibre in both sample systems have not started to break. As shown in Figure 8.18, the ineffective stress transfer length was calculated from the left end of the fibre to the vertical dotted line which was drawn when the fitted data beginning to plateau. The determined ineffective stress transfer lengths are shown in Table 8.3. The system using COOH SWNTs as strain sensors have shorter ineffective stress transfer lengths except at a matrix strain level of 0.3%. The shorter the ineffective stress transfer length, the better the interfacial bonding. Clearly the sample coated with COOH SWNTs could therefore have higher interfacial shear strength than the system that used HiPCO SWNTs as strain sensors.

Table 8.3 *Ineffective stress transfer length of sample systems sensed by both types of SWNTs at lower applied matrix strain levels.*

Matrix Sample systems / Strain level	LMCF/Epoxy + HiPCO SWNTs	LMCF/Epoxy + COOH SWNTs
	Ineffective transfer length(mm)	
0.3%	0.89 ±0.07	1.41 ±0.06
0.6%	2.09 ±0.05	1.32 ±0.05
0.9%	2.52 ±0.07	1.3 ±0.05
1.2%	1.36 ±0.05	1.03 ±0.04
1.5%	1.18 ±0.07	0.69 ±0.05

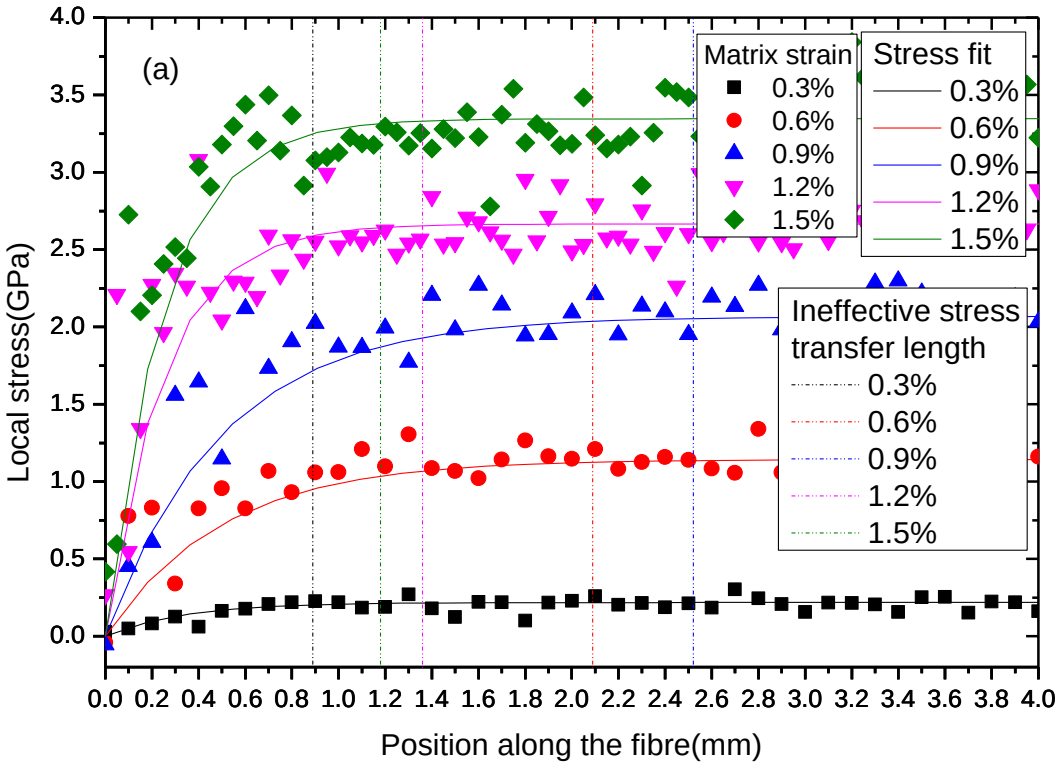

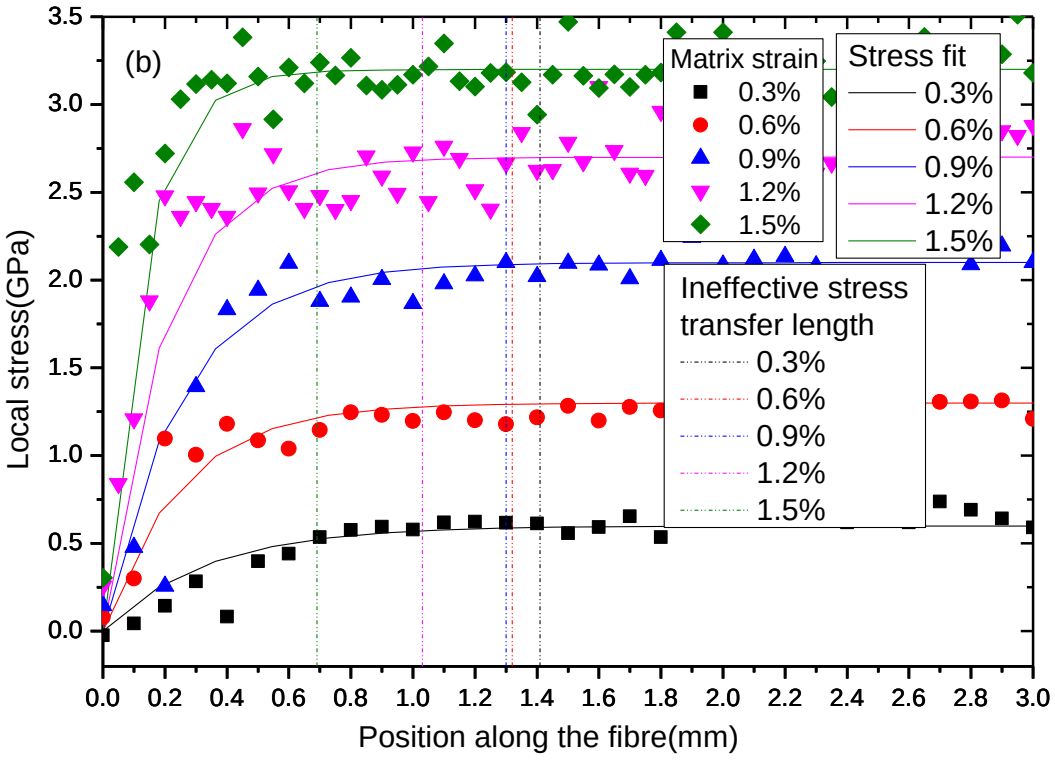

Figure 8.18 *Ineffective stress transfer length measurements for composite interfaces sensed using HiPCO SWNTs (a) and COOH SWNTs (b) at matrix strain levels of 0.3%, 0.6%, 0.9%, 1.2% and 1.5%.*

8.4.1.2 Interfacial Shear Stress (ISS) Determination

The strain maps along the low modulus carbon fibres for both nanotube systems were then converted into interfacial shear stress using Equation 8.4. The variations of interfacial shear stress along the low modulus carbon fibres at elevated matrix strain are shown in Figures 8.19 and 8.20 for the systems with HiPCO and COOH SWNTs as strain sensors respectively. Again, similar to other systems of the same morphology, higher ISS was determined at the end of each of the fragments, and ISS approaches zero in the central region of each fragment.

When comparing the ISS distribution along the low modulus carbon fibre for the systems sensed by HiPCO SWNTs and COOH SWNTs it is first noted that the highest ISS obtained for the system sensed by HiPCO SWNTs is 53.93±0.06 MPa which is at the central region of the sample when the matrix strain is at the highest level of 2.3%. However, for the system sensed using COOH SWNTs, the highest ISS determined was 62.29±0.06 MPa, significantly higher than for the HiPCO system. Both values are

higher than a reasonable epoxy matrix yield stress (40-50 MPa), however, there were no matrix yield determined in Figure 19 and Figure 20 for both types of sample systems. This could be due to that the coating of SWNTs at the interface has improved the matrix yield stress since the SWNTs on fibre surface will diffuse into epoxy matrix. Previous study by Sager *et al.*(2009) reported that the presence of CNTs at matrix can improve the interfacial yield strength. Secondly, it can be seen that there is no fully debonding occurred for the sample system using HiPCO SWNTs as strain sensor as mostly are partly debonding model. When applied matrix strain is 2.1%, the fragments in the system using COOH SWNTs show mostly in elastic deformation with just two fragments fully debonded, but for system using HiPCO SWNTs, most fragments are in partly debonding model. Thirdly, according to Figure 8.19(b) and 8.19(c) and Figure 8.20(b) and 8.20(c), when the matrix strain is at 2.1% and 2.3%, the determined highest ISS at the end of each fragment is slightly higher for the system sense using COOH SWNTs than for the system using HiPCO SWNTs. It can be concluded from the interfacial behaviour and ISS values described above that interfacial bonding between the matrix and low modulus carbon fibre of the system sensed by COOH SWNTs was better than the system using HiPCO SWNTs.

During a fragmentation, the stored energy of a sample was normally released from matrix yield or interfacial debonding between fibre and matrix or in most cases them both together. In this study, according to Figure 8.19 and Figure 8.20 debonding is the main factor that resulted in the energy release during fragmentation process for both types of sample systems. However, there is one matrix yielding detected at the right end of the fibre for the system using COOH SWNTs. An evidence of this shows in Figure 8.20(b) and(c), the highest ISS was obtained at the right end of fibre with the value of 62.29 ± 0.06 MPa when the applied matrix strains of 2.1%. However, this ISS at the right end of fibre stopped increasing when the applied matrix strain increased to 2.3%, it remains constant with the value of 62.29 ± 0.06 MPa for the length of 0.18 ± 0.05mm at both ends of this fragment. Since the matrix yield stress of a pure epoxy was about 40 ~ 50 MPa, the presence of SWNTs at the interface (diffused into epoxy matrix) could possibly improved the matrix yield strength, so 62.29 ± 0.06 MPa could be the value of improved matrix yield strength. An optical microscope image taken at the right end of the low modulus carbon fibre for this sample (see Figure 8.21) also give a solid proof of matrix yielding happened at this place.

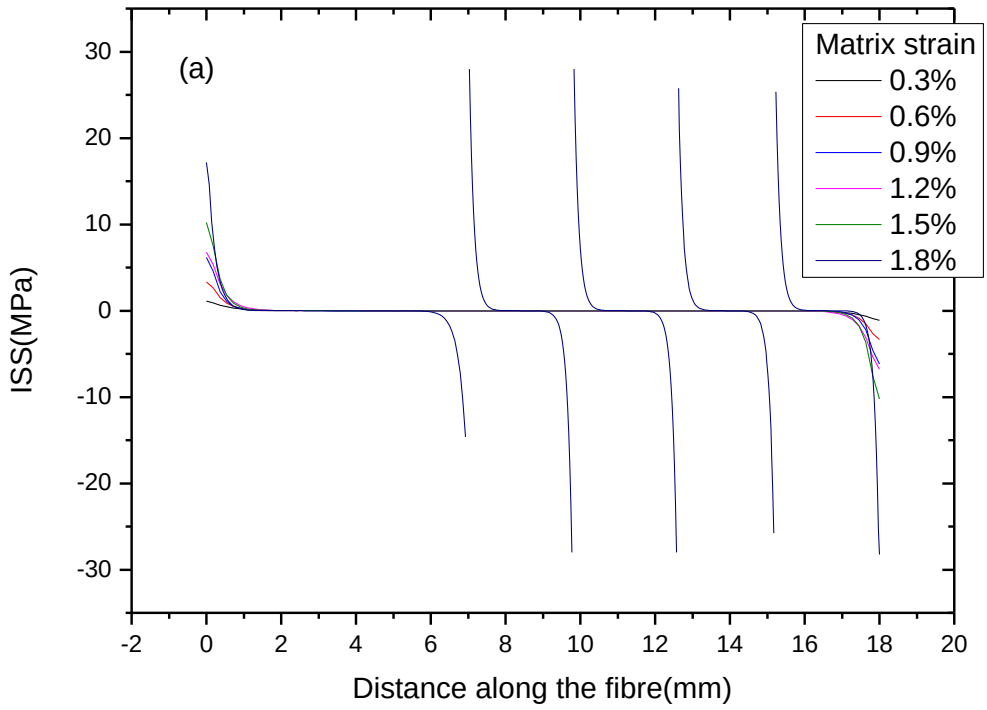
(a)
Matrix strain
0.3%
0.6%
0.9%
1.2%
1.5%
1.8%
ISS(MPa)
Distance along the fibre(mm)
30
20
10
0
-10
-20
-30
-2
0
2
4
6
8
10
12
14
16
18
20

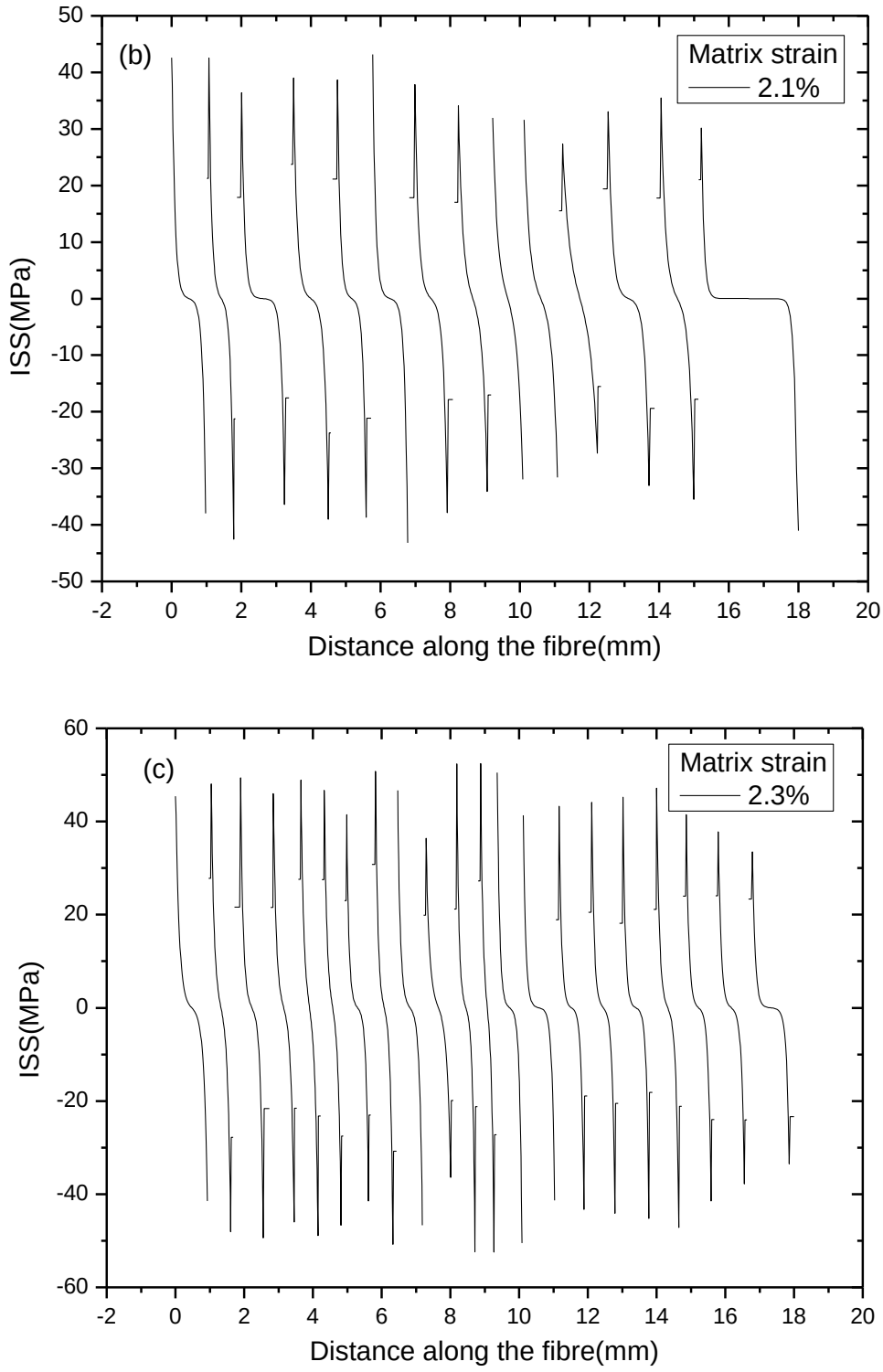

Figure 8.19 *Interfacial shear stress distributions for a low modulus carbon fibre and an epoxy resin system sensed using HiPCO SWNTs at different matrix strain levels; (a) matrix strain levels of 0.3%, 0.6%, 0.9%, 1.2%, 1.5% and 1.8% and (b) matrix strain levels of 2.1% and 2.3%.*

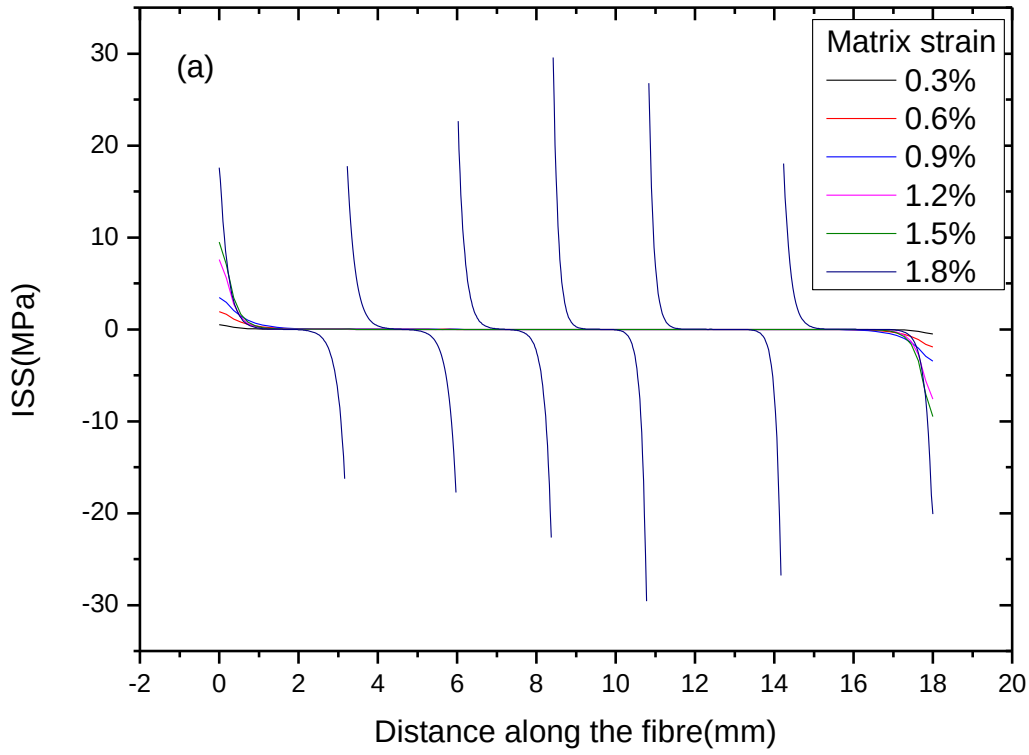
(a)
Matrix strain
0.3%
0.6%
0.9%
1.2%
1.5%
1.8%
ISS(MPa)
Distance along the fibre(mm)

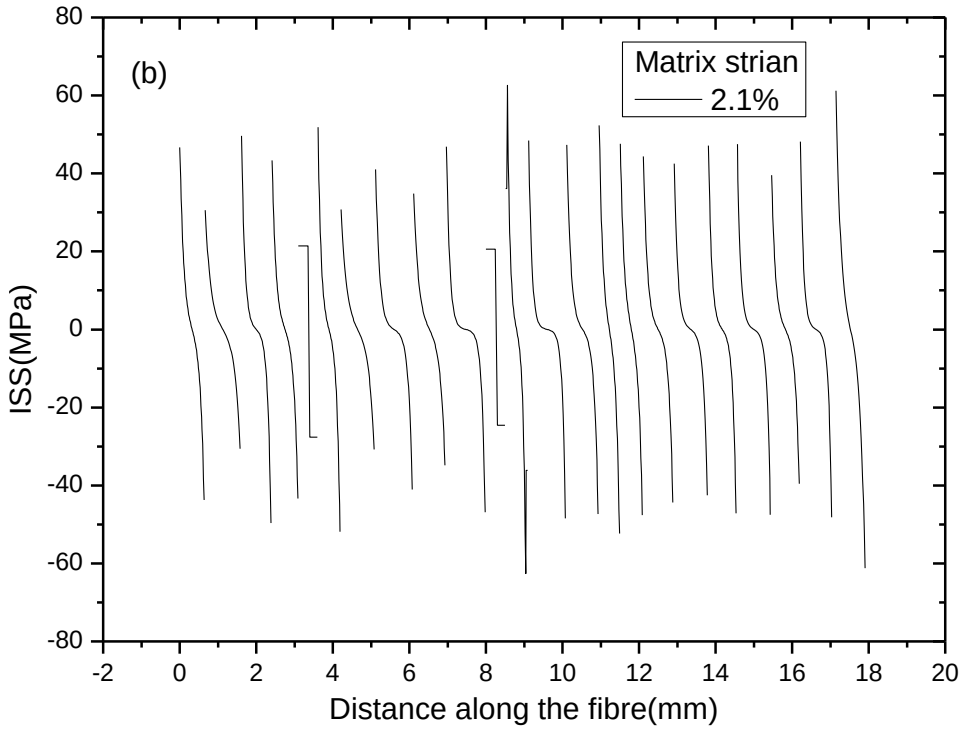
(b)
Matrix strian
2.1%
ISS(MPa)
Distance along the fibre(mm)

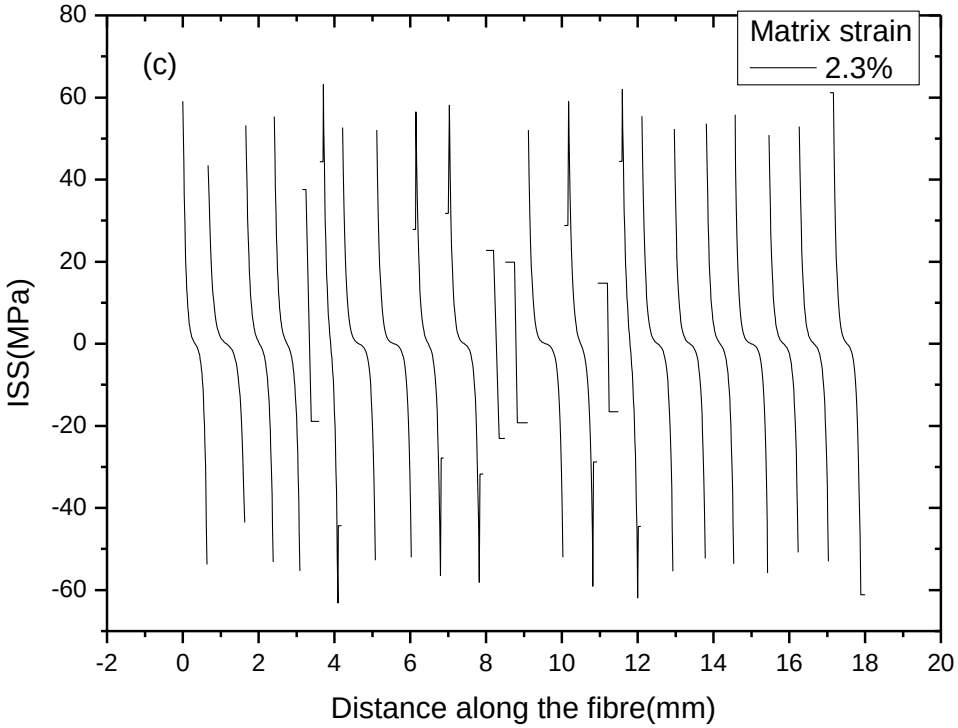

Figure 8.20 *Interfacial shear stress distributions for a low modulus carbon fibre and an epoxy resin system sensed using COOH SWNTs at different matrix strain levels; (a) matrix strain levels of 0.3%, 0.6%, 0.9%, 1.2%, 1.5% and 1.8% and (b) matrix strain levels of 2.1% and 2.3%.*

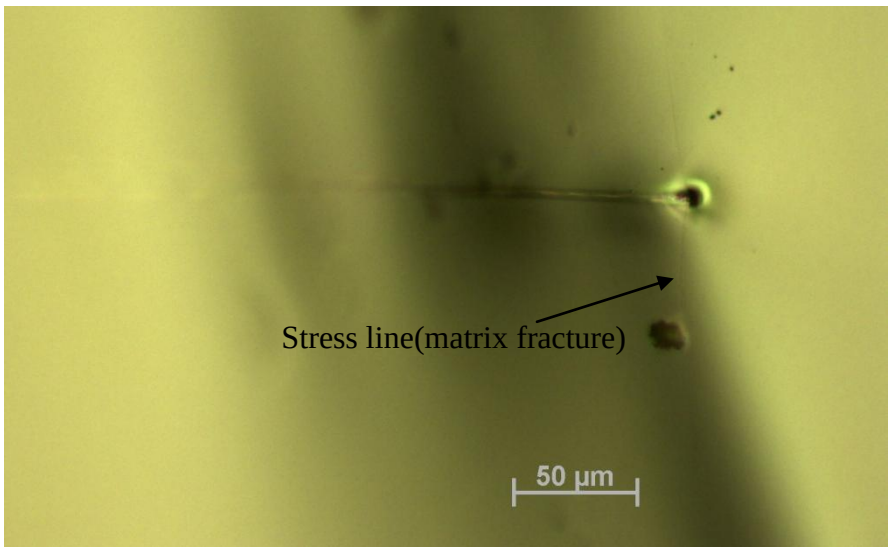

Figure 8.21 *Optical image of the right end of a low modulus carbon fibre for the sample that used COOH SWNTs as strain sensors at the matrix strain level of 2.3%.*

8.4.2 Conventional Fragmentation Test

After the analysis of the fragmentation process by using Raman technique, both types of sample systems were studied using the conventional method of observing and measuring each fragment under the optical microscope in the Raman system (see Figure 8.22). It should be noted that the crack of the fibre have also extended into the matrix according to Figure 8.22.

Every fragment length for each of the systems sensed by HiPCO SWNTs and COOH SWNTs at matrix strain levels of 1.8%, 2.1% and 2.3% were measured using the micrometer which was mounted on the optical microscope stage. All data are reported in Table E.2 of Appendix E. The numbers of fragments were counted and plotted against the matrix strain as shown in Figure 8.23. It can be seen that when the applied matrix strain is 2.1%, the number of fragments for the system using COOH SWNTs reaches saturation. However, for the sample system using HiPCO SWNTs as a strain sensor, this still increases beyond 2%. The epoxy resin matrix normally fractures at a strain level of 2.3%. Therefore saturation is not achieved before the failure of the matrix.

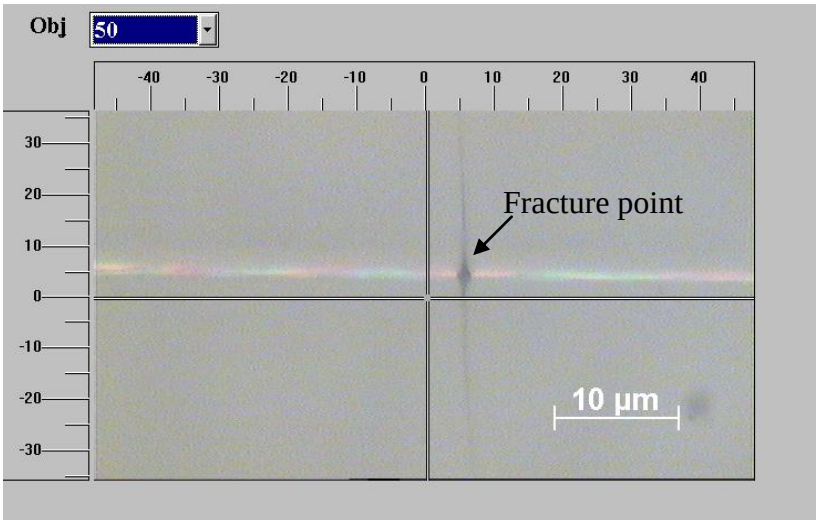

Figure 8.22 *Typical fracture observed under an optical microscope of Raman system for the sample of low modulus carbon fibre/epoxy composite with SWNTs coated on the fibre surface.*

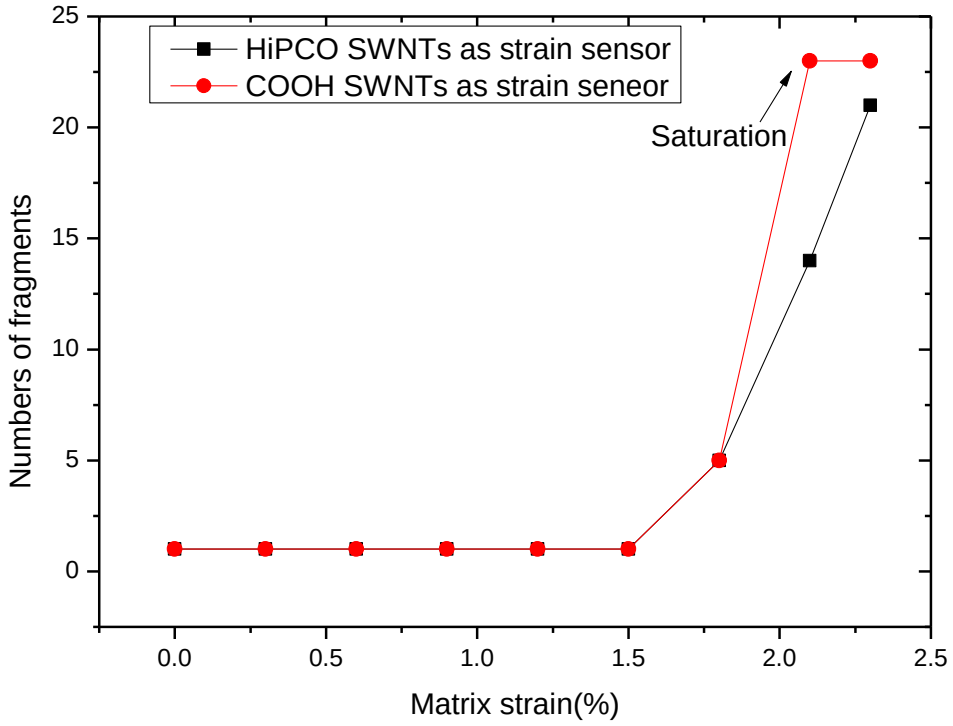

Figure 8.23 *The numbers of fragments for both types of composite sample at elevated matrix strain levels.*

According to Table E.2 of Appendix E, the average fragment lengths at matrix strain levels of 1.8%, 2.1% and 2.3% for both types of sample systems were calculated. Then using Equation 8.3, with the average fragment length at the matrix strain level of 2.3% and the breaking strength of a low modulus carbon fibre determined from tensile testing, the interfacial shear strength for both systems were calculated. These data are reported in Table 8.4. The fragmentation tests for both the conventional and Raman approaches show that the COOH SWNTs system has a higher ISS. This indicates that this form of nanotube forms a better interface between the resin and the fibre. As have discussed before, the ISS determined using the Raman technique is normally higher than that determined using the conventional method.

Table 8.4 *The determined average fragment length, critical length, IFSS obtained in conventional method (C) and Raman method (R) for both types of sample systems.*

Sample system	$l_f(mm)$	$l_c(mm)$	$\tau_c(MPa)$	$\tau_{R_{max}}(MPa)$
LMCF/Epoxy + HiPCO SWNTs	0.87 ±0.05	1.16 ±0.01	25.21 ±0.02	53.93 ±0.06
LMCF/Epoxy + COOH SWNTs	0.79 ±0.05	1.05 ±0.01	27.93 ±0.02	62.29 ±0.06

8.5 High Modulus Carbon Fibre Composite System using SWNTs as Strain Sensors

Fragmentation tests for high modulus carbon fibres coated with HiPCO SWNTs and COOH SWNTs were also carried out. Again, fragmentation tests were carried out using both the Raman technique method and the conventional approach.

8.5.1 Fragmentation Test Analysed by Using Raman Technique

8.5.1.1 Strain/Stress Mapping by Using Raman Spectroscopy

The experimental process was the same as that for the high modulus carbon fibre/epoxy sample system. The scanning time at each point was however reduced to 10s as the SWNTs are highly Raman active and a strong 2D band can be easily obtained in a short time. Figure 8.24 reports typical Raman 2D band positions from HiPCO SWNTs and COOH SWNTs respectively as a function of the distance along a high modulus carbon fibre.

Again, the 2D Raman band positions along the fibre were converted into local fibre strain and stress by using the calibration from a single fibre deformation test. The obtained strain and stress maps for both nanotube systems are shown in Figure 8.25 and Figure 8.27 respectively.

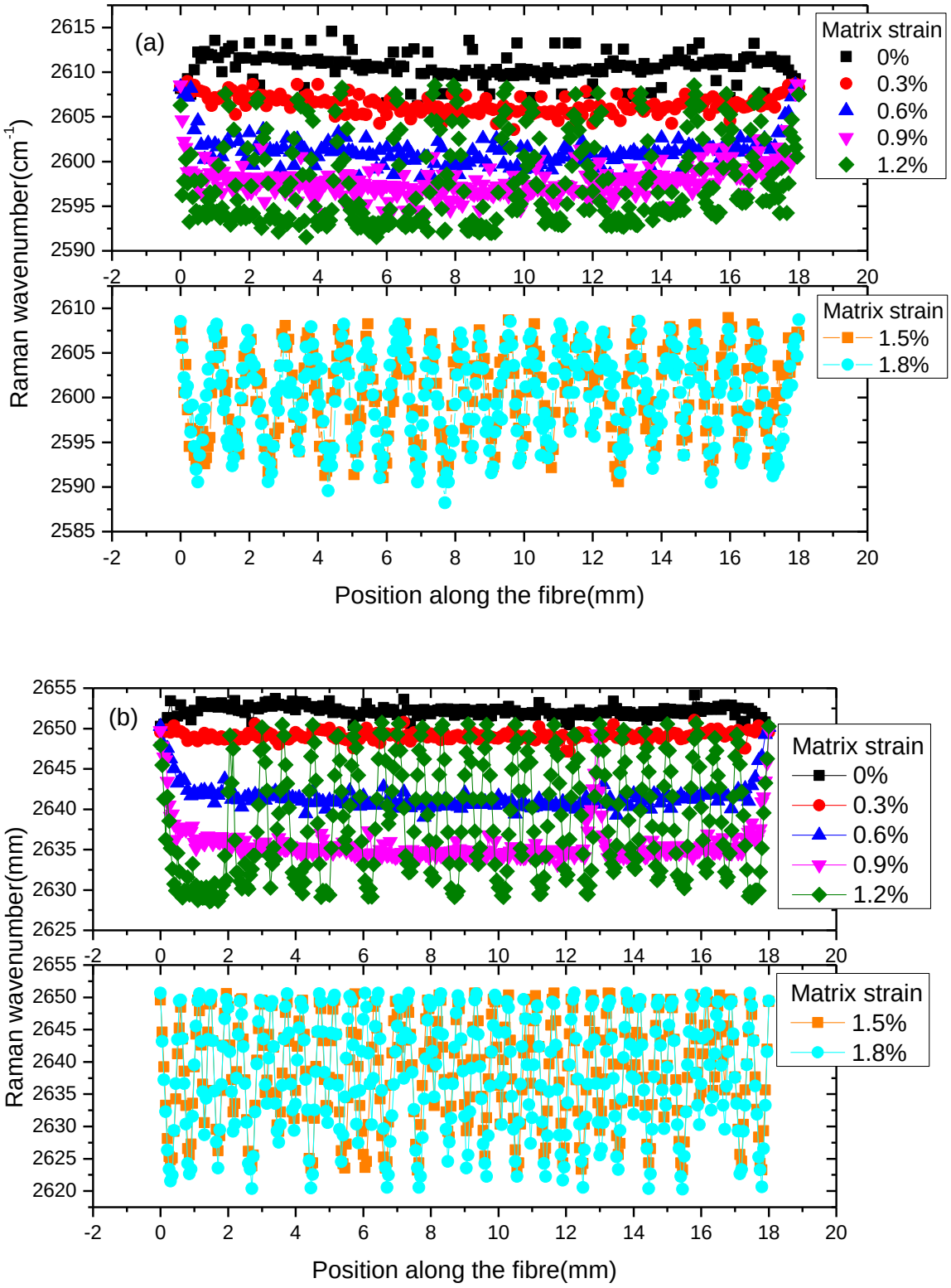

Figure 8.24 *Typical Raman 2D band frequencies from HiPCO SWNTs (a) and COOH SWNTs (b) related to the distance along the high modulus carbon fibre at elevated matrix strain.*

As for all the previous hot cured composite systems, the high modulus carbon fibres were in compression with no external deformation, as shown in Figure 8.25. It is also important to note that the local strain along the embedded fibre length at all applied matrix strain levels was slightly lower than the matrix strain, and again this is thought to be caused by the thermal compressive stress and possibly the fragment lengths are below the critical length.

The high modulus carbon fibre coated with HiPCO SWNTs started to fragment when the matrix strain level reached 1.2% (see Figure 8.25(a)). However, for the sample system coated with COOH SWNTs, as shown in Figure 8.25(b), the fracture started earlier at a matrix strain level of 0.9%. Furthermore, it can also be generally seen that for both types of sample the number of fragments reached a saturation stage when applied matrix level increased to 1.5%. The details will be discussed together with the fragmentation in conventional method.

For both types of sample, due to the uniformly distributed compressive stress along the fibre embedded length, the data can be fitted using Nairn's shear-lag model as expressed in Equations 8.7 and 8.8 respectively(Nairn, 1997). When the applied matrix level reached 1.5% and 1.8%, the debonded model by Piggott (1980) was applied to most fragments, as can been from the linear line fits displayed in Figure 8.25. In order to show these fits more clearly, the strain distribution of a magnified region for both types of sample at matrix strain levels of 1.5% and 1.8% are shown in Figure 8.26.

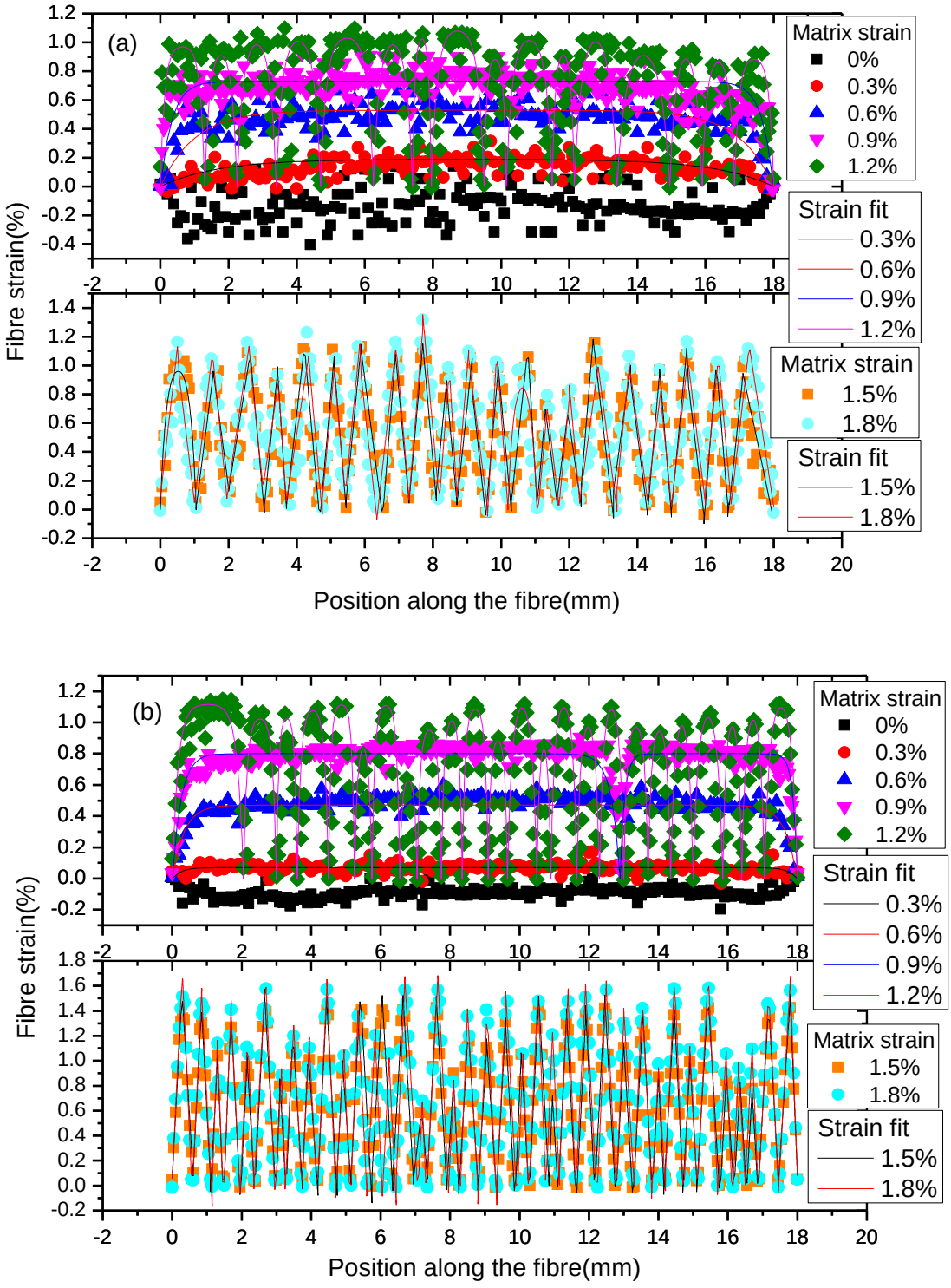

Figure 8.25 *Typical fibre local strain with respect to the distance along a high modulus carbon fibre at elevated applied matrix strain levels with HiPCO SWNTs (a) or COOH SWNTs (b) used as strain sensors.*

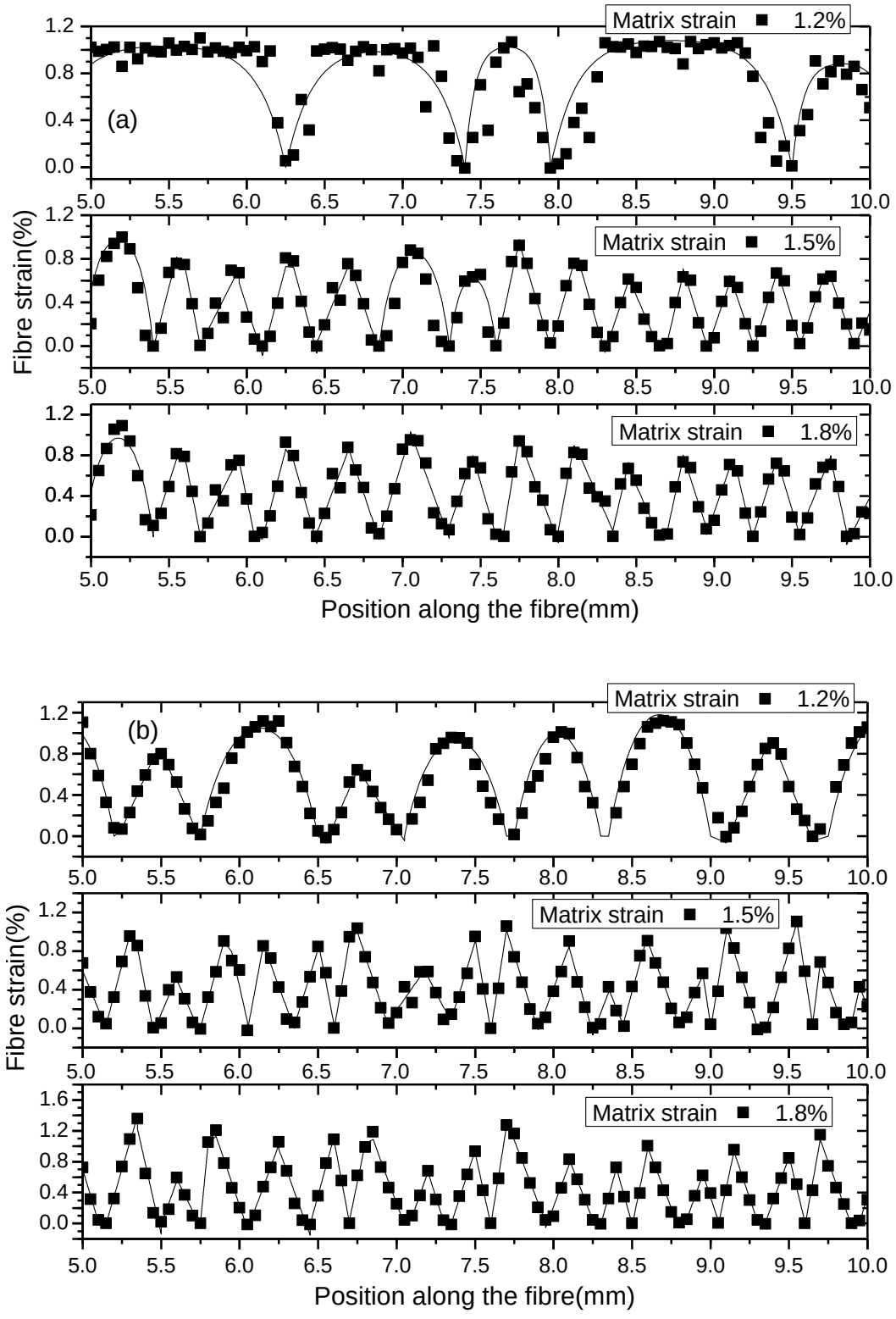

Figure 8.26 *Fibre local strain with respect to the distance of a certain region from 5mm to 10mm along a high modulus carbon fibre at matrix strain levels of 1.2%,1.5% and 1.8% with HiPCO SWNTs (a) or COOH SWNTs (b) used as strain sensors.*

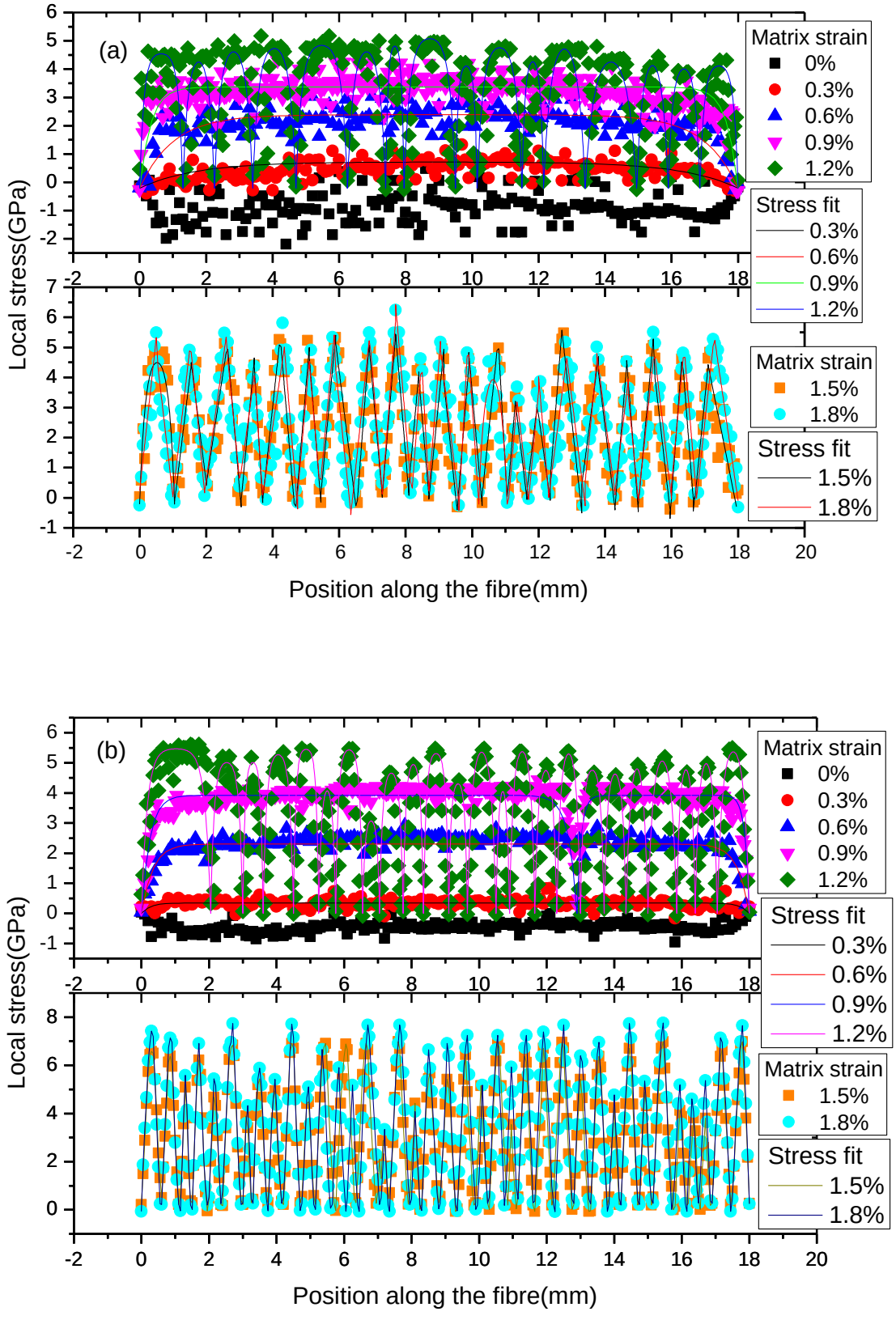

Figure 8.27 *Typical fibre local stress regard the distance along high modulus carbon fibre at elevated applied matrix strain levels with HiPCO SWNTs (a) or COOH SWNTs (b) as strain sensors.*

Raman band positions along the fibre were converted into fibre local stress as shown in Figure 8.27. It is generally observed that at higher applied strain levels of 1.2%, 1.5% and 1.8%, the average maximum stress of each fragment from the sample system sensed by COOH SWNTs is higher than that of sample system sensed by HiPCO SWNTs. This indicates that a better interfacial bonding occurs for the sample system used COOH SWNTs as strain sensor as the highly polar COOH groups reacted with the polar groups from epoxy, thus created better bonding at the interface. More details of the reacting is given in Section 7.7.

Ineffective stress transfer length which is defined as the length from fibre left end to the point stress plateau was analysed for both types of sample as shown in Figure 8.28. The determined ineffective transfer lengths varied significantly for both systems as displayed in Table 8.5. First of all, it is clear that the value for the sample system using COOH SWNTs as strain sensor is much smaller than for HiPCO SWNTs. This could be due to the fact that the former system has a better interfacial bonding with the matrix.

Table 8.5 *Ineffective stress transfer lengths for composite samples sensed using both types of SWNTs at lower applied matrix strain levels.*

Matrix / Sample systems / Strain level	Samples using HiPCO SWNTs as strain sensor	Samples using COOH SWNTs as strain sensor
	Ineffective transfer length(mm)	
0.3%	2.76 ±0.03	0.77 ±0.05
0.6%	2.12 ±0.04	1.01 ±0.03

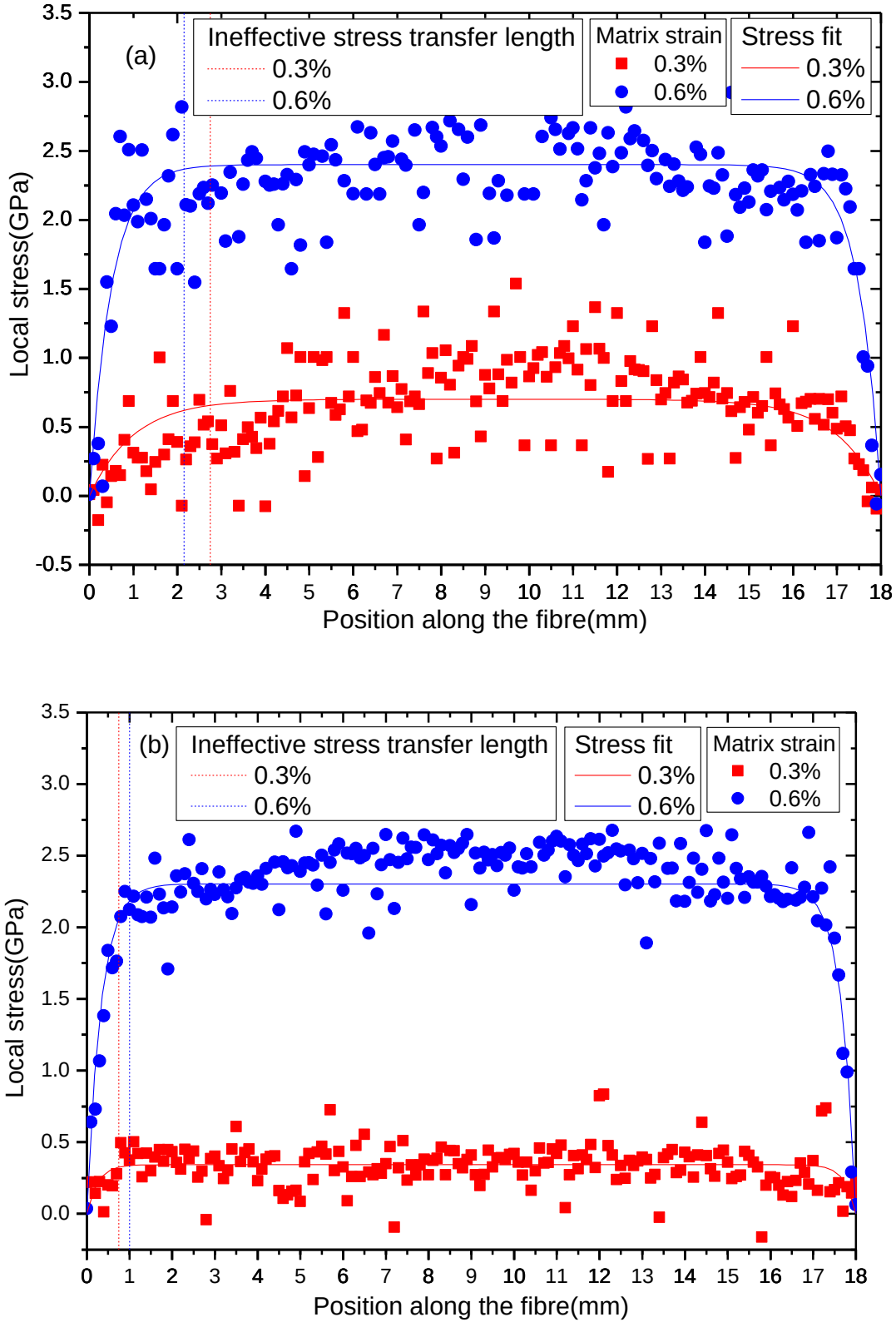

Figure 8.28 *Ineffective stress transfer length measurement for samples systems sensed by HiPCO SWNTs (a) and COOH SWNTs (b) at matrix strain levels of 0.3% and 0.6%.*

8.5.1.2 Interfacial Shear Stress (ISS) Determination

By using Equation 8.4, the strain mappings of the two types of system using HiPCO SWNTs and COOH SWNTs were converted into interfacial shear stresses as shown in Figure 8.29 and Figure 8.30 respectively. It is clear that a higher ISS was always obtained from the elastic deformation fragments which are not fully debonded for both types of sample. For the samples made using HiPCO SWNTs as strain sensors, the maximum interfacial shear stress was 53.14 ± 0.30 MPa from the left end of a partly debonded fragment when the applied matrix strain was at 1.8%. Meanwhile, the maximum ISS obtained for a sample using COOH SWNTs as strain sensors was much higher with a value of 64.82 ± 0.50 MPa.

When comparing the ISS between these two types of samples systems, according to Figure 8.29 and Figure 8.30, the ISS of the system using COOH SWNTs as strain sensors have higher values than for HiPCO SWNTs at each matrix strain level. When the matrix strain level was at 1.2%, it can be seen for Figure 8.29 (a) that the maximum ISS for most fragments was between 20 MPa and 30 MPa; and according to Figure 8.30(a), the values of the maximum ISS for most fragments were between 30MPa and 40MPa. While at a matrix strain level of 1.5%, the maximum values of ISS for fully-bonded or partly-debonded fragments of the HiPCO SWNTs system were between 30MPa and 40 MPa. For the COOH SWNTs system, as shown in Figure 8.30(b), the maximum values were around 60MPa. As the matrix strain level increased to 1.8%, it can be seen from Figure 8.29(c) that the HiPCO SWNTs sample has several fragments that remained fully-bonded along the left hand end of the fibre length. However, the COOH SWNTs system has just one fragment that remains fully-bonded at the position of 4.73 ± 0.05mm. The highest ISS value of 64.82 ± 0.50 MPa was determined from a partly debonded fragment at the right end of fibre for the COOH SWNTs system. These data first indicate that the interface has been significantly improved by the coating COOH SWNTs on the high modulus carbon fibres. Furthermore, with the value greater than the pure epoxy matrix yield strength (40 ~ 50 MPa), again it could be due to that the existence of SWNTs have improved the matrix yield strength.

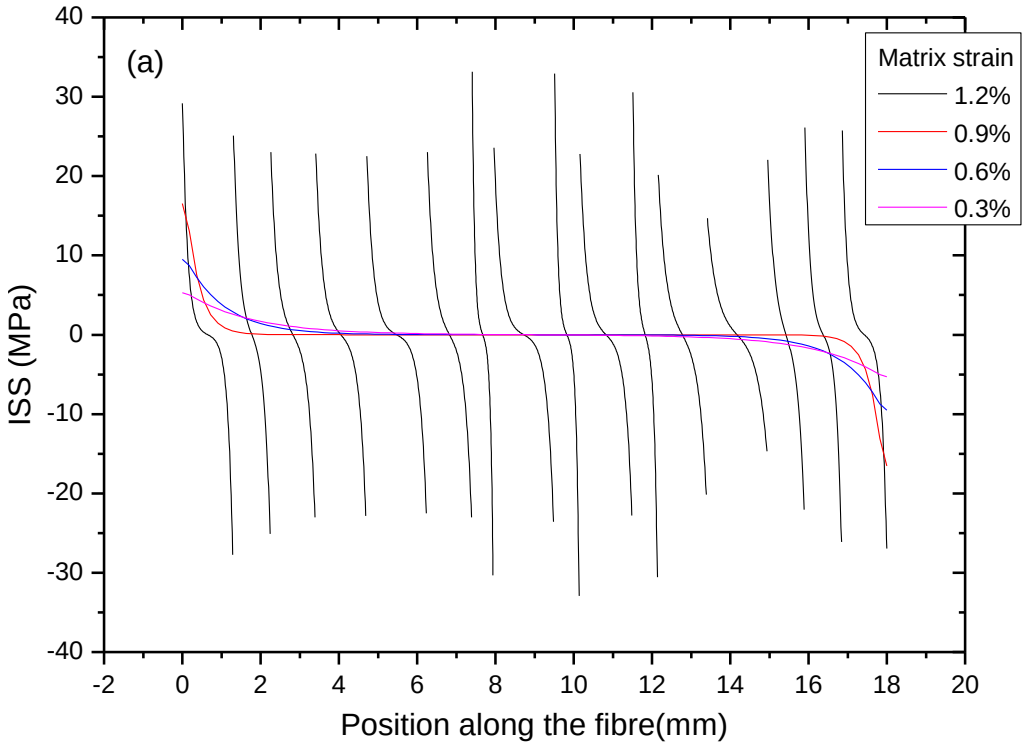
(a)
Matrix strain
1.2%
0.9%
0.6%
0.3%
ISS (MPa)
Position along the fibre(mm)

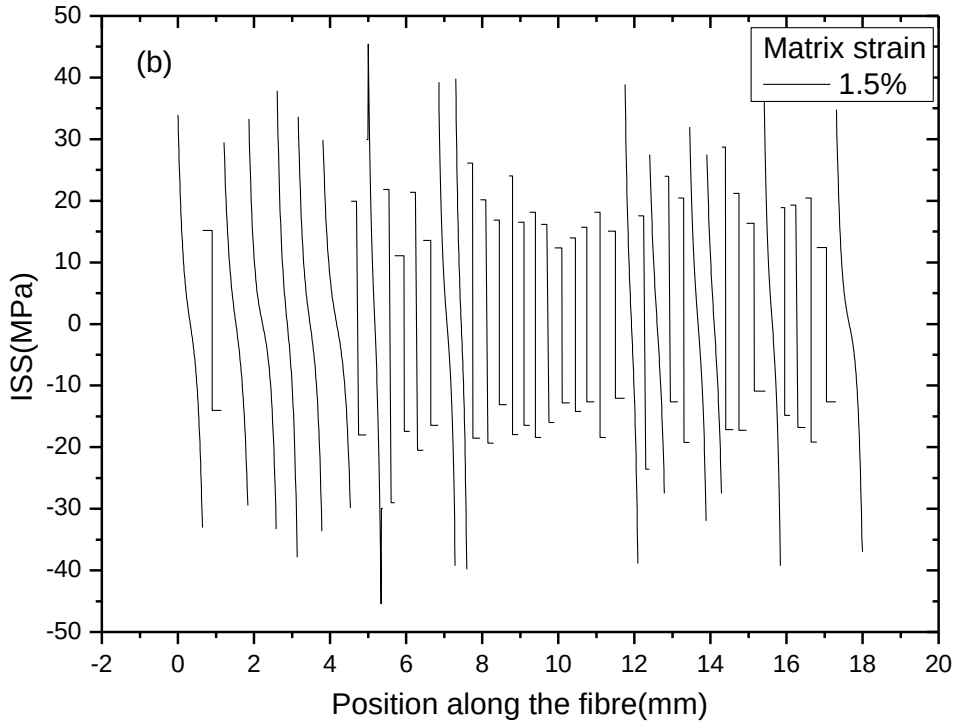
(b)
Matrix strain
1.5%
ISS(MPa)
Position along the fibre(mm)

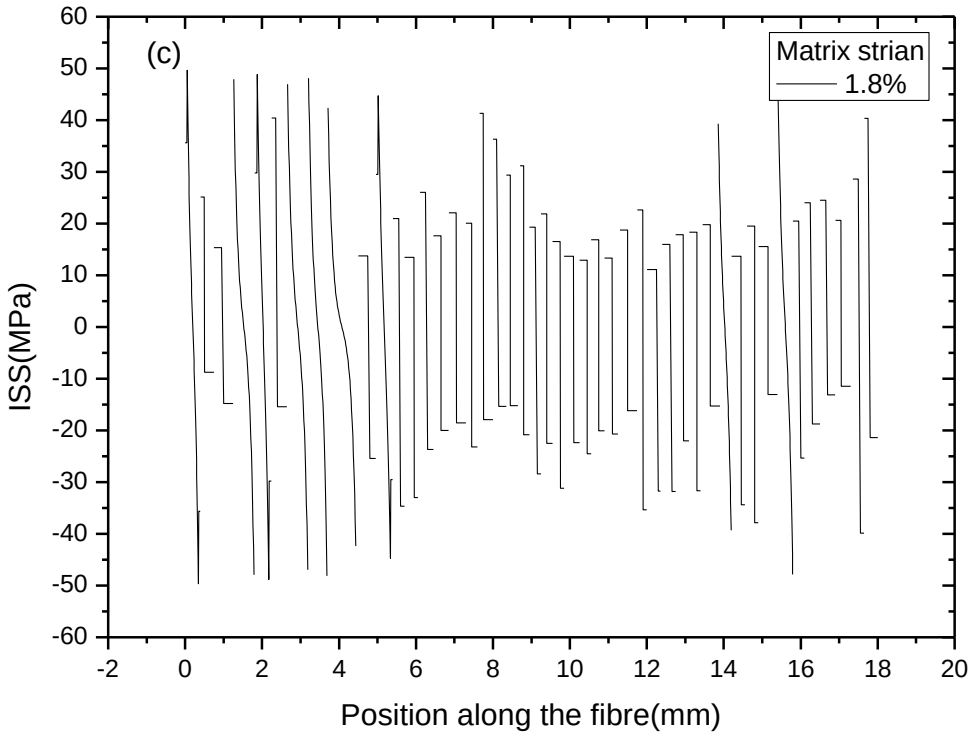

Figure 8.29 *Interfacial shear stress distributions for a high modulus carbon fibre and an epoxy resin system with HiPCO SWNTs used as strain sensor at different matrix strain levels; (a) matrix strain levels of 0.3%,0.6%,0.9% and 1.2%; (b) matrix strain of 1.5%; (c) matrix strain of 1.8%.*

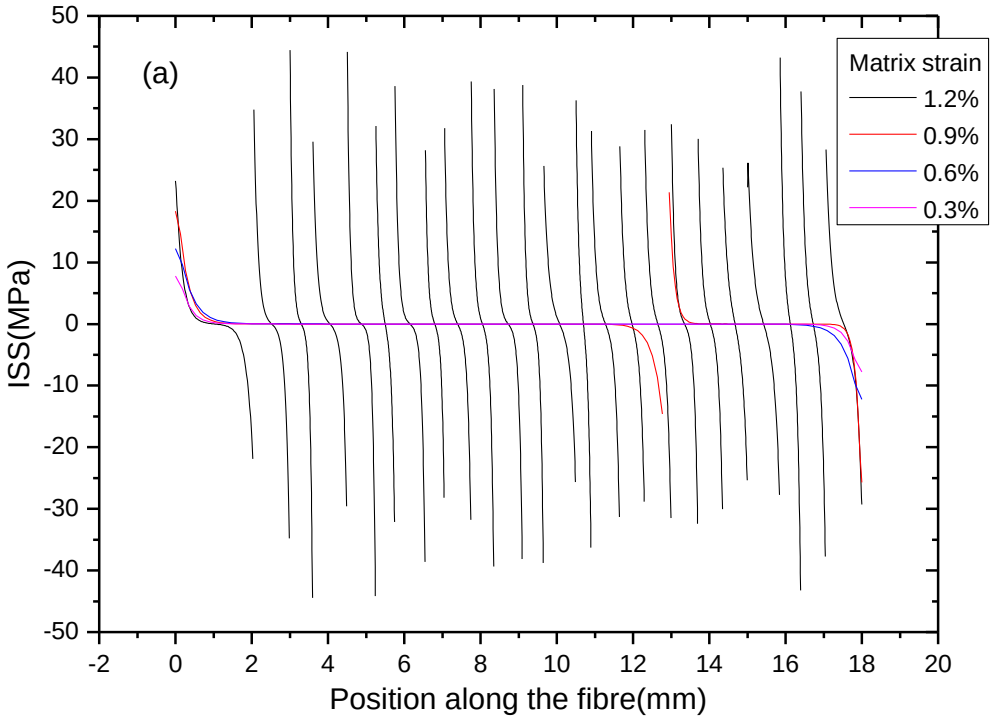

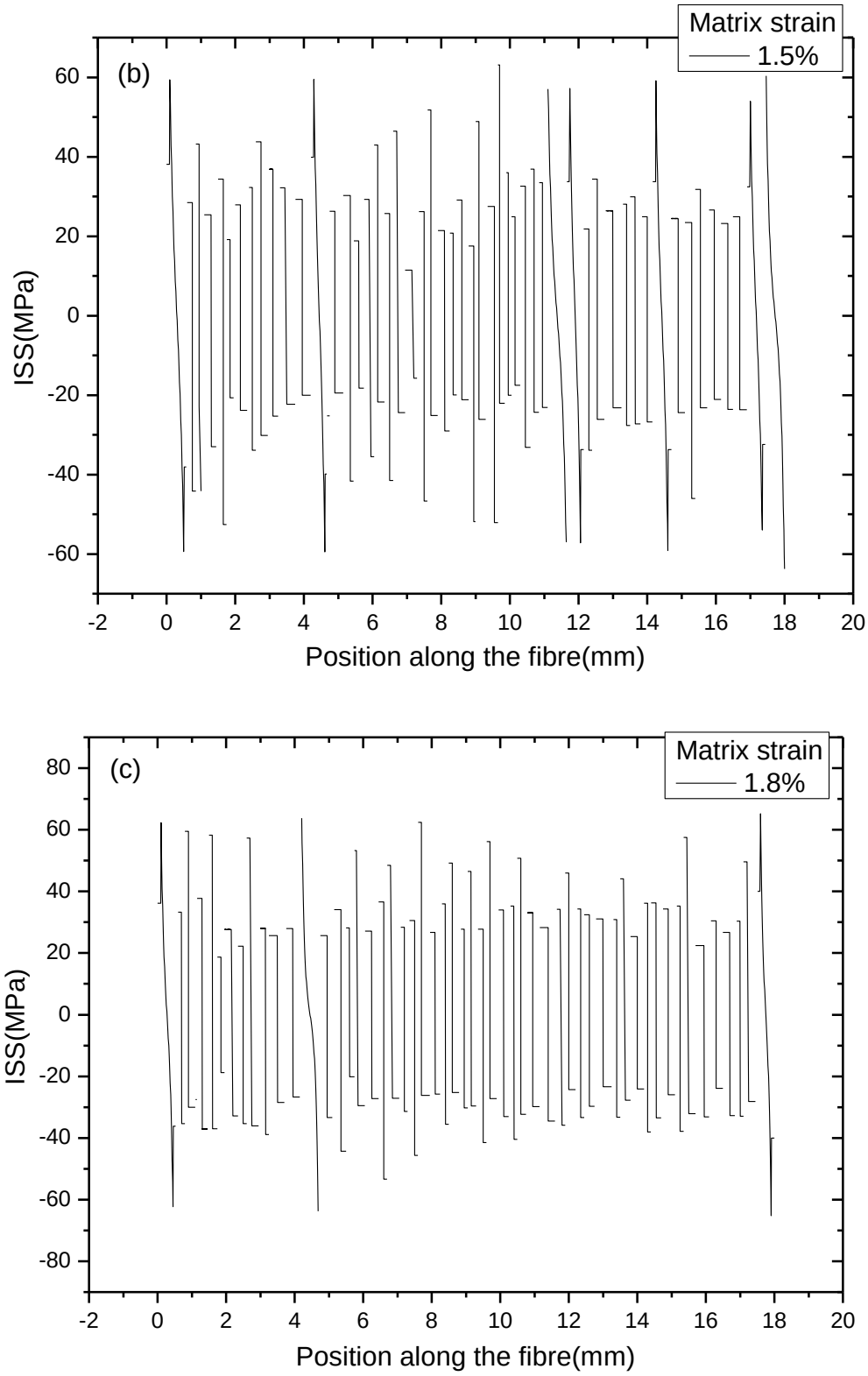

Figure 8.30 *Interfacial shear stress distribution for a high modulus carbon fibre and an epoxy resin system with COOH SWNTs used as strain sensors at different matrix strain levels; (a) matrix strain levels of 0.3%,0.6%,0.9% and 1.2%; (b) a matrix strain of 1.5%; (c) a matrix strain of 1.8%.*

8.5.1.3 Matrix Yield Strength Improved Evidence

In order to prove that the SWNTs at the interface improve the interfacial (matrix) yield strength, the high modulus carbon fibre/epoxy samples have been deformed to strains of 2.1% and 2.3%.The maximum values of ISS from the fragments where inelastic deformation occurs in these three types of sample system (HMCF without SWNTs, HMCF with HiPCO SWNTs and HMCF with COOH SWNTs) have been recorded and are reported in Figure 8.31. For all samples it can be seen the ISS of the fragments increases to a maximum at a matrix strain of 1.8%. Following this the ISS decreases slightly, which suggests that it initially exceeds the matrix yield strength of the resin (which is reported to be around 43 MPa by Young and Andrews in 1994) after which inelastic deformation (matrix fracture) occurs with an increase in the matrix strain. The system with COOH SWNTs present appears to increase the point at which yield occurs to to 62.3 ± 3.0 MPa. A coating of HiPCO SWNTs increases the interfacial shear strength at which this occurs by a smaller amount to 52.6 ± 2.7 MPa. The reason that COOH SWNTs dramatically improved the interfacial yield strength could due to its better reinforcement of epoxy matrix as the carboxylic group on COOH SWNTs clearly have its advantages in chemical reaction with the amino and hydroxyl group from epoxy as described previously in Figure 7.17.

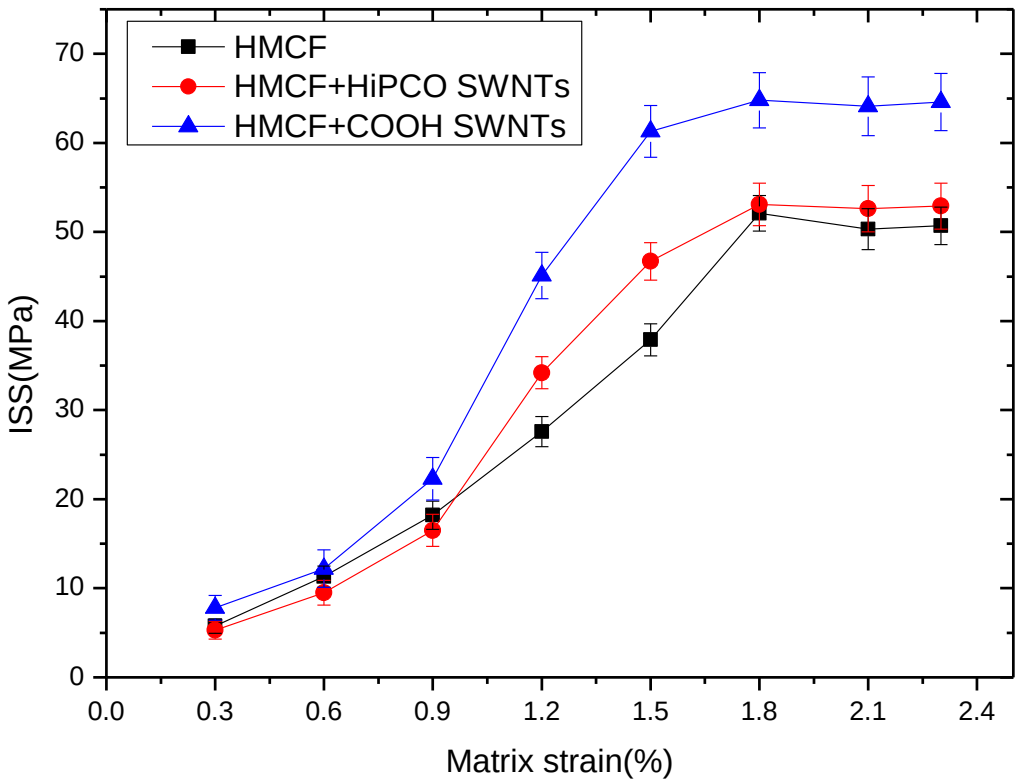

Figure 8.31*The maximum interfacial shear stress (ISS) from fragments exhibiting inelastic deformation observed from the three types of composite sample systems at elevated strain levels.*

8.5.2 Conventional Fragmentation Test

Same as other types of sample systems, conventional fragmentation tests of a high modulus carbon fibre and an epoxy resin composite with both HiPCO and COOH SWNTs as strain sensors have been analysed and the numbers of fragments at every matrix strain level for both systems were calculated, as shown in Figure 8.32. It can be seen the numbers of fragments for both types of sample systems reached a saturation level when applied matrix strain increased to 1.5%. The numbers of fragment for the COOH sample increased more rapidly with matrix strain. Furthermore, this sample has more fragments at the final saturation level.

The length of each fragment was measured at each applied matrix strain level for both samples and the average fragment length was calculated at the relevant matrix strain level; all these data are shown in Table E.3 of Appendix E. Using Equations 8.2 and 8.3,

the critical fragment length and interfacial shear strengths for both systems was calculated respectively and are reported in Table 8.6. The maximum interfacial shear stress using the Raman technique is also reported in Table 8.6 for comparison.

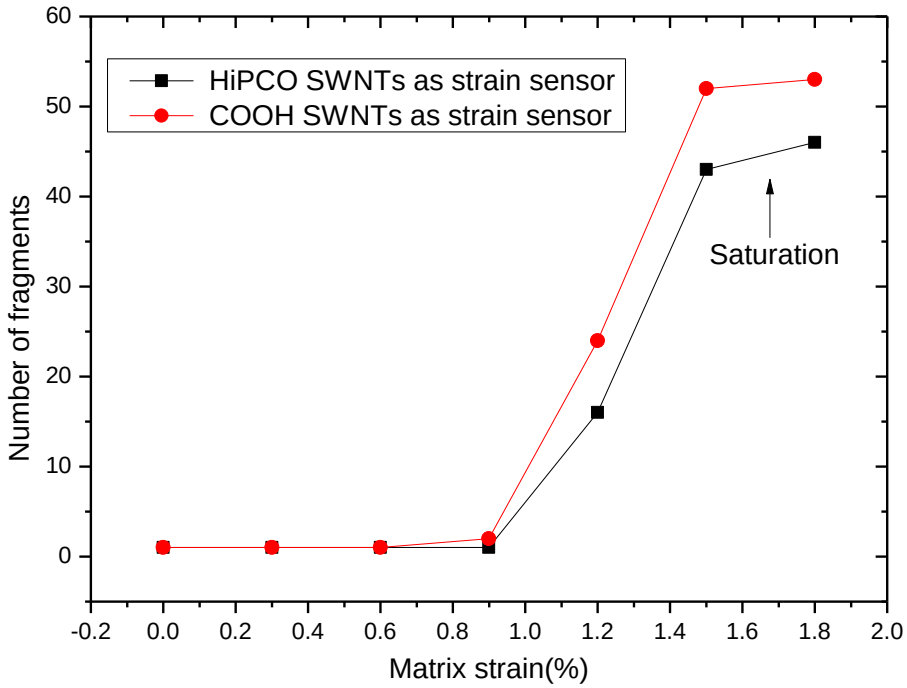

Figure 8.32 *The numbers of fragments for the composite sample systems using HiPCO SWNTs and COOH SWNTs as strain sensors at elevated matrix strain levels.*

Table 8.6 *The average fragment lengths, critical lengths, and ISS obtained using the conventional method and Raman method for both types of composite systems.*

Sample system	$l_f(mm)$	$l_c(mm)$	$\tau_c(MPa)$	$\tau_{R_{max}}(MPa)$
HMCF/Epoxy + HiPCO SWNTs	0.39 ±0.01	0.52 ±0.01	37.72 ±0.36	53.14 ±0.30
HMCF/Epoxy + COOH SWNTs	0.33 ±0.01	0.44 ±0.01	44.61 ±0.30	64.82 ±0.50

8.6 Conclusions

First of all, both HiPCO SWNTs and COOH SWNTs coated on carbon fibre surface have been effectively sensed the change of fibre local strain during the deformation of matrix samples.

Secondly, fragmentation test both in Raman technique and conventional ways for different types of sample systems have been carried out successfully as all the determined results were shown in Table 8.7. The sample system of high modulus carbon fibre and epoxy resin matrix microcomposites with COOH SWNTs as strain sensor was proved to have the highest interfacial shear stress. Obviously the existence of COOH SWNTs at the interface has significantly improved the interfacial bonding as the interfacial shear stress of the sample with COOH SWNTs coated on the fibre surface is much higher that of the sample without COOH SWNTs. However, when compared the sample systems of high modulus carbon fibre/epoxy matrix microcomposites with and without HiPCO SWNTs at the interface, it can be seen in Table 8.7 that either the value of interfacial shear strength determined in conventional method or the maximum interfacial shear stress obtained in Raman technique for both types of samples were very close with each other. This indicated that the coating of HiPCO SWNTs on fibre surface in this study have not modified the interfacial bonding too much beyond its original property. Therefore, it proved that HiPCO SWNTs could be a better strain sensor when comes to analyse fibre/matrix interface by using Raman spectroscopy without amending the interfacial bonding between the fibre and matrix. Thirdly, the interfacial shear strengths determined by using conventional method for low modulus carbon fibre/epoxy matrix microcomposite samples with both types of SWNTs as strain sensors are much lower than that of the high modulus carbon fibre/ epoxy microcomposite samples with the gap around 13 MPa. One reason for this is attributed to the higher breaking strain of the low modulus carbon fibre, the average fragment length is about twice of that for the high modulus carbon fibre samples, thus resulted in a low value of interfacial shear strength as it is inverse proportional to the average fragment length. The other reason could be due to number of breaking fragments may have not reached a saturation level for the sample system using HiPCO SWNTs as strain sensor since matrix fractured when the applied strain reached above 2.3%, and the calculated interfacial shear strength could possibly be lower than its true value. However, the maximum interfacial

shear stress determined by using Raman spectroscopy for the low modulus carbon fibre/epoxy microcomposite system just have small gap of about 9 MPa. This is an advantage of using Raman technique for fragmentation test.

Finally, this study proved that the epoxy matrix yield strength have been significant improved to a value around 62 MPa with the coating of SWNTs at the interface (SWNTs could diffuse into epoxy matrix).

Table 8.7 *The determined average fragment length, critical length, IFSS obtained in conventional method and Raman method.*

Sample system	$l_f(mm)$	$l_c(mm)$	$\tau_c(MPa)$	$\tau_{R_{max}}(MPa)$
HMCF/Epoxy	0.40 ±0.01	0.53 ±0.01	36.81 ±0.25	52.83 ±0.22
LMCF/Epoxy + HiPCO SWNTs	0.87 ±0.05	1.16 ±0.01	25.21 ±0.02	53.93 ±0.06
LMCF/Epoxy + COOH SWNTs	0.79 ±0.05	1.05 ±0.01	27.93 ±0.02	62.29 ±0.06
HMCF/Epoxy + HiPCO SWNTs	0.39 ±0.01	0.52 ±0.01	37.72 ±0.36	53.14 ±0.30
HMCF/Epoxy + COOH SWNTs	0.33 ±0.01	0.44 ±0.01	44.61 ±0.30	64.82 ±0.50

Reference

Huang, Y. and Young, R.J. (1994) Analysis of the fragmentation test for carbon-fibre/epoxy model composites by means of Raman spectroscopy. *Composites Science and Technology*, 52, pp. 505-517.

Netravali, A.N., Henstenburg, R.B., Phoenix, S.L. and Schwartz, P. (1989) Interfacial shear strength studies using the single-filament-composite test Part 1: experiments on graphite fibres in epoxy. *Polymer Composites*, 10(4), pp. 226-241.

Herrera-Franco, P.J. and Drzal, L.T. (1992) Comparison of methods for the measurement of fibre/matrix adhesion in composites. *Composites*, 23(1), pp. 2-27.

Kelly, A. and Tyson, W.R. (1965) Tensile properties of fibre-reinforced metals: copper/tungsten and copper/molybdenum. *Journal of the Mechanics and Physics of Solids*, 13 (6), pp. 329-338.

Ohsawa, T., Nakayama, A., Miwa, M., and Hasegawa, A. (1978) Temperature dependence of critical fibre length for glass fibre reinforced thermosetting resins. *Journal of Applied Polymer Science*, 22, pp. 3203-3212.

McCrum, N.G., Buckley, C.P. and Bucknall, C.B. (1997) Principles of polymer engineering. Oxford University Press.

Huang, Y. and Young, R.J. (1995) Interfacial behaviour in high temperature cured carbon fibre/epoxy resin model composite. *Composites*, 26(8), pp. 541-550.

Nairn, J.A. (1997) On the use of shear-lag methods for analysis of stress transfer in unidirectional composites. *Mechanics of Materials*, 26, pp. 63-80.

Sureeyatanapas, P., Hejda, M., Eichhorn, S.J. and Young, R.J. (2010) Comparing single-walled carbon nanotubes and samarium oxide as strain sensors for model glass-fibre/epoxy composites. *Composites Science and Technology*, 70, pp. 88-93.

Sureeyatanapas, P. (2009) Carbon nanotubes as strain sensors for glass fibres/epoxy model composites. Unpublished thesis (PhD), University of Manchester.

Cox, H.L. (1952) The elasticity and strength of paper and other fibrous materials. *Brit J Appl Phys*, 3, pp. 9-72.

Piggott, M.R. (1980) Load bearing fibre composites. Pergamon, Oxford, pp.83.

Kim, J.K. (1997) Stress transfer in the fibre fragmentation test part3 effects of interface debonding and matrix yielding. *Journal of Materials Science*, 32, pp. 701-711.

CHAPTER 9 Conclusions and Suggestions for Future Work

9.1 Conclusions

In this project, low modulus carbon fibres have been rendered more Raman active in order to study interfacial properties and stress transfer in a number of microcomposites. The theme of this project has been to compare production methods, forms of nanotubes and testing methods. The stress transfer of low modulus carbon fibre/epoxy microcomposites in three different micromechanical tests of epoxy microdroplet method, epoxy film method and fragmentation test have been analysed. These results were then compared with those obtained from high modulus carbon fibre microcomposite samples. Moreover, the results from three different micromechanical tests were compared with each other, the pros and cons of each micromechanical test have been assessed. The fragmentation test was found to give the highest values of interfacial shear stress. For the fragmentation test, a conventional approach and one using a Raman technique to map local strain have also been compared. The Raman method proved to be more efficiency due to the fact that it can fully monitor the fragmentation process point by point.

9.1.1 Material Characterization and Mechanical Properties

In this work, the properties of both high modulus and low modulus carbon fibres have been analysed. The diameters of the high and low modulus carbon fibres have been measured with values of 5.23 ± 0.25 μm and 5.35 ± 0.32 μm by using SEM. These values are consistant with data reported by their manufacturers; both of them are 5.0 μm.SEM is a method to study the morphology of carbon fibres compared to optical microscopy due to its high resolution and higher depth of field. It is observed by SEM that there are no significant differences in surface morphology between the two types of carbon fibre with both of them having shallow furrows parallel to the fibre axis, typical PAN precursor carbon fibres (Bascom and Drzal, 1987). However, the morphology of the cross sections of two types of fibre are quite different as the low modulus fibre has a smooth fractured cross section, but the high modulus fibre has a clear skin-core structure, within which the turbostratic graphite layers can be clearly observed. This is due to the different manufacturing processes; the high modulus carbon fibres are produced using a higher graphitization temperature. It may also be due to micro

structural differences; the high modulus carbon fibre has highly oriented graphene layers parallel to the fibre axis, Raman spectra of the two types of carbon fibres show significant differences. The high modulus carbon fibre has a sharp and well-defined D band, a G band, a G' band and a 2D band, but the spectrum from the low modulus carbon fibre only shows broad but weak D band and a G band; no 2D band is present. Other characterization methods such as X-ray diffraction and Atomic force microscopy have not detected significant differences between these two types of carbon fibres as both types of carbon fibres have no other chemical elements present other than carbon. It has also been shown that they have similar average crystal sizes.

Tensile testing of the fibres was then carried out to determine their mechanical behaviour. The effect of sample gauge length has also been considered as Young's modulus of a short gauge length can be underestimated (Arridge *et al.*, 1976). The breaking strength for a high modulus and a low modulus carbon fibre were determined to be 3.75 ±0.17GPa and 5.74 ± 0.21GPa respectively. Both breaking strength values are slightly lower than the values reported from their manufacturer; 4.2 GPa and 5.8 GPa respectively. The breaking strains were found to be 0.95% ±0.07% and 1.74 ±0.10% respectively; the value from their manufacturers are1.0% and 2.0%. The Young's moduli were calculated to be 451.1 ±0.7 GPa and 264.8 ±0.4 GPa for the high modus and low modulus carbon fibre respectively; the values reported by their manufacturers are 436 GPa and 290 GPa. The differences between the experimental data and the manufacturer's values could be due to the testing environment and protocols.

The dispersion of SWNTs in different solvents have been tested, ethanol have been found to be the best dispersion solvent with the highest solubility. The HiPCO and COOH SWNTs have been characterized using Raman spectroscopy, as both of them were highly Raman sensitive materials, with D band, G band, 2D bands and radial breathing modes clearly observed. However, the band positions of each types of band from these two types SWNTs are slightly different due to their differences in microstructure. All bands were fitted using a Lorentzian function and their positions were recorded. Additionally the diameters of HiPCO SWNTs and COOH SWNTs have been calculated to be 0.9-1.0 nm and 1.4-1.7 nm from their RBMs respectively.

Thirdly, the mechanical properties of epoxy dumbbell shaped microcomposite specimens have been determined with the average breaking strain of 2.3% ±0.1%,

average Young's modulus of 2.63±0.28 GPa and average breaking strength of 59.6GPa. This means deformation of single carbon fibre/epoxy microcomposite in the fragmentation test cannot exceed 2.3% as the dumbbell shaped microcomposite fractured when deformation is above this level.

9.1.2 Single Fibre deformation

In this section, Raman 2D band shift rates with respect to fibre strain under different polarised configurations for a range of single carbon fibre samples have been determined.

Since the weak D and G bands obtained from low modulus carbon fibres were not useable to monitor fibre deformation, two types of single walled carbon nanotubes (HiPCO SWNTs and COOH SWNTs) were coated on the fibre surface to be used as strain sensors. Different coating methods including SWNTs in a silane layer with and without an epoxy layer, SWNTs in an epoxy layer with and without a silane layer, the effect of epoxy layer curing methods (hot cured or cold cured), effects of epoxy layer preparation method (SWNTs first in hardener or ethanol), the effects of different concentrations of SWNTs and the effects of laser polarisation have all been analysed. The best curing method was chosen according to the magnitude of the Raman 2D band shift rates with respect to the fibre strain. A higher 2D band shift rates from the same sample system was taken to imply a better adhesion of SWNTs to the fibre and better stress transfer efficiency. Finally the coating method of dispersing SWNTs in a silane layer, followed by coating with epoxy and hot curing was found to be the best approach, giving the highest 2D band shift rates with respect to fibre strain. Additionally, it was also found that higher 2D band shift rates can be achieved by using a laser polarisation configuration of VV. Under this polarisation condition the direction of polarised laser is parallel to the fibre axis. With the direction of the stress parallel to the direction of the polarised laser, larger shifts are obtained when the polarisation direction is coincident with the principal stress axis.

Furthermore, in order to compare the results from low modulus carbon fibre samples, both types of SWNTs have been coated on high modulus carbon fibres as well. Interestingly, two Raman 2D bands from high modulus carbon fibre and SWNTs

respectively were expected to be obtained from the samples. However, only one 2D band was observed from the spectra due to possibly the high intensity 2D band observed from SWNTs which overshadowed the one from high modulus carbon fibre. Then 2D band shift rates from high modulus carbon fibre samples were determined to be in the order of HMCF> HMCF+COOH SWNTs > HMCF + HiPCO SWNTs, and this was explained by the theory of stress transfer efficiency from fibre to SWNTs, COOH SWNTs could have better bonding with the fibre than that of HiPCO SWNTs. The fact that the stress induced shift rate of a high modulus carbon fibre on its own is greater than that with SWNTs coated on fibre surface could be caused by two reasons. One is the microstructural difference as the high modulus carbon fibre have highly aligned graphene layers parallel to the fibre axis, resulting in the hexagonal microstructure being more sensitive to fibre deformation along the fibre axis giving a high Raman band shift rate. For the SWNTs, since the determined Raman band shift rate is a contribution of all SWNTs, and they are randomly dispersed on the fibre surface in all directions, the shift may be reduced by a factor, as previously reported by Deng *et al.* (2011) in an intensity weighted function (Function 5.5 and 5.6). The other reason is that during the fibre deformation the stress is transferred from the fibre to SWNTs, as the bond between the fibre and SWNTs is perhaps not perfect, fibre is more deformed than that of SWNTs, thus turned out to be a higher Raman band shift rates.

These Raman shift rates from all types of samples have been recorded and will be used as calibration in analyse the interface of single carbon fibre/epoxy microcomposites by using Raman spectroscopy. It should be noted that the tensile properties of single fibres have not been significantly changed after coating SWNTs on the fibre surface using the best coating method which will give the highest Raman shift rates.

9.1.3 Monitoring the Interface of Single Carbon Fibres and Epoxy Microcomposites in Different Micromechanical Geometries.

9.1.3.1 Epoxy Microdroplet Method

The micromechanical geometry of a microdroplet on a carbon fibre has been analysed. The size and shape of a range of microdroplets on carbon fibre was initially characterized and the droplets with the embedded length of a specific range of 200 ±

20μm were selected under optical microscopy, in order to minimize the effect of embed length. Raman spectroscopy has been effectively used in obtaining comprehensive information about the interface between an epoxy droplet and carbon fibres due to its high sensitivity, high spatial resolution, point–to-point measurement, non-destructive and non-contact measurement. The interfacial shear stress along the fibre has been determined for the epoxy microdroplet and high modulus carbon fibre system; the obtained results varied significantly between different samples. Subsequently the study found that the microdroplet geometry shape by means of edge contact angle has a dominant effect on the interfacial properties. This geometric effect has been investigated numerically using a 2D dimensional model. It was found that a larger interfacial edge angle of the microdroplet is normally equivalent to a shorter stress transfer length and a sharper decrease in fibre stress at the edge of microdroplet, thus generating a higher interfacial shear stress. This also means a greater possibility of interfacial failure and breakage will occur in this region. Due to the high ISS values obtained for the microdroplet model it was deemed unreliable.

9.1.3.2 Epoxy Film method

In order to avoid the effects of the edge contact angle on the measured interfacial properties, a thin epoxy film on a carbon fibre was created and investigated. The determined maximum ISS for the high modulus carbon fibre/epoxy film model system without SWNTs have been determined to be 24.3 ±0.11MPa.The ISS values from films samples with HiPCO SWNTs and COOH SWNTs were determined to be 30.7±0.09 MPa and 38.4±0.07 MPa respectively, indicating the improvement of the interface with the presence of nanotubes. The maximum ISS determined for the low modulus carbon fibre/epoxy film model system with HiPCO SWNTs and COOH SWNTs as strain sensors has been obtained to be 39.8±0.12 MPa and 51.1±0.18 MPa respectively. This does not mean that the interface between low modulus carbon fibre and epoxy is better than that between the high modulus carbon fibre and epoxy. Because the maximum stress (strain) applied on low modulus carbon fibre samples is 3.2 GPa (1.2%) which is higher than the maximum stress (strain) applied on the high modulus carbon fibre is 3.2 GPa (1.1%), thus there is no doubt that the maximum ISS generated from the low modulus carbon fibre/epoxy film system is higher than the high modulus carbon fibre/ epoxy film system. For the epoxy film model with a low modulus carbon fibre, the

systems sensed by both types of SWNTs were found to exhibit interfacial debonding at the edge regions when the applied strains were above 0.6% .It should be noted that the applied strain level can only reach a maximum level of 0.7% for the epoxy film model of high modulus carbon fibre systems; this could be a very important reason that such interfacial debonding performance of corresponding applied strain level of 0.9% and 1.2% for the low modulus carbon fibre system cannot be found for the high modulus carbon fibre systems. For the epoxy film model with high modulus carbon fibre, the system without SWNTs has been found interfacial debonding occurred at the edge region even when the applied strain was as low as 0.3%. Therefore, adding SWNTs on the high modulus carbon fibre surface clearly improves the interface; this is especially true for COOH SWNTs. The reasons that SWNTs improve the interface have been previously investigated They have been reported to act as a strong catalyst (Puglia *et al.*, 2002), and significantly benefitting chemical bonding between epoxy resin and a bisphenol A sized carbon fibre (Toray Industry Inc., 2011). Since the coating of SWNTs at the interface has offered a large surface area (the total outer surface area of the individual tubes is about 1300 m^2/g) for chemical reaction (Colon and Meador, 2006). Furthermore, the chemical reaction among the carboxylic group hybrid on the COOH SWNTs, the amino group from silane or epoxy (Isophorone diamine and cyclohexylamine), the hydroxy group from carbon fibre (Bisphenol A) and epoxy in the interfacial area have improved the interfacial bonding even better.

9.1.3.3 Fragmentation Test

Since both micromechanical tests, epoxy microdroplet and epoxy film methods, are based on the performance of stress transferring from the fibre to the matrix, another micromechanical test method of fragmentation where stress was transferred from the matrix to fibre was carried out in order to monitor the interface. The embedded fibre length was kept the same as for the epoxy film method. Fragmentation tests, both using a Raman technique to map strain along individual fragments, and the conventional approach have been successfully performed. The highest value of ISS of 64.82 ± 0.50 MPa was achieved using Raman technique from a high modulus carbon fibre coated with COOH SWNTs and a layer of epoxy resin. The presence of COOH SWNTs at the interface clearly improves the interfacial bonding, due to its carboxylic group involved in the chemical reaction and formed better bonding. This was not the case for HiPCO

SWNTs. The test found out the determined value of ISS from the high modulus carbon fibre/epoxy sample system with HiPCO SWNTs was just about 1 MPa higher than the value of ISS from the system without HiPCO SWNTs. This means that the coating of HiPCO SWNTs on fibre surface is a better method than coating COOH SENTs, as it is capable of measuring the inherent properties of the interface for the low modulus carbon fibres without affecting the interface too much. However, it is no doubt that the coating of HiPCO SWNTs still improved the interface as it offered large surface areas for the chemical reaction at the interface.

For the conventional fragmentation test, the determined interfacial shear strength determined from the high modulus carbon fibre/epoxy sample system is about 10 MPa higher than the interfacial shear strength determined from the low modulus carbon fibre/epoxy sample systems.. This is due to the higher breaking strength of the low modulus carbon fibre which resulted in higher average fragment length of the low modulus carbon fibre/epoxy sample system. The other reason could also due to possibly the numbers of fragment have not reached a saturation level even when the applied matrix strain reach 2.3% and matrix fractured later for the sample system of low modulus carbon fibre/epoxy sensed by HiPCO SWNTs. However, it shows that the gap of obtained maximum ISS from Raman technique method was not that large with just 5MPa between these two types of sample systems. This again proved the fragmentation test monitored by using Raman spectroscopy can provide a lot more information about the interface during the fragmentation procedure due to its point to point scan along the interface at each elevated matrix strain levels, but the conventional method just can give one value of ISS after saturation. Moreover, it proves that the coating of SWNTs at the interface improves the matrix yield strength due to that SWNTs have diffused into epoxy matrix. COOH SWNTs has improved the interfacial (matrix)yield strength even better due to its carboxylic group involved in the chemical reaction with the amino and hydroxyl group from epoxy resin.

Finally, compared with the epoxy microdroplet method or the epoxy film method, the micromechanical test of fragmentation obtained higher values of ISS for all sample systems due to it can deform the interface into a ultimate stage and break carbon fibres into their critical length , but the experimental process stopped once carbon fibre broke at outside of epoxy microdroplet or epoxy film for both the epoxy microdroplet and

epoxy film method and the interfacial failure only occurred at the edge area of microdroplet or epoxy film.

9.2 Suggestion for Future Work

9.2.1 Graft SWNTs on Carbon Fibres

In this study, it has determined that the adhesion bonding of SWNTs on the carbon fibre surface have tremendous impact on the single fibre deformation results, while if the carbon nanotubes were grown on carbon fibre, it could exhibit a perfect bonding between the fibre and carbon nanotubes. A recent work demonstrated that carbon nanotubes can be well grown on a single carbon fibre homogenously by using chemical vapour deposition (Lachman *et al.*, 2012). Then the fibre with grafted carbon nanotubes can be used to do single fibre deformation test and micromechanical test such as epoxy microdroplet method, epoxy film method and fragmentation test. The results can then be compared with that from this project. It can expect that the interface properties can be significantly enhanced due to the incorporation of carbon nanotubes and carbon fibre can make fibre surface tougher.

9.2.2 Try Using other Method to Coat SWNTs on Fibre Surface

In this study, the coating of SWNTs on carbon fibre surface was carried out by soak fibre into ethanol solvent contain SWNTs. It was found out that some area on the carbon fibre surface have the agglomeration of SWNTs. The work carried by Zhao *et al* (2009) suggested that a ambient spray deposition technique could prepare particularly well SWNTs layer coating. This technique could be used to eliminate the agglomeration of SWNTs on carbon fibre surface in this study.

9.2.3 Use Raman Spectroscopy to Monitor Interface of Other Matrix Reinforced by Carbon Fibres

In this work, the successfully coating of SWNTs on low modulus carbon fibre surface has made the fibre Raman active. COOH SWNTs was found to have chemical reaction with epoxy resin matrix. However, in industry low modulus carbon fibre have been used to reinforce a lot of matrix materials, except epoxy resin, there are polyester resin, vinyl ester resin and phenolic resin. Then COOH SWNTs may have chemical reaction with other matrix systems. Therefore, their interfacial properties could also be studied by using Raman spectroscopy while coating SWNTs on the fibre surface.

9.2.4 Compare the Results by Using Other Strain Sensors

Apart from using SWNTs as strain sensor, there are other types of Raman sensitive materials can be used to sense the strain fibre surface. Polyurethanes which is highly stress sensitive under resonant Raman scattering used to be studied by Halary *et al* (2004), could also applied on the carbon fibre surface to monitor interfacial properties and then compare its efficiency with SWNTs as strain sensors.

References

Arridge, R.G.C., Folkes, M.J. (1976) Effective of sample geometry on the measurement of mechanical properties of anisotropic materials, *Polymer*, 17, pp. 495-500.

Bascom, W.D., Drzal, L.T. (1987) The surface properties of carbon fibre and their adhesion to Organic Polymers, *NASA Contractor Reports*, 4084, pp. 13.

Colon, M.L. and Meador, M.A. (2006) Modified single-wall carbon nanotubes for reinforce thermoplastic polyimide, *NASA Glenn Research Centre Technical report*, pp. 1-8.

Deng, L., Eichhorn, S.J., Kao, C.C. and Young, R.J. (2011) The effective Young's modulus of carbon nanotubes in composites. *ACS Applied Materials Interfaces*, 3, pp. 433-440.

Eichhorn, S.J. and Young, R.J. (2004) Composite micromechanics of hemp fibres and epoxy resin microdroplets, *Composites Science and Technology, Science direct*, 64. pp. 767–772.

Halary, J., Cookson, P., Stanford, J.L., Lovell, A. and Young, R.J.(2004) Smart Nanostructured Polymeric Coating for Use as Remote optical Strain sensors, *Advanced Engineering Materials*, 6(9). pp. 729-733.

Kurti, J., Zolyomi, V., Kertesz, M., Sun, G. (2003) The geometry and radial breathing mode of carbon nanotubes: beyond the ideal behaviour, *New Journal of physics*, 5(125), pp. 1-21.

Lachman, N., Carey, B.J., Hashim, D.P., Ajayan, P.M. and Wagner, H.D. (2012) Application of continuously-monitored single fibre fragmentation tests to carbon nanotube/carbon microfiber hybrid composites, *Composites Science and Technology* , 72, pp. 1711-1717.

Puglia, D., Valentini, L. and Kenny, J.M. (2002) Analysis of the cure reaction of carbon nanotubes/epoxy resin composites through thermal analysis and Raman spectroscopy. *Journal of Applied Polymer Science*, 88, pp. 452-458.

Zhao, X., Chu, B.T.T., Ballesteros, B., Wang, W., Johnston, C., Sykes, J.M. and Grant, P.S. (2009) Spray deposition of steam treated and functionalized single-walled and multi-walled carbon nanotube lms for super capacitors, *Nanotechnology*, 20(065605). pp. 1-9.

Appendix

Appendix A

The diameters of both high modulus and low modulus carbon fibre have been measured by using SEM as the results are shown in Table A.1 and Table A.2.

Table A.1 *Fibre diameters for the high modulus carbon fibre.*

Sample	1	2	3	4	5
Diameter(μm)	5.31±0.20	4.98±0.30	5.55±0.30	5.52±0.20	5.36±0.30
Sample	6	7	8	9	10
Diameter(μm)	4.98±0.20	5.44±0.20	5.59±0.30	4.99±0.20	5.11±0.20
Sample	11	12	13	14	15
Diameter(μm)	5.05±0.20	5.20±0.10	5.14±0.10	5.06±0.20	5.07±0.20
Sample	16	17	18	19	20
Diameter(μm)	5.06±0.20	5.27±0.20	5.38±0.20	5.40±0.20	4.92±0.20
Average Diameter(μm)		5.23±0.20			

Table A.2 *Fibre diameters for the low modulus carbon fibre.*

Sample	1	2	3	4	5
Diameter(μm)	5.22±0.30	5.16±0.40	5.69±0.20	5.16±0.30	5.62±0.40
Sample	6	7	8	9	10
Diameter(μm)	5.79±0.20	5.58±0.30	5.75±0.20	4.99±0.30	5.66±0.30
Sample	11	12	13	14	15
Diameter(μm)	5.11±0.30	5.63±0.30	5.08±0.30	5.56±0.20	5.33±0.20
Sample	16	17	18	19	20
Diameter(μm)	4.82±0.30	4.83±0.30	5.15±0.30	5.77±0.40	4.83±0.30
Average Diameter(μm)		5.35±0.30μm			

Appendix B

Table B.1 *The Young's Modulus for the high modulus CF and low Modulus CF (10mm gauge length).*

Modulus of High Modulus CF(GPa)	439.3±0.8	422.4±0.6	406.8±0.9	431.9±0.8	420.8±0.7	Average
	422.9±0.6	418.8±0.9	424.1±0.8	420.1±0.7	420.6±0.6	423.7±0.8
	422.7±0.9	424.7±0.9	423.3±0.8	440.8±1.0	427.1±0.7	
	436.9±0.6	408.9±0.6	407.1±0.7	428.5±0.7	427.6±0.8	
Modulus of Low Modulus CF(GPa)	220.2±0.2	238.3±0.6	240.2±0.1	228.4±0.1	226.8±0.1	Average
	219.6±0.6	221.4±0.3	240.7±0.2	224.7±0.2	233.8±0.6	229.3±0.3
	235.9±0.3	235.8±0.5	233.9±0.2	231.2±0.5	220.1±0.5	
	212.4±0.4	236.1±0.4	246.4±0.1	223.2±0.5	217.3±0.3	

Table B.2 *The Young's Modulus for the high modulus CF and low Modulus CF (20mm gauge length).*

Modulus of High Modulus CF(GPa)	433.2±0.7	431.4±0.5	436.7±0.6	422.7±0.6	420.6±0.9	Average
	434.8±0.6	436.1±0.6	427.2±0.6	420.5±0.5	414.2±0.4	429.2±0.6
	421.6±0.8	435.9±0.7	444.2±0.7	439.2±0.6	426.6±0.8	
	436.3±0.5	427.9±0.9	424.2±0.5	433.1±0.9	416.6±0.6	
Modulus of Low Modulus CF(GPa)	225.2±0.4	232.1±0.3	246.8±0.2	232.0±0.4	225.8±0.2	Average
	224.2±0.1	222.1±0.2	243.1±0.1	239.4±0.3	234.5±0.5	237.1±0.2
	250.7±0.3	243.2±0.1	239.4±0.1	236.7±0.4	229.7±0.3	
	227.1±0.1	252.1±0.1	248.7±0.4	239.3±0.1	250.7±0.2	

Table B.3 *The Young's Modulus for the high modulus CF and low Modulus CF (30mm gauge length).*

Modulus of High Modulus CF(GPa)	455.8±0.8	433.3±0.6	449.9±0.7	447.6±0.9	445.7±0.7	Average
	437.8±0.7	425.2±0.6	450.2±0.6	451.7±0.6	440.8±0.8	437.6±0.7
	418.7±0.6	425.8±0.9	429.6±0.5	436.7±0.8	449.1±0.5	
	428.2±0.9	422.5±0.4	429.2±0.6	456.6±0.5	428.6±0.5	
Modulus of Low Modulus CF(GPa)	260.4±0.3	241.5±0.5	234.3±0.1	254.7±0.6	254.5±0.6	Average
	244.9±0.3	245.7±0.1	260.3±0.1	256.7±0.4	236.7±0.4	243.3±0.4
	224.3±0.5	238.3±0.5	228.2±0.1	237.6±0.5	262.3±0.5	
	249.5±0.3	225.4±0.5	225.1±0.4	243.3±0.5	242.6±0.3	

Table B.4 *The Young's Modulus for the high modulus CF and low Modulus CF (40mm gauge length).*

Modulus of High Modulus CF(GPa)	454.2±0.9	454.7±0.4	449.1±0.6	429.1±0.7	423.8±0.7	Average
	429.9±0.8	427.9±0.5	433.9±0.8	429.3±0.5	429.7±0.7	440.8±0.6
	449.1±0.5	446.5±0.7	432.1±0.6	456.5±0.7	453.7±0.5	
	457.6±0.8	457.8±0.5	424.3±0.6	431.1±0.6	445.5±0.5	
Modulus of Low Modulus CF(GPa)	241.0±0.4	264.1±0.3	244.7±0.2	245.1±0.4	252.6±0.2	Average
	247.9±0.1	270.5±0.2	249.8±0.1	264.5±0.3	266.1±0.5	254.9±0.2
	245.1±0.3	243.7±0.1	266.9±0.1	248.2±0.4	271.9±0.3	
	258.7±0.1	237.9±0.1	249.0±0.4	263.8±0.1	266.2±0.2	

Table B.5 *The Young's Modulus for the high modulus CF and low Modulus CF (50mm gauge length).*

Modulus of High Modulus CF(GPa)	467.4±0.5	437.4±0.5	446.8±0.6	443.2±0.9	439.2±0.5	Average
	448.2±0.5	436.6±0.5	437.2±0.7	457.3±0.7	429.2±0.4	446.4±0.6
	453.1±0.4	447.6±0.7	443.5±0.6	454.7±0.5	467.2±0.7	
	441.3±0.5	436.1±0.8	474.7±0.7	440.3±0.9	456.8±0.4	
Modulus of Low Modulus CF(GPa)	277.0±0.3	250.6±0.4	275.2±0.2	267.5±0.2	249.5±0.3	Average
	246.7±0.3	261.9±0.1	263.4±0.3	272.7±0.2	263.3±0.5	262.4±0.3
	249.2±0.4	252.3±0.2	267.7±0.6	270.6±0.3	259.8±0.5	
	245.2±0.5	275.6±0.6	272.4±0.3	267.5±0.2	259.7±0.6	

Table B.6 *The Young's Modulus for the high modulus CF and low Modulus CF (100mm gauge length).*

Modulus of High Modulus CF(GPa)	440.2±0.9	451.4±0.8	445.0±0.8	435.5±0.4	453.9±0.8	Average
	451.6±0.7	448.2±0.6	446.7±0.6	460.4±0.8	432.2±0.9	451.1±0.7
	431.5±0.8	434.8±0.8	450.3±0.6	467.1±0.5	454.7±0.5	
	465.4±0.7	449.1±0.4	462.5±0.5	457.8±0.6	464.5±0.7	
Modulus of Low Modulus CF(GPa)	279.1±0.5	253.1±0.1	274.7±0.6	264.9±0.3	251.9±0.3	Average
	268.5±0.2	272.9±0.3	250.9±0.2	267.3±0.2	281.2±0.2	263.2±0.3
	255.2±0.6	264.4±0.3	254.8±0.3	256.5±0.2	245.2±0.4	
	278.7±0.3	245.2±0.4	274.9±0.4	266.3±0.1	268.4±0.2	

Table B.7 *The breaking strength of all the samples for the high modulus carbon fibre and low modulus carbon fibre (10mm gauge length).*

Breaking strength of High Modulus CF(GPa)	3.77±0.29	3.59±0.24	3.60±0.24	3.44±0.11	3.57±0.23	Average
	3.66±0.18	3.62±0.38	3.72±0.13	3.72±0.39	3.89±0.19	3.63±0.26
	3.58±0.22	3.55±0.13	3.55±0.12	3.63±0.27	3.44±0.18	
	3.70±0.35	3.37±0.36	3.86±0.17	3.50±0.26	3.85±0.13	
Breaking strength of Low Modulus CF(GPa)	5.37±0.30	5.22±0.11	5.32±0.18	5.30±0.29	5.41±0.18	Average
	5.10±0.18	5.15±0.19	5.25±0.27	5.09±0.10	5.23±0.11	5.25±0.20
	5.40±0.20	5.41±0.26	5.23±0.21	5.25±0.13	5.20±0.13	
	5.24±0.27	5.26±0.17	5.13±0.30	5.27±0.21	5.13±0.27	

Table B.8 *The breaking strength of all the samples for the high modulus carbon fibre and low modulus carbon fibre (20mm gauge length).*

Breaking strength of High Modulus CF(GPa)	3.45±0.24	3.48±0.30	3.55±0.36	3.64±0.14	3.61±0.19	Average
	3.38±0.10	3.31±0.40	3.37±0.10	3.67±0.47	3.48±0.44	3.52±0.28
	3.61±0.34	3.49±0.22	3.35±0.30	3.51±0.24	3.61±0.18	
	3.68±0.34	3.68±0.17	3.69±0.44	3.37±0.19	3.51±0.46	
Breaking strength of Low Modulus CF(GPa)	5.08±0.20	4.99±0.22	5.16±0.22	5.10±0.15	5.08±0.11	Average
	5.18±0.28	4.98±0.16	5.20±0.16	5.03±0.22	4.96±0.22	5.02±0.19
	4.83±0.22	4.89±0.15	5.03±0.23	5.00±0.14	5.02±0.15	
	5.21±0.16	5.04±0.11	4.85±0.20	4.88±0.29	4.93±0.19	

Table B.9 *The breaking strength of all the samples for the high modulus carbon fibre and low modulus carbon fibre (30mm gauge length).*

Breaking strength of High Modulus CF(GPa)	3.37±0.10	3.35±0.48	3.63±0.17	3.64±0.50	3.40±0.42	Average
	3.73±0.27	3.41±0.17	3.53±0.18	3.64±0.11	3.44±0.33	3.53±0.31
	3.67±0.46	3.58±0.41	3.40±0.11	3.33±0.31	3.71±0.42	
	3.61±0.43	3.66±0.45	3.46±0.28	3.42±0.44	3.55±0.21	
Breaking strength of Low Modulus CF(GPa)	4.94±0.16	5.01±0.30	4.61±0.25	4.72±0.21	4.87±0.25	Average
	4.75±0.15	4.92±0.16	4.69±0.10	4.98±0.29	4.83±0.12	4.82±0.19
	4.91±0.28	4.74±0.11	4.61±0.16	4.92±0.13	5.03±0.28	
	4.84±0.20	4.78±0.10	4.82±0.20	4.64±0.13	4.87±0.29	

Table B.10 *The breaking strength of all the samples for the high modulus carbon fibre and low modulus carbon fibre (40mm gauge length).*

Breaking strength of High Modulus CF(GPa)	3.46±0.24	3.25±0.27	3.50±0.34	3.49±0.39	3.64±0.25	Average
	3.27±0.20	3.42±0.26	3.35±0.23	3.58±0.26	3.38±0.45	3.41±0.29
	3.18±0.42	3.48±0.29	3.33±0.46	3.49±0.21	3.26±0.24	
	3.42±0.21	3.41±0.29	3.45±0.47	3.21±0.22	3.60±0.11	
Breaking strength of Low Modulus CF(GPa)	4.60±0.25	4.45±0.25	4.70±0.20	4.73±0.19	4.44±0.22	Average
	4.42±0.11	4.61±0.14	4.65±0.10	4.73±0.22	4.50±0.11	4.59±0.17
	4.63±0.28	4.42±0.18	4.76±0.10	4.51±0.19	4.70±0.10	
	4.50±0.12	4.74±0.11	4.65±0.11	4.57±0.10	4.51±0.27	

Table B.11 *The breaking strength of all the samples for the high modulus carbon fibre and low modulus carbon fibre (50mm gauge length).*

Breaking strength of High Modulus CF(GPa)	3.72±0.43	3.47±0.45	3.16±0.11	3.31±0.37	3.74±0.27	Average
	3.25±0.24	3.69±0.31	3.12±0.24	3.17±0.23	3.20±0.11	3.35±0.27
	3.59±0.34	3.38±0.19	3.25±0.24	3.46±0.16	3.19±0.27	
	3.34±0.35	3.10±0.43	3.39±0.14	3.06±0.24	3.31±0.35	
Breaking strength of Low Modulus CF(GPa)	4.38±0.19	4.51±0.17	4.63±0.12	4.73±0.28	4.53±0.22	Average
	4.57±0.28	4.55±0.22	4.75±0.22	4.38±0.24	4.70±0.20	4.57±0.20
	4.46±0.22	4.68±0.11	4.71±0.21	4.72±0.27	4.44±0.15	
	4.37±0.24	4.36±0.11	4.41±0.23	4.77±0.25	4.81±0.17	

Table B.12 *The breaking strength of all the samples for the high modulus carbon fibre and low modulus carbon fibre (100mm gauge length).*

Breaking strength of High Modulus CF(GPa)	3.18±0.42	3.34±0.22	3.30±0.43	3.28±0.49	3.22±0.20	Average
	3.07±0.24	3.35±0.48	3.30±0.43	3.04±0.25	3.32±0.11	3.17±0.31
	3.05±0.35	3.04±0.48	3.02±0.25	2.99±0.20	3.16±0.47	
	3.23±0.17	3.01±0.16	3.09±0.36	3.13±0.33	3.30±0.14	
Breaking strength of Low Modulus CF(GPa)	4.02±0.19	3.95±0.28	3.93±0.21	3.87±0.20	3.80±0.16	Average
	4.09±0.15	4.01±0.17	3.85±0.11	4.01±0.21	3.93±0.28	3.96±0.19
	4.13±0.14	3.81±0.15	4.00±0.17	3.90±0.29	3.91±0.26	
	3.78±0.16	4.14±0.18	3.93±0.10	4.10±0.15	3.94±0.24	

Table B.13 *The breaking strain of all the samples for the high modulus carbon fibre and low modulus carbon fibre (10mm gauge length).*

Breaking strain of High Modulus CF(%)	0.86±0.02	0.85±0.06	0.80±0.03	0.92±0.06	0.92±0.09	Average
	0.80±0.06	0.89±0.08	0.84±0.03	0.93±0.03	0.83±0.07	0.86±0.05
	0.88±0.04	0.79±0.03	0.83±0.04	0.88±0.08	0.93±0.08	
	0.83±0.03	0.82±0.08	0.81±0.09	0.89±0.02	0.83±0.05	
Breaking strain of Low Modulus CF(%)	1.55±0.04	1.64±0.05	1.56±0.10	1.56±0.07	1.69±0.06	Average
	1.64±0.06	1.65±0.07	1.65±0.09	1.59±0.05	1.64±0.09	1.62±0.08
	1.62±0.09	1.58±0.03	1.60±0.08	1.64±0.11	1.60±0.07	
	1.66±0.07	1.57±0.08	1.67±0.08	1.61±0.08	1.68±0.08	

Table B.14 *The breaking strain of all the samples for the high modulus carbon fibre and low modulus carbon fibre (20mm gauge length).*

Breaking strain of High Modulus CF(%)	0.87±0.06	0.86±0.02	0.86±0.05	0.77±0.09	0.79±0.02	Average
	0.82±0.02	0.84±0.02	0.79±0.09	0.80±0.02	0.81±0.02	0.82±0.04
	0.85±0.02	0.75±0.09	0.84±0.06	0.86±0.02	0.78±0.05	
	0.89±0.04	0.81±0.05	0.86±0.05	0.88±0.02	0.75±0.09	
Breaking strain of Low Modulus CF(%)	1.62±0.06	1.63±0.06	1.64±0.10	1.54±0.11	1.61±0.07	Average
	1.63±0.09	1.64±0.04	1.65±0.04	1.52±0.09	1.66±0.07	1.59±0.07
	1.62±0.03	1.59±0.08	1.54±0.04	1.64±0.04	1.60±0.10	
	1.53±0.03	1.52±0.09	1.64±0.10	1.53±0.10	1.52±0.09	

Table B.15 *The breaking strain of all the samples for the high modulus carbon fibre and low modulus carbon fibre (30mm gauge length).*

Breaking strain of High Modulus CF(%)	0.84±0.06	0.82±0.02	0.77±0.07	0.76±0.08	0.81±0.03	Average
	0.84±0.08	0.75±0.08	0.79±0.08	0.72±0.05	0.71±0.08	0.79±0.05
	0.85±0.02	0.71±0.07	0.80±0.05	0.87±0.04	0.74±0.07	
	0.81±0.05	0.78±0.03	0.85±0.04	0.85±0.05	0.81±0.03	
Breaking strain of Low Modulus CF(%)	1.49±0.12	1.41±0.10	1.44±0.10	1.46±0.11	1.47±0.10	Average
	1.45±0.07	1.43±0.05	1.42±0.04	1.48±0.08	1.49±0.10	1.47±0.09
	1.42±0.10	1.50±0.05	1.43±0.06	1.51±0.05	1.44±0.09	
	1.51±0.10	1.44±0.11	1.53±0.09	1.51±0.08	1.47±0.10	

Table B.16 *The breaking strain of all the samples for the high modulus carbon fibre and low modulus carbon fibre (40mm gauge length).*

Breaking strain of High Modulus CF(%)	0.65±0.07	0.72±0.04	0.69±0.04	0.65±0.06	0.71±0.04	Average
	0.63±0.03	0.76±0.05	0.71±0.06	0.64±0.03	0.61±0.07	0.69±0.05
	0.66±0.05	0.68±0.04	0.64±0.02	0.75±0.06	0.74±0.03	
	0.77±0.04	0.74±0.04	0.70±0.06	0.66±0.06	0.64±0.05	
Breaking strain of Low Modulus CF(%)	1.39±0.11	1.38±0.07	1.42±0.07	1.46±0.09	1.42±0.05	Average
	1.31±0.06	1.39±0.07	1.39±0.06	1.39±0.08	1.40±0.07	1.39±0.07
	1.39±0.08	1.47±0.07	1.40±0.05	1.40±0.08	1.33±0.11	
	1.40±0.13	1.44±0.12	1.37±0.04	1.36±0.07	1.33±0.04	

Table B.17 *The breaking strain of all the samples for the high modulus carbon fibre and low modulus carbon fibre (50mm gauge length).*

Breaking strain of High Modulus CF(%)	0.64±0.03	0.60±0.06	0.69±0.02	0.59±0.06	0.67±0.04	Average
	0.69±0.06	0.68±0.03	0.57±0.05	0.72±0.03	0.66±0.03	0.63±0.05
	0.57±0.05	0.54±0.07	0.63±0.07	0.59±0.07	0.56±0.04	
	0.67±0.05	0.66±0.06	0.58±0.04	0.59±0.07	0.68±0.04	
Breaking strain of Low Modulus CF(%)	1.31±0.09	1.36±0.08	1.39±0.04	1.30±0.05	1.30±0.05	Average
	1.31±0.07	1.44±0.13	1.32±0.09	1.45±0.05	1.27±0.10	1.34±0.07
	1.37±0.04	1.43±0.10	1.37±0.05	1.45±0.06	1.24±0.06	
	1.23±0.04	1.31±0.08	1.34±0.04	1.26±0.04	1.37±0.06	

Table B.18 *The breaking strain of all the samples for the high modulus carbon fibre and low modulus carbon fibre (100mm gauge length).*

Breaking strain of High Modulus CF(%)	0.56±0.05	0.44±0.04	0.45±0.07	0.54±0.05	0.50±0.06	Average
	0.53±0.04	0.47±0.06	0.52±0.06	0.42±0.07	0.49±0.07	0.49±0.05
	0.49±0.03	0.47±0.05	0.51±0.05	0.55±0.03	0.56±0.03	
	0.55±0.04	0.46±0.05	0.43±0.05	0.45±0.05	0.46±0.06	
Breaking strain of Low Modulus CF(%)	1.26±0.05	1.25±0.07	1.12±0.05	1.22±0.04	1.13±0.09	Average
	1.17±0.04	1.15±0.06	1.28±0.07	1.18±0.10	1.22±0.08	1.19±0.07
	1.21±0.06	1.24±0.04	1.24±0.07	1.18±0.07	1.15±0.10	
	1.20±0.05	1.13±0.04	1.27±0.10	1.15±0.05	1.16±0.06	

Appendix C

The measured thickness of epoxy films are shown in Table C.1.

Table C.1 *The measured thickness of 20 epoxy film samples by Optical microscopy.*

The thickness of 20 epoxy film samples(μm)	217.39 ± 0.22	204.71 ±0.17	233.24 ±0.27	221.47 ±0.20	215.58 ±0.18
	203.59 ±0.19	227.12 ±0.21	229.91 ±0.23	224.14 ±0.19	214.46 ±0.14
	216.12 ±0.20	238.15 ±0.28	219.69 ±0.17	239.04 ±0.22	237.50 ±0.24
	231.27 ±0.26	215.44 ±0.19	225.85 ±0.20	206.83 ±0.16	239.65 ±0.29

Appendix D

There are no significant differences for the obtained IFSS of 5 different epoxy film/high modulus carbon fibre samples as shown in the following five Figures. The thickness of the 5 different samples are in the range of 200~240 μm.

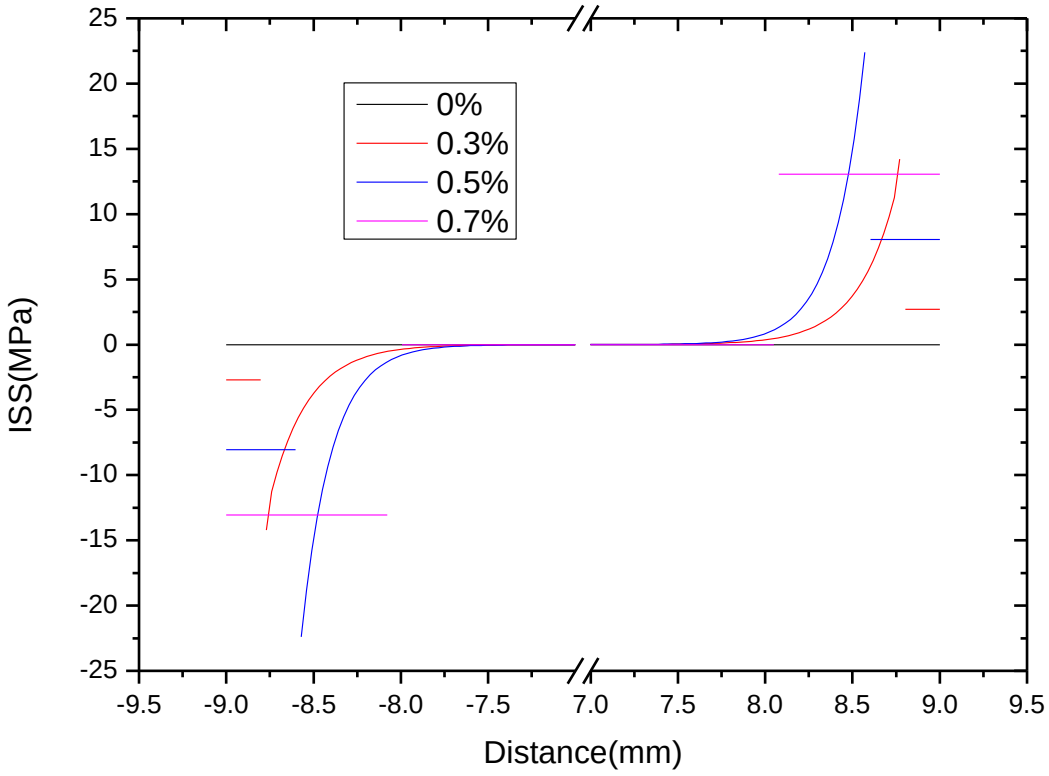

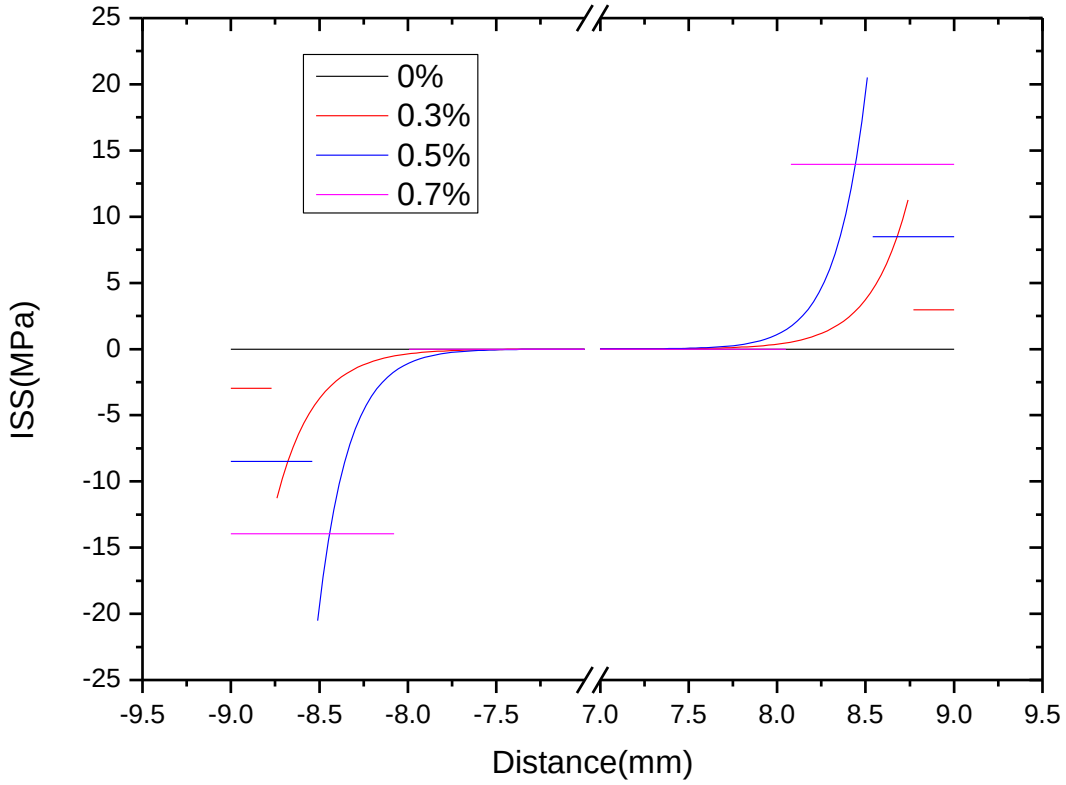
0%
0.3%
0.5%
0.7%
ISS(MPa)
Distance(mm)
25
20
15
10
5
0
-5
-10
-15
-20
-25
-9.5
-9.0
-8.5
-8.0
-7.5
7.0
7.5
8.0
8.5
9.0
9.5

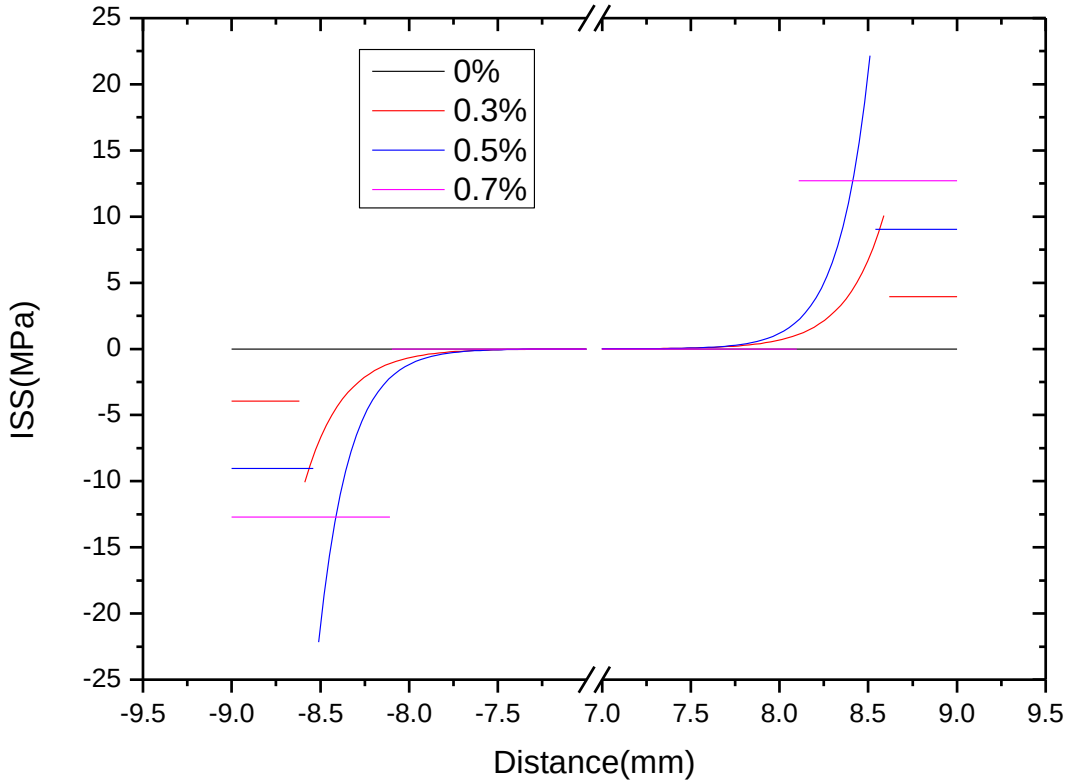
0%
0.3%
0.5%
0.7%
ISS(MPa)
Distance(mm)
25
20
15
10
5
0
-5
-10
-15
-20
-25
-9.5
-9.0
-8.5
-8.0
-7.5
7.0
7.5
8.0
8.5
9.0
9.5

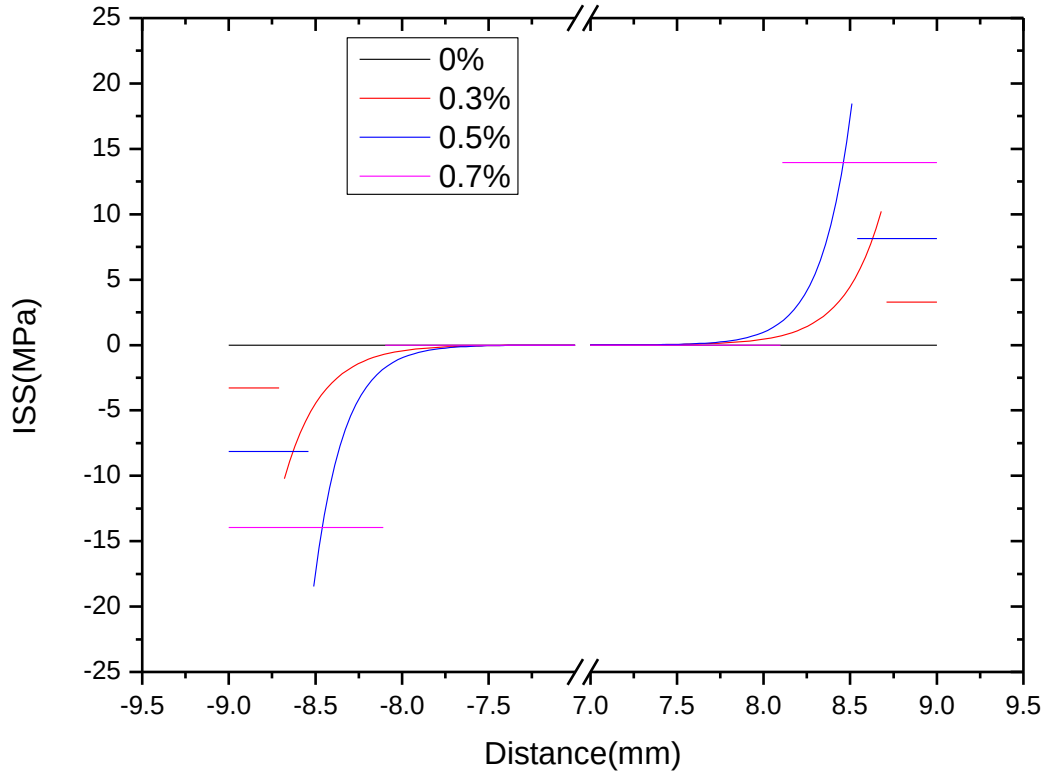
0%
0.3%
0.5%
0.7%
ISS(MPa)
Distance(mm)
25
20
15
10
5
0
-5
-10
-15
-20
-25
-9.5
-9.0
-8.5
-8.0
-7.5
7.0
7.5
8.0
8.5
9.0
9.5

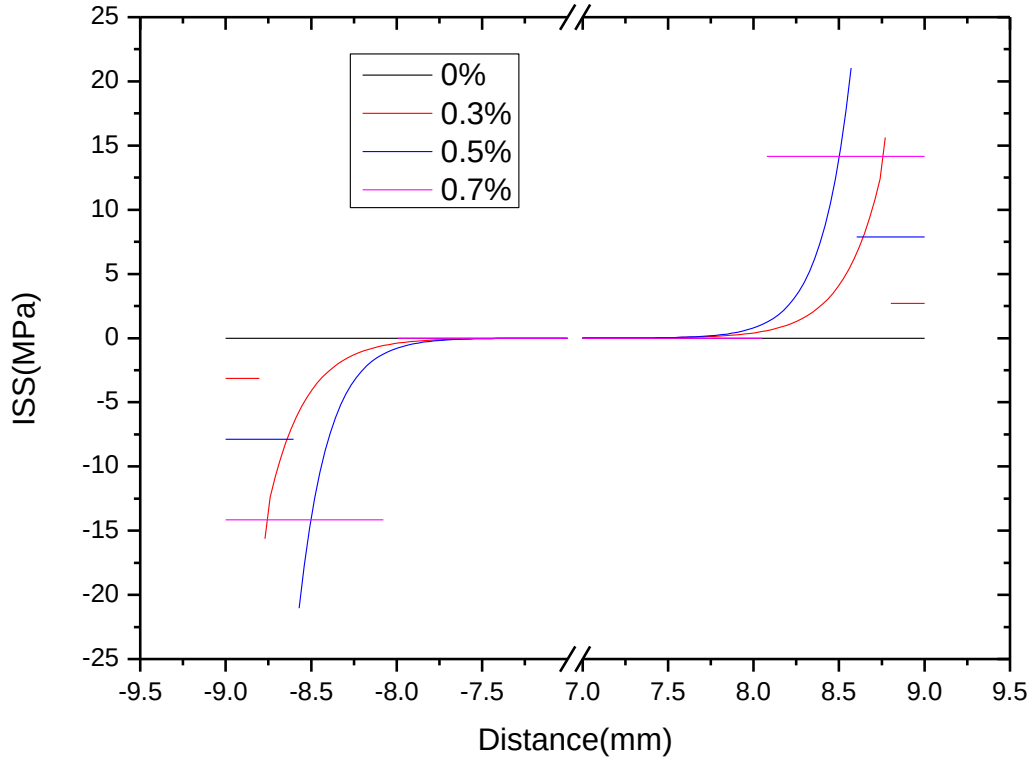
0%
0.3%
0.5%
0.7%
ISS(MPa)
Distance(mm)
25
20
15
10
5
0
-5
-10
-15
-20
-25
-9.5
-9.0
-8.5
-8.0
-7.5
7.0
7.5
8.0
8.5
9.0
9.5

Appendix E

Table E.1 *Fragment lengths at 1.8% matrix strain for a high modulus carbon fibre/epoxy resin composite system.*

$l_f(mm)$	0.49 ±0.003	0.38 ±0.005	0.29 ±0.003	0.57 ±0.004	0.22 ±0.003
0.56 ±0.003	0.64 ±0.004	0.57 ±0.004	0.46 ±0.005	0.38 ±0.003	0.41 ±0.004
0.29 ±0.005	0.32 ±0.005	0.25 ±0.004	0.28 ±0.005	0.19 ±0.004	0.33 ±0.004
0.57 ±0.003	0.28 ±0.004	0.37 ±0.005	0.18 ±0.004	0.29 ±0.004	0.22 ±0.005
0.20 ±0.004	0.19 ±0.004	0.31 ±0.004	0.33 ±0.004	0.28 ±0.004	0.19 ±0.004
0.67 ±0.005	0.36 ±0.005	0.38 ±0.004	0.56 ±0.005	0.23 ±0.005	0.29 ±0.005
0.68 ±0.004	0.24 ±0.003	0.27 ±0.005	0.32 ±0.004	0.35 ±0.005	Average= 0.40 ±0.005
0.61 ±0.004	0.26 ±0.003	0.24 ±0.004	0.37 ±0.005	0.16 ±0.004	

Table E.2 *The determined fragment length at matrix strain level of 1.8%, 2.1% and 2.3% for the sample system of low modulus carbon fibre/epoxy use HiPCO SWNTs and COOH SWNTs as strain sensor.*

Matrix strain level	Fragment length(mm)				
	Samples using HiPCO SWNTs as strain sensor		Samples using COOH SWNTs as strain sensor		
1.8 %	7.03 ±0.004	2.83 ±0.006	3.22 ±0.004	2.84 ±0.005	2.46 ±0.005
	2.86 ±0.004	2.64 ±0.005	2.49 ±0.004	3.41 ±0.003	3.81 ±0.003

	2.82 ±0.005		Average 3.64 ±0.05		Average 3.04 ±0.04			
2.1 %	0.95 ±0. 003	0.92 ±0. 004	1.55 ±0. 004	1.23 ±0. 004	0.65 ±0. 005	1.07 ±0. 004	0.75 ±0. 005	0.73 ±0. 006
	1.15 ±0.004	1.05 ±0. 004	1.32 ±0. 005	1.13 ±0. 003	0.56 ±0. 005	0.62 ±0. 005	0.95 ±0. 005	0.95 ±0. 004
	0.91 ±0. 004	1.03 ±0. 005	1.25 ±0. 004	1.52 ±0. 005	0.85 ±0. 006	1.05 ±0. 004	0.53 ±0. 004	0.65 ±0. 005
	1.33 ±0. 005	2.75 ±0. 004	Average 1.29 ±0.04		0.95 ±0. 004	0.85 ±0. 005	0.55 ±0. 003	0.61 ±0. 004
					0.83 ±0. 006	0.91 ±0. 005	0.75 ±0. 004	0.92 ±0. 003
					0.75 ±0. 004	0.85 ±0. 004	0.95 ±0. 005	Averag e 0.79 ±0. 05
2.3 %	0.95 ±0. 005	0.85 ±0. 003	0.92 ±0. 004	0.85 ±0. 005	0.65 ±0. 006	1.03 ±0. 005	0.75 ±0. 005	0.75 ±0. 004
	0.74 ±0. 005	0.61 ±0. 004	0.85 ±0. 005	0.76 ±0. 005	0.45 ±0. 005	0.63 ±0. 004	0.92 ±0. 004	0.95 ±0. 005
	0.82 ±0. 005	0.94 ±0. 004	0.76 ±0. 003	0.55 ±0. 005	0.85 ±0. 004	1.05 ±0. 005	0.55 ±0. 004	0.55 ±0. 005
	0.75 ±0. 005	0.92 ±0. 004	1.01 ±0. 003	0.93 ±0. 005	1.07 ±0. 004	0.91 ±0. 004	0.55 ±0. 005	0.63 ±0. 004
	1.04 ±0. 005	0.85 ±0. 004	0.95 ±0. 005	0.95 ±0. 004	0.85 ±0. 005	0.85 ±0. 004	0.75 ±0. 004	0.91 ±0. 003

	1.35±0.005	Average 0.87±0.05	0.82±0.004	0.82±0.003	0.95±0.005	Average 0.79±0.05

Table E.3 *The determined fragment length at matrix strain level of 1.8%, 2.1% and 2.3% for the high modulus carbon fibre/epoxy system use HiPCO SWNTs and COOH SWNTs as strain sensors.*

Matrix strain level	Fragment length(mm)									
	Samples using HiPCO SWNTs as strain sensor					Samples using COOH SWNTs as strain sensor				
1.2%	1.26±0.004	1.55±0.003	0.94±0.004	0.95±0.003	1.02±0.005	2.05±0.005	0.95±0.003	0.61±0.003	0.92±0.004	0.70±0.005
	1.28±0.004	0.95±0.003	1.15±0.005	1.31±0.005	0.55±0.003	0.55±0.005	0.78±0.004	0.51±0.003	0.69±0.003	0.55±0.003
	1.55±0.004	1.13±0.003	0.64±0.005	1.01±0.003	1.55±0.004	0.79±0.003	0.55±0.003	0.81±0.006	0.45±0.004	0.75±0.003
	Average 1.12±0.004					0.65±0.005	0.69±0.003	0.71±0.004	0.65±0.005	0.65±0.006
						0.85±0.004	0.55±0.005	0.65±0.004	0.95±0.003	Average 0.75±

										0.004
1.5 %	0.65 ± 0.003	0.51 ± 0.005	0.68 ± 0.003	0.72 ±0 .006	0.59 ± 0.004	0.61 ± 0.003	0.26 ± 0.003	0.25 ± 0.005	0.41 ± 0.006	0.23 ± 0.003
	0.54 ± 0.004	0.81 ± 0.006	0.44 ± 0.004	0.46 ±0 .003	0.31 ± 0.005	0.19 ± 0.003	0.43 ± 0.004	0.23 ± 0.005	0.35 ± 0.003	0.33 ± 0.006
	0.39 ± 0.005	0.35 ± 0.005	0.42 ± 0.003	0.45 ±0 .006	0.30 ± 0.003	0.44 ± 0.004	0.45 ± 0.003	0.51 ± 0.003	0.44 ± 0.005	0.31 ± 0.006
	0.35 ± 0.004	0.35 ± 0.004	0.35 ± 0.006	0.29 ±0 .005	0.28 ± 0.006	0.31 ± 0.005	0.29 ± 0.003	0.31 ± 0.003	0.26 ± 0.004	0.35 ± 0.005
	0.29 ± 0.003	0.34 ± 0.003	0.40 ± 0.005	0.31 ±0 .006	0.35 ± 0.006	0.38 ± 0.004	0.25 ± 0.003	0.29 ± 0.005	0.35 ± 0.006	0.21 ± 0.003
	0.35 ± 0.004	0.45 ± 0.004	0.35 ± 0.006	0.29 ±0 .003	0.42 ± 0.005	0.35 ± 0.003	0.20 ± 0.003	0.34 ± 0.004	0.31 ± 0.006	0.22 ± 0.003
	0.35 ± 0.003	0.28 ±0.00 5	0.45 ± 0.004	0.41 ±0 .003	0.28 ± 0.006	0.20 ± 0.004	0.24 ± 0.003	0.31 ± 0.003	0.24 ± 0.006	0.23 ± 0.004
	0.35 ± 0.003	0.45 ± 0.005	0.38 ± 0.003	0.29 ±0 .006	0.39 ± 0.004	0.55 ± 0.005	0.49 ± 0.005	0.25 ± 0.006	0.35 ± 0.003	0.51 ± 0.003
	0.28 ± 0.003	0.49 ± 0.005	0.68 ±0.00 3	Average 0.42 ±0.00 3		0.24 ± 0.006	0.31 ± 0.005	0.35 ± 0.004	0.55 ± 0.003	0.39 ± 0.005
						0.29 ± 0.004	0.35 ± 0.004	0.41 ± 0.003	0.39 ± 0.006	0.27 ± 0.003
						0.61 ± 0.005	0.57 ± 0.004	Average 0.35 ±0.004		
1.8 %	0.41 ± 0.003	0.35 ± 0.003	0.50 ± 0.005	0.54 ±0 .002	0.45 ± 0.006	0.59 ± 0.004	0.21 ± 0.003	0.29 ± 0.005	0.35 ± 0.006	0.31 ± 0.006

	0.39 ± 0.004	0.55 ± 0.005	0.49 ± 0.003	0.81 ±0.004	0.41 ± 0.002	0.19 ± 0.003	0.41 ± 0.005	0.25 ± 0.006	0.35 ± 0.005	0.29 ± 0.004
	0.49 ± 0.005	0.31 ± 0.003	0.35 ± 0.004	0.39 ±0.005	0.39 ± 0.003	0.51 ± 0.006	0.39 ± 0.005	0.54 ± 0.003	0.44 ± 0.004	0.35 ± 0.006
	0.46 ± 0.003	0.29 ± 0.004	0.39 ± 0.006	0.35 ±0.003	0.31 ± 0.002	0.25 ± 0.003	0.29 ± 0.005	0.35 ± 0.006	0.29 ± 0.004	0.33 ± 0.005
	0.31 ± 0.002	0.29 ± 0.005	0.30 ± 0.003	0.35 ±0.005	0.34 ± 0.004	0.23 ± 0.003	0.32 ± 0.003	0.35 ± 0.005	0.31 ± 0.005	0.24 ± 0.003
	0.31 ± 0.005	0.30 ± 0.005	0.38 ± 0.003	0.45 ±0.004	0.29 ± 0.003	0.29 ± 0.006	0.27 ± 0.004	0.25 ± 0.006	0.31 ± 0.004	0.30 ± 0.002
	0.35 ± 0.004	0.39 ± 0.003	0.33 ± 0.005	0.38 ±0.005	0.38 ± 0.005	0.35 ± 0.004	0.24 ± 0.003	0.25 ± 0.006	0.33 ± 0.005	0.49 ± 0.005
	0.34 ± 0.004	0.36 ± 0.004	0.34 ± 0.005	0.51 ±0.006	0.42 ± 0.004	0.28 ± 0.005	0.33 ± 0.005	0.21 ± 0.003	0.30 ± 0.003	0.48 ± 0.003
	0.31 ± 0.006	0.39 ± 0.002	0.41 ± 0.005	0.43 ±0.005	0.29 ± 0.003	0.24 ± 0.004	0.31 ± 0.004	0.39 ± 0.005	0.21 ± 0.004	0.29 ± 0.004
	0.36 ± 0.005	Average 0.39 ±0.004				0.40 ± 0.005	0.23 ± 0.004	0.34 ± 0.004	0.39 ± 0.003	0.41 ± 0.006
						0.36 ± 0.002	0.25 ± 0.005	0.33 ± 0.005	0.57 ± 0.004	Average 0.33 ± 0.005